IMPERIAL

Hypersonic Boundary Layer Transition Control Using Non-Uniform Surface Temperature Distributions

Kazuki Ozawa

Supervised by

Dr Paul Bruce

Thesis submitted in part fulfilment of the requirements for the degree of Doctor of Philosophy in Aeronautics of Imperial College London

Department of Aeronautics

Faculty of Engineering

Imperial College London

February 2026

Declaration of Originality

I hereby declare that all the work and material presented in this thesis are composed and reported as my own. All information and data obtained from external sources are properly acknowledged and cited in text with the full list of references given in the final bibliography section.

Kazuki Ozawa

Copyright Declaration

The copyright of this thesis rests with the author. Unless otherwise indicated, its contents are licensed under a Creative Commons Attribution-Non Commercial 4.0 International Licence (CC BY-NC).

Under this licence, you may copy and redistribute the material in any medium or format. You may also create and distribute modified versions of the work. This is on the condition that: you credit the author and do not use it, or any derivative works, for a commercial purpose.

When reusing or sharing this work, ensure you make the licence terms clear to others by naming the licence and linking to the licence text. Where a work has been adapted, you should indicate that the work has been changed and describe those changes.

Please seek permission from the copyright holder for uses of this work that are not included in this licence or permitted under UK Copyright Law.

Acknowledgements

I would like to express my sincere gratitude to the many people and organisations that supported me throughout my PhD.

First and foremost, I am deeply grateful to my supervisor, Assoc. Prof. Paul Bruce, for his outstanding guidance and mentorship. His technical insight, high standards, and steady encouragement were central to my development as a researcher and to the completion of this thesis. I am also sincerely grateful to Assoc. Prof. Georgios Rigas for his generous support and collaboration. Our discussions on linking computations with experiments strongly shaped my experimental design and data interpretation.

I gratefully acknowledge the financial support of the Nakajima Foundation, which made my PhD possible. I also thank the Department of Aeronautics at Imperial College London for supporting my research and providing an excellent environment for experimental work.

This thesis benefited greatly from access to national facilities and the dedication of many staff members. I thank the National Wind Tunnel Facility (NWTF) for supporting the Manchester experiments. I thank Dr Mark Quinn for access and support at the Manchester facility, and M. Tayyip Gurbuz and Ozgun Ozer for their dedicated assistance during a week of wind-tunnel operations.

I am grateful to the colleagues who directly supported the technical development of this work. I thank Dr Kshitij Sabnis for his help in setting up and assessing the LDA measurements. I also thank Dr Luca Boscagli for many valuable discussions on hypersonic simulations and for his advice during the design of the waverider model. I am grateful to Chengwei Xia for running hypersonic simulations and for the many helpful conversations that clarified the data and guided my interpretation.

The experimental work in this thesis would not have been possible without excellent technical and workshop support. I would like to thank Mark Grant, Ian Pardew, Roland Hutchins, Mark Thornton, Jordan Farrar, and Dominica Rohozinski for their skill and support in manufacturing and instrumentation. I am especially grateful to Mark Grant and Ian Pardew for helping translate early concepts into robust and manufacturable designs. I also thank Franco Giammaria for his support in developing the LabVIEW code and heating hardware, and Ian James for his assistance with supersonic wind-tunnel operations.

I am also thankful to Jake and Pietro for their teamwork during wind-tunnel testing—supporting

operations, helping solve practical problems quickly, and continually improving the measurement and operational procedures.

Beyond the research itself, I am profoundly grateful for the friendships I formed at Imperial. The shared experience, encouragement, and support made my time there truly special. My sincere thanks to Mario, Benita, Kaloyan, Grace, Joanne, Francisco, Di, Josephine, Lidia, Stef, Christian, and Dou.

Finally, I would like to thank my parents and my brother for their unwavering support, patience, and for always welcoming me home.

Abstract

Hypersonic vehicle performance is strongly constrained by laminar–turbulent transition, which produces drastic increases in skin-friction drag and surface heat flux. This thesis presents the first experimental demonstration that passive spanwise non-uniform wall-temperature variations can generate streamwise velocity streaks and measurably modify instability amplification in high-speed boundary layers. To achieve this, a novel, experimentally realisable actuation architecture was developed and tested. Two practical actuation concepts were developed: a multi-material conduction approach and a variable-thickness conduction approach. Both are designed using a three-dimensional thermal model.

A hybrid copper–ceramic flat-plate model is tested at Mach 2.75 to validate the generation of controlled spanwise temperature gradients produced passively by supersonic cooling. For an initial model temperature of 423 K, a maximum spanwise temperature difference of approximately 50 K is achieved, corresponding to $\Theta = \Delta T/T_\infty \approx 0.4$, and Laser Doppler anemometry indicates a streak amplitude of approximately 3 % in the highest-ΔT condition. Infrared thermography confirms the imposed surface-temperature field and the repeatability of the thermal actuation.

The concept is then assessed on a Mach 5 configuration, where the spanwise temperature non-uniformity is imposed prior to the run and provides $\Delta T \approx 90$ K across cases (e.g. $\Theta \approx 0.75$ for a representative condition). High-frequency wall-pressure measurements show attenuation of the dominant instability band centred near 170 kHz, with additional reductions in peaks in the $200 - 300$ kHz range relative to a uniform-temperature baseline, and infrared thermography is used to assess the corresponding surface heat-transfer response. The results demonstrate that wall-temperature patterning can be implemented in a physically realisable manner and can measurably attenuate dominant instability bands through thermally induced streak generation.

Contents

1 Introduction **1**

1.1 Motivation 1

1.2 Research Objectives 3

1.3 Thesis Structure 5

1.4 Publications 6

1.4.1 International Journal Papers 6

1.4.2 International Conference Papers 7

1.5 Scholarships and Awards 8

2 Literature Review **9**

2.1 Hypersonic Flight Environment 9

2.2 Hypersonic Boundary-Layer Transition: Modal and Non-modal Instability Mechanisms 11

2.3 Influence of Geometry and Wall Conditions on Hypersonic Transition 15

2.3.1 Effect of Leading-Edge Curvature Radius 15

2.3.2 Wall Cooling/Heating Effect 19

2.3.3 Porous and Ultrasonically Absorptive Materials 23

2.4 Streamwise Streaks as Transition Control Mechanisms 26

2.4.1 Streaks in Low-Speed Boundary Layer 27

2.4.2 Streaks in Hypersonic Flows 30

3 Actuation Methods for Non-Uniform Surface Temperature Distributions 40

3.1 Overview 40

3.2 Control Methodology and Performance Under Flight Conditions 41

3.2.1 Principles of Three-Dimensional Steady-State Condition 41

3.2.2 Thermal Modelling for Three-Dimensional Steady-State Condition 42

3.2.3 Spanwise Surface Temperature Distributions 46

3.2.4 Discussion 49

3.3 Passive Control Approach for Ground Test Implementation 49

3.3.1 Principles of Passive Transient Temperature Control in Short Wind Tunnel Operation 50

3.3.2 Conceptual Design 51

3.3.3 Thermal Modelling for Transient Surface Temperature 54

3.3.4 Prediction of the Transient Temperature 56

3.3.5 Discussion 58

3.4 Summary 59

4 Characterisation of Non-Uniform Surface Temperature Distributions 61

4.1 Overview 61

4.2 Experimental Facility and Flat-Plate Model 62

4.2.1 Imperial College Supersonic Wind Tunnel and Operating Condition 62

4.2.2 Flat Plate Test Article 63

4.2.3 Mounting of the Flat Plate Test Article 65

4.2.4 Pre-Heating System . . . 66
4.2.5 Surface Coating . . . 69
4.3 Measurement Methodology . . . 70
4.3.1 Infrared Thermography (IRT) Calibration and Measurement . . . 70
4.3.2 Laser Doppler Anemometry (LDA) Measurement and Datum Calibration . . . 73
4.3.3 Test Matrix for IRT and LDA Campaign . . . 75
4.4 Thermal Modelling . . . 79
4.4.1 Heat Transfer Coefficient and Thermal Model . . . 79
4.4.2 Freestream Characterisation for Thermal Boundary Conditions . . . 81
4.5 Surface Temperature Characterisation . . . 84
4.5.1 IRT Measurements . . . 84
4.5.2 Discussion . . . 87
4.6 Boundary-Layer Characterisation . . . 93
4.6.1 Time-Resolved Boundary Layer Measurement Strategy . . . 93
4.6.2 LDA Measurements . . . 101
4.6.3 Generated Streak Amplitude . . . 107
4.7 Summary . . . 111

5 Hypersonic Transition Control via Surface Temperature Variations on a Waverider Model 114

5.1 Overview . . . 114
5.2 Numerical Guidance for Experimental Design . . . 115
5.2.1 LST Guidance: Second Mack Mode Band and Amplification Region . . . 115
5.2.2 DNS Guidance for Streak Amplitude Response and Heating-Patch Geometry . 116

5.3 Experimental Model and Heating System . . . 119
5.3.1 Waverider Model and Sensor Layout . . . 119
5.3.2 Sensor Placement Based on LST . . . 120
5.3.3 Heating Patch Thermal Design . . . 122
5.3.4 Heater Fabrication and Validation . . . 128
5.4 Facility, Diagnostics, and Test Matrix . . . 131
5.4.1 High Supersonic Wind Tunnel . . . 131
5.4.2 High-Frequency Pressure Instrumentation . . . 132
5.4.3 Infrared Thermography System . . . 132
5.4.4 Test Matrix and Experimental Conditions . . . 133
5.4.5 Measurement Uncertainty and Interpretation . . . 135
5.5 Results and Discussion . . . 141
5.5.1 Boundary Layer State Characterisation . . . 141
5.5.2 Effect of Uniform Wall Temperature . . . 143
5.5.3 Impact of Spanwise Non-Uniform Heating . . . 144
5.6 Summary . . . 146

6 Conclusion and Future Work **149**

6.1 Thesis Objectives and Scope Revisited . . . 149
6.2 Summary of Main Contributions . . . 150
6.3 Synthesis and Implications . . . 151
6.4 Limitations of the Present Work . . . 151
6.5 Future Work . . . 152

Bibliography **154**

List of Figures

1.1 Conceptual illustration of the aerothermodynamic penalty of boundary layer transition. The top panel depicts the structural evolution of the boundary layer from laminar flow to turbulent breakdown, while the bottom panel shows the corresponding surface heat flux (q_w) distribution. 2

1.2 Structural damage to the X-15A-2 ventral pylon caused by aerodynamic heating during Mach 6.7 flight. Complex shock-boundary layer interactions triggered premature transition and localised heating peaks that burned through the ablative thermal protection system. Image adapted from Watts [1]. 3

2.1 Velocity-altitude map showing critical aerothermodynamic phenomena for various hypersonic vehicle classes. Reproduced from Bertin and Cummings [2, 3]. 10

2.2 Canonical transition pathways in boundary layers as a function of disturbance environment, illustrating modal, transient-growth, and bypass routes to turbulence. Reproduced from Morkovin et al. [5] and Fedorov [6]. 12

2.3 Rayleigh-scattering visualisation of boundary-layer transition in quiet Mach 6 flow over a flared cone. The marked locations indicate (A) initial appearance of the second Mack mode disturbances, (B) decay of second Mack mode amplitude, and (C) onset of turbulent breakdown. Figure reproduced from Zhang et al. [15]. 14

2.4 Pressure RMS spectra showing second Mack mode waves at $Re/x = 8.0 \times 10^6$ to 12.8 $\times 10^6$ in the Boeing/AFOSR Mach-6 Quiet Tunnel (MAB6QT) under noisy and quiet flow, obtained using a PCB132B38 pressure sensor. Reproduced from Casper et al. [16]. 14

2.5 Transition Reynolds number based on freestream as a function of the nose Reynolds number at Mach 6. Adapted from Paredes et al. [32] 16

2.6 Power spectral density (PSD) of wall-pressure fluctuations at (a) $R_N = 0.1\,\mathrm{mm}$ and (b) $R_N = 2\,\mathrm{mm}$ for Mach 6 flow ($T_w = 300\,\mathrm{K}$, $Re = 4 \times 10^6\,\mathrm{m}^{-1}$). Reproduced from Huang et al. [33]. 17

2.7 Streamwise evolution of non-modal oblique disturbances and stationary streaks within the entropy layer at Mach 6. Reproduced from Paredes et al. [36]. 18

2.8 Neutral stability curves illustrating the effect of wall cooling on a 5-degree cone at Mach 5.6. Reproduced from Kara et al. [37] 20

2.9 Effect of wall cooling on instability growth rates. Comparison of amplification factors for the first and second Mack modes under cooled-wall condition (Reproduced from Masad [39]). 20

2.10 Instability dynamics of the hypersonic boundary layer under cooled and uncooled wall conditions at Mach 6. (a) Fundamental dominant second Mack mode frequency, (b) first harmonic, and (c) second harmonic measured with LA-FLDI for various freestream unit Reynolds numbers on a flared cone [20]. (d) Intermittency comparison between cooled and uncooled walls on 7° half-angle cone [41]. 22

2.11 Effect of local wall cooling placement on instability growth rates in a Mach 6 sharp-cone boundary layer (after Oz et al. [48]). 23

2.12 (a) Magnified image of stainless-steel perforated sheet used as a porous insert and (b) schematic of the cone model. Transition comparison on a cone model with (c) smooth and (d) porous surfaces. Adapted from Rasheed et al. [52]. 24

2.13 Carbon–carbon ceramic performance in hypersonic boundary-layer control: (a) cone model with integrated C/C insert, (b) estimated absorption coefficient of C/C material across second Mack mode-relevant frequencies, and (c) heat flux distribution comparing porous and smooth surfaces, with transition Reynolds numbers marked by circles. Adapted from Wagner et al. [53, 54]. 25

2.14 Silicon-carbide foam performance in hypersonic boundary-layer control: (a) magnified view of SC foam wall-normal surface topography, and (b) power spectra of pressure fluctuations comparing impermeable (solid line) and porous (dashed line) surfaces at $Re = 13.7 \times 10^6$ [1/m] at Mach 6. Adapted from Running et al. [56]. 26

2.15 Schematic of the lift-up mechanism responsible for streak formation in a boundary layer. Streamwise vortices induce vertical motion, lifting low-momentum fluid away from the wall and pushing high-momentum fluid downward. 27

2.16 Effect of roughness-induced streamwise streaks (A_{st}) on boundary-layer structure and TS wave amplification. (a) Experimental visualisation of boundary-layer modification using cylindrical roughness elements: baseline case (R), streaky boundary layer with $A_{st} = 11.6\%$ (S_1), and $A_{st} = 12.4\%$ (S_2). Solid lines show velocity isolines; dashed lines show spanwise mean deviation. (b) Spatial growth rates of TS waves ($\alpha_i^* \delta$) as a function of frequency F for the three flow cases, showing reduction in TS wave growth due to the presence of streaks (Fransson et al. [58]). 28

2.17 Optimal spanwise streak spacing for transition delay based on global stability analysis. (a) Streamwise evolution of streak amplitude $A_{st} = 10\,\%$ for two different spanwise wavenumbers, $\beta = 0.45$ (solid) and 0.65 (dashed). (b) Temporal TS wave energy growth E for different spanwise wavenumbers with the absence of streaks case (dotted), reproduced from Bagheri et al. [60]. 30

2.18 N-factor envelopes for nominally 2D second Mack mode disturbances (mode MM0, solid lines; $F \in [350, 800]$ kHz) and sinuous modes originating from first-mode waves with one half the azimuthal wavenumber of the underlying streaks (mode FM1/2,S, dashed lines; $F \in [50, 150]$ kHz). (Reproduced from Paredes et al. [63].) 31

2.19 (a) Sketch of the flat-plate model assembly with interchangeable leading-edge pieces and spherical roughness elements. (b) Surface heating-rate distributions at Mach 6.0, illustrating delayed transition for sub-critical roughness heights. Smooth-surface and smallest-roughness cases are highlighted. Figure adapted from Holloway and Sterrett [69]. 32

2.20 (a) Geometry of the spaced wire, spherical, and wavy-wall roughness elements applied to a sharp cone, and (b) Stanton number distributions at Mach 7.1 showing transition delay for wavy-wall and spherical configurations compared to a smooth surface. (Adapted from Fujii [70].) 33

2.21 (a) Predicted mean streamwise velocity contours at $x = 250\,\text{mm}$ for elliptical roughness elements with heights of $382\,\mu\text{m}$ and $529\,\mu\text{m}$. (b) Streamwise evolution of streak amplitude for the same configurations. (c) Computed second Mack mode N-factors. (Adapted from Leidy et al. [72].) 34

2.22 (a) Isosurface of streaks generated by spanwise varying wall temperature Θ at $\lambda_z^* = 1.2$, where y^* and z^* are normalised by L_{ref}. (b) Streak amplitude for different spanwise wavelengths λ_z^* of non-uniform temperature distributions. Reproduced from Ozawa et al. [77]. 36

2.23 Instantaneous pressure perturbation field for Case 1, Case 2, Case 3 (cold side) and Case 3 (hot side) on the $x^* - y^*$ plane. Reproduced from Ozawa et al. [77]. 37

2.24 N-factors of the Case 1 (uniform cold wall), the Case 2 (uniform hot wall), and the Case 3 (spanwise-varying wall temperature). For the Case 3, also the N-factor is separately evaluated only in the hot ("hot side") and cold wall ("cold side") regions, respectively. Reproduced from Ozawa et al. [77]. 37

2.25 (a) Influence of streak wavelength on second Mack mode stabilisation $\Delta\varepsilon_{chu}^{10}$ and maximum streak amplitude As_u, and (b) instantaneous skin-friction coefficient c_f for uncontrolled and controlled configurations. Adapted from Boscagli et al. [78]. 39

3.1 Schematic of the steady state wall condition under aerodynamic heating by hypersonic cruising with a cooling system. 42

3.2 Schematic of the thermal modelling domain, including the cold and hot strips. The domain shows the convection Q_{in} at the aerodynamic test surface and the stronger (Θ_{BSL}) and the weaker (Θ_{BSH}) cooling at each strip. 45

3.3 Surface normalised temperature at the steady state-under aluminium wall with $\Theta_{BSL} = 2$ and $\Theta_{BSH} = 4$ (a to c) and $\Theta_{BSL} = 1$ and $\Theta_{BSH} = 5$ (d to f). 47

3.4 Streamwise and spanwise normalised temperature in different aluminium wall thickness cases. 47

3.5 Surface normalised temperature for the reference cases AL-5-2-4 and AL-10-2-4, and for T-5-2-4, T-10-2-4, M-5-2-4, and M-10-2-4, with $\Theta_{BSL} = 2$ and $\Theta_{BSH} = 4$. 48

3.6 Variation of temperature difference with $\Theta_{BSL} = 2$ and $\Theta_{BSH} = 4$ on each strip at $x = 150\,\text{mm}$ with varying materials (MACOR, titanium, and aluminium) and wall thickness of 2.5, 5 and 10 mm. Solid lines represent the hot, and dash lines represent the cold strips. 49

3.7 Sketches of the wall temperature profile and boundary conditions (a) and the three conceptual designs for achieving spanwise temperature difference approached by varying the materials (b) and (c), and thickness of the wall (d). 52

3.8 Thermal properties across materials and their temperature sensitivity. 53

3.9 The geometries of three conceptual designs in the thermal modelling. 55

3.10 Surface normalised temperature of the conceptual designs calculated by the thermal modelling. 56

3.11 Surface normalised temperature plot along the spanwise direction and transient normalised temperature at $x = 150\,\text{mm}$. 57

3.12 Normalised temperature at the strips' centre surface at $x = 150\,\text{mm}$ at $t = 15\,\text{s}$ for MACOR and titanium multiplied by thermal diffusivity and the insulator thickness ($t_{insulator} = [1, 2, 3, 4]\,\text{mm}$). 59

4.1 Schematic diagram of the Imperial College London supersonic wind tunnel. 63

4.2 Photograph of the assembled flat plate test article, including steel leading edge, MACOR and copper strips with the diagram of the heating system. 64

4.3 Prototype fabrication of MACOR–copper interface. Two slot configurations in the copper base: one empty and one fitted with a coated MACOR strip, used to validate fit and surface treatment. 64

4.4 Experimental arrangement and flow field schematic. The test article is positioned at a 3° incidence angle for (a) IRT (vertical) and (b) LDA (horizontal) measurements, resulting in (c) the anticipated shock wave structure. 67

4.5 Photograph of the test article covered with the insulator on the test surface side and bottom side to maintain uniform thermal conditions before the wind tunnel run. . . . 68

4.6 Schematic representation of the experimental setup for IRT measurements, showing the aerodynamic test surface and optical access via a Zinc Selenide window ($D = 70\,\text{mm}$). 71

4.7 Representative spectral transmissivity of an uncoated ZnSe optical window with a thickness of 20 mm. The shaded region indicates the 7.5–14.0 μm spectral response range of the FLIR A655SC camera. 72

4.8 IRT camera calibration curves. 72

4.9 The steel target used in the experiments with an inset showing its raw IRT image. . . 74

4.10 Schematic diagram of the LDA measurement system. 76

4.11 Photographs of the LDA measurement setup and the datum calibration plate inserted into the test article. 77

4.12 Schematic of LDA measurement locations (marked by red circles) on the flat plate geometry for Cases 1–3 at $x = 50$, 100, and 150 mm with $\lambda = 0, 1/3, 2/3$, and 1, and for Case 4 at $x = 50$ and 100 mm with $\lambda = 0, 1/3, 2/3$, and 1. 78

4.13 (a) The thermal model geometry showing the alternating conductor-insulator strips and the convective heat flux boundary condition (Q) applied to the aerodynamic test and back surfaces. (b) The unstructured mesh for the thermal modeling. 82

4.14 Time history of the isentropic Mach number for repeated runs (gray lines) and their ensemble average (black line) in Case 1. 84

4.15 Initial surface temperature (T_i) distribution for Case 2 from the IRT measurement, overlaid on the test article outline. Inset: Pixel count histogram for Window 2 (Case 2) showing distinct temperature peaks for insulator (359.7 K) and conductor (364.8 K) regions. 86

4.16 Overlay of experimental results onto the thermal modelling predictions of temperature distributions at 15 s for (a) Case 1, (b) Case 2, and (c) Case 3. 88

4.17 Spanwise normalized temperature profiles at $t = 15\,\text{s}$ at streamwise locations $x = 15$ (black), 50 (red), and 100 mm (blue). Experimental results (dashed lines) are compared with thermal modelling predictions (solid lines) for (a) Case 1, (b) Case 2, and (c) Case 3 89

4.18 Streamwise normalized temperature profiles at $t = 15\,\mathrm{s}$ for (a) Case 1, (b) Case 2, and (c) Case 3. Thermal model predictions (solid lines) are compared with experimental results (dashed lines) for the center insulator (blue) and conductor (red). 91

4.19 Schlieren visualization of the flow field during wind tunnel start-up. The images show the evolution of shock structures at (a) $t = 4.0\,\mathrm{s}$ and (b) $t = 4.3\,\mathrm{s}$ during the initial acceleration phase, and (c) the final steady-state flow at $t = 5.0\,\mathrm{s}$. 91

4.20 Transient temperature evolution at $x = 100\,\mathrm{mm}$ during wind tunnel operation for (a) Case 1, (b) Case 2, and (c) Case 3. Comparison between experimental results (dashed lines) and thermal modelling predictions (solid lines) for the insulator and conductor. 92

4.21 Normalised temperature profiles of the insulator and conductor at $x = 100\,\mathrm{mm}$ at $t = 15\,\mathrm{s}$ comparing the thermal model and the experimental results across different initial temperatures of the test article. 94

4.22 Thermal modeling predictions of the surface temperature distributions at $t = 20\,\mathrm{s}$ for Case 4 95

4.23 Transient evolution of the non-dimensional surface temperature ($\Theta_w = T_w/T_\infty$) on the copper conductor at $x = 50$, 100, 150 mm during wind tunnel operation for Case 4 . . 96

4.24 Normalized surface temperature excess relative to the recovery temperature ($\Theta_w - \Theta_r$) for the insulator and conductor at $x = 100\,\mathrm{mm}$ and $t = 20\,\mathrm{s}$, plotted against the initial pre-heating temperature (Θ_i). 96

4.25 Traverse location history at T_i=250 K at $x = 100\,\mathrm{mm}$ (Case 4). 98

4.26 Raw velocity data measured by (a) LDA 1 and (b) LDA 2, colored by transient measurement time. Conditions: $T_i = 523\,\mathrm{K}$, $x = 100\,\mathrm{mm}$ 102

4.27 (a) Reconstructed vector velocity from v_1 and v_2 after time-averaging. (b) Number of measured particles per time-averaged window. 102

4.28 LDA-measured velocity profiles and a fitted composite boundary layer model for Case 4. The composite profile combines a Musker near-wall fit with a Sun & Childs outer wake profile. 103

4.29 Wall-normal velocity profile for Case 4. The wall-normal coordinate y includes the same wall-offset correction applied in Fig. 4.28. 103

4.30 Baseline streamwise velocity profiles, U/U_∞, measured by LDA and fitted with the compound inner–outer model at streamwise stations $x = 50$, 100 and 150 mm. Symbols denote LDA measurements (circles) and solid and dashed lines denote the corresponding compound-model fits with $\delta_{99.5}$. 104

4.31 Reconstructed compound streamwise velocity profiles at $x = 100$ mm for Case 4 ($T_i = 523\,\mathrm{K}$) at four spanwise locations $\lambda = [0, 1/3, 2/3, 1]$. Hot wall ($\lambda = 1$) shows the thickest boundary layer, cold wall ($\lambda = 0$) the thinnest, and intermediate locations are linearly distributed. 107

4.32 Transient evolution of the streamwise boundary layer profile at $x = 100$ mm, $\lambda = 0$, for Case 4 ($T_i = 523\,\mathrm{K}$) between $t \approx 9$–18 s. 108

4.33 Streamwise velocity profiles at $\lambda = 0$ with the measured LDA data (blue line and circle) and $\lambda = 1$ with the measured LDA data (red line and circle) for Case 4 ($x = 100\,\mathrm{mm}$, $t \approx 17.5\,\mathrm{s}$). The velocity difference gives reconstructed streak amplitudes of approximately $A_{st}^{\mathrm{buf}} = 4.8\,\%$ and $A_{st}^{\mathrm{log}} = 2.4\,\%$ over the near-wall/buffer-layer and outer/lower-log-region intervals, respectively (black line). The two operational peak amplitudes are denoted A_{st}^{buf} and A_{st}^{log}, respectively (Eq. (4.17)–(4.18)). 110

4.34 Streamwise evolution of the reconstructed near-wall/buffer-layer streak amplitude A_{st}^{buf} for all cases between $x = 100$ and 150 mm. 111

4.35 Streak amplitude in the buffer layer and log-law region versus normalized wall temperature difference ($\Delta\Theta = \Delta T_w/T_\infty$) at $x = 100\,\mathrm{mm}$ for all four initial temperature cases, with a linear fit. 112

5.1 (a) Self-similar temperature profile and (b) second Mack mode neutral stability curves for a Mach 5 configuration with $T_0 = 300\,\mathrm{K}$ (from the SciTech 2026 collaborative study [103]). 116

5.2 Imposed wall-temperature distributions used in the DNS parametric study for three streamwise strip configurations (from the SciTech 2026 collaborative study [103]). . . . 118

5.3 (a) Streamwise evolution of the base-flow boundary-layer thickness and (b) corresponding streak amplitude for three heating-strip configurations (from the SciTech 2026 collaborative study [103]). 118

5.4 Effect of streak wavelength on the streamwise distribution of the streak amplitude (from the SciTech 2026 collaborative study [103]). 118

5.5 3D CAD model of (a) the assembled waverider-based hypersonic test article, and (b) an exploded view illustrating individual components, including the zirconia heating plate and modular sensing patches. 121

5.6 3D CAD model of (a) the assembled waverider-based hypersonic test article, and (b) an exploded view illustrating individual components, including the zirconia heating plate and modular sensing patches. 121

5.7 Schematic of the waverider-based Mach 5 experimental configuration. (a) Side view showing the freestream direction, leading-edge shock, shock surface, aerodynamic test surface, upstream heating surface, downstream measurement surface, and approximate boundary-layer development. (b) Front view showing the model planform and the shock surface generated by the leading edge. 122

5.8 Predicted second Mack mode instability onset and growth range ($Re_x = 1400$ to 2100) shown for non-dimensional frequency $F = 1.0 \times 10^{-4}$ ($f = 278\,\text{kHz}$), used to guide sensor placement. 123

5.9 3D CAD representation of the setup: (a) cross-sectional view of the assembly highlighting the thermal modelling domain; and (b) the spanwise unit cell showing the heating cartridge contact surfaces and test surface geometry (12 mm spanwise configuration). . 124

5.10 Predicted time evolution of spanwise temperature difference (ΔT) and surface temperature contours for MACOR plates with thickness: (a) 6 mm and (b) 3 mm. T_I is the surface temperature directly above the cartridge heater, while T_C is the surface temperature at the centerline of the plate between adjacent heaters. 125

5.11 Comparison of ΔT evolution and surface temperature distributions with 3 mm thickness for (a) zirconia, and (b) ATZ. 126

5.12 Bench-top thermal characterisation results. (a) Temporal evolution of the streamwise-averaged temperature difference ($\Delta\overline{T}$) for 12 mm and 20 mm configurations, comparing experimental measurements (red) with thermal model predictions (black). (b,c) Infrared temperature contour plot of the 12 mm, and 20 mm configurations, respectively, at the evaluation time (t=62 s). 130

5.13 Representative spectral transmissivity of an uncoated germanium optical window used for infrared thermography. The shaded region indicates the 3–5 μm sensitivity range of the FLIR A6750 MWIR camera. 133

5.14 Schlieren visualisation at Mach 5 (Case 1). The waverider leading edge (LE) is positioned internally within the nozzle to ensure mitigation of blockage. The visible LE shock wave originates upstream of the nozzle exit plane. 142

5.15 Comparison of wall pressure power spectral density (PSD) at $x = 232$ mm. The Case 1 ($Re = 11 \times 10^6\,\mathrm{m}^{-1}$) spectrum exhibits broadband turbulent fluctuations, while Case 2 ($Re = 4.8 \times 10^6\,\mathrm{m}^{-1}$) retains a laminar baseline with a distinct second Mack mode instability peak visible near $f \approx 170$ kHz. 143

5.16 Evolution of wall pressure power spectral density (PSD) at (a) $x = 192$ mm and (b) $x = 232$ mm. The plots compare uniform wall heating cases ranging from 423 K (green) to 513 K (red), with non-uniform heating cases (black). 144

5.17 Surface heat flux ($\dot{q}$) measurements derived from infrared thermography. 2D contours for (a) the uniform heating baseline ($T_w = 473$ K) and (b) the non-uniform forcing case (T_{var}). 147

5.18 Infrared-derived heat-transfer profiles over the downstream resin sensing insert. (a) Reconstructed heat flux, $\dot{q}$. (b) Stanton number, St. The solid coloured lines show spanwise-mean profiles for the uniform $T = 473$ K case and the non-uniform T_{var} case. The shaded bands indicate representative combined uncertainties of $\pm 13\%$ for $\dot{q}$ and $\pm 15\%$ for St. The vertical dash-dot lines mark the PCB pressure-sensor locations, where the infrared-derived values should be interpreted with additional caution. . . . 147

List of Tables

2.1 DNS cases for assessing the transition effect of spanwise-varying wall temperature. Source: Ozawa et al. [77]. 36

3.1 DNS freestream parameters from Ozawa et al. [76], corresponding to Mach 6 free flight in the International Standard Atmosphere at 20 km. 44

3.2 Aluminium wall test cases with varying wall thickness and stronger Θ_{BSL} and weaker Θ_{BSH} cooling temperatures inputs behind the wall. 46

3.3 Different wall material cases for sensitivity study. 48

3.4 Materials selection for the conceptual models in the thermal modelling. 55

3.5 Thermal diffusivity ratio of the insulator and conductor materials. 58

4.1 Freestream and post-shock flow configurations. 62

4.2 List of model components and material properties. 65

4.3 Summary of the infrared camera calibration. 73

4.4 Integrated case definition for IRT and LDA campaigns. Cases are defined by the nominal initial plate temperature T_i (target setpoint). 78

4.5 LDA test matrix and measurement locations. 78

4.6 Number of windows and initial surface temperature. 86

4.7 Incompressible boundary-layer integral parameters for the baseline (unheated) flat plate. Integral parameters are calculated using the specified boundary-layer modeling approach, based on Sun & Childs [96] combined with Musker [97] models. 105

4.8 Summary of hot and cold wall temperatures ($\lambda = 0, 1$) and corresponding incompressible boundary layer integral parameters at $x = 100$ mm. Data includes transient wall temperature, measurement time, $\delta_{99.5}$, displacement thickness δ_i^*, momentum thickness θ_i, and shape factor H_i for each case. 108

5.1 Thermal and mechanical properties of candidate materials used in the design trade study. 124

5.2 Structural safety analysis: Estimated critical temperature difference (ΔT_{crit}) versus operating conditions. 126

5.3 Nominal flow conditions for the experimental campaign. Post-shock values correspond to the flow properties downstream of the waverider leading edge shock. 132

5.4 Summary of the experimental test matrix. The uniform $T_w = 473\,\text{K}$ case serves as the baseline for comparison with the non-uniform heating configuration ($\overline{T}_w = 462\,\text{K}$). . . 135

Nomenclature

α	Thermal conductivity [$\mathrm{W\,m^{-1}\,K^{-1}}$]
α_{TE}	Coefficient of thermal expansion [$\mathrm{K^{-1}}$]
β	Shock angle [deg]
ΔT	Temperature difference [K]
$\Delta\Theta$	Normalised temperature difference, $\Delta\Theta = \Delta T_w/T_\infty$ [−]
δ_i^*	Incompressible displacement thickness [m]
$\delta_{99.5}$	Boundary-layer thickness based on 99.5% criterion [m]
$\dot{q}$	Heat flux [$\mathrm{W\,m^{-2}}$]
ϵ	Emissivity [−]
γ	Ratio of specific heats [−]
κ	Thermal diffusivity [$\mathrm{m^2\,s^{-1}}$]
λ	Spanwise measurement-location coordinate, e.g. $\lambda = 0, 1/3, 2/3, 1$ [−]
λ_z	Spanwise wavelength or pitch of imposed heating pattern [m]
Λ_{span}	Physical spanwise wavelength of the material/heating pattern [m]
μ	Dynamic viscosity [Pa s]
ν	Kinematic viscosity [$\mathrm{m^2\,s^{-1}}$]
ρ	Density [$\mathrm{kg\,m^{-3}}$]
σ	Stefan–Boltzmann constant [$\mathrm{W\,m^{-2}\,K^{-4}}$]

σ_f Fracture strength [Pa]

τ_w Wall shear stress [Pa]

Θ Non-dimensional temperature, $\Theta = T/T_\infty$ [−]

θ_i Incompressible momentum thickness [m]

$A(y)$ Streak-amplitude distribution, $A(y) = \frac{1}{2U_\infty(t)}\left[U_{\lambda=1}(y,t) - U_{\lambda=0}(y,t)\right]$ [−]

A_{st} Maximum streak amplitude, $A_{st} = \max_y A(y)$ [−]

A_{st}^{buf} Reconstructed near-wall/buffer-layer streak amplitude [−]

A_{st}^{log} Reconstructed outer/lower-log-region streak amplitude [−]

C_f Skin-friction coefficient [−]

c_p Specific heat at constant pressure [$\mathrm{J\,kg^{-1}\,K^{-1}}$]

E Young's modulus [Pa]

F Non-dimensional instability frequency [−]

f Frequency [Hz]

h Convective heat-transfer coefficient [$\mathrm{W\,m^{-2}\,K^{-1}}$]

H_i Incompressible shape factor, $H_i = \delta_i^*/\theta_i$ [−]

k_s Equivalent sand-grain roughness height [m]

k_s^+ Roughness Reynolds number, $k_s^+ = u_\tau k_s/\nu_e$ [−]

M Mach number [−]

N Instability amplification factor [−]

Nu Nusselt number [−]

p Static pressure [Pa]

Pr Prandtl number [−]

r Recovery factor [−]

R_N Nose radius [m]

Re Unit Reynolds number [m^{-1}]

Re_x Local Reynolds number, $Re_x = Re\, x$ [$-$]

Re_{R_N} Nose Reynolds number, $Re_{R_N} = U R_N/\nu$ [$-$]

St Stanton number [$-$]

T Temperature [K]

t Time [s]

u, v, w Velocity components in x, y, z [$\mathrm{m\,s}^{-1}$]

u_τ Friction velocity [$\mathrm{m\,s}^{-1}$]

x, y, z Streamwise, wall-normal, and spanwise coordinates [m]

$(\cdot)_0$ Stagnation condition

$(\cdot)_{aw}$ Adiabatic-wall condition

$(\cdot)_e$ Boundary-layer edge condition

$(\cdot)_i$ Initial or incompressible quantity, depending on context

$(\cdot)_{\mathrm{rad}}$ Radiative quantity

$(\cdot)_{\mathrm{ref}}$ Reference condition

$(\cdot)_{\mathrm{sur}}$ Surrounding condition used for radiation estimate

$(\cdot)_w$ Wall condition

$(\cdot)_x$ Local quantity at streamwise location x

$(\cdot)_\infty$ Freestream condition

$(\cdot)^*$ Non-dimensional quantity

$\overline{(\cdot)}$ Time-averaged quantity

Chapter 1

Introduction

1.1 Motivation

The development of sustained hypersonic flight represents one of the most critical challenges in modern aerospace engineering. Hypersonic vehicles—defined as those capable of operating at speeds exceeding Mach 5—offer transformative potential for rapid global transport and reliable, cost-effective access to space. However, the realisation of these technologies is fundamentally constrained by the severe aerothermodynamic environment, which imposes high aerodynamic drag and extreme thermal loads on the vehicle.

The primary driver of the drag and thermal loads in this regime is the state of the boundary layer. As a vehicle accelerates through the atmosphere, the immense kinetic energy of the freestream is converted into internal energy (heat) via viscous dissipation within the boundary layer. This process is intrinsically linked to surface friction. As illustrated in Fig. 1.1, a turbulent boundary layer is characterised by chaotic mixing that dramatically increases the shear stress at the wall. Consistent with the Reynolds analogy, this increase in skin friction is accompanied by a proportional rise in surface heat transfer, often by a factor of several (order 2–5) relative to laminar flow, depending on conditions. Consequently, the transition from laminar to turbulent state precipitates an abrupt increase in both aerodynamic drag and thermal loading, triggering peak heating rates that can often exceed the limits of conventional materials.

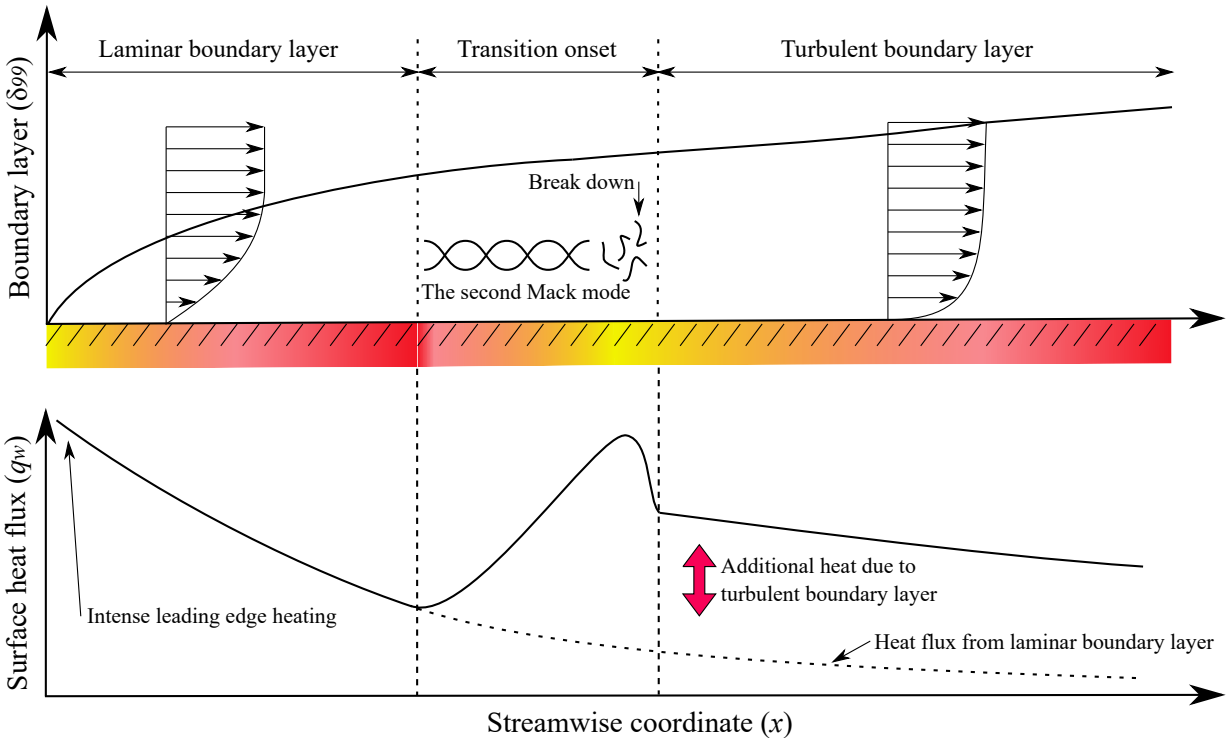


Figure 1.1: Conceptual illustration of the aerothermodynamic penalty of boundary layer transition. The top panel depicts the structural evolution of the boundary layer from laminar flow to turbulent breakdown, while the bottom panel shows the corresponding surface heat flux (q_w) distribution.

The consequences of failing to manage this transition process have been clearly illustrated by historical flight tests. The X-15 research program, while highly successful, encountered critical aerodynamic and thermal challenges during high-Mach sorties. Notably, during the record-breaking flight of the X-15A-2, complex shock-boundary layer interactions triggered premature transition (see Fig. 1.2). This resulted in localised heating severe enough to burn through the ventral pylon, despite the application of ablative thermal protection. Such examples underscore that merely surviving peak heating is insufficient. To maximise payload mass and vehicle range—by minimising both thermal protection weight and aerodynamic drag—the critical engineering objective is to delay transition as far downstream as possible.

However, developing effective transition-delay strategies requires targeting the specific instability mechanisms responsible for turbulence onset. While low-speed boundary-layer transition is typically governed by Tollmien–Schlichting waves, hypersonic boundary layers on slender bodies are dominated by acoustic instabilities known as the second Mack modes. Among these, the second Mack mode exhibits particularly high amplification rates and is widely regarded as the dominant transition mechanism at Mach numbers exceeding four.



Figure 1.2: Structural damage to the X-15A-2 ventral pylon caused by aerodynamic heating during Mach 6.7 flight. Complex shock-boundary layer interactions triggered premature transition and localised heating peaks that burned through the ablative thermal protection system. Image adapted from Watts [1].

Accordingly, the central challenge addressed in this research is the development of robust transition-control strategies capable of stabilising these high-speed instabilities. While conventional smooth surfaces permit the natural amplification of the second Mack modes, recent theoretical and experimental studies suggest that modifying the base flow—specifically through the generation of streamwise streaks—can significantly attenuate their growth. This thesis experimentally investigated a novel and passive approach for generating such streaks using non-uniform surface temperature distributions. By examining suppression of second Mack mode instabilities through thermal flow control, this work contributes to the development of effective drag-reduction strategies and lighter, more efficient Thermal Protection Systems capable of enduring sustained hypersonic flight.

1.2 Research Objectives

Given the significant aerothermal challenges associated with hypersonic flight, it is essential to develop effective flow control methods to enhance the performance and reliability of next-generation vehicles.

The primary aim of this thesis was to establish a novel actuation method for generating controlled surface temperature gradients and to evaluate its effectiveness as a transition control strategy. The research investigated the associated heat transfer, structural integrity, and flow physics of these non-uniform temperature distributions, progressing from thermal design to supersonic validation, and finally to hypersonic application.

Specifically, the thesis addressed the following objectives:

- **Objective 1: Actuation Design and Thermal Modelling**

  To develop and assess feasible passive thermal actuation concepts capable of generating spanwise temperature gradients under distinct operating environments. This objective is an exploratory study to quantify the achievable spanwise temperature non-uniformity as a function of material selection, geometry, and thermal boundary conditions. A three-dimensional thermal model was developed to compare performance under steady-state Mach 6 flight-relevant heating versus short-duration wind-tunnel conditions, thereby establishing practical limits and scalability for subsequent experimental implementation.

- **Objective 2: Proof of Concept and Streak Characterisation**

  To validate the generation of surface temperature gradients and the induction of streamwise streaks by developing a prototype flat-plate test article tested in a Mach 2.75 supersonic flow. This objective included characterising the induced boundary-layer modifications using Infrared Thermography (IRT) and a custom-developed Laser Doppler Anemometry (LDA) system for local velocity measurements. The key outputs were the repeatability of the imposed surface-temperature field and the resulting streak amplitude in the boundary layer.

- **Objective 3: Transition Control on a Waverider at Mach 5**

  To quantify the control effectiveness of non-uniform surface temperature distributions by developing a Mach 5 waverider model integrating a thermal actuation system. Transition behaviour was assessed through thermal footprint visualisation using Infrared Thermography (IRT), while the attenuation of dominant boundary-layer instabilities is quantified using high-frequency pressure transducers.

1.3 Thesis Structure

This thesis begins by outlining the motivation and objectives of the research, followed by chapters that establish the necessary background and theoretical foundations. Conceptual actuation methods for generating non-uniform surface temperature distributions are then introduced. The main body of the work presents proof-of-concept supersonic testing, followed by a dedicated hypersonic test campaign. The thesis concludes with a discussion of the key findings and recommendations for future research. A chapter-by-chapter overview is provided below:

- **Chapter 2: Literature Review**

  Chapter 2.4.2 provides a comprehensive review of the existing literature on hypersonic boundary-layer transition, conventional control methods, and past ground test programs. The concept of non-uniform surface temperature distributions is introduced, and the remaining challenges motivating this work are identified.

- **Chapter 3: Actuation Methods for Non-Uniform Surface Temperature Distributions**

  Chapter 3.4 introduces conceptual actuation strategies for generating controlled surface temperature variations under both flight and wind tunnel conditions. A three-dimensional thermal model is developed to simulate heat transfer and to assess material choices and wall designs required to achieve the desired temperature gradients.

- **Chapter 4: Characterisation of Non-Uniform Temperature Distributions via a Proof-of-Concept Flat Plate Model**

  Chapter 4.7 details the experimental methodology and validation of the control concept in the Imperial College supersonic wind tunnel at Mach 2.75. The design of the flat-plate test article, supporting heating system, and surface coatings are described, alongside the measurement techniques and calibration procedures. Experimental results are presented and compared with thermal model predictions, and local boundary-layer profiles are characterised to quantify the amplitudes of the induced streamwise streaks.

- **Chapter 5: Hypersonic Transition Control via Surface Temperature Variations on a Waverider Model**

Chapter 5.6 reports on the hypersonic test campaign conducted in the Manchester High Supersonic Tunnel (HSST) at Mach 5. A waverider model incorporating the non-uniform surface temperature actuation system is introduced. The chapter documents the development of dominant boundary-layer instabilities and the associated surface heat transfer behaviour. Experimental results demonstrated that the non-uniform surface temperature distributions attenuate these instabilities and modify the transition behaviour, highlighting the viability of this control strategy.

- **Chapter 6: Conclusions and Future Work**
  Chapter 6.5 summarises the main findings of the thesis and provides recommendations for future investigations to further advance hypersonic transition control research.

1.4 Publications

The publications and conference presentations derived from the work presented in this thesis are listed below.

1.4.1 International Journal Papers

- Kazuki Ozawa, Kshitij Sabnis, and Paul Bruce, "Measurement of boundary layer velocity profiles with spatially and temporally varying surface temperature in high-speed flow," *Experiments in Fluids*, 67, article 84, 2026. DOI: 10.1007/s00348-026-04243-w

- Kazuki Ozawa and Paul Bruce, "Experimental generation of non-uniform surface temperature distributions in high-speed flow," *Experiments in Fluids*, 67, article 26, 2026. DOI: 10.1007/s00348-026-04177-3

- Kazuki Ozawa, Chengwei Xia, Georgios Rigas, and Paul Bruce, "Spanwise Nonuniform Surface Temperature Distributions for High-Speed Boundary-Layer Transition Control," *AIAA Journal*, 63(10), 2025, pp. 1–12. DOI: 10.2514/1.J064991.

1.4.2 International Conference Papers

- Kazuki Ozawa, Luca Boscagli, Georgios Rigas, Paul Bruce, Muhammet Tayyip Gurbuz, Ozgun Ozer, and Mark Quinn, "Influence of Non-uniform Surface Temperature Distributions on Hypersonic Boundary Layer," AIAA SciTech 2026 Forum, 2026. DOI: 10.2514/6.2026-1147.

- Kazuki Ozawa and Paul Bruce, "Generation of Streaks by Non-Uniform Surface Temperature Distributions for Hypersonic Boundary Layer Transition Control," AIAA SciTech 2025 Forum, 2025. DOI: 10.2514/6.2025-0262.

- Kazuki Ozawa and Paul Bruce, "Temperature Measurement of Non-Uniform Surface Temperature Distributions for Delaying High-Speed Boundary Layer Transition," 58th 3AF International Conference AERO2024, 2024. Paper AERO2024-23-OZAWA.

- Kazuki Ozawa and Paul Bruce, "High-Speed Boundary Layer Transition Control with Non-Uniform Surface Temperature Distributions," 57th 3AF International Conference AERO2023, 2023. Paper AERO2023-63-OZAWA.

- Kazuki Ozawa, Chengwei Xia, Georgios Rigas, and Paul Bruce, "Passive Control of High-Speed Boundary Layer Transition Using Non-Uniform Surface Temperature Distributions," AIAA SciTech 2023 Forum, 2023. DOI: 10.2514/6.2023-0849.

  This publication comprises studies related to the second, and third chapters. The DNS and theoretical analyses investigating the generation of stationary streaks and their influence on boundary-layer stability were used to define the initial conditions for the DNS presented in this thesis, and provided an essential foundation for the subsequent experimental work. The DNS work in that publication was conducted by Xi and Rigas prior to the author's contribution to the present thesis, and is therefore summarised as previous work in the Introduction.

1.5 Scholarships and Awards

Financial Support for Conferences and Travel

- **PhD Travel Award Scheme (Department of Aeronautics, Imperial College London):** to support attendance at AIAA SciTech 2026 (internal award, £500).
- **Old Centralians' Trust Postgraduate Travel Award (Imperial College London):** to support attendance at AIAA SciTech 2023, 2024, 2026, and the 3AF International Conference 2024 (internal award, £2,600 across four occasions).
- **Imperial College Trust General Fund (Imperial College London):** to support attendance at the 3AF International Conference 2023 (internal award, £500).
- **Aerospace Speakers Travel Grant (Royal Aeronautical Society):** to support presentation at AIAA SciTech 2023 (external award, £600).

Academic Recognition

- **Best Poster Award (Royal Aeronautical Society):** winner of the poster session at the RAeS Specialist Group Conference: "High-Speed Aerodynamics – Towards Hypersonic Flight," London, October 2023 (external award).

Chapter 2

Literature Review

2.1 Hypersonic Flight Environment

Hypersonic flight is commonly defined as the regime in which the free-stream Mach number exceeds five. While this threshold does not represent a sharp physical boundary, it marks the onset of flow phenomena—such as strong compressibility, elevated aerodynamic heating, and increased sensitivity of boundary-layer stability—that fundamentally distinguish hypersonic flows from their supersonic counterparts. For hypersonic vehicles, these effects are tightly coupled to laminar–turbulent boundary-layer transition, which directly governs skin-friction drag, surface heat transfer, and overall vehicle performance. A clear definition of the hypersonic flight environment is therefore essential for contextualising the transition control strategies examined in this thesis.

The operational envelope of hypersonic vehicles is effectively illustrated using the velocity–altitude map shown in Fig. 2.1, reproduced from Bertin and Cummings [2, 3]. This map delineates distinct hypersonic flight regimes according to the dominant aerothermodynamic mechanisms and associated vehicle classes. Two categories are particularly relevant: hypersonic cruise vehicles and hypersonic reentry vehicles.

At lower hypersonic velocities, typically in the range Mach 5-10 (approximately 1.5–3.0 km/s) and at moderate altitudes, the flow environment is commonly described as viscous-effects dominated relative to higher-enthalpy reentry regimes. This region is characteristic of hypersonic cruise vehicles employing

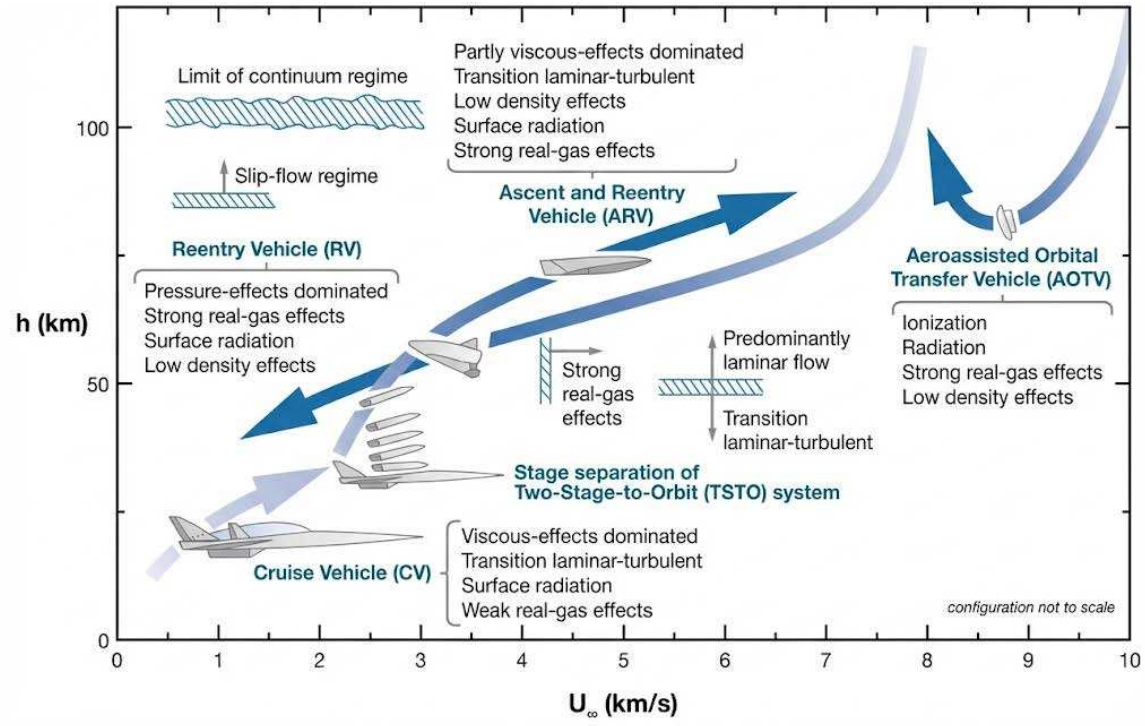


Figure 2.1: Velocity-altitude map showing critical aerothermodynamic phenomena for various hypersonic vehicle classes. Reproduced from Bertin and Cummings [2, 3].

slender aerodynamic configurations. In such cases, pressure (wave) drag is comparatively modest, and vehicle performance is strongly influenced by skin-friction drag and boundary-layer behaviour. As indicated in Fig. 2.1, laminar–turbulent transition occurs squarely within this flight corridor. Real-gas effects in this regime are weak; although compressibility is high and surface radiation may be present, the flow thermodynamics remain close to ideal-gas behaviour.

In contrast, hypersonic reentry vehicles operate at much higher velocities, approaching orbital speeds ($\gtrsim$7 km/s). These vehicles typically employ blunt geometries that generate strong bow shocks, converting kinetic energy into intense thermal loads. Under these conditions, pressure effects dominate the aerodynamics, and strong real-gas phenomena—including vibrational excitation, molecular dissociation, ionisation, and radiative heating—become significant. While such effects are central to reentry vehicle design, they are not the primary focus of the present study.

At sufficiently high altitudes, rarefaction effects may arise as the mean free path of gas molecules becomes comparable to characteristic length scales of the vehicle, leading to slip-flow or transitional regimes. However, the Mach 5 conditions considered in this work lie well within the continuum regime, and such effects are negligible.

Regime of the Present Study

The experimental investigations presented in this thesis were conducted at Mach 5, placing the study squarely within the hypersonic cruise-vehicle regime shown in the lower-left region of Fig. 2.1. This regime is particularly well suited for fundamental studies of hypersonic boundary-layer transition for two key reasons. First, the flow is viscous dominated relative to reentry conditions, meaning that boundary-layer transition has a first-order impact on skin-friction drag and surface heat transfer—quantities of direct relevance to hypersonic cruise vehicle performance. Second, real-gas effects are weak, allowing the flow to be accurately modelled as a calorically perfect gas with $\gamma = 1.4$, an assumption widely adopted in Mach 5 wind-tunnel experiments. The absence of strong thermochemical effects enables isolation of the fundamental instability mechanisms governing transition, notably the first and second Mack modes. Consequently, the Mach 5 configuration provides an ideal canonical framework for examining how modifications to wall conditions—specifically non-uniform surface temperature distributions—can alter boundary-layer stability and transition behaviour. This motivates the detailed discussion of hypersonic boundary-layer instability mechanisms presented in the following section.

2.2 Hypersonic Boundary-Layer Transition: Modal and Non-modal Instability Mechanisms

Laminar–turbulent transition in hypersonic boundary layers remains a central challenge in high-speed aerothermodynamics due to its profound impact on surface heat transfer, skin-friction drag, and vehicle performance. Hypersonic transition is governed by a hierarchy of instability mechanisms whose relative importance depends strongly on Mach number, wall thermal conditions, and the disturbance environment. A clear understanding of these mechanisms is essential for the development of effective transition control strategies.

Extensive experimental, theoretical, and numerical investigations conducted since the 1970s have established the fundamental pathways through which boundary-layer transition to turbulence at high speeds [4]. These pathways have been systematically classified by Morkovin et al. [5] and Fedorov [6], resulting in the canonical transition diagram shown in Fig. 2.2. The diagram illustrates that the route to turbulence depends primarily on the level and nature of external disturbances, as well as the

receptivity characteristics of the boundary layer.

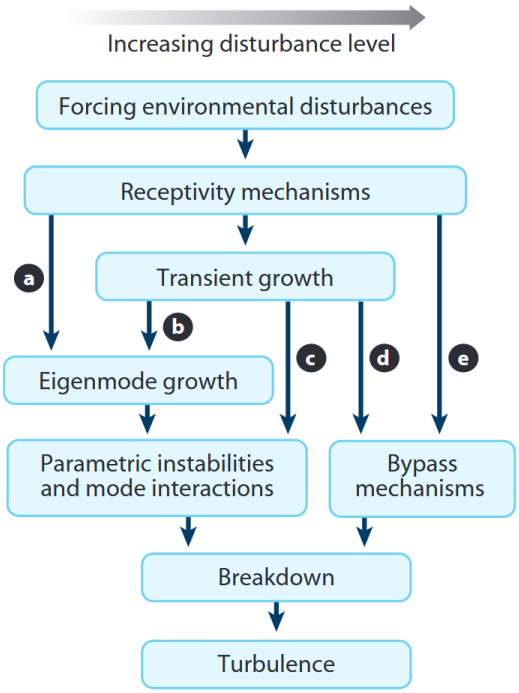


Figure 2.2: Canonical transition pathways in boundary layers as a function of disturbance environment, illustrating modal, transient-growth, and bypass routes to turbulence. Reproduced from Morkovin et al. [5] and Fedorov [6].

In low-disturbance environments—such as those encountered in quiet hypersonic wind tunnels or high-altitude flight [7]—transition typically follows a modal route (Path "a"). In this scenario, external disturbances excite discrete linear eigenmodes through receptivity mechanisms, which subsequently undergo exponential amplification over long streamwise distances. This modal growth may be preceded by a stage of algebraic transient growth (Path "b"), which amplifies disturbances prior to the onset of exponential instability. In contrast, under moderate to high disturbance levels, transition may proceed via bypass routes, where strong non-modal transient growth of oblique disturbances generates large-amplitude streamwise streaks (Path "c"), or where nonlinear breakdown is triggered directly by roughness, shock–boundary-layer interaction, or intense freestream forcing (Paths "d" and "e") [8]. Despite these differing initiation mechanisms, all pathways ultimately converge toward a highly nonlinear breakdown and the formation of a fully turbulent boundary layer.

At low Mach numbers, laminar–turbulent transition is dominated by the first instability mode, commonly referred to as the Tollmien–Schlichting (TS) wave. TS waves are viscous, hydrodynamic instabilities that arise from the interaction between mean shear and viscous effects. Their growth is

typically triggered by upstream perturbations [9] and proceeds through linear amplification followed by nonlinear interactions. Oblique TS waves provide an especially efficient route to transition, as they can undergo breakdown at relatively low disturbance amplitudes [10]. Direct numerical simulations (DNS) have demonstrated that nonlinear interactions between oblique TS waves generate streamwise vortices, which then amplify rapidly and precipitate transition [11,12]. Because the remaining discrete modes are stable and spectrally well separated, modal coupling outside the TS family is generally weak and can often be neglected.

In hypersonic boundary layers, the dominant instability mechanisms differ fundamentally from those at low Mach numbers. In addition to the first mode, strong acoustic instabilities arise due to the trapping of acoustic waves within the boundary layer [13, 14]. These waves are confined between the wall and the relative sonic line, which acts as an acoustic waveguide. Repeated reflection of acoustic rays at the wall and turning near the relative sonic line gives rise to the second instability mode, commonly known as the second Mack mode. While higher-order acoustic modes may also exist, their amplification rates are generally smaller and they play a secondary role [14].

The second Mack mode becomes increasingly dominant with increasing Mach number and typically overtakes the first mode above Mach 4 for adiabatic walls. For cooled walls, second Mack mode instabilities may appear at even lower Mach numbers [14]. Owing to its substantially higher amplification rate, the second Mack mode is widely regarded as the primary driver of hypersonic boundary-layer transition. At still higher Mach numbers (above approximately Mach 7), a third instability mode has been predicted to exhibit growing amplification rates, although its relevance at Mach 5 remains limited [14]. Within the second Mack mode family, two-dimensional planar disturbances are usually the first to emerge, followed by oblique variants that also experience rapid growth.

The existence and characteristics of second Mack mode instabilities have been confirmed experimentally in numerous studies. Flow visualisations using Rayleigh scattering have revealed the distinctive rope-like wave structures associated with the second Mack mode in hypersonic boundary layers [15–17], as illustrated in Fig. 2.3.

In cryogenic wind tunnels, seeding with carbon dioxide enables condensation into fine droplets, providing enhanced visualisation of instability evolution along flared-cone models [18]. Quantitative measurements of second Mack mode disturbances have also been obtained using piezoelectric wall-

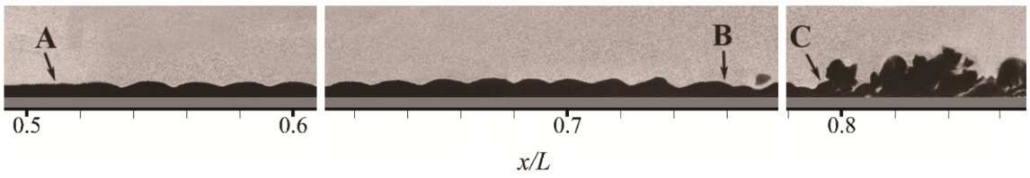


Figure 2.3: Rayleigh-scattering visualisation of boundary-layer transition in quiet Mach 6 flow over a flared cone. The marked locations indicate (A) initial appearance of the second Mack mode disturbances, (B) decay of second Mack mode amplitude, and (C) onset of turbulent breakdown. Figure reproduced from Zhang et al. [15].

pressure sensors [16, 19] and optical diagnostics such as Focused Laser Differential Interferometry (FLDI) [20, 21]. Typical second Mack mode frequencies reported in Mach 6 flows lie in the range of 200–300 kHz, depending on the local boundary-layer thickness and flow conditions, as exemplified by the pressure spectra shown in Fig. 2.4.

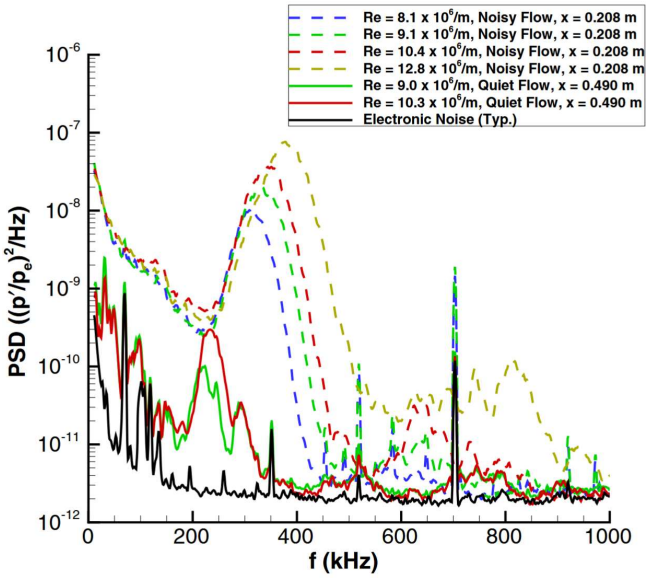


Figure 2.4: Pressure RMS spectra showing second Mack mode waves at $Re/x = 8.0 \times 10^6$ to 12.8 $\times 10^6$ in the Boeing/AFOSR Mach-6 Quiet Tunnel (MAB6QT) under noisy and quiet flow, obtained using a PCB132B38 pressure sensor. Reproduced from Casper et al. [16].

As second Mack mode disturbances amplify in the streamwise direction, they eventually reach amplitudes at which linear theory breaks down, and nonlinear interactions become dominant. These interactions generate strong vortical motions that destabilise the boundary layer and initiate transition to turbulence [22–24]. Several nonlinear breakdown routes have been identified [25]. In the fundamental (K-type) resonance, a two-dimensional second Mack mode wave interacts with oblique waves of the same frequency and streamwise wavelength, producing aligned Λ-shaped vortices and peak–valley splitting prior to breakdown. DNS studies of Mach 6 sharp cones have confirmed this mechanism as a

viable transition pathway [26]. In the subharmonic (H-type) resonance, the primary two-dimensional wave interacts with three-dimensional oblique disturbances at half its frequency, leading to staggered vortical structures and nonlinear growth [27,28]. Finally, oblique breakdown arises from the excitation of symmetric pairs of three-dimensional waves, generating steady streamwise vortices, streaks, higher harmonics, and a spanwise-periodic arrangement of streamwise vortical structures [25]

2.3 Influence of Geometry and Wall Conditions on Hypersonic Transition

Hypersonic transition is fundamentally governed by boundary-layer receptivity, whereby external disturbances are admitted into the boundary layer, propagate, and ultimately trigger the growth of instabilities. Nose bluntness, wall temperature, and the use of porous or ultrasonically absorptive surfaces can significantly modify receptivity characteristics and disturbance amplification rates. This subsection reviews the influence of these geometric and thermal conditions on hypersonic transition and their relevance to passive transition-control strategies.

2.3.1 Effect of Leading-Edge Curvature Radius

The nose geometry of a hypersonic vehicle represents a fundamental design compromise: while blunt noses reduce the intense stagnation-point heating by forming a detached bow shock, they also increase drag. Beyond this classical trade-off, nose bluntness significantly modifies boundary-layer stability and thus the laminar–turbulent transition process [29].

A key feature of a blunt configuration, characterised by the nose Reynolds number $Re_{R_N} = UR_N/\nu$, where R_N is the nose radius, U is the freestream velocity, and ν is the kinematic viscosity, is the formation of an entropy layer downstream of the curved bow shock, which can extend well beyond the nose-tip region. This entropy layer alters the stability properties of the boundary layer and is generally associated with a suppression of second Mack mode instabilities. Experiments consistently show that increasing nose-tip radius displaces the transition onset downstream, indicating a stabilising trend with moderate bluntness. However, this behaviour does not persist indefinitely: beyond a critical bluntness

level, the downstream movement of transition saturates and eventually reverses, a phenomenon known as *transition reversal* [29, 30].

The transition-reversal phenomenon is illustrated in Fig. 2.5, which shows the transition Reynolds number Re_{ξ_T} as a function of nose Reynolds number Re_{R_N} for Mach 6 flows. Initially, increasing nose-tip Reynolds number leads to higher transition Reynolds numbers, indicating delayed transition. Beyond a critical nose radius, such as cone A11 with $R_N = 15.2\,\text{mm}$, the trend reverses, and transition begins to occur earlier despite further increases in bluntness. The close agreement between datasets obtained by Stetson [29] and Aleksandrova et al. [31], as compiled by Paredes et al. [32], demonstrates that transition reversal is a robust and repeatable feature of hypersonic blunt-body flows across different facilities and experimental conditions.

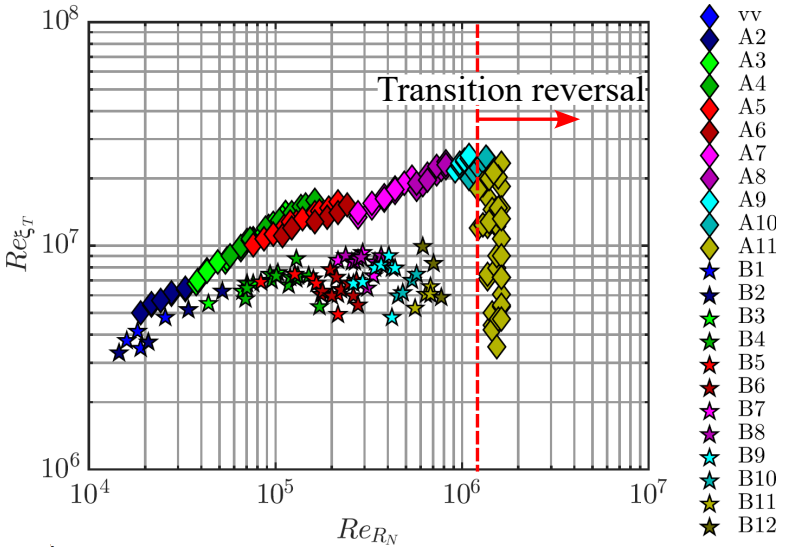


Figure 2.5: Transition Reynolds number based on freestream as a function of the nose Reynolds number at Mach 6. Adapted from Paredes et al. [32]

Stabilising Regime with Increasing Bluntness

In the moderate nose-bluntness regime ($Re_{R_N} \lesssim 10^6$), increasing bluntness produces a systematic delay in transition onset, as shown in Fig. 2.5. This stabilising behaviour has been consistently attributed to the attenuation of second Mack mode instabilities, which otherwise dominate transition on sharp cones and slender bodies [29, 32, 33].

Linear stability analyses indicate that the entropy layer generated by the curved bow shock modifies the mean velocity and temperature profiles in a manner that weakens the acoustic wave-trapping mechanism responsible for second Mack mode growth [34]. As a result, the amplification rates of

second Mack mode disturbances are substantially reduced, delaying the onset of nonlinear breakdown.

This stabilising effect is illustrated in Fig. 2.6, which compares the power spectral density (PSD) of wall-pressure fluctuations measured on sharp and moderately blunt cones. In the sharp-nose case ($R_N = 0.1\,\mathrm{mm}$), pronounced second Mack mode activity is observed, characterised by high-amplitude spectral peaks in the 120–300 kHz range. In contrast, the moderately blunt cone ($R_N = 2\,\mathrm{mm}$) exhibits a marked reduction in spectral energy across this frequency band, indicating effective suppression of second Mack mode instabilities. Complementary experiments by Horvath et al. [35] on straight and flared cones at Mach 6 further confirmed this trend, demonstrating a progressive downstream displacement of the transition front with increasing nose radius. Collectively, these results support the interpretation that moderate bluntness stabilises the hypersonic boundary layer primarily through entropy-layer-induced damping of modal instabilities.

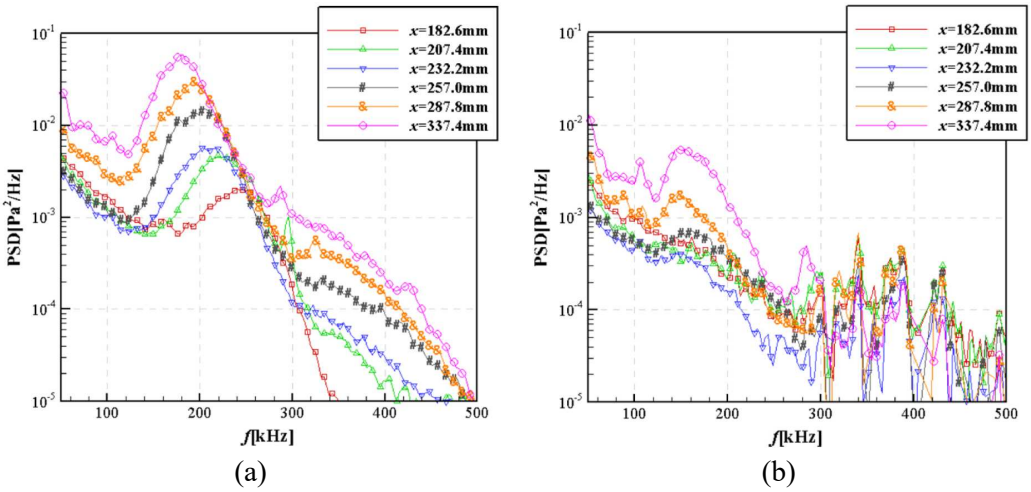


Figure 2.6: Power spectral density (PSD) of wall-pressure fluctuations at (a) $R_N = 0.1\,\mathrm{mm}$ and (b) $R_N = 2\,\mathrm{mm}$ for Mach 6 flow ($T_w = 300\,\mathrm{K}$, $Re = 4 \times 10^6\,\mathrm{m}^{-1}$). Reproduced from Huang et al. [33].

Reversal Regime at Large Bluntness

When the nose bluntness is increased further ($Re_{R_N} \gtrsim 10^6$), the stabilising influence of the entropy layer saturates and ultimately breaks down. In this regime, transition onset moves upstream despite continued suppression of linear second Mack mode instabilities, marking the onset of the transition-reversal phenomenon. Recent experimental and numerical studies indicate that transition in this regime is governed not by modal growth, but by non-modal mechanisms associated with transient growth and nonlinear interactions [32, 36].

In particular, oblique travelling disturbances developing within the entropy layer can undergo non-

linear interactions that transfer energy into stationary modes, leading to the formation of streamwise streaks. These streaks become susceptible to secondary instabilities, providing an effective bypass route to turbulence even in the absence of strong second Mack mode amplification. This mechanism is illustrated in Fig. 2.7, which shows the streamwise evolution of root-mean-square (RMS) velocity disturbances for different azimuthal Fourier modes. While the fundamental oblique mode ($n = 1$) initiates the disturbance field, nonlinear interactions rapidly amplify the stationary mode ($n = 0$), resulting in the growth of streaks. Higher harmonics ($n \geq 2$) remain comparatively weak, indicating that the dominant energy transfer occurs between the oblique travelling wave and the stationary streak component.

The sensitivity of highly blunt configurations to external disturbances further amplifies this bypass mechanism. Roughness elements located near the relative sonic line on the nose tip are particularly effective at exciting oblique disturbances within the entropy layer. Experiments show that roughness arrays placed on highly blunt cones (e.g., $R_N = 15.24\,\text{mm}$) induce significantly earlier transition, whereas identical perturbations applied to moderately blunt cones (e.g., $R_N = 5.08\,\text{mm}$) produce little effect. This demonstrates that excessive bluntness enhances receptivity to roughness-induced disturbances, thereby increasing susceptibility to non-modal transition pathways and highlighting the importance of surface condition and environmental noise.

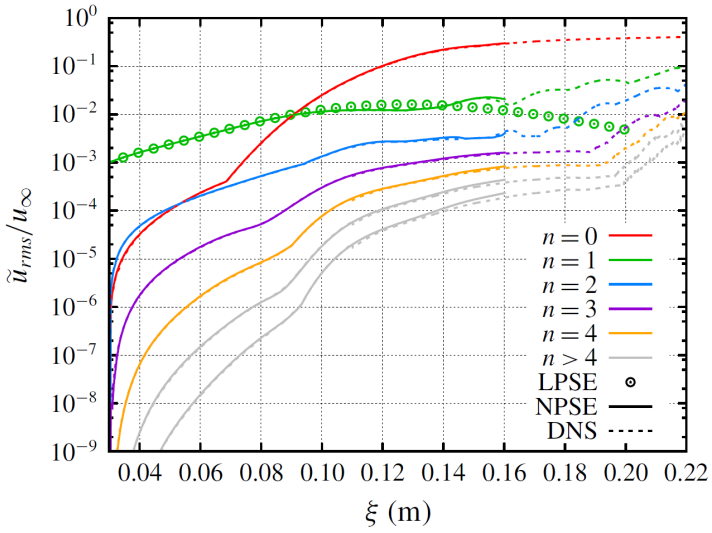


Figure 2.7: Streamwise evolution of non-modal oblique disturbances and stationary streaks within the entropy layer at Mach 6. Reproduced from Paredes et al. [36].

2.3.2 Wall Cooling/Heating Effect

Wall-temperature effects are reported using the normalisation adopted in each cited study, such as T_w/T_∞, T_w/T_e, or T_w/T_{aw}, where T_w denotes the wall temperature, T_∞ the free-stream temperature, T_e the boundary-layer edge temperature, and T_{aw} the adiabatic wall temperature. The influence of wall temperature on hypersonic boundary-layer stability has long been recognised as a critical factor in transition. Mack demonstrated that wall temperature strongly modifies the amplification characteristics of instability modes: wall cooling stabilises Tollmien–Schlichting waves, while significantly destabilising the second Mack mode due primarily to the associated reduction in boundary-layer thickness and increase in acoustic trapping [14].

To characterise the stability properties of the boundary layer, neutral stability curves obtained from linear stability theory (LST) are commonly employed to delineate the boundary between stable and unstable disturbances in a selected parameter space, typically Reynolds number and frequency. Along a neutral curve, the disturbance growth rate is zero, such that perturbations neither amplify nor decay. For a fixed frequency, the intersections with the neutral curve define upstream and downstream neutral points, commonly referred to as Branch I and Branch II [6,14]. Branch I marks the streamwise location where disturbances first become unstable, while Branch II denotes the point downstream where the flow restabilises and disturbance amplification ceases. Figure 2.8 presents neutral stability curves for a 5-degree cone at a freestream Mach number of Mach 5.6 for several wall-temperature ratios [37]. At higher wall temperatures, such as the adiabatic-wall condition ($T_w = T_{aw}$), a low-frequency neutral branch is observed, which is commonly associated with first-mode instability. As the wall temperature is reduced, this low-frequency branch is progressively suppressed and ultimately disappears, while the second Mack mode neutral curves shift upstream and extend to higher frequencies. These trends indicate both an earlier onset of second Mack mode instability and an expansion of the unstable frequency band under wall-cooling conditions. The destabilising effect of wall cooling on the second Mack mode has been further quantified by Masad, who examined the variation of N-factors with wall-to-recovery temperature ratios over a range of Mach numbers. His results show that decreasing wall temperature progressively suppresses first-mode growth while promoting dominant second Mack mode amplification [38, 39] (see Fig. 2.9).

The impact of wall cooling on the nonlinear regime has also been investigated. Franko and Lele

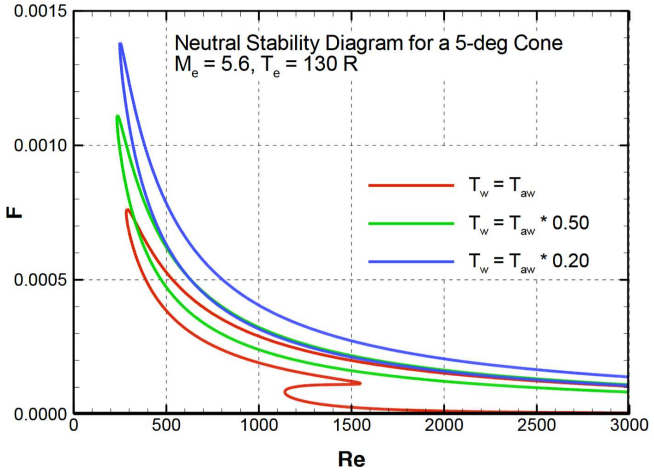


Figure 2.8: Neutral stability curves illustrating the effect of wall cooling on a 5-degree cone at Mach 5.6. Reproduced from Kara et al. [37]

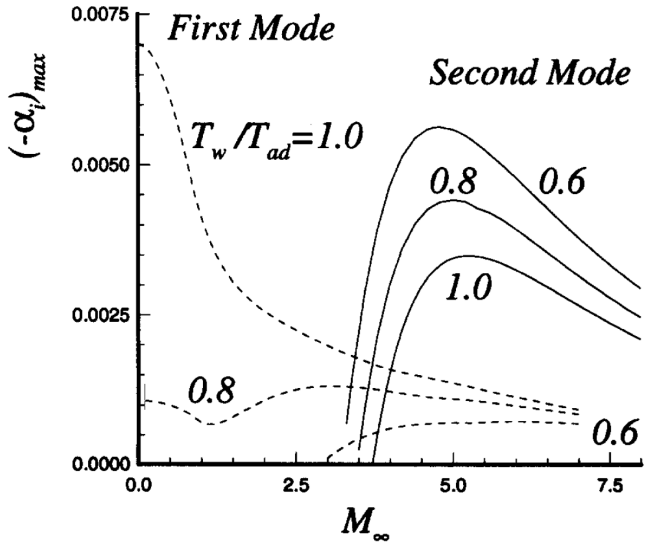


Figure 2.9: Effect of wall cooling on instability growth rates. Comparison of amplification factors for the first and second Mack modes under cooled-wall condition (Reproduced from Masad [39]).

performed DNS of a flat plate at Mach 6 and showed that the fundamental resonance mechanism persists under cooling, with no major quantitative change in the nonlinear processes [25]. In contrast, Siddiqui et al. investigated transition over a cooled flared cone at Mach 6, with instabilities induced by distributed roughness elements [20]. They identified second Mack mode frequencies in the range of 281–315 kHz, observed periodic mass-flux fluctuations attributed to Görtler vortices, and reported an upstream shift of the transition location with decreasing wall temperature. Their Linear Array (LA)- Focused Laser Differential Interferometry (FLDI) measurements, an extension of the FLDI technique employing multiple spatially distributed beam pairs, captured both the fundamental and second harmonics. As the freestream Reynolds number increased, these spectral features diminished as turbulence developed, as shown in Fig. 2.10(a)–(c).

More recently, Unnikrishnan and Gaitonde investigated the structure of wavepackets in cooled-wall boundary layers [40]. They found that wavepackets amplified more strongly and displayed nonlinear distortion, with transition occurring more rapidly. The structure depended on cooling intensity: moderate cooling ($T_w/T_\infty \gtrsim 3$) produced a bifurcation into a turbulent head and a trailing harmonic region, whereas stronger cooling ($T_w/T_\infty \lesssim 0.5$) slowed convection, elongated the wavepacket, and produced intermittent turbulent spots in its wake.

Beyond uniform cooling, researchers have investigated the use of localised heating or cooling to manipulate instabilities. In supersonic flow, Masad and Abid showed that applying local heating at Mach 3.5 stabilised the first mode [39]. For hypersonic flow, Polivanov et al. studied strips of local heating and cooling on a Mach 6 cone and showed that local cooling delayed transition by reducing second Mack mode amplitude, but that the effect critically depended on strip location relative to the neutral point [42]. Soudakov et al. confirmed these findings, but cautioned that e^N-based predictions may be misleading due to the strong non-uniformities induced near the strip [43]. Fedorov and Sidorenko combined numerical and experimental approaches on a Mach 6 cone and confirmed that local cooling stabilises the second Mack mode, in contrast with global cooling, while local heating shifted transition upstream [44, 45]. Oddo et al. provided experimental confirmation on a global cooled 7° half-angle cone, comparing a cooled case ($T_w/T_e = 1.4$) with an uncooled case ($T_w/T_e = 4.3$) at Mach 6 [41]. Second Mack mode instabilities were observed in both cases. As the wall cooling intensity increased, the flow exhibited reduced turbulent intermittency, as evidenced in Fig. 2.10(d), where the cooled case (blue curve) shows consistently lower intermittency levels than the uncooled case (red curves) along

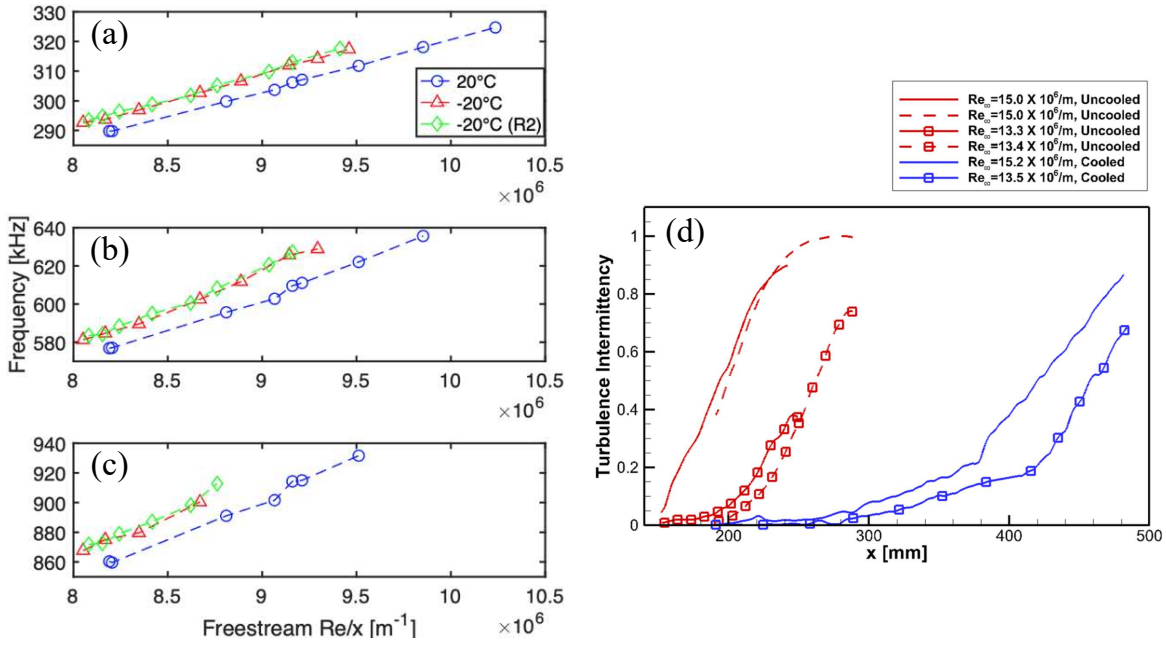


Figure 2.10: Instability dynamics of the hypersonic boundary layer under cooled and uncooled wall conditions at Mach 6. (a) Fundamental dominant second Mack mode frequency, (b) first harmonic, and (c) second harmonic measured with LA-FLDI for various freestream unit Reynolds numbers on a flared cone [20]. (d) Intermittency comparison between cooled and uncooled walls on 7° half-angle cone [41].

the streamwise direction. Although the frequency of the most unstable waves increased, the onset of transition was delayed (see Fig. 2.10(d)). Notably, the critical N-factor associated with transition was substantially higher in the cooled-wall case ($N = 9.8$) compared with the uncooled case ($N = 4.5$).

The position of local thermal perturbations relative to the synchronisation point, defined as the streamwise location where the phase speeds of the first and second Mack mode instabilities coincide, has been shown to be particularly important. Zhao et al. studied local cooling and heating on a Mach 6 flat plate and demonstrated that heating strips located upstream of the synchronisation point destabilised the primary mode, while strips downstream had the opposite effect [46]. Cooling exhibited the reverse behaviour: upstream strips stabilised, while downstream strips destabilised. Batista and Kuehl extended this concept using a computational approach, combining strips on a flared cone at Mach 6, showing that the most effective stabilisation strategy was upstream cooling paired with downstream heating [47]. Oz et al. recently examined partial versus full wall cooling on a Mach 6 cone [48]. They confirmed that entire wall cooling destabilised the boundary layer, but that local cooling upstream of the synchronisation point suppressed disturbances, with longer strips providing stronger stabilisation. In contrast, downstream cooling strips enhanced instability, shown in Fig. 2.11. More recently,

Poulain et al. employed adjoint-based linear sensitivity analysis within a global resolvent framework to evaluate the impact of steady wall heating and cooling on a Mach 4.5 boundary layer [49]. Their findings showed that heating near the leading edge effectively stabilised both the first and second Mack modes, while downstream cooling selectively damped the first mode.

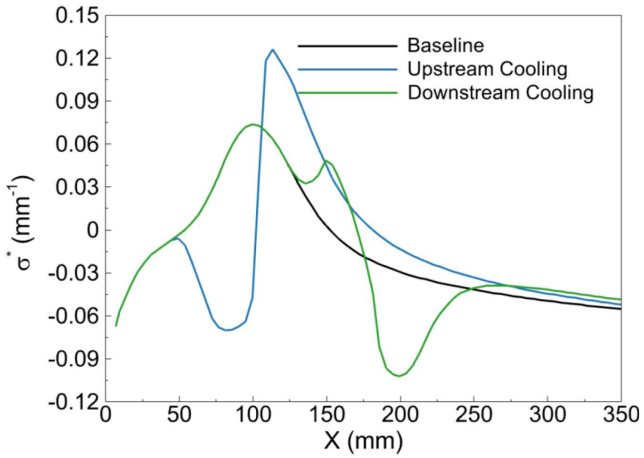


Figure 2.11: Effect of local wall cooling placement on instability growth rates in a Mach 6 sharp-cone boundary layer (after Oz et al. [48]).

2.3.3 Porous and Ultrasonically Absorptive Materials

Porous surfaces have emerged as a promising solution for damping the growth rate of hypersonic second Mack mode instabilities. The fundamental working principle of ultrasonically absorptive coatings (UACs) is to absorb the high-frequency acoustic waves (second Mack mode) trapped between the wall and the sonic line. By extracting energy from these instability waves—whose unsteady pressure footprints are measurable at the wall—porous walls can be geometrically designed or tuned to target the frequency range of the second Mack mode, thereby reducing the amplification of unstable disturbances and delaying transition [50, 51]. Both regular and random microstructures have been explored as candidate UAC materials, including carbon–carbon (C/C) ceramics and silicon-carbide (SC) foams. Early foundational work by Fedorov et al. [50] and Rasheed et al. [52] demonstrated, through linear stability theory (LST) and shock tunnel experiments, that porous surfaces with regularly spaced blind holes could significantly suppress second Mack mode instabilities and delay transition on sharp cones at Mach 5, as illustrated in Fig. 2.12. These studies established the principle that passive, frequency-selective acoustic absorption at the wall can be used to control boundary-layer stability. While regular microstructures such as blind holes proved effective in early experiments [50, 52], they pose challenges

for integration into realistic TPS due to manufacturing complexity and limited adaptability to curved surfaces. To address this, Fedorov et al. [51] investigated felt-metal coatings with random microstructure, which are more representative of TPS materials and easier to fabricate over complex geometries. Their experiments at Mach 6 confirmed strong second Mack mode damping and extended laminar flow, demonstrating the viability of random porous structures for practical applications.

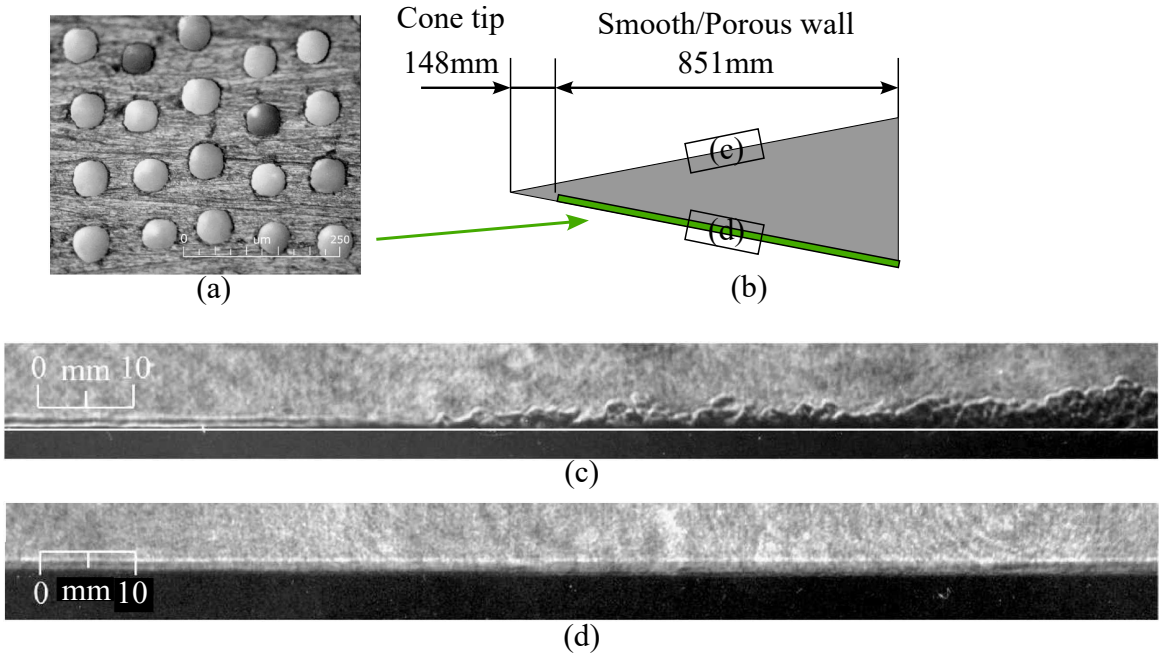


Figure 2.12: (a) Magnified image of stainless-steel perforated sheet used as a porous insert and (b) schematic of the cone model. Transition comparison on a cone model with (c) smooth and (d) porous surfaces. Adapted from Rasheed et al. [52].

Carbon–Carbon Ceramics

Wagner et al. [53] introduced carbon–carbon (C/C) ceramics with random microstructure as a TPS-relevant material. In a series of experiments conducted in the DLR HEG shock tunnel at Mach 7.5, a cone model with a C/C insert (see Fig. 2.13(a)) exhibited clear suppression of second Mack mode instability amplitudes and a measurable delay in transition onset compared to a smooth reference surface. The C/C material, characterised by a peak pore diameter of 28–30 μm and an open porosity of approximately 15 %, demonstrated robustness under high-enthalpy conditions and compatibility with TPS integration. To quantify the acoustic absorption properties, Wagner et al. [54] performed ultrasonic bench tests, measuring absorption coefficients β up to 19 % in the 200–400 kHz range—directly relevant to the second Mack mode frequencies observed in hypersonic boundary layers (see Fig. 2.13(b)). The

absorption was found to be largely independent of the porous layer thickness, and the results agreed well with predictions from quasi-homogeneous absorber theory, confirming that C/C ceramics possess strong acoustic damping characteristics with a pressure- and frequency-dependent response. The heat flux distribution along the cone surface (Fig. 2.13(c)) further demonstrated the delay in transition onset on the porous side, validating the damping effect. Building on these findings, Sousa et al. [55] conducted DNS using impedance boundary conditions (IBCs) derived from inverse Helmholtz solver (IHS) analysis of C/C surfaces. These IBCs model the acoustic response of the porous wall by linking pressure and wall-normal velocity fluctuations, enabling accurate simulation of energy absorption without resolving internal pore geometry. Their simulations revealed up to an order-of-magnitude reduction in pressure perturbation amplitude for the second Mack mode, validating the experimental observations and confirming the effectiveness of porous surfaces in delaying transition. The study also compared several impedance models and highlighted the importance of accurate pore-scale characterisation for predictive modelling.

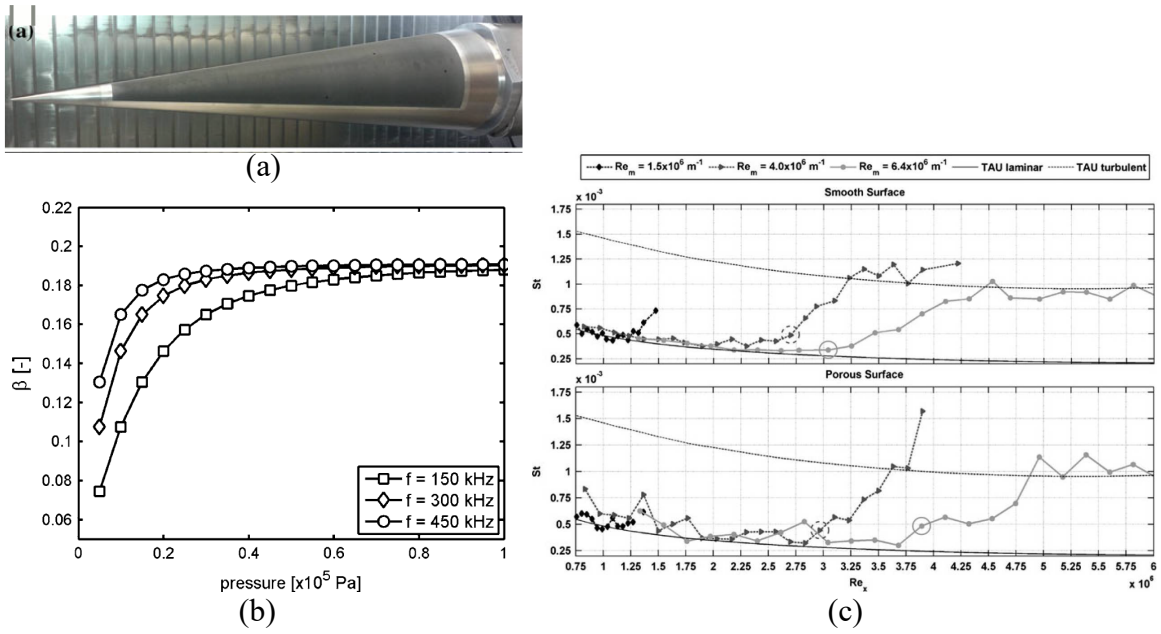


Figure 2.13: Carbon–carbon ceramic performance in hypersonic boundary-layer control: (a) cone model with integrated C/C insert, (b) estimated absorption coefficient of C/C material across second Mack mode-relevant frequencies, and (c) heat flux distribution comparing porous and smooth surfaces, with transition Reynolds numbers marked by circles. Adapted from Wagner et al. [53, 54].

Silicon-Carbide Foam

Running et al. [56] introduced silicon-carbide (SC) foam as a novel ultrasonically absorptive material,

notable for its high porosity (80 %) and low flow resistivity (0.02–0.04 MPa·s/m^2), as illustrated in Fig. 2.14(a). Experiments conducted in the AFRL Mach-6 Ludwieg Tube using a flat-plate test article revealed strong second Mack mode damping on SC foam inserts. Unlike the impermeable reference surface, which exhibited clear second Mack mode spectral peaks, the SC foam spectra lacked such features, indicating highly effective absorption and suppression of instability growth (see Fig. 2.14(b)). Ultrasonic bench tests confirmed absorption coefficients exceeding 0.90 across the relevant frequency range (75–300 kHz), demonstrating the material's strong acoustic damping capability. LST, incorporating impedance boundary conditions (IBCs) derived from these bench tests, showed that the N-factors were reduced to approximately 30 % of the impermeable case over the porous insert. However, downstream of the insert, growth rates returned to baseline, suggesting that the damping effect is spatially localised to the region of the porous material. The study also noted that at higher Reynolds numbers, transition to turbulence could still occur, potentially due to surface roughness effects or the finite axial extent of the porous insert.

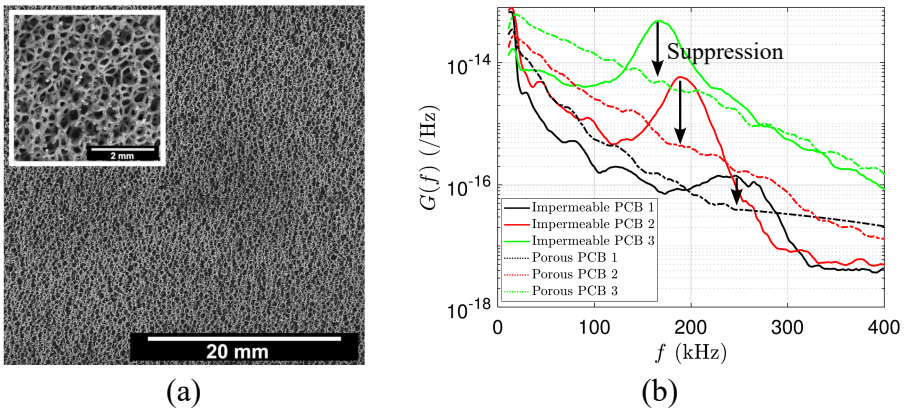


Figure 2.14: Silicon-carbide foam performance in hypersonic boundary-layer control: (a) magnified view of SC foam wall-normal surface topography, and (b) power spectra of pressure fluctuations comparing impermeable (solid line) and porous (dashed line) surfaces at $Re = 13.7 \times 10^6$ [1/m] at Mach 6. Adapted from Running et al. [56].

2.4 Streamwise Streaks as Transition Control Mechanisms

The use of artificially generated streamwise streaks, elongated regions of alternating high and low velocity, is a well-regarded strategy for controlling boundary-layer transition. Their ability to suppress the growth of Tollmien–Schlichting (TS) waves in low-speed boundary layers has been thoroughly established through extensive experimental and numerical research [57–61]. More recently, this control

strategy has demonstrated significant promise in high-speed flows, with studies showing its effectiveness in damping the highly amplified second Mack modes present in hypersonic regimes [62, 63]. For both regimes, the efficacy of control is critically dependent on key parameters, particularly the streak amplitude and spanwise wavelength. Therefore, to build upon the foundational concepts before addressing their modern application, the following subsections provide a comprehensive review of streak-based control for TS waves. Subsequently, the discussion will extend to the high-speed regime, examining the more recent developments concerning the interaction between streaks and the second Mack modes.

2.4.1 Streaks in Low-Speed Boundary Layer

Small amounts of streamwise vorticity are highly effective in redistributing momentum within incompressible boundary layers. Through the lift-up effect, an inviscid mechanism first described by Landahl [64], low-momentum fluid parcels are lifted away from the wall while high-momentum fluid is transported downward. This process generates elongated streamwise-aligned structures, referred to as streaks, characterised by spanwise modulations in streamwise velocity, sketched in Fig. 2.15.

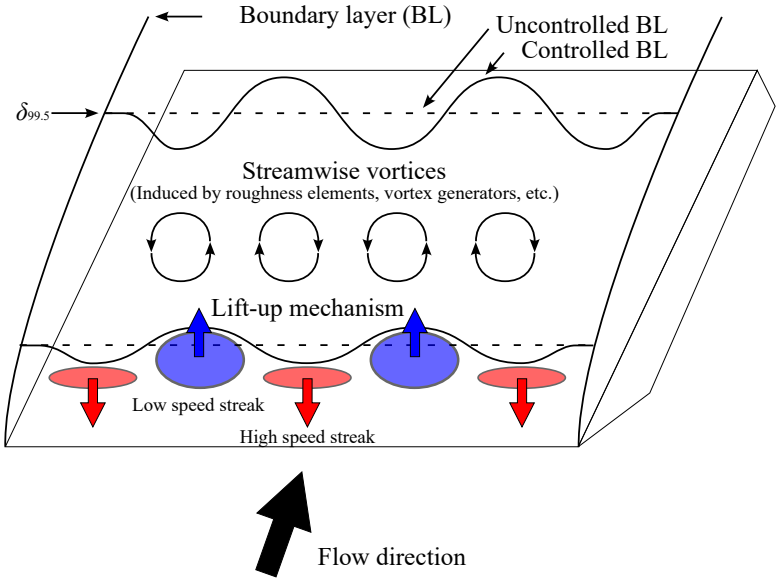


Figure 2.15: Schematic of the lift-up mechanism responsible for streak formation in a boundary layer. Streamwise vortices induce vertical motion, lifting low-momentum fluid away from the wall and pushing high-momentum fluid downward.

Fransson et al. [65] experimentally demonstrated the generation of stable streaks in a boundary layer using small cylindrical roughness elements. In a subsequent study [58], they showed that the streak

amplitude A_{st}, controlled by the height of these roughness elements, could reach up to 12 % of the freestream velocity, as illustrated in Fig. 2.16(a). Moreover, they provided the first direct experimental

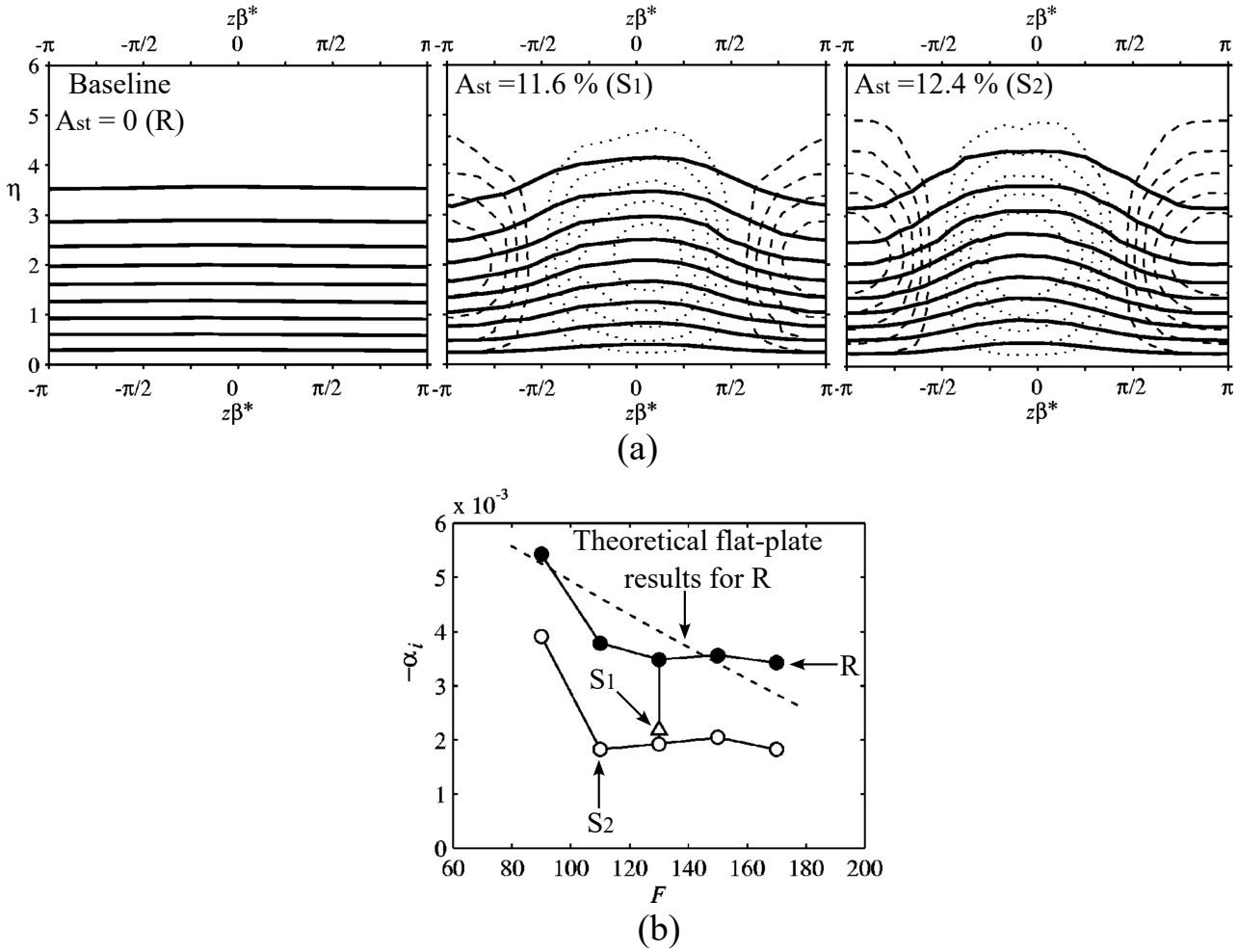


Figure 2.16: Effect of roughness-induced streamwise streaks (A_{st}) on boundary-layer structure and TS wave amplification. (a) Experimental visualisation of boundary-layer modification using cylindrical roughness elements: baseline case (R), streaky boundary layer with $A_{st} = 11.6\%$ (S_1), and $A_{st} = 12.4\%$ (S_2). Solid lines show velocity isolines; dashed lines show spanwise mean deviation. (b) Spatial growth rates of TS waves ($\alpha_i^* \delta$) as a function of frequency F for the three flow cases, showing reduction in TS wave growth due to the presence of streaks (Fransson et al. [58]).

evidence that increasing streak amplitude suppresses Tollmien–Schlichting (TS) wave growth (see Fig. 2.16(b)), corroborating earlier theoretical predictions and establishing a clear correlation between streak amplitude and TS wave stabilisation. Building upon these results, Fransson et al. [59] showed that such streaks could delay the onset of laminar–turbulent transition. By monitoring the root-mean-square of the streamwise velocity fluctuations (U_{rms}), they visualised suppression of transition in a TS-wave-dominated flow. The most effective streaks, which closely resembled those predicted by linear optimal perturbation theory, delayed transition across the full 2100 mm test section—far downstream

of the conventional transition range (1000–1600 mm).

Bagheri et al. [60] investigated the optimal spanwise spacing of streaks for stabilising TS waves. They found that streaks peaking near the first neutral point of the TS wave most effectively distorted the mean flow in the unstable region, thereby enhancing stabilisation, shown in Fig. 2.17. To generate higher-amplitude streaks, Fransson and Talamelli [61] employed miniature vortex generators (MVGs), which outperformed traditional roughness elements in terms of amplitude generation. They observed that streak amplitude scaled with the MVG height Reynolds number (Re_h), up to a critical value of approximately $Re_h \approx 547$. Beyond this threshold, secondary instabilities appeared. Additionally, they showed that a second MVG array could regenerate decaying streaks, although its effectiveness depended critically on its streamwise placement relative to the pre-existing streak structures. Notably, despite the initial increase in the induced-drag component associated with the MVG-generated vortices, this component could fall below the corresponding base-flow value farther downstream, particularly for moderate streak amplitudes (25 %). The emergence of secondary instabilities at large streak amplitudes is consistent with the breakdown mechanisms of coherent shear-flow structures described in related low-speed configurations. Marxen, Lang, and Rist [66] investigated vortex formation and subsequent breakdown in laminar shear flows, demonstrating that large-scale, nominally two-dimensional vortical structures undergo rapid three-dimensionalisation through secondary instability mechanisms, including elliptic and hyperbolic instabilities. Their combined numerical and experimental analysis showed that once a critical amplitude is exceeded, these secondary instabilities lead to spanwise deformation, vortex breakup, and rapid transition to turbulence. Although their study focused on laminar separation bubbles rather than controlled streaks, the underlying physics of secondary instability and coherent-structure breakdown provide a relevant framework for interpreting the onset of streak instabilities observed at high amplitudes in streak-based transition control strategies.

Shahinfar et al. [67] extended these findings by demonstrating that MVGs could delay transition even when upstream disturbances were present. This setup permitted full interaction between free-stream disturbances and the MVG array, thereby validating the robustness of the streak-based control mechanism. In a subsequent study, Shahinfar et al. [68] examined the efficacy of MVGs in attenuating more complex modal disturbances, including both single and paired oblique waves. Their quantitative analysis of disturbance energy, intermittency, and spectral content revealed significant transition delay, confirming the broader applicability of MVGs as a passive flow control strategy in boundary-layer

transition management.

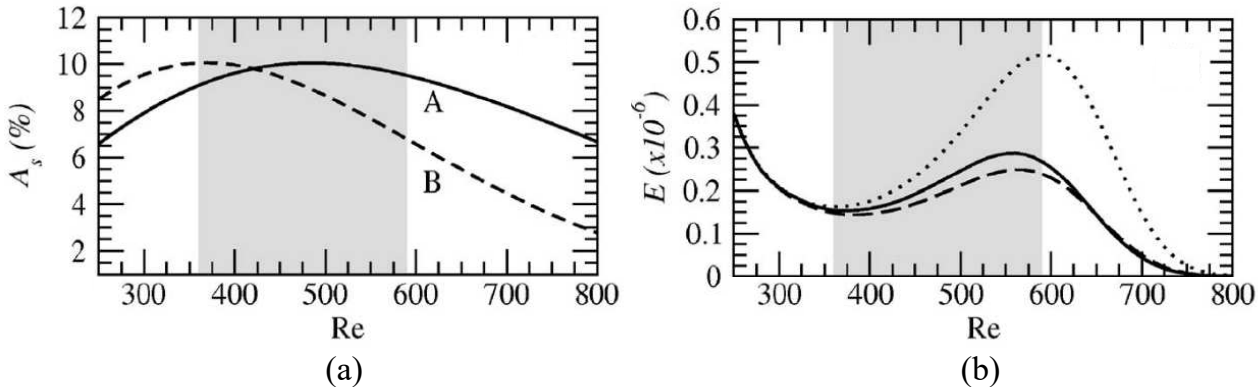


Figure 2.17: Optimal spanwise streak spacing for transition delay based on global stability analysis. (a) Streamwise evolution of streak amplitude $A_{st} = 10\,\%$ for two different spanwise wavenumbers, $\beta = 0.45$ (solid) and 0.65 (dashed). (b) Temporal TS wave energy growth E for different spanwise wavenumbers with the absence of streaks case (dotted), reproduced from Bagheri et al. [60].

2.4.2 Streaks in Hypersonic Flows

The stabilising effect of stationary streaks in high-speed boundary layers has attracted increasing attention as a passive flow-control strategy for delaying laminar–turbulent transition. This research builds on earlier investigations in low-speed boundary layers, where artificially generated streaks were shown to alter instability dynamics and suppress transition. Ren et al. [62] investigated the influence of streamwise streaks—generated either by optimal perturbations (Klebanoff-type) or centrifugal instabilities (Görtler-type)—on hypersonic boundary layers. Using nonlinear parabolised stability equations (PSE), they demonstrated that carefully tuned streak amplitudes can reshape the base flow to suppress both first mode and second Mack mode instabilities. Klebanoff-type streaks were found to be more controllable and less prone to secondary instabilities, whereas Görtler-type streaks, while initially stabilising, could become unstable due to curvature-induced exponential growth. Complementary work by Paredes et al. [63] examined azimuthally periodic streaks in a Mach 6 flow over a 7° half-angle cone. Their analysis using PSE revealed that such streaks can strongly suppress dominant planar the second Mack modes, preventing them from reaching the critical amplification threshold ($N = 6$) within the cone length, shown in Fig. 2.18. Stronger streaks may also suppress the growth of the second Mack mode, but may simultaneously destabilise the oblique sinuous first mode, creating a tradeoff in their effectiveness. Despite this, an optimal streak amplitude has been identified that

can delay the onset of transition by simultaneously suppressing both the first mode and the second Mack mode. These findings suggest that streaks induced, for example, by roughness elements, offer a promising passive control strategy for hypersonic transition.

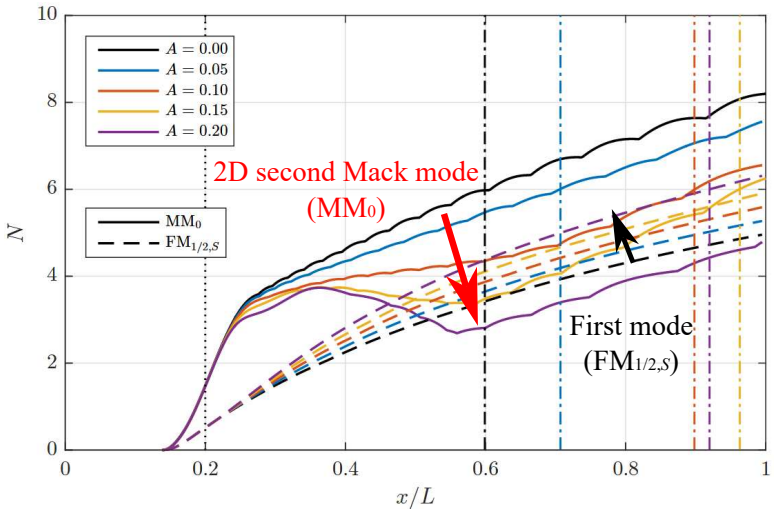


Figure 2.18: N-factor envelopes for nominally 2D second Mack mode disturbances (mode MM0, solid lines; $F \in [350, 800]$ kHz) and sinuous modes originating from first-mode waves with one half the azimuthal wavenumber of the underlying streaks (mode FM1/2,S, dashed lines; $F \in [50, 150]$ kHz). (Reproduced from Paredes et al. [63].)

Roughness Elements

Surface roughness elements have been extensively investigated, revealing both stabilising and destabilising influences depending on their geometry, placement, and the surrounding flow conditions. Unlike in low-speed flows—where vortex shedding and wake dynamics dominate—the transition process in hypersonic boundary layers is governed primarily by interactions among roughness-induced disturbances, acoustic modes, and streamwise streak instabilities. Consequently, roughness elements can either delay or promote transition depending on how they modify the receptivity and amplification of instability modes. Early experimental evidence of transition delay caused by surface roughness was reported by Holloway and Sterrett [69], who investigated a flat plate with spherical roughness elements mounted on interchangeable leading-edge strips in the NASA Langley 20-Inch Mach 6 Tunnel and a Mach 6.2 blowdown tunnel. They observed that for roughness heights smaller than the local boundary-layer thickness, transition could be delayed, particularly at edge Mach numbers M_e above 3.7 (see Fig. 2.19). While their study did not explicitly address modal instability mechanisms, this threshold roughly corresponds to the onset of second Mack mode dominance under typical hypersonic conditions, suggesting that roughness-induced streaks may suppress certain instability growth.

Conversely, larger roughness elements promoted earlier transition shown in Fig. 2.19(b), consistent with the idea that sufficiently strong disturbances can trigger breakdown. An alternative stabilisation

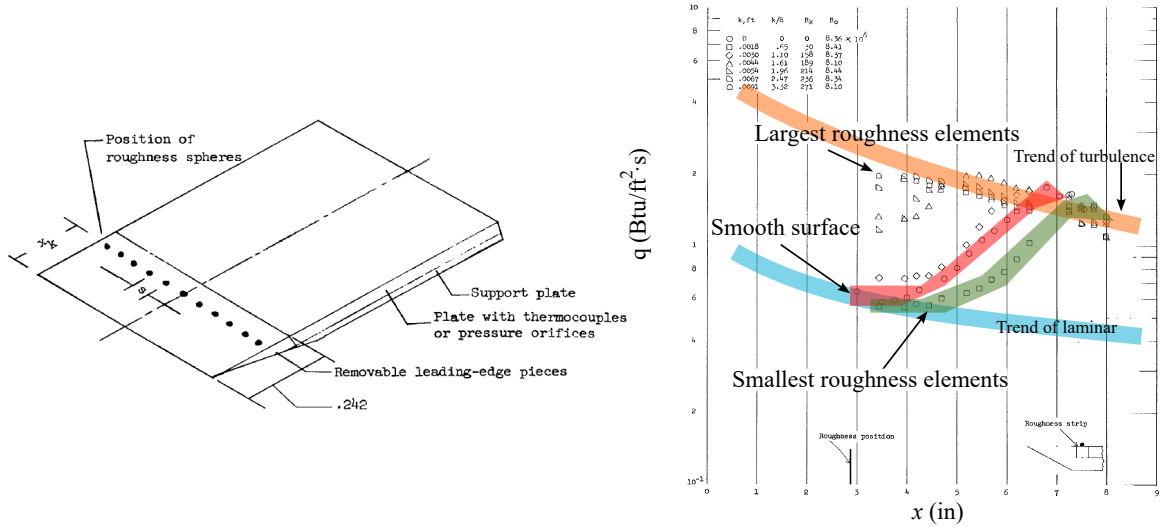


Figure 2.19: (a) Sketch of the flat-plate model assembly with interchangeable leading-edge pieces and spherical roughness elements. (b) Surface heating-rate distributions at Mach 6.0, illustrating delayed transition for sub-critical roughness heights. Smooth-surface and smallest-roughness cases are highlighted. Figure adapted from Holloway and Sterrett [69].

mechanism was proposed by Fujii [70], who investigated two-dimensional roughness configurations, including spaced wires, wavy-wall patterns, and spherical elements on a sharp 10° cone at Mach 7.1, as shown in Fig. 2.20(a). Under high stagnation temperatures (1000 K), the wavy-wall roughness—with a 2 mm wavelength and amplitudes of 0.45 and 0.9 mm—delayed transition when its wavelength coincided with the most unstable second Mack mode frequency, as illustrated in Fig. 2.20(b). Notably, both the wavy-wall and spherical roughness configurations exhibited delayed transition compared to the smooth surface, although the mechanism for the wavy-wall effect is attributed to acoustic-mode interaction rather than streak generation. At lower stagnation temperatures (620 K), however, this stabilising effect disappeared, and all roughness types behaved similarly to conventional tripping elements, again highlighting the sensitivity of roughness-induced stabilisation.

On blunt configurations, roughness often induces localised turbulent wedges. Fiala et al. [71] investigated isolated roughness on a blunt cylinder using surface heat-transfer measurements and observed distinct transition behaviour depending on roughness height. When the element height approached approximately 60 % of the boundary-layer thickness, it acted as an effective trip, generating a fully developed turbulent wedge immediately downstream. Intermediate-height elements produced extended

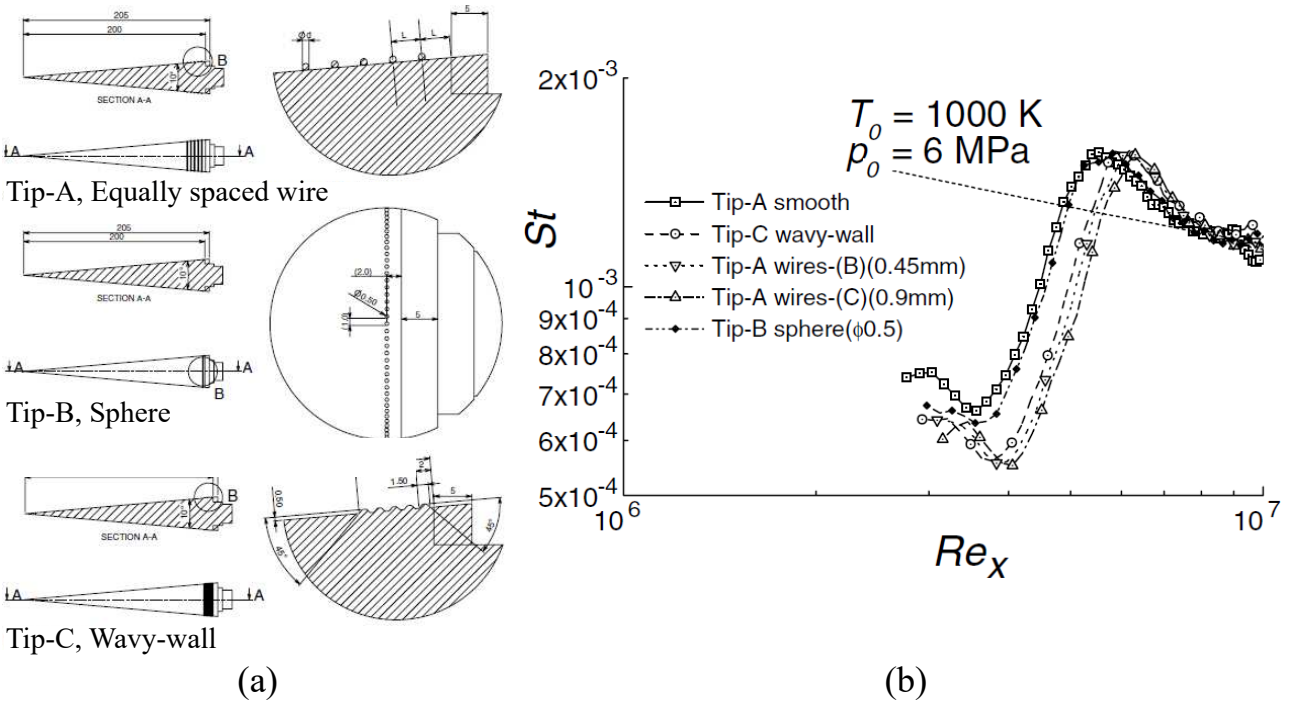


Figure 2.20: (a) Geometry of the spaced wire, spherical, and wavy-wall roughness elements applied to a sharp cone, and (b) Stanton number distributions at Mach 7.1 showing transition delay for wavy-wall and spherical configurations compared to a smooth surface. (Adapted from Fujii [70].)

wakes that transitioned farther downstream, whereas the smallest elements preserved laminar flow. The resulting turbulent wedges exhibited lateral spreading similar to turbulent jets, and intermittency in spot formation appeared near critical roughness heights. Transition onset was further influenced by local pressure gradients and entropy-layer effects, underscoring the complexity of roughness-induced transition on blunt bodies. Beyond roughness height, the orientation and planform geometry of discrete roughness elements have also been shown to exert a strong influence on wake stability and streak development. Groskopf and Kloker [73] performed DNS and biglobal linear stability analyses of three-dimensional roughness elements in a Mach 4.8 flat-plate boundary layer, comparing symmetric and skewed configurations at identical roughness heights. They demonstrated that obliquely oriented roughness elements generate significantly stronger low-speed streaks in their wake than symmetric elements, leading to enhanced amplification of both first and second Mack mode disturbances. For identical roughness heights, the skewed configuration exhibited substantially larger modal growth rates, indicating that roughness orientation can promote transition by intensifying streak–instability interactions rather than by acting as a purely geometric trip. These findings highlight that roughness-induced transition is governed not only by roughness height, but also by the detailed three-dimensional

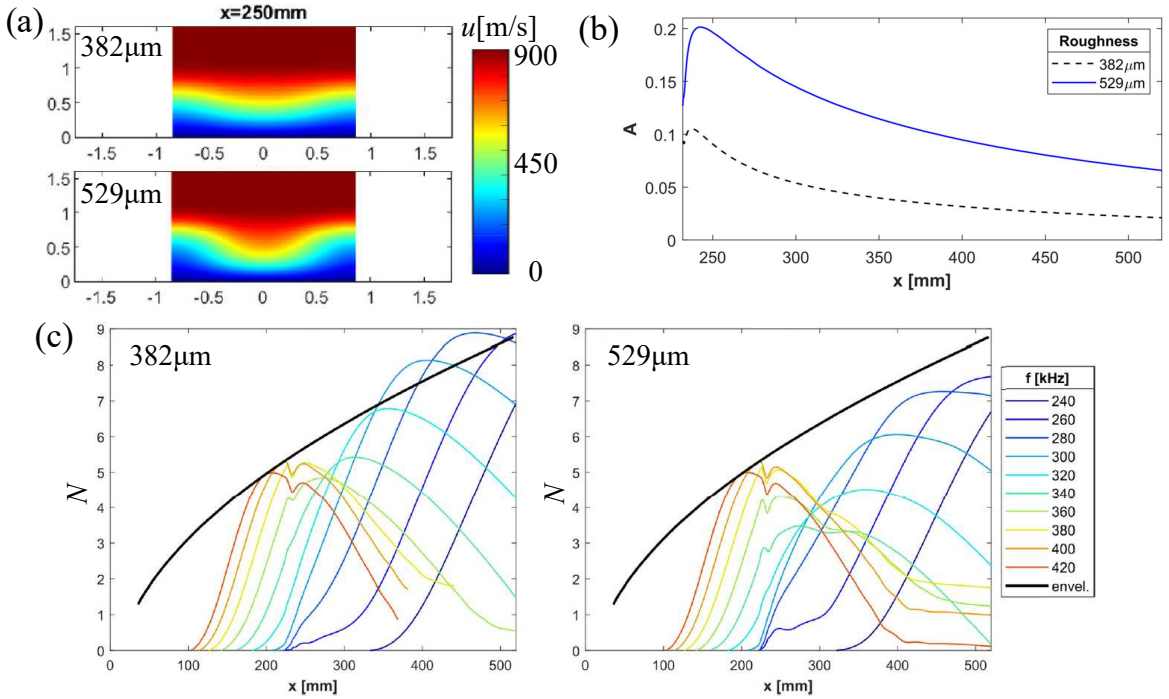


Figure 2.21: (a) Predicted mean streamwise velocity contours at $x = 250\,\text{mm}$ for elliptical roughness elements with heights of $382\,\mu\text{m}$ and $529\,\mu\text{m}$. (b) Streamwise evolution of streak amplitude for the same configurations. (c) Computed second Mack mode N-factors. (Adapted from Leidy et al. [72].)

structure of the induced wake. The influence of inter-element spacing has also been examined in detail by Taylor and Bruce [74, 75], who investigated isolated and paired square-planform roughness elements on a blunt cylinder at Mach 9 using the Imperial College Hypersonic Gun Tunnel. For isolated elements, roughness heights corresponding to $h/\delta_{99} \lesssim 0.2$ generated intermittent trains of turbulent spots, whereas larger elements ($h/\delta_{99} \gtrsim 0.3$) triggered complete boundary-layer transition. When two elements were present, the inter-element spacing, characterised by the ratio s/w, here s is the spanwise edge-to-edge separation between neighbouring roughness elements and w is the planform width of a single element, strongly influenced the downstream flow development. Closely spaced elements ($s/w \leq 1$) produced compound turbulent spots through early wake interaction, while widely spaced configurations ($s/w \geq 4$) increased spot frequency and spatial intermittency. Complementary flow visualisation and numerical studies demonstrated that these trends arise from spacing-dependent modifications to the symmetry, strength, and lateral position of the counter-rotating vortex pairs, thereby modulating the amplitude of roughness-induced velocity streaks within the boundary layer. Measurement of turbulent-spot convection velocities—approximately $0.8U_e$ near the leading edge and $0.4U_e$ near the trailing edge—further demonstrated the strongly evolving, non-frozen nature of these structures.

Leidy et al. [72] examined elliptical, triangular, and trapezoidal ramp-shaped roughness elements on a 7° half-angle cone at Mach 6 and Reynolds numbers of $Re_x = 9.8$–13.1×10^6/m. For the elliptical configuration, moderate-height elements (382 μm, producing 10 % streak amplitude) suppressed second Mack mode instability growth, whereas taller elements (529 μm, producing 20 % streak amplitude) induced premature breakdown, shifting transition upstream, as illustrated in Fig. 2.21(a-c). The taller elements promoted streak instabilities and enhanced first-mode interactions, demonstrating that roughness height—and thus the resulting streak amplitude—can switch the dominant transition pathway from the second Mack mode suppression to streak breakdown. These studies indicate that roughness elements influence transition primarily through the generation and subsequent evolution of velocity streaks, with the transition outcome determined by the induced streak amplitude, wavelength, and stability characteristics rather than by roughness geometry alone. This motivates actuation approaches that can prescribe the streak field (amplitude and wavelength) without geometric protrusions and with reduced sensitivity to off-design conditions. One such approach is to generate streaks thermally using spanwise non-uniform wall temperature distributions.

Non-Uniform Surface Temperature Distributions

Velocity streaks have been shown to suppress the growth of the second Mack mode, and an optimal streak amplitude has been identified that can delay the onset of transition by simultaneously attenuating both first-mode and second Mack mode instabilities. This behaviour highlights the potential of velocity streaks as a passive flow-control strategy in hypersonic boundary layers [62, 63]. Roughness elements have therefore been widely studied as an indirect means of streak generation; however, this approach requires careful tuning for each flow condition and may lead to earlier transition under off-design scenarios [69, 75].

To address this limitation, Ozawa et al. [76] proposed an alternative control mechanism based on spanwise surface temperature variations. DNS were performed at Mach 6 with imposed non-uniform wall temperature distributions. The resulting thermal gradients generated streaks with amplitudes up to 9 %, as shown in Fig. 2.22. Low-momentum fluid near the wall was lifted in high-temperature regions (Θ_H), forming streak-like structures in the near-wall region due to the redistribution of momentum driven by local density variations (see Fig. 2.22(a)). In effect, the spanwise gradients introduce steady secondary motions that reorganise near-wall momentum, producing persistent low-/high-speed streaks that modify modal growth. Figure 2.22(b) shows the streak amplitude for different spanwise wave-

lengths $\lambda_z^* = 0.6$, 0.9, and 1.2, normalised by a reference length $L_{ref} = 9.1\,\text{mm}$. Larger λ_z^* values maintained higher streak amplitudes downstream, suggesting that viscous dissipation becomes dominant when hot and cold strips are closely spaced, whereas wider spacing allows thermal effects to dominate and sustain stronger streaks. To assess the impact on transition, three DNS cases were

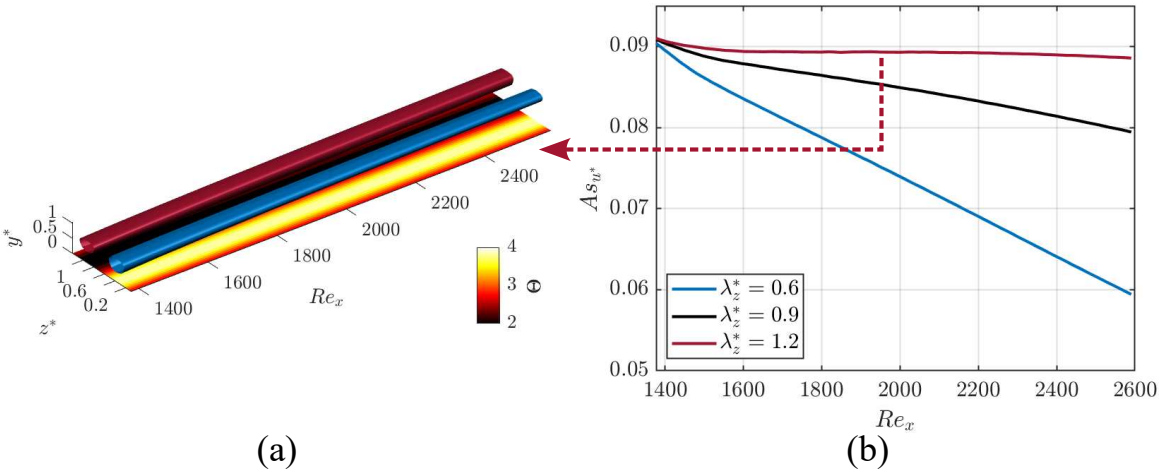


Figure 2.22: (a) Isosurface of streaks generated by spanwise varying wall temperature Θ at $\lambda_z^* = 1.2$, where y^* and z^* are normalised by L_{ref}. (b) Streak amplitude for different spanwise wavelengths λ_z^* of non-uniform temperature distributions. Reproduced from Ozawa et al. [77].

considered (Table 2.1): Case 1 and Case 2 used uniform wall temperatures ($\Theta = 2$ and $\Theta = 4$, respectively), while Case 3 employed a spanwise-varying temperature distribution between $\Theta_L = 2$ and $\Theta_H = 4$ with $\lambda_z^* = 1.2$. Figure 2.23 shows the pressure perturbation fields for all cases. Cases

Table 2.1: DNS cases for assessing the transition effect of spanwise-varying wall temperature. Source: Ozawa et al. [77].

Case name	Description	Θ_L	Θ_H	λ_z^*
Case 1	Constant wall temperature ($\Theta(z^*) = \text{const.}$)	2	2	∞
Case 2	Constant wall temperature ($\Theta(z^*) = \text{const.}$)	4	4	∞
Case 3	Variations of wall temperature ($\Theta(z^*) = f(z^*)$)	2	4	1.2

1 and 2 exhibit the classical amplification of the second Mack mode, with Case 1 showing stronger albeit later growth due to the destabilising effect of a lower wall temperature [14]. In contrast, Case 3 shows significantly reduced pressure fluctuation amplitudes on both hot and cold sides, indicating effective suppression of instability. The suppression occurs even though the local wall temperature alternates between stabilising and destabilising regions, implying that the thermally induced streaks themselves play the dominant stabilising role. Figure 2.24 presents the corresponding N-factor evolution. Case 1 reaches a peak $N_E \approx 5$ near $Re_x = 2800$, while Case 2 peaks earlier at $Re_x \approx 2500$ with $N_E < 4$. Case 3 shows a substantially reduced and delayed amplification, both in spatially averaged

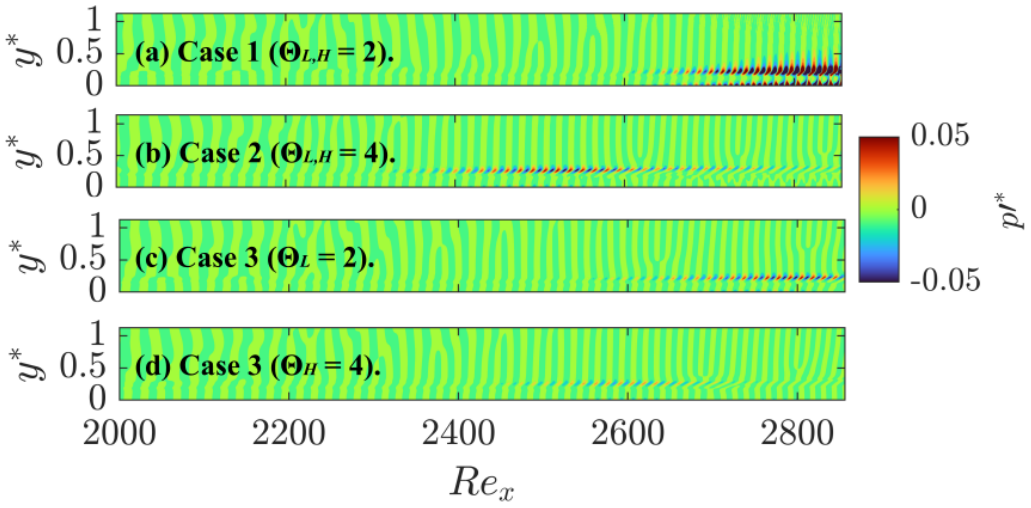


Figure 2.23: Instantaneous pressure perturbation field for Case 1, Case 2, Case 3 (cold side) and Case 3 (hot side) on the $x^* - y^*$ plane. Reproduced from Ozawa et al. [77].

and hot/cold-separated evaluations. On the hot side, amplification begins later than in Case 2, with two moderate peaks. On the cold side, amplification starts earlier than in Case 1 but grows more slowly and remains below the Case 1 peak. These results demonstrated that spanwise temperature variations can effectively suppress second Mack mode instabilities and delay transition by inducing steady streaks that modify the mean flow structure and reduce local receptivity.

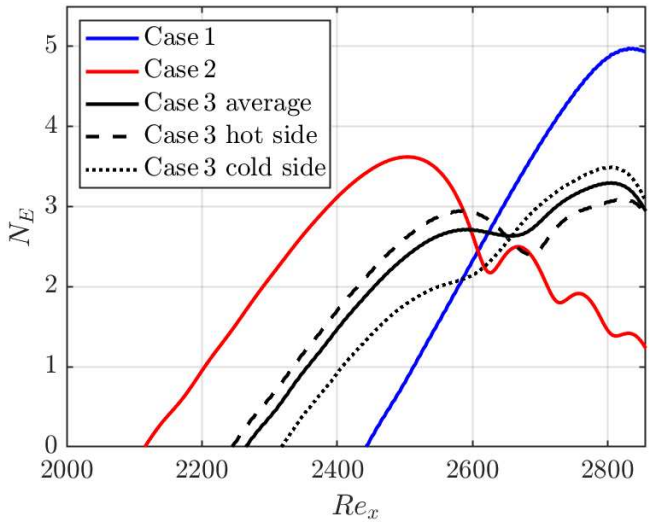


Figure 2.24: N-factors of the Case 1 (uniform cold wall), the Case 2 (uniform hot wall), and the Case 3 (spanwise-varying wall temperature). For the Case 3, also the N-factor is separately evaluated only in the hot ("hot side") and cold wall ("cold side") regions, respectively. Reproduced from Ozawa et al. [77].

Building on the results of Ozawa et al. [76], Boscagli et al. [78] performed DNS combined with Linear

Stability Theory (LST) analyses to further investigate the stabilising mechanisms associated with spanwise non-uniform wall temperature distributions. The study was conducted for a Mach 6 flat-plate boundary layer with sinusoidal temperature variations imposed in the spanwise direction. They examined the effect of the spanwise wavelength of the control streaks, varying λ_z from 0.9 to 4.8, and demonstrated that stabilisation up to 60 % relative to the uncontrolled configuration was achieved at $\lambda_z = 2.4$, as shown in Fig. 2.25(a). The stabilising effect remained beneficial even at larger λ_z values. Figure 2.25(b) shows the instantaneous distribution of the skin-friction coefficient c_f for both uncontrolled and controlled configurations at $\lambda_z = 1.6$, resolving four spanwise periodic conditions. Around $x \approx 700$, the control method significantly reduces the peak value of c_f associated with the high-frequency fluctuations of the second Mack mode. Further downstream, for the controlled configuration, the large-amplitude streaks generated through non-linear interactions and constructive interference with the control streaks remain coherent over a longer streamwise distance.

Taken together, these studies demonstrate, through high-fidelity DNS and stability analyses, the potential of spanwise non-uniform wall temperature distributions to induce steady velocity streaks and suppress second Mack mode instabilities in hypersonic boundary layers. However, all results reported to date are based on idealised numerical simulations in which the wall temperature distribution is prescribed a priori and maintained without practical constraints. Before the present work, the feasibility, robustness, and effectiveness of thermally driven streak control under realistic experimental conditions remained largely unexplored. In particular, the development of a practical actuation strategy for generating controlled spanwise temperature variations, and the experimental verification of their influence on hypersonic boundary-layer transition, remained outstanding. These limitations motivated the implementation-focused experimental studies presented in this thesis. Accordingly, the central contribution of this thesis was the development of a physically realisable passive thermal actuation strategy and the wind-tunnel validation of repeatable spanwise wall-temperature patterning and its influence on hypersonic instability development and transition behaviour.

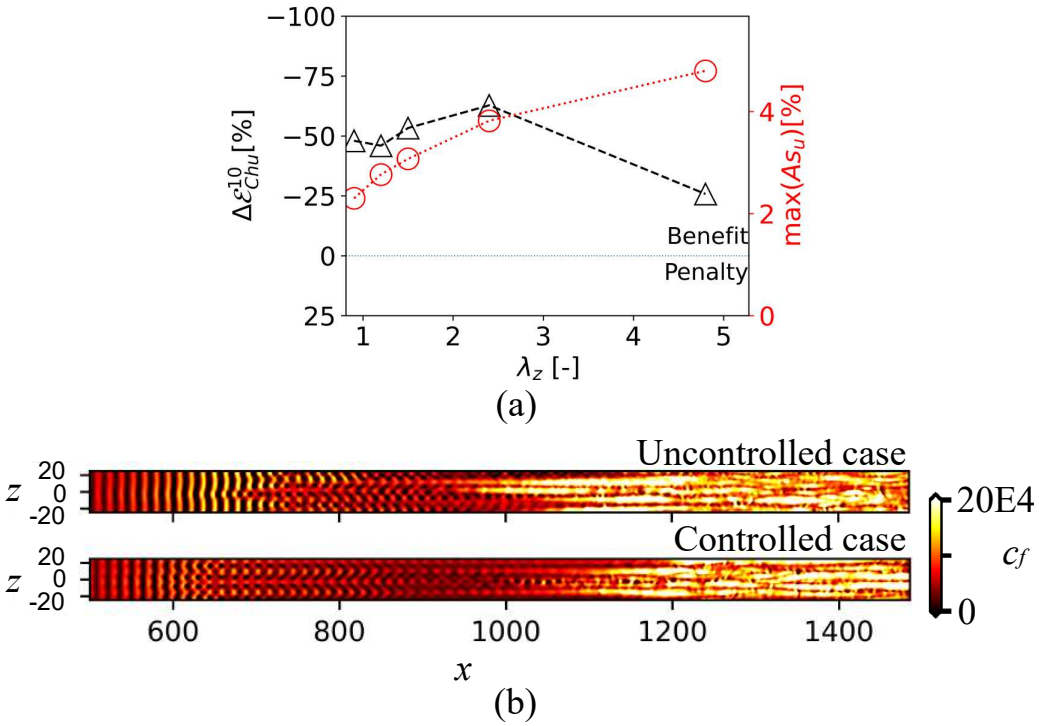


Figure 2.25: (a) Influence of streak wavelength on second Mack mode stabilisation $\Delta\varepsilon^{10}_{chu}$ and maximum streak amplitude As_u, and (b) instantaneous skin-friction coefficient c_f for uncontrolled and controlled configurations. Adapted from Boscagli et al. [78].

Chapter 3

Actuation Methods for Non-Uniform Surface Temperature Distributions

3.1 Overview

This chapter established the thermal actuation concepts and modelling framework used throughout the thesis to generate controlled spanwise non-uniform wall-temperature distributions. A three-dimensional heat-transfer model was introduced to quantify how material properties, wall geometry, and thermal boundary conditions govern the magnitude and persistence of surface-temperature non-uniformity under hypersonic convection.

The chapter first considered steady operating conditions relevant to sustained hypersonic environments, using parametric studies to identify key design trends and practical limitations. It then addressed transient, wind-tunnel-relevant operation, where non-uniform temperature fields must be generated within short test times. Several passive concepts were assessed to determine their achievable spanwise temperature contrast and temporal evolution. The resulting design insights provide the basis for selecting the experimental configurations implemented in the subsequent chapters.

3.2 Control Methodology and Performance Under Flight Conditions

This section evaluated the control methodology required to achieve spanwise non-uniform surface temperature distributions by examining the heat transfer between a high-speed boundary layer and a solid surface. The influence of wall thickness and wall material was explored in controlling the local surface temperature. Control effectiveness was characterised using different materials such as aluminium, titanium, and MACOR.

3.2.1 Principles of Three-Dimensional Steady-State Condition

To achieve the desired steady-state temperature distributions under hypersonic cruising conditions, an actuation method is essential, such as an internal cooling system, to regulate the surface temperature distributions and mitigate aerodynamic heating from the boundary layer. As the temperature of the boundary layer increases due to viscous effects, heat transfer to the vehicle's surface occurs based on the temperature gradient. Consequently, the cooling system plays a critical role by continuously absorbing the heat. This absorption maintains equilibrium with the incoming heat, thereby ensuring the desired temperature distributions are steadily achieved.

The basic design of a cooling system is explored through the three-dimensional steady state heat transfer equation, defined as:

$$\frac{\partial^2 T}{\partial x^2} + \frac{\partial^2 T}{\partial y^2} + \frac{\partial^2 T}{\partial z^2} = 0, \tag{3.1}$$

where T and x, y, and z represent temperature and the three-dimensional axes, respectively. Figure 3.1 illustrates the wall temperature gradient, accounting for convection from the boundary layer and a cooling system input. The heat flux on the vehicle surface varies locally due to boundary layer conditions, with aerodynamic heating being more intense upstream as a result of a higher convection coefficient. This spatially varying aerodynamic heating induces three-dimensional heat diffusion within the wall. Thus, designing the desired surface temperature distribution requires a 3D model that incorporates these effects.

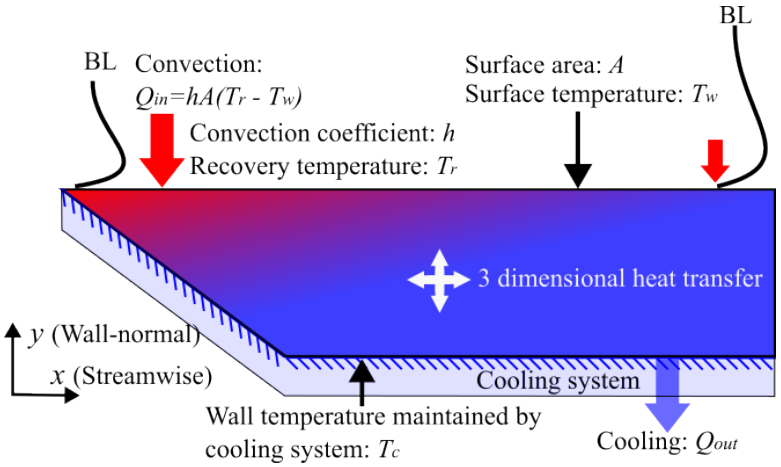


Figure 3.1: Schematic of the steady state wall condition under aerodynamic heating by hypersonic cruising with a cooling system.

3.2.2 Thermal Modelling for Three-Dimensional Steady-State Condition

This subsection studied the control actuation methodology used to generate non-uniform surface temperature distributions in a three-dimensional wall at steady state. A thermal model was developed to approximate the surface temperature distributions. The performance of the resulting surface temperature distributions was evaluated for various cooling temperatures, wall thicknesses, and materials.

Heat Transfer Coefficient

An accurate estimation of the convective heat transfer between the boundary layer and the test surface is a pivotal step in the thermal design process. Therefore, a three-dimensional steady-state heat-transfer equation is solved for the solid model. On the aerodynamic test surface, the convective heat-transfer coefficient h, the recovery temperature T_r, and the wall surface temperature T_w are specified as boundary conditions [76, 79–82]. The recovery temperature is estimated as

$$T_r = T_e \left(1 + r\frac{\gamma - 1}{2} M_e^2\right), \tag{3.2}$$

where T_e and M_e are the boundary-layer edge temperature and Mach number, respectively, γ is the ratio of specific heats, and r is the recovery factor. Since the edge-flow conditions are assumed to be uniform over the model surface, T_r is treated as constant in both the streamwise and spanwise directions. The local convective heat-transfer coefficient h is estimated from the local Stanton number

St_x, which depends on the local Reynolds number Re_x and the Prandtl number Pr. The Stanton number is defined as

$$St_x = \frac{h}{\rho_{ref} U_\infty c_p}, \tag{3.3}$$

where ρ_{ref}, U_∞, and c_p are the reference density, freestream velocity, and specific heat at constant pressure, respectively. Equivalently, using the local Nusselt number $Nu_x = hx/\alpha$, where α is the thermal conductivity of the fluid, the Stanton number can be written as

$$St_x = \frac{Nu_x}{Re_x Pr}, \tag{3.4}$$

$$Re_x = xRe = \frac{\rho_{ref} U_\infty x}{\mu_{ref}}, \tag{3.5}$$

where Re is the unit Reynolds number and x is the streamwise distance from the leading edge. For a laminar boundary layer on a flat plate, the local Nusselt number is approximated by the classical laminar heat-transfer correlation [83],

$$Nu_x = 0.332 Re_x^{1/2} Pr^{1/3}. \tag{3.6}$$

Substituting this expression into Eq. 3.4 gives

$$St_x = \frac{0.332}{\sqrt{Re_x}} Pr^{-2/3}. \tag{3.7}$$

The use of this expression is an engineering approximation for estimating the convective thermal boundary condition in the solid heat-transfer model. Although the coefficient (0.332) and the $Re_x^{-1/2}$ dependence originate from incompressible laminar flat-plate boundary-layer theory, the expression is used here only to provide an approximate local heat-transfer coefficient. It is not intended to represent a full compressible hypersonic boundary-layer similarity solution. However, the maximum error associated with using the incompressible expression has been reported to be approximately 2% for Mach numbers up to 16 [84]. This error is sufficiently small for the purpose of the present thermal model, whose objective is to estimate the imposed surface-temperature distribution rather than to

predict hypersonic boundary-layer heat transfer with high fidelity.

The present formulation assumes a locally flat-plate laminar boundary layer with negligible pressure-gradient effects. For configurations involving significant pressure gradients, such as a cone with a non-linear radial profile or a surface affected by shock/wave impingement, the same convective boundary-condition framework could still be used, but the estimation of h would need to be modified. In such cases, St_x, Re_x, T_r, and the relevant edge-flow quantities should be evaluated locally along the surface, and the flat-plate Stanton-number correlation should be replaced by a geometry- or pressure-gradient-dependent heat-transfer model. A higher-fidelity approach would be to obtain h from a compressible boundary-layer calculation or a CFD solution that accounts for pressure-gradient, curvature, axisymmetric, and shock-interaction effects. These extensions are beyond the scope of the present thesis, since the thermal model is used to estimate the imposed surface-temperature distribution for the flat-plate actuation cases considered here.

Here, the unit Reynolds number Re was calculated as $6.49 \times 10^5\,\mathrm{m}^{-1}$ at Mach 6, consistent with the DNS conditions of Ozawa et al. [76] listed in Table 3.1, with $Pr = 0.71$. Ozawa et al. [76] selected these freestream conditions to represent free flight in the International Standard Atmosphere at 20 km altitude. ρ_{ref} and μ_{ref} are the reference density and the reference viscosity, respectively, utilising the reference temperature based on the Meador-Smart method. The local convection coefficient can then be estimated using the expression

$$h = St_x \rho_{ref} U_\infty C_p \tag{3.8}$$

where U_∞ represents the freestream velocity and C_p =1010 J/(kgK) denotes the specific heat at constant pressure. Additionally, viscosity is determined using Sutherland's law considering the reference temperature. Density and viscosity are evaluated based on reference temperatures to account for conditions near the wall.

Table 3.1: DNS freestream parameters from Ozawa et al. [76], corresponding to Mach 6 free flight in the International Standard Atmosphere at 20 km.

T_∞ (K)	p_∞ (Pa)	Ma	Pr	$Re_{L_{ref}}$	L_{ref} (mm)	γ	Θ_L	Θ_H
216.7	5475.0	6.0	0.71	1.0×10^5	9.1	1.4	2	4

Thermal Model and Geometry

A parabolic differential equation solver available in MATLAB's Partial Differential Equation Toolbox is employed to calculate heat transfer. Based on the DNS parameters in Tab. 3.1, the spanwise wavelength is defined as $\lambda_z = 1.2$, corresponding to a physical length of $z = 10.9\,\text{mm}$. As a result, the hot and cold strips each have a width of 5.45 mm. The fundamental geometry is defined by a surface with length of 250 mm and a sharp 12 ° leading edge. The thermal modelling parameters are the wall thickness and the cooling temperature imposed on the wall.

A sketch of the geometry is depicted in Fig.3.2. The geometry consists of cooling inputs to implement hot and cold strips, respectively. The hot strip is sandwiched between the half-width cold strips to simulate periodic conditions. On the aerodynamic test surface, a convectional heat flux is imposed, based on Eq. 3.8, considering T_r of 1531 K, consistent with the DNS conditions [76] listed in Tab. 3.1. Each backside surface maintains a uniform cooling temperature, defined by Θ normalised by T_∞. Behind the cold strips, a stronger cooling wall, denoted as Θ_{BSL}, is set. A weaker cooling wall, denoted as Θ_{BSH}, is defined behind the hot strip. The DNS defines a spanwise pair of strips to generate the cold and hot wall. Θ_{BSL} and Θ_{BSH} were selected as combinations of $\Theta_{BSL,BSH} = [2, 4]$ and $[1, 5]$. Other surfaces are defined as adiabatic walls. Aluminium was chosen as the wall material and the wall thickness t_{model} was varied between 2.5 and 10 mm, outlined in Tab. 3.2. The 3D geometry model utilised an unstructured mesh, and a mesh resolution study was conducted, ultimately settling on a resolution of 0.85 mm.

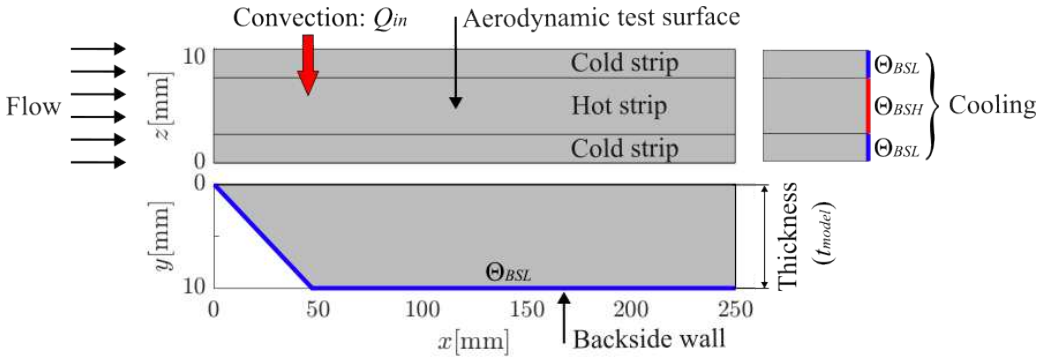


Figure 3.2: Schematic of the thermal modelling domain, including the cold and hot strips. The domain shows the convection Q_{in} at the aerodynamic test surface and the stronger (Θ_{BSL}) and the weaker (Θ_{BSH}) cooling at each strip.

Table 3.2: Aluminium wall test cases with varying wall thickness and stronger Θ_{BSL} and weaker Θ_{BSH} cooling temperatures inputs behind the wall.

Name (Material - t_{model} - Θ_{BSL} - Θ_{BSH})	t_{model} (mm)	Θ_{BSL}	Θ_{BSH}
AL-2.5-2-4	2.5	2	4
AL-5-2-4	5	2	4
AL-10-2-4	10	2	4
AL-2.5-1-5	2.5	1	5
AL-5-1-5	5	1	5
AL-10-1-5	10	1	5

3.2.3 Spanwise Surface Temperature Distributions

Performance with Uniform Wall Thicknesses and Differential Cooling Under an Aluminium Wall

The steady-state non-dimensional surface temperature profiles with $\Theta_{BSL} = 2$ and $\Theta_{BSH} = 4$ are shown in Figs. 3.3a-c. Spanwise temperature differences were observed in all cases. Overall, the leading edge showed both the highest temperature on the central hot region and the lowest temperature on the outer cold region due to the cooling extending to the leading edge. Downstream of the leading edge, each strip sustained a temperature level that depended on t_{model}, as shown in Fig. 3.4a. Specifically, for AL-2.5-2-4 (Fig. 3.3a), pronounced temperature differences appeared between the hot and cold surface regions. Fig. 3.4b shows the temperature distribution in the spanwise direction at $x = 150$ mm. The temperature variations showed a peak at the centre of each strip and a continuous distribution between neighbouring peaks. In contrast, AL-10-2-4 exhibited an almost uniform surface-temperature distribution, as shown in Figs. 3.3c, 3.4a and 3.4b. AL-5-2-4 showed slight temperature variations (Fig. 3.3b).

Figs. 3.3d-f show cases with a higher imposed temperature gradient ($\Theta_{BSL} = 1$ and $\Theta_{BSH} = 5$). Comparison of Figs. 3.3d-f with 3.3a-c showed that the temperature distributions remained similar. However, the hot and cold surfaces attained higher and lower temperatures, respectively, shown in Figs. 3.3d and 3.3e. AL-10-1-5, with the thickest wall of 10 mm, exhibited a less noticeable temperature variation similar to that of AL-10-2-4 (Fig. 3.3c) due to the dominant effect of thermal diffusion in the wall.

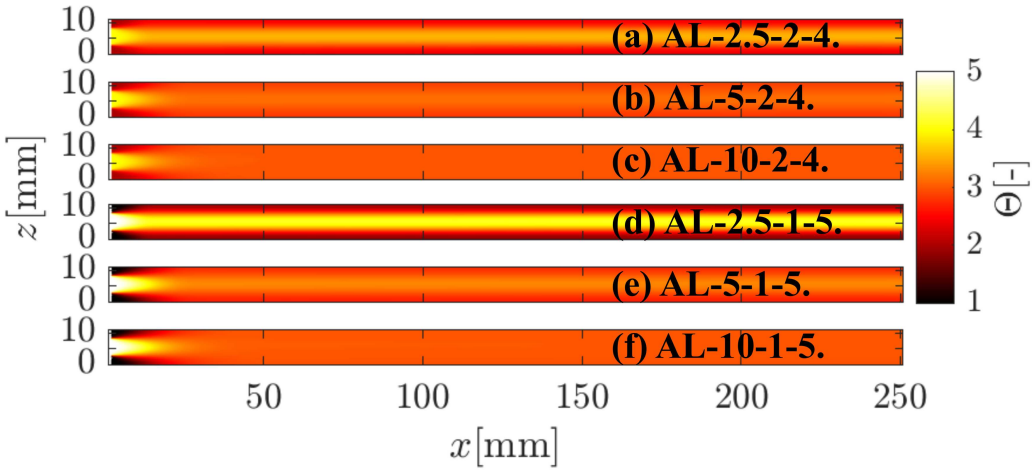
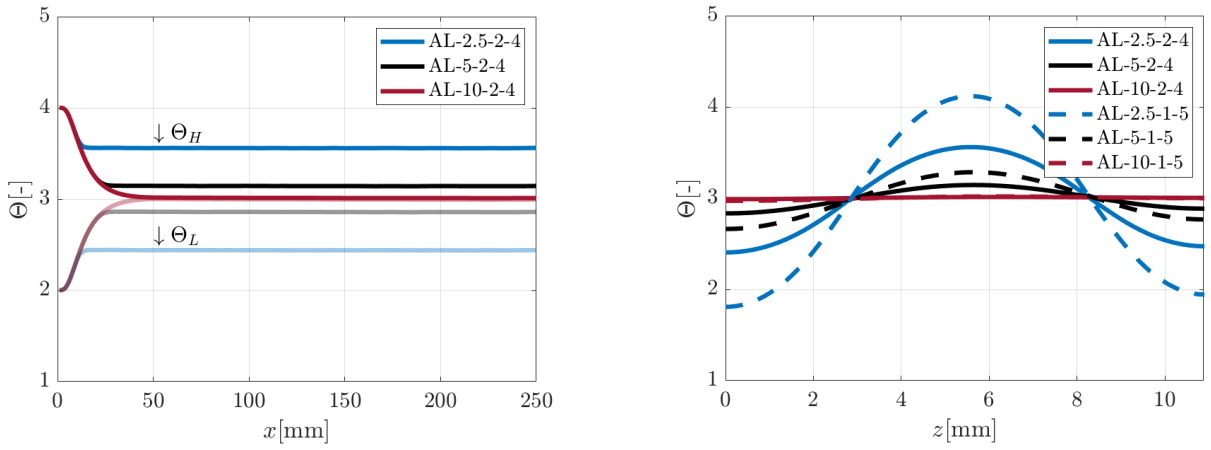


Figure 3.3: Surface normalised temperature at the steady state-under aluminium wall with $\Theta_{BSL} = 2$ and $\Theta_{BSH} = 4$ (a to c) and $\Theta_{BSL} = 1$ and $\Theta_{BSH} = 5$ (d to f).



(a) Streamwise normalised temperature (Solid and light lines are at the strips' centreline on the hot Θ_H and cold Θ_L regions, respectively).

(b) Spanwise normalised temperature with $\Theta_{BSL} = 1$ and $\Theta_{BSH} = 5$ (dash line) at $x = 150$ mm.

Figure 3.4: Streamwise and spanwise normalised temperature in different aluminium wall thickness cases.

Table 3.3: Different wall material cases for sensitivity study.

Name (Material - t_{model} - Θ_{BSL} - Θ_{BSH})	Material	t_{model} (mm)	Θ_{BSL}	Θ_{BSH}
T-5-2-4	Titanium	5	2	4
T-10-2-4	Titanium	10	2	4
M-5-2-4	MACOR	5	2	4
M-10-2-4	MACOR	10	2	4

Temperature Distribution Dependence on Material

This subsection examined the sensitivity of the surface-temperature distributions to different materials. Titanium and MACOR were selected to assess the effect of material thermal response, with titanium having 20 times lower thermal conductivity than aluminium, and MACOR 10 times lower than titanium. Table 3.3 outlines four test cases, maintaining consistent geometry and mesh conditions from previous cases. Thicknesses of 5 and 10 mm were chosen, with temperature inputs of $\Theta_{BSL} = 2$ and $\Theta_{BSH} = 4$.

Fig. 3.5 shows the surface-temperature distributions for all cases. T-5-2-4 and T-10-2-4 exhibited slight temperature differences similar to AL-5-2-4 and T-10-2-4. M-5-2-4 showed a larger temperature difference than the titanium cases. Conversely, M-10-2-4 exhibited high surface temperatures with a smaller temperature difference. These results demonstrated that the surface temperature varied less over the strips when materials with lower thermal conductivities were used.

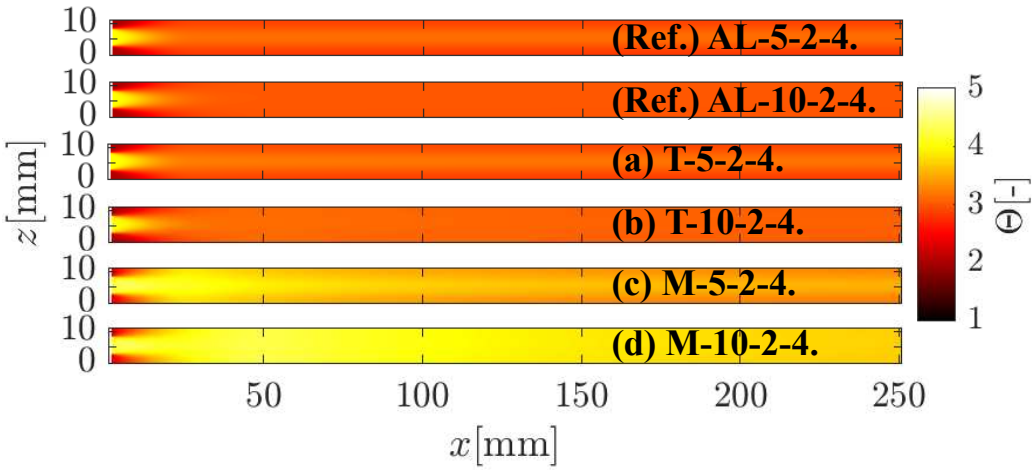


Figure 3.5: Surface normalised temperature for the reference cases AL-5-2-4 and AL-10-2-4, and for T-5-2-4, T-10-2-4, M-5-2-4, and M-10-2-4, with $\Theta_{BSL} = 2$ and $\Theta_{BSH} = 4$.

3.2.4 Discussion

Fig. 3.6 shows the surface temperature on the hot and cold strips' centres at 150 mm along aluminium, titanium, and MACOR with 2.5, 5 and 10 mm wall thickness. All materials showed similar behaviour. With $t_{model} = 2.5$ mm, high and low temperatures were observed, while the $t_{model} = 10$ mm cases showed minimal temperature differences. One exception is for $t_{model} = 10$ mm, where thick MACOR achieves higher temperatures than thin MACOR since low thermal diffusion decreases the cooling effect and increases the surface temperature. Overall, metals more readily sustained temperature differences caused by cooling input due to their high conductivity. Moreover, the combination of wall thickness, cooling temperature, and material choice was found to be key to generating complex temperature distributions.

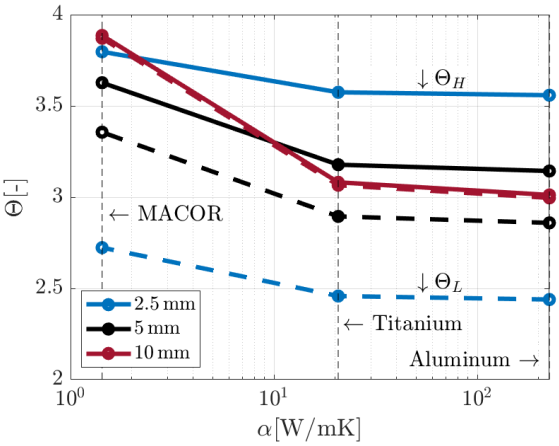


Figure 3.6: Variation of temperature difference with $\Theta_{BSL} = 2$ and $\Theta_{BSH} = 4$ on each strip at $x = 150$ mm with varying materials (MACOR, titanium, and aluminium) and wall thickness of 2.5, 5 and 10 mm. Solid lines represent the hot, and dash lines represent the cold strips.

3.3 Passive Control Approach for Ground Test Implementation

In this section, a strategy to generate spanwise non-uniform surface temperature distributions in short-duration wind-tunnel tests was explored. The passive control method was introduced, along with control parameters used to achieve surface-temperature variations. Three conceptual designs were considered, and their performance was evaluated using thermal modelling. The performance of the insulator was characterised by its material properties and thickness.

3.3.1 Principles of Passive Transient Temperature Control in Short Wind Tunnel Operation

Practical testing in wind tunnels is crucial for validating the flow control methodology using spanwise non-uniform surface temperature distributions. However, achieving a steady state presents a significant challenge within the constraints of short-duration experiments or insufficient incoming enthalpy for wind tunnel conditions. Rather, it is necessary to assess performance based on instantaneous states of the time-dependent surface temperature evolution during a wind tunnel test. The transient wall temperature can be described using Fourier's law of heat transfer:

$$\begin{aligned} \frac{\partial T}{\partial t} &= \frac{\alpha}{\rho c_p} \nabla^2 T \\ &= \kappa \left(\frac{\partial^2 T}{\partial x^2} + \frac{\partial^2 T}{\partial y^2} + \frac{\partial^2 T}{\partial z^2} \right), \end{aligned} \tag{3.9}$$

where T, t, α, ρ, c_p, κ, x, y, and z represent temperature, time, thermal conductivity, density, specific heat, thermal diffusivity, and spatial directions, respectively. To reach steady-state conditions, steady-state temperature distributions dominated by material properties must converge. Since the system's response speed is also governed by material properties, reaching the desired surface temperature distribution through active control takes time, making the process challenging in short-duration wind tunnel tests. Conversely, passive control methods can simplify the system by using heat flux from the flow to passively increase the local wall temperature. While the surface temperature may not reach steady-state conditions, the instantaneous flow field can still be evaluated under transient wall surface temperature conditions. Therefore, a passive control method was chosen to demonstrate spanwise non-uniform temperature distributions.

High-enthalpy tunnels can reach high heat fluxes. This high heat flux allows control of the local heating process and achieves hot and cold strips as long as the initial wall temperature is lower than the recovery temperature. While heat transfer occurs during a wind tunnel run, alternating material properties κ and spatial temperature distribution $\nabla^2 T$ act as key parameters to passively achieve different temperatures on the hot and cold strips simultaneously, as explained in Eq. 3.9. For alternating material properties, the local material of the wall can be modified to change local temperature sensitivity. Conversely, altering the spatial temperature distributions, achieved by changing the local

inner wall structure to control heat flux diffusing through the wall, can generate different local temperatures, as demonstrated in Sec 3.2.3. In the subsequent section, conceptual flat-plate models were initially designed based on the alternating-material approach and spatial temperature distributions.

3.3.2 Conceptual Design

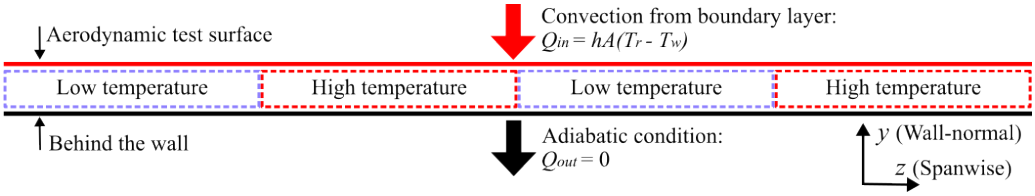
Three conceptual flat-plate models were considered in this section to passively achieve non-uniform temperature distributions during the transient state that exists in wind-tunnel operation. The mechanism for achieving different temperatures and the practicality of each concept were discussed.

Spanwise Arrangement of Two Dissimilar Materials

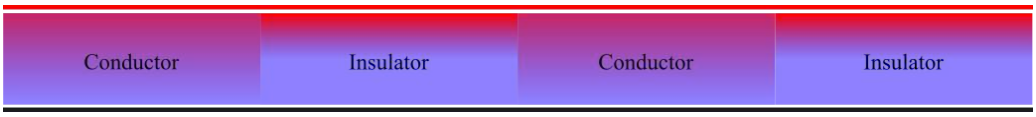
The dissimilar materials approach achieves non-uniform surface temperatures during high-enthalpy wind tunnel tests, where the surface is exposed to high heat flux, depicted in Fig. 3.7b, with the targeted wall temperature distributions and assumed boundary conditions shown in Fig. 3.7a. Two materials with dissimilar thermal properties are periodically combined in the spanwise direction on the surface: one material with low thermal diffusivity acting as an insulator strip and another with high thermal diffusivity functioning as a thermal conductor strip. This different thermal diffusivity allows the generation of different transient surface temperatures during high heat flux conditions.

The lower diffusivity materials for the insulator strip facilitate slower heat diffusion. As a result, under exposure to high heat flux, the surface temperature in the insulator strips increases, rapidly approaching the recovery temperature. In contrast, materials with higher diffusivity play a role in maintaining material temperature, as their high heat diffusion capabilities help distribute heat quickly. Figure 3.8a visualises multiple materials' thermal conductivities and diffusivities. Within Fig. 3.8a, it is essential to note that metals and graphite exhibit the highest thermal diffusivity, followed by ceramics, composites, foams, and polymers, each successively exhibiting lower diffusivity levels. Various materials are selected based on manufacturing availability and explored for their diffusivity properties as temperature increases, exemplified in Fig. 3.8b. Copper and aluminium are exceptional conductors, with copper offering superior performance due to its higher density and greater thermal capacity. Titanium, titanium alloys, and Inconel 625, have significantly lower diffusivity which are suitable for the insulator material. Graphite (G348) is versatile, potentially acting as either the insulator or conductor

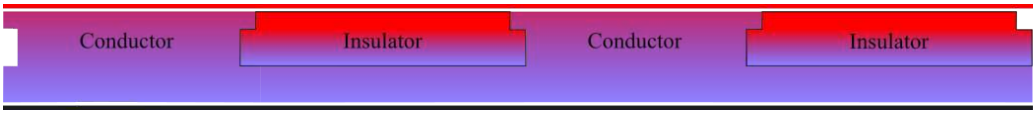
depending on the operation temperature. MACOR (ceramics) has the lowest diffusivity among all materials, making it highly preferable as an insulator.



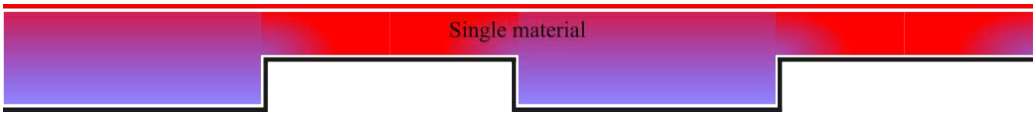
(a) Spanwise wall temperature profile and boundary conditions: The top and bottom surfaces are subjected to alternating low and high temperature strips along the spanwise direction, with specified boundary conditions applied.



(b) Spanwise arrangement of two dissimilar materials.



(c) Practical arrangement of two dissimilar materials.

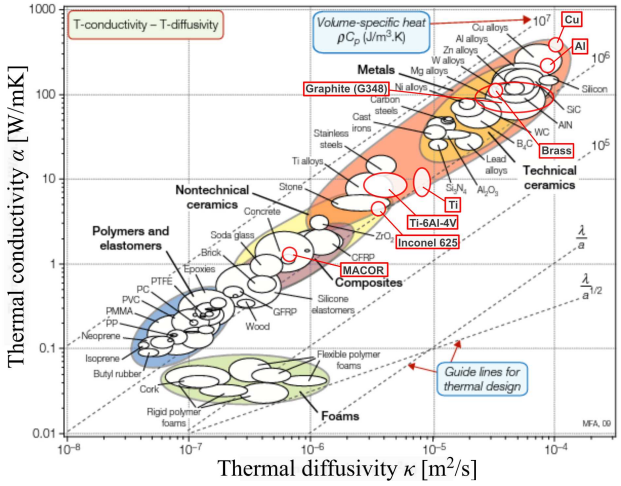


(d) Single material with non-uniform spanwise thickness.

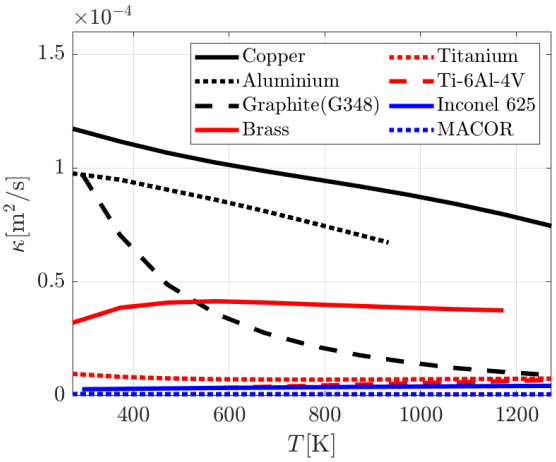
Figure 3.7: Sketches of the wall temperature profile and boundary conditions (a) and the three conceptual designs for achieving spanwise temperature difference approached by varying the materials (b) and (c), and thickness of the wall (d).

Practical Arrangement of Two Dissimilar Materials

The spanwise arrangement of two dissimilar materials aims to exploit varying thermal properties to generate different surface temperatures. However, this leads to practical challenges in combining materials with differing thermal expansion properties to achieve the desired wall temperature. For instance, handling the considerable tensile and shear stresses that occur on bolts can be challenging when dealing with materials that expand at different rates. High-temperature adhesives, commonly used for bonding, may also introduce uncertainties when applied in similar conditions. Therefore, exploring alternative bonding methods that avoid reliance on bolts or adhesives is recommended. Figure 3.7c illustrates a practical configuration in which thin strip-shaped insulators are embedded within an otherwise solid conducting base material.



(a) Thermal conductivity plotted against thermal diffusivity, highlighting the selected materials property. Adapted from Ashby [85].



(b) Thermal diffusivity changes with temperature with the selected materials.

Figure 3.8: Thermal properties across materials and their temperature sensitivity.

A preferred approach involves having the materials hold their positions relative to each other through the use of geometric shapes achieved by machining. This is illustrated in Fig. 3.7c, where tooth-shaped slots are cut into the base material. In essence, these tooth-shaped slots serve as receptacles for the insulator strips. This method of employing toothed slots has the advantage that these grooves securely hold the insulator strip in place, even when materials with different thermal expansion coefficients are involved. While there is a risk of small gaps forming due to differential thermal expansion, this is mitigated by the relatively small dimensions of the slots. This approach mitigates the risk of cracks or structural issues that might arise during the assembly process using screws or other traditional fasteners. In cases where the expansion of the insulator material is larger than the conductor material, roles can be reversed; tooth-shaped conductors can be slotted into the insulator instead.

Single Material with Non-Uniform Spanwise Thickness

A single material with a non-uniform spanwise thickness generates surface temperature distributions by controlling heat flux through variations in the inner wall structure, as illustrated in Fig. 3.7d. In thin walls, owing to limitation of heat flux through the small cross-sectional area, the surface temperature increases rapidly. With a cold wall initial condition, in the beginning, uniform heat transfer via convection takes place at the same streamwise location. Once both walls begin to heat, the temperature of the thinner wall rises more rapidly than that of the thicker wall, due to the restricted

heat flux passing through its smaller cross-sectional area. The spanwise non-uniform temperature distribution appears until both walls reach the same temperature. This approach is advantageous when the entire rig needs to be made from a single type of material and/or single manufacturing method.

3.3.3 Thermal Modelling for Transient Surface Temperature

The performance of all concepts was assessed based on the heat transfer estimated using the method described in Sec. 3.2.2. The freestream condition was consistent with Sec. 3.2.2. The geometries of the conceptual models are shown in Fig. 3.9. Figures 3.9a and 3.9b illustrate the spanwise arrangement of two dissimilar materials and the practical arrangement of two dissimilar materials, respectively. In both cases, the central material acts as an insulator sandwiched between conductors to simulate periodic conditions. The insulator thickness of the practical arrangement was chosen to be 4 mm for manufacturing simplicity. The heat transfer in the model included lateral heat transfer to account for the interaction between the dissimilar materials. Figure 3.9c displays the single material with non-uniform spanwise thickness where the central part serves as an insulator sandwiched by conductors. The central thickness is varied parameter for the insulator.

All test cases selected for each approach and material combination are listed in Table 3.4. For the spanwise arrangement of two dissimilar materials and their practical arrangement, a machinable ceramic, MACOR, was selected as the insulator for its low thermal diffusivity, as illustrated in Fig. 3.8b. Conversely, copper, with high thermal diffusivity, was designated as the conductor. The case of M-C (Base) and M-C (Practical) is the spanwise arrangement of two dissimilar materials and their practical arrangement, respectively. In order to assess the insulator's sensitivity, titanium and aluminium were selected as an additional case (T-A) based on the practical arrangement configuration, for the insulator and conductor, respectively. To evaluate the sensitivity of the insulators, titanium and aluminium were selected as the add-on case (T-A) for the insulator and conductor, respectively, based on the practical arrangement configuration. For the single material with non-uniform spanwise thickness approach, MACOR was chosen because of its low thermal diffusivity, which causes temperature gradients quickly. The insulation thicknesses of $t_{\text{insulator}} = 1\,\text{mm}$ (M-M (1 mm)) and 4 mm (M-M (4 mm)) were chosen. Additionally, A-A and T-T were investigated, using 1 mm insulator thickness employing

Table 3.4: Materials selection for the conceptual models in the thermal modelling.

Name	Approach	Insulator	Conductor
M-C (Base)	The spanwise arrangement of two dissimilar materials	MACOR	Copper
M-C (Practical)	The practical arrangement of two dissimilar materials	MACOR	Copper
T-A	The practical arrangement of two dissimilar materials	Titanium	Aluminium
M-M (1 mm)	The single material with non-uniform spanwise thickness	MACOR (1 mm)	MACOR
M-M (4 mm)	The single material with non-uniform spanwise thickness	MACOR (4 mm)	MACOR
A-A (1 mm)	The single material with non-uniform spanwise thickness	Aluminium (1 mm)	Aluminium
T-T (1 mm)	The single material with non-uniform spanwise thickness	Titanium (1 mm)	Titanium

aluminium and titanium, respectively.

The 3D models were designed using CAD software before the geometry data were imported into MATLAB. For the 3D geometry model, a resolution study of the unstructured mesh was conducted, ultimately settling on a test surface and base resolution of 2.5 and 5 mm, respectively. A time step of 0.1 s was chosen, and the transient thermal analysis spanned a duration of 15 s, mirroring a typical wind-tunnel experimental time frame. Regarding boundary conditions, except for the test surface, all other surfaces were defined as adiabatic walls. The initial temperature across the entire plate was set at 300 K.

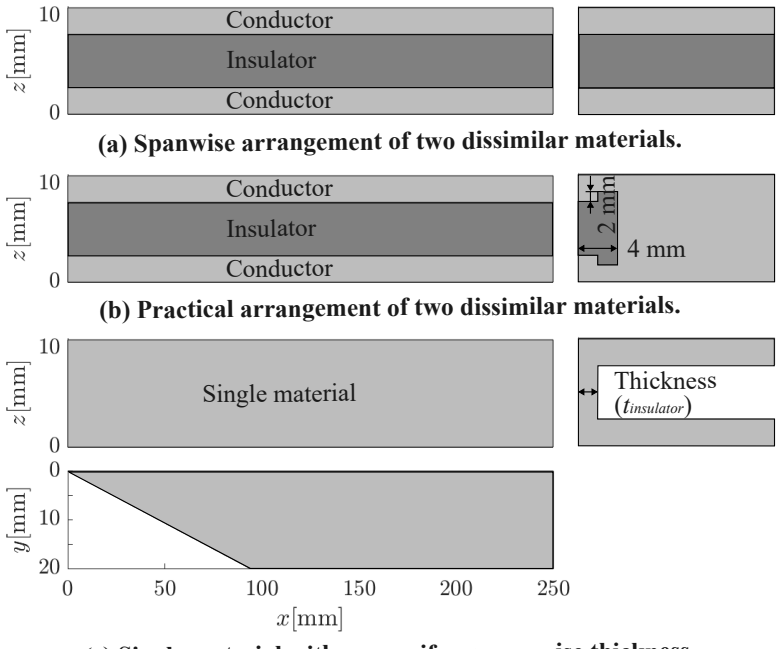


Figure 3.9: The geometries of three conceptual designs in the thermal modelling.

3.3.4 Prediction of the Transient Temperature

The surface-temperature distributions of all cases based on the three conceptual models at $t = 15\,\mathrm{s}$ are shown in Fig. 3.10. The spanwise temperature profile at the strip centres after $t = 15\,\mathrm{s}$ is shown in Fig. 3.11a. In all cases, the temperature was high at the leading edge due to the highest convection and thinner wall. After the leading edge, both M-C cases (Figs. 3.10a and 3.10b) exhibited apparent temperature differences between the insulator Θ_H and conductor Θ_L. After $x = 100\,\mathrm{mm}$, the changes in Θ_H and Θ_L become smaller, respectively. Along the spanwise direction, there is a smooth and monotonic temperature increase towards the centre to of the insulating strip. Peak temperatures were observed at the centre of the insulating strip, as illustrated in the spanwise temperature profiles plotted in Fig. 3.11a. Meanwhile, the conductor maintains a uniform temperature due to its higher thermal diffusivity. The spanwise temperature profiles confirmed that the practical arrangement of two dissimilar materials yielded results similar to the spanwise arrangement approach, as illustrated in Fig. 3.11a for the M-C (Base) and M-C (Practical) cases. The temperature difference between the peak temperature of the insulator and conductor reached 0.37 in both cases at $x = 150\,\mathrm{mm}$, demonstrating the possibility of generating spanwise non-uniform temperature distributions. On the other hand, the T-A case showed an approximately uniform temperature across the spanwise direction. This indicated that the thermal diffusivity of titanium was not sufficiently low, being ten times higher than that of MACOR.

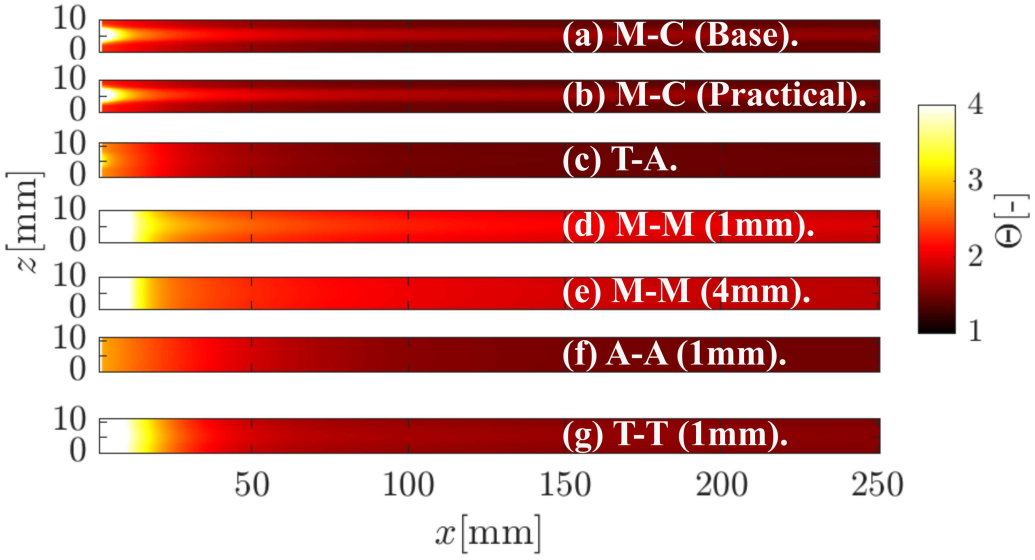
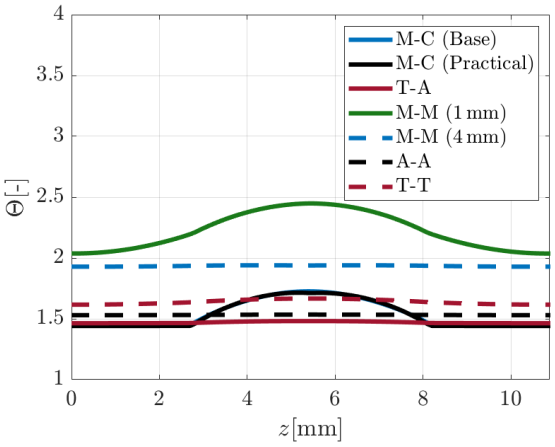
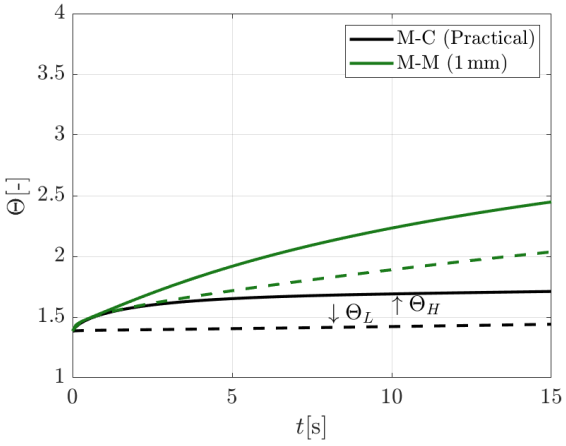


Figure 3.10: Surface normalised temperature of the conceptual designs calculated by the thermal modelling.

Temperature distributions of the single-material, non-uniform spanwise-thickness cases are shown in Figs. 3.10d-g. The M-M (1 mm) case showed apparent temperature variations, while the M-M (4 mm) case showed only weak temperature variations in the spanwise direction shown in Fig. 3.11a. The conductor temperature distribution of the M-M (1 mm) case showed a more gradual temperature gradient than the dissimilar-material approach across the spanwise direction. The thinner wall of the insulator demonstrated greater sensitivity to temperature changes. For A-A, the surface temperature showed a uniform distribution. Meanwhile, T-T showed a slight temperature difference between the insulator and conductor. The insulator temperature for T-T was higher than that for T-A, suggesting that the thinner titanium insulator can generate higher temperatures. To generate higher temperature differences, both approaches of two dissimilar materials and the single material with non-uniform spanwise thickness require less thermal diffusivity material or a thinner insulator.



(a) Spanwise normalised temperature profile at the aerodynamic test surface at $x = 150\,\text{mm}$ at $t = 15\,\text{s}$.



(b) Transient normalised temperature at the strips' centre at $x = 150\,\text{mm}$ along exposure time (Solid and dash lines are the insulator and conductor, respectively).

Figure 3.11: Surface normalised temperature plot along the spanwise direction and transient normalised temperature at $x = 150\,\text{mm}$.

Fig. 3.11b shows the temperature evolution over time at the strip's centre ($x = 150\,\text{mm}$) for the M-C (Practical) and M-M (1 mm), both selected for their higher temperature distributions. Notably, both cases exhibited distinct temperature differences from the outset, maintaining a consistent difference throughout the exposure time. The M-C (Practical) case maintained the temperature difference without further heating, while the M-M (1 mm) case gradually attained a larger temperature difference as time increased. In the M-C (Practical), a temperature difference is initially established, after which

the temperatures of both the insulator and conductor remain constant, maintaining the temperature difference. Conversely, in the M-M (1 mm), the temperature difference gradually increases over time after $t = 2$ s. These results highlighted the importance of the insulator geometry in achieving significant temperature differences.

3.3.5 Discussion

Impact on Performance of Insulator Material Selection

The insulators utilised in both the practical arrangement of dissimilar materials and the structural heat-flux approaches were selected based on their low diffusivity and/or reduced thickness, aimed at increasing local temperatures to achieve significant temperature differences compared to the conductors. Table 3.5 presents the thermal diffusivity ratio between the insulator and conductor, along with the temperature difference ($\Delta\Theta$) at t =15 s for the materials employed in the practical arrangement cases. Notably, $\Delta\Theta$ is 16 times higher with MACOR and copper than titanium and aluminium, while the $\kappa_{conductor}/\kappa_{insulator}$ ratio is 24 times higher.

Table 3.5: Thermal diffusivity ratio of the insulator and conductor materials.

Insulator, Conductor	MACOR, Copper	Titanium, Aluminium
$\kappa_{conductor}/\kappa_{insulator}$	261	11
$\Delta\Theta_{t=15}$	0.38	0.024

Characterisation of Insulator's Thickness

The results showed that the thickness of the insulator, $t_{\text{insulator}}$, was a crucial parameter that significantly affected temperature distributions in cases with a single non-uniform thickness material, along with material thermal diffusivity κ. Figure 3.12 shows the temperature at the centre of a thin strip at $x = 150$ mm at $t = 15$ s plotted against the product of κ and $t_{insulator}$ for a range of the MACOR and titanium test cases. Two trends are evident from Fig. 3.12: (1) low values of $\kappa t_{insulator}$ produce high wall temperatures for both the thick and thin parts of the wall, and (2) low values of $\kappa t_{insulator}$ lead to an increase in the temperature difference between the thick and thin regions of the wall. The parameter $\kappa t_{\text{insulator}}$ (with units of volumetric flow rate) effectively characterises the efficiency at which a configuration is able to transfer heat between the thin and thick parts of the wall structure

and thus inhibit or promote the volumetric flow of thermal energy (i.e. heat transfer) between the thick and thin parts. In both MACOR and titanium, as $\kappa t_{\text{insulator}}$ decreased, i.e., the wall became thinner, the local temperature of the insulator increased approximately linearly on a logarithmic scale. Given MACOR's lower thermal diffusivity, it achieved the highest local temperature with the thinnest wall. On the other hand, Θ_L effectively sustained the equilibrium temperature due to a relatively large wall thickness. In terms of $\Delta\Theta$, the reduction in $\kappa t_{\text{insulator}}$ exhibited a more apparent impact across different materials, indicating the critical role of insulator thickness in achieving temperature differences.

This result suggested that using a low-diffusivity material with a thin profile can increase the temperature on the insulator surface, while the opposite properties are optimal for the conductor to maintain surface temperature. To achieve even greater temperature differences, adjustments such as altering the incident flow angle or freestream pressure to enhance convection or implementing additional heating on the insulator and cooling on the conductor may be necessary.

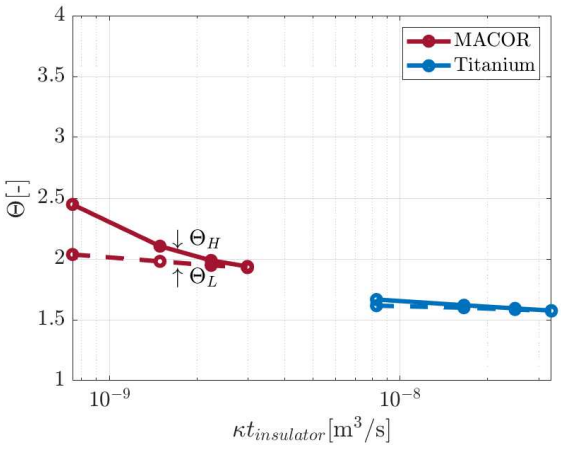


Figure 3.12: Normalised temperature at the strips' centre surface at $x = 150\,\text{mm}$ at $t = 15\,\text{s}$ for MACOR and titanium multiplied by thermal diffusivity and the insulator thickness ($t_{insulator} = [1, 2, 3, 4]\,\text{mm}$).

3.4 Summary

This chapter considered two complementary thermal-control scenarios: a steady-state actuation strategy and passive concepts suitable for short-duration wind-tunnel experiments.

Steady-State Spanwise Thermal Actuation

A steady-state temperature control strategy was proposed for actuation methods to demonstrate the spanwise non-uniform surface temperature distributions. Behind a finite wall, differential cooling is imposed across the spanwise direction. Thermal modelling assessed the performance of the surface temperature distribution for an aluminium wall. The results indicated that a thinner wall or stronger local cooling can produce apparent surface-temperature variations. Titanium and MACOR were also explored to investigate the sensitivity of thermal conductivity. Both titanium and MACOR were found to induce temperature differences, provided that the wall was sufficiently thin.

Passive Thermal Control for Short-Duration Facilities

Passive control approaches were explored for short-duration wind-tunnel tests. To achieve non-uniform temperature distributions within a brief experimental time frame, heat transfer is utilised to heat the local surface from the boundary layer passively. Three conceptual approaches were proposed. A spanwise arrangement of dissimilar materials utilised materials with two extremely different thermal properties, MACOR and copper, for the insulator and the conductor, respectively. Due to the difference in thermal diffusion rates, the insulator rapidly increased in surface temperature while the conductor maintained its surface temperature. These different thermal properties allowed the surface to achieve temperature differences. To implement this method in a wind tunnel, a practical arrangement was proposed using tooth slots to be assembled to overcome potential problems due to differential thermal expansion. This approach achieved equivalent surface-temperature variation performance to that of the spanwise arrangement of two dissimilar materials approach. A single-material approach with non-uniform spanwise thickness was also proposed to achieve surface temperature distributions by modifying the wall structure. Local regions of low wall thickness limit internal heat transfer, resulting in increased local temperatures. The insulator temperature was characterised by the thermal-diffusivity ratio between the insulator and conductor and by the insulator thickness.

Chapter 4

Characterisation of Non-Uniform Surface Temperature Distributions

4.1 Overview

This chapter presented a proof-of-concept experimental framework for generating and characterising spanwise non-uniform wall-temperature distributions on a flat plate in Mach 2.75 flow, and for quantifying the associated boundary-layer response. The test article combined streamwise strips of thermally dissimilar materials (copper conductor and MACOR insulator) to passively impose a spanwise-periodic thermal boundary condition when subjected to transient convective cooling. Surface temperature fields were quantified using infrared thermography (IRT) and reconstructed using a physics-informed thermal model.

Building on this thermal characterisation, time-resolved Laser Doppler Anemometry (LDA) was used to measure turbulent boundary-layer velocity profiles under spatially and temporally varying wall temperature, enabled by a continuous-motion traverse strategy that captured full profiles on timescales commensurate with the thermal transient. The resulting profiles were fitted with a composite boundary-layer model and used to quantify the formation and scaling of streamwise velocity streaks with the strength of thermal forcing.

The chapter is structured as follows: Section 4.2 describes the facility, flat-plate model, and common

experimental apparatus. Section 4.3 details the temperature measurement and reconstruction methodology (IRT and thermal model) and the time-resolved LDA methodology. Section 4.4 characterises the generated wall-temperature distributions, and Section 4.5 presents the boundary-layer response and streak quantification.

4.2 Experimental Facility and Flat-Plate Model

4.2.1 Imperial College Supersonic Wind Tunnel and Operating Condition

Experiments were conducted in the Imperial College Supersonic Wind Tunnel, a blow-down facility capable of producing high-speed flow up to Mach 2.75. The facility utilises dried compressed air stored at 2.7 MPa in a 48 m^3 supply tank. The stagnation temperature (T_0) corresponds to ambient conditions, typically 283 K. During operation, both stagnation pressure (P_0) and temperature were continuously measured. Typical operational runtime is approximately 25 s per shot. A schematic of the tunnel layout is shown in Fig. 4.1. The nozzle employed in the present experiments produces a freestream Mach number of 2.75, and the test section consists of a constant-area square cross-section measuring 150 mm × 150 mm. Optical-grade glass windows are installed on both sides of the test section to provide optical access for Laser Doppler Anemometry (LDA). A summary of the freestream condition is provided in Table. 4.1. Once the target static-stagnation pressure ratio is attained, the test window begins, and the flow is assumed to be steady and uniform. This assumption is supported by previous characterisation of the facility at Mach 2, where the tunnel is operated in an equivalent manner and the freestream spatial variation is reported to be within 1.3 % [86]. The operating condition is common to both the IRT and LDA campaigns.

Table 4.1: Freestream and post-shock flow configurations.

	M	Re (m^{-1})	T_∞ (K)	p_∞ (Pa)	T_r (K)	Shock angle β (deg.)
Freestream	2.75	3.5×10^7	116.7	15910.7	274.1	-
Post-shock	2.61	-	124.0	19663.3	274.9	23.5

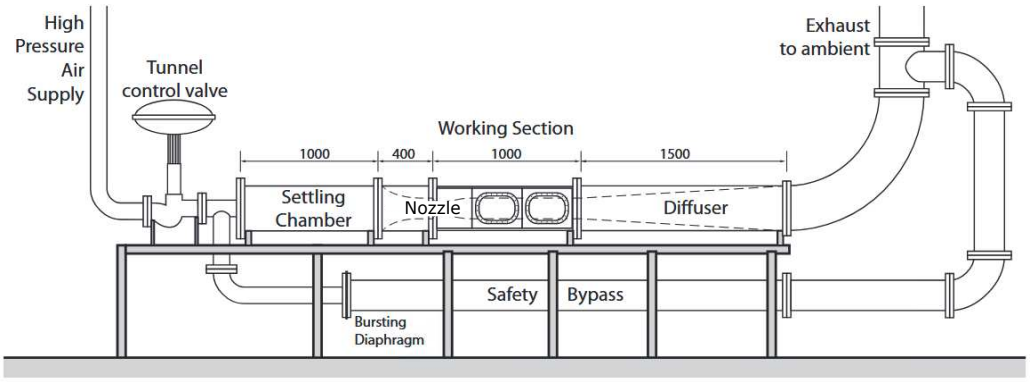


Figure 4.1: Schematic diagram of the Imperial College London supersonic wind tunnel.

4.2.2 Flat Plate Test Article

To achieve non-uniform surface temperature distributions, the implementation of dissimilar materials or a single material with non-uniform spanwise thickness is crucial. These approaches regulate heat flux by manipulating material characteristics or the internal wall heat transfer to locally increase or decrease surface temperatures. This behaviour can be described by the transient heat transfer equation

$$\begin{aligned} \frac{\partial T}{\partial t} &= \frac{\alpha}{\rho c_p} \nabla^2 T \\ &= \kappa \left(\frac{\partial^2 T}{\partial x^2} + \frac{\partial^2 T}{\partial y^2} + \frac{\partial^2 T}{\partial z^2} \right) \end{aligned} \tag{4.1}$$

where T, t, α, ρ, c_p, κ, x, y, and z represent temperature, time, thermal conductivity, density, specific heat, thermal diffusivity, and spatial directions, respectively. The previous chapter demonstrated through thermal modelling that the dissimilar material approach results in a higher temperature difference between insulating and conducting regions compared to the single material with non-uniform spanwise thickness. Additionally, a practical arrangement for bonding two dissimilar materials using tooth-shaped slots was proposed to enhance structural integrity and thermal performance. In this study, the practical arrangement of two dissimilar materials was selected for implementation. This choice was based on its ability to achieve significant temperature variations and its potential feasibility for real-world applications, as validated by prior thermal modelling and design considerations.

Figure 4.2 presents the fully assembled test article, comprising copper and MACOR strips embedded into a copper base, with a sharp steel leading-edge. The test surface measures 270 mm in the stream-

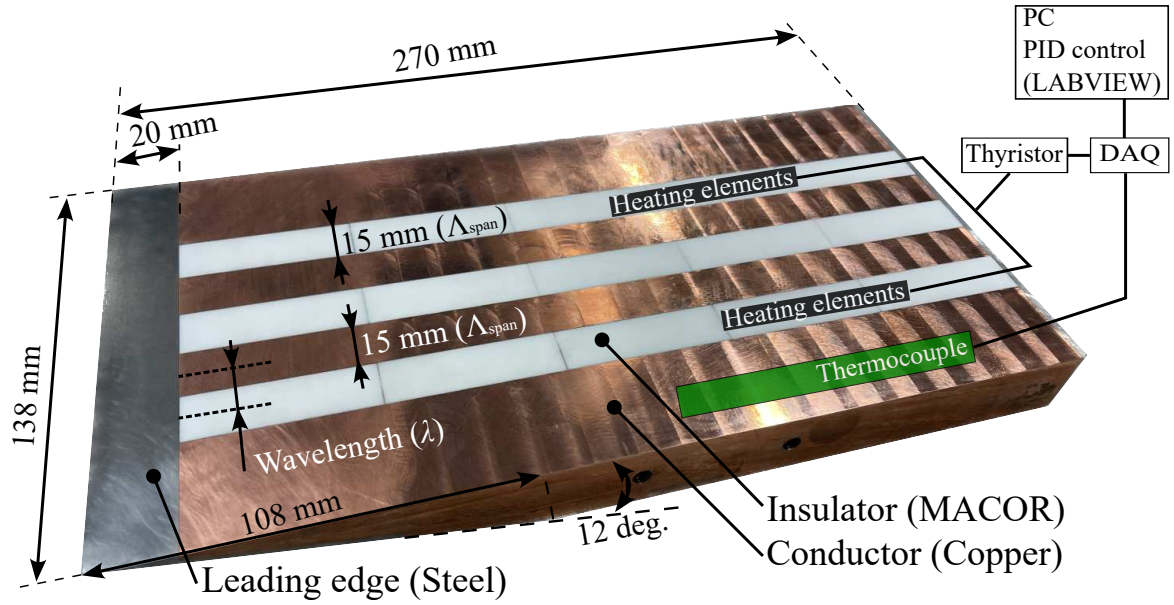


Figure 4.2: Photograph of the assembled flat plate test article, including steel leading edge, MACOR and copper strips with the diagram of the heating system.

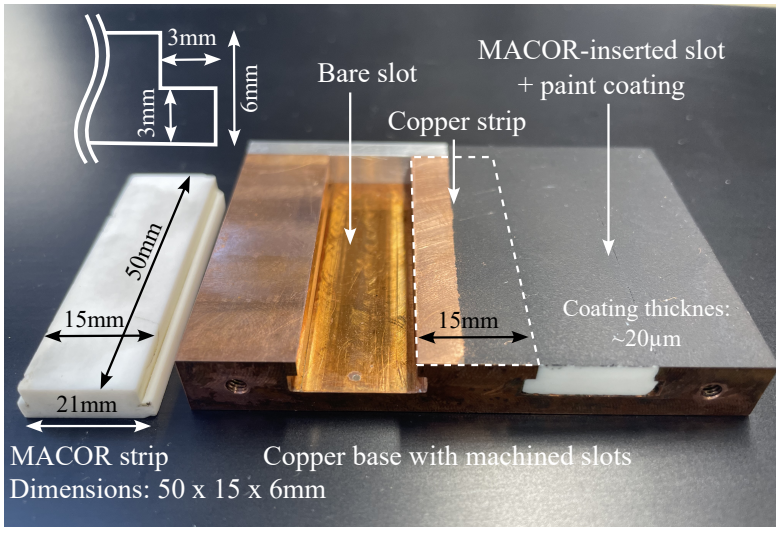


Figure 4.3: Prototype fabrication of MACOR–copper interface. Two slot configurations in the copper base: one empty and one fitted with a coated MACOR strip, used to validate fit and surface treatment.

wise direction and 138 mm in the spanwise direction, and the plate includes a 12-degree bevelled leading-edge made of steel for robustness and sharpness. To generate spanwise surface temperature variations passively, materials with contrasting thermal properties were selected: MACOR, a machinable glass–ceramic, was employed as the insulating material due to its low thermal diffusivity ($0.73\times10^{-6}\,\mathrm{m}^2/\mathrm{s}$), high strength, and ease of precision fabrication; copper was selected as the conducting material for its high thermal diffusivity ($110.7\times10^{-6}\,\mathrm{m}^2/\mathrm{s}$) and heat capacity (further properties are listed in Table. 4.2).

Table 4.2: List of model components and material properties.

Component	Material	Diffusivity (m^2/s)	Conductivity (W/m·K)	Specific heat (J/kg·K)	Density ($\mathrm{kg/m^3}$)
Leading-edge	Steel	12.2×10^{-6}	45	466	7900
Conductor	Copper	110.7×10^{-6}	386	389	8960
Insulator	MACOR	0.73×10^{-6}	1.43	777	2520

The surface featured three MACOR strips alternating with two copper segments, arranged in a spanwise pattern. Each MACOR strip measured 250 × 15 mm and was subdivided into five 50 mm-long segments to facilitate manufacturing. The strips were embedded into the copper base using a tooth-slot configuration, where each tooth was 3 mm wide and 3 mm deep on both sides, forming a symmetric interlock. The dimensional tolerance between the MACOR teeth and the copper slots was maintained within ±0.05 mm to ensure a snug fit and reliable thermal contact. All inserts were 6 mm thick and assembled flush with the copper surface. After integration, the entire surface was machined and polished together to ensure smoothness across interfaces and to minimise aerodynamic disturbance. A prototype assembly, shown in Figure 4.3, was first manufactured to verify the slot geometry, confirm coating behaviour, and evaluate the assembly process.

4.2.3 Mounting of the Flat Plate Test Article

The flat plate was installed in the wind tunnel test section at a fixed angle of incidence of 3° for all experiments. The angle was selected to prevent blockage and mitigate flow separation on the back side of the test section.

Two mounting configurations were employed to accommodate the optical requirements of different measurement techniques. For IRT measurements, the plate was installed vertically and secured by mounting bolts (Fig. 4.4(a)). Conversely, for the LDA configuration, a dedicated horizontal mounting

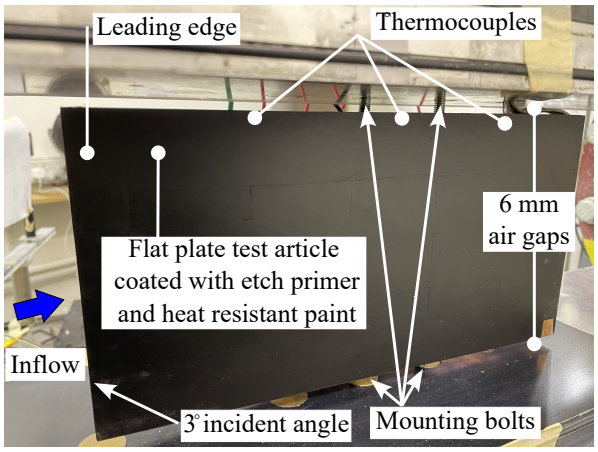
rig was designed and manufactured from stainless steel to ensure sufficient stiffness and repeatable alignment. To provide optical access through the side window while maintaining a constant 6 mm clearance between the model and the tunnel wall, the copper base of the flat-plate assembly was modified. Specifically, a machined pocket was introduced in the base so that the plate could be inserted and clamped into the mounting rig without changing the exposed test surface geometry (Fig. 4.4(b)).

Figure 4.4(c) illustrates the general flow field common to both configurations. The 3° incidence resulted in an attached oblique shock at the leading edge with an angle of $\beta = 23.5°$. This yielded a local post-shock Mach number of $M = 2.61$. Under assumed turbulent boundary layer conditions, the boundary-layer edge static and recovery temperatures were calculated as $T_\infty = 124\,\mathrm{K}$ and $T_r = 275\,\mathrm{K}$, respectively (see Table 4.1).

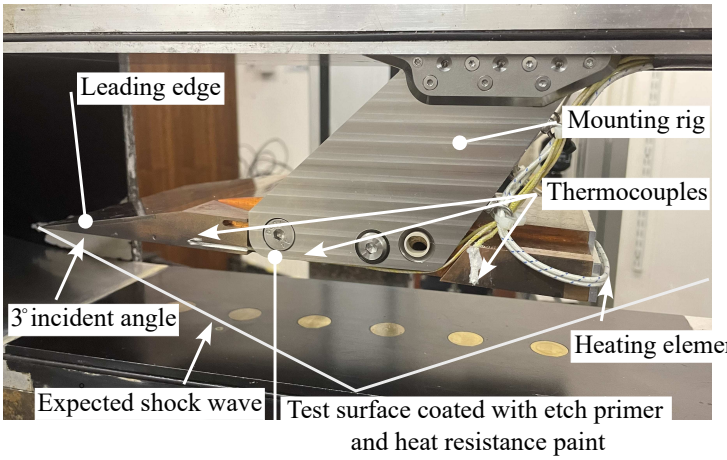
4.2.4 Pre-Heating System

The recovery temperature (T_r) plays a pivotal role in facilitating heat transfer between the test surface and the surrounding flow, enabling the establishment of spanwise non-uniform surface temperature distributions. In hypersonic free-flight conditions, T_r is high and naturally promotes heat transfer to the surface via aerodynamic heating. In contrast, in conventional low-enthalpy wind tunnels (including the present facility), T_r is substantially lower and instead acts as a cooling mechanism for the plate. Despite this reversal in directionality, the surface heat-transfer physics can be treated as analogous to flight conditions provided that a sufficiently large temperature gradient is imposed between the surface and the recovery temperature.

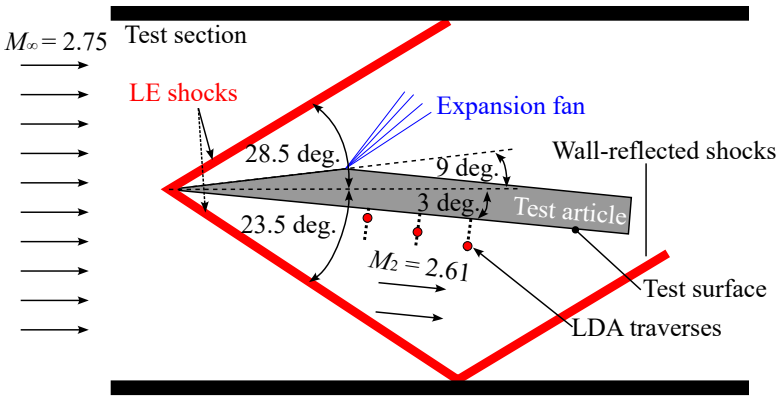
A key distinction arises in the thermal response of the conductor and insulator strips under this heat-and-cool condition. Unlike the simplified assumption introduced previously, where insulator strips are heated by the flow to temperatures relatively higher than the surrounding conducting surface, the present experiments are characterised by surface cooling of the insulator strips due to their low thermal diffusivity. Following wind-tunnel start-up, the insulator material (MACOR) cools rapidly toward T_r. In contrast, the copper conductor strips retain a higher surface temperature during the run, owing to their high thermal conductivity and volumetric heat capacity. As a result, the imposed spanwise patterning is realised through differential cooling rates rather than differential heating.



(a) Photo of the vertical configuration for IRT measurements



(b) Photo of the horizontal configuration for LDA measurements



(c) Schematic of inviscid shock wave structure ($M_\infty = 2.75$)

Figure 4.4: Experimental arrangement and flow field schematic. The test article is positioned at a 3° incidence angle for (a) IRT (vertical) and (b) LDA (horizontal) measurements, resulting in (c) the anticipated shock wave structure.

Preheating was achieved using two 600 W heating elements controlled by a Proportional-Integral-Derivative (PID) controller. To monitor the bulk temperature, three Type-K thermocouples were embedded within the copper base along one side at streamwise intervals of 67.5 mm. In the IRT campaign, the model is thermally isolated during heating using a 6 mm-thick rigid insulation board made of alumina–silica ceramic fibre (Fig. 4.5). The board covered both the test-surface side and the underside of the plate to suppress heat loss to the surroundings and to promote a uniform initial boundary condition. The material was selected for its low thermal conductivity (0.13 W/m·K at 1100 K), high temperature resistance (up to 1700 K), and practical cost. Once the PID system reached the target temperature, heating was sustained for 5 min to ensure thermal uniformity throughout the test article. The insulation board was then manually removed immediately prior to sealing the test section. To mitigate potential thermal interference and avoid contact with the tunnel walls, a 6 mm air gap was maintained between both sides of the plate (Fig. 4.4(a)).

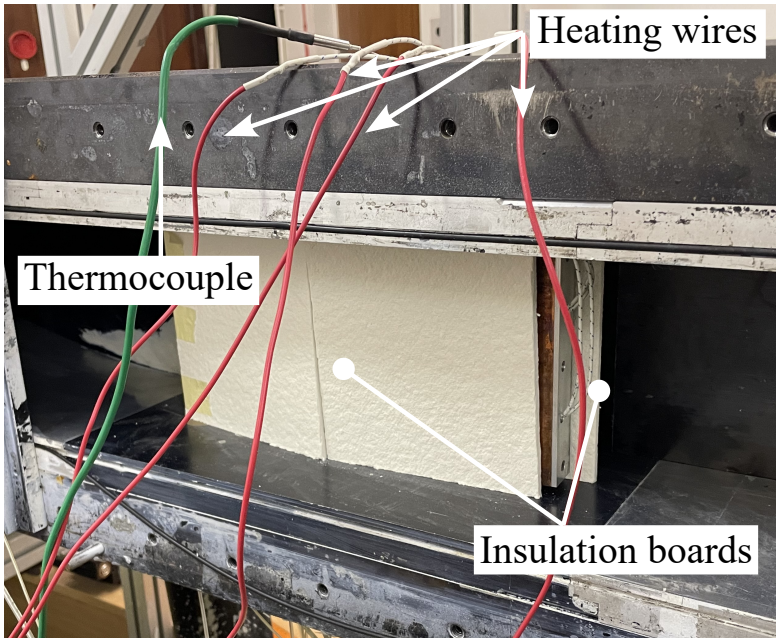


Figure 4.5: Photograph of the test article covered with the insulator on the test surface side and bottom side to maintain uniform thermal conditions before the wind tunnel run.

For the LDA campaign, the preheating process was refined to improve the initial temperature condition. The same fundamental heating hardware was used (two 600 W elements with PID control monitored by three thermocouples), but the procedure was modified such that the plate was heated to approximately 10 % above the target temperature, and the tunnel was started once the surface naturally cooled down to the desired level. This modification removed the need for an external insulation

shield while enabling improved repeatability of the initial surface temperature at the measurement start time. The uniformity of the initial temperature was verified using three embedded thermocouples distributed in the streamwise direction (Fig. 4.4(b)); at the start of each run, these readings consistently show less than 1 % variation, indicating a uniform initial temperature distribution. The same 6 mm side-wall air gap was maintained for consistency with the IRT configuration and to minimise thermal interaction with the facility structure.

4.2.5 Surface Coating

The surface coating plays a critical role in ensuring both a smooth surface and consistent surface emissivity for accurate measurements. When copper strips are exposed to the atmosphere, they undergo an inevitable oxidation process, which intensifies after heating the plate. This oxidation results in the formation of cupric oxide (CuO) and cuprous oxide (Cu_2O), significantly altering the emissivity of the surface. Additionally, determining the emissivity of polished copper surfaces at low temperatures is challenging due to their inherently low emissivity, which further changes as oxidation progresses during measurements.

To address these challenges and ensure uniform high emissivity, surface coating was applied. Two primary techniques can achieve this: oxidation coating and spray coating. Oxidation coating involves forming a CuO layer on the copper surface by initially oxidising (Cu_2O) at temperatures above 573 K [87]. This process creates a nanometer-thick CuO layer with an emissivity of approximately 0.87, significantly higher than that of polished copper, which has an emissivity of around 0.03 [88]. However, the CuO layer is fragile and difficult to control, as its properties are highly sensitive to heat temperature and exposure time [89]. This fragility makes oxidation coating unsuitable for supersonic testing, as the coating may degrade or fail under such conditions.

In contrast, thermal spray paint coating was adopted as a more reliable and practical solution. It provided a smooth surface with uniform emissivity not only for copper but also for MACOR and steel leading-edge surfaces. The process involved applying an etch primer paint, capable of withstanding temperatures up to 660 K, to enhance adhesion. This was followed by a heat-resistant paint that can endure temperatures up to 970 K. After application, the surface was polished to achieve a smooth finish, as illustrated in Fig. 4.4(a). The thickness of the paint layers was measured to be approximately

20 μm using a micrometer.

4.3 Measurement Methodology

4.3.1 Infrared Thermography (IRT) Calibration and Measurement

Surface temperature measurement can be achieved through contact or non-contact methods. While contact methods, such as thermocouples and thin-film gauges, offer high durability and accuracy, they physically cover the surface and disrupt heat convection from the boundary layer's recovery temperature. This makes them unsuitable for assessing surface temperature distributions. Therefore, non-contact temperature measurement methods are preferred to avoid interference with heat transfer. Infrared thermography (IRT) is a non-intrusive, high-resolution technique for measuring surface temperature and offers advantages in calibration simplicity compared to methods like temperature-sensitive paint (TSP) [90]. IRT has been widely used for intuitive surface temperature measurements in various applications. For instance, Avallone et al. employed IRT to measure the surface temperature of a flat plate at Mach 7.5 [91], while Cardone et al. used it to measure the complex surface temperature distribution of a double cone geometry [92]. These studies demonstrate the versatility and reliability of IRT for temperature measurement in aerodynamic testing.

In this study, an infrared thermography system was used to measure the surface temperature of the test plate. The system consisted of a FLIR A655SC camera equipped with a 25 ° field-of-view (FOV) lens, positioned such that the viewing angle ranges from 75 to 81 ° (Fig. 4.6). The camera observed the test surface through a Zinc-Selenide (ZnSe) window (D = 70 mm) installed in the test section. ZnSe is suitable for long-wave infrared thermography because it transmits over the spectral response range of the FLIR A655SC camera. For the present window thickness, bulk absorption is expected to be small within the 7.5–14.0 μm camera band, and the transmission loss is dominated primarily by Fresnel reflection at the two air–ZnSe interfaces. A representative transmissivity estimate for an uncoated 20 mm-thick ZnSe window is shown in Fig. 4.7. Since the in-situ calibration was performed through the same window and optical path, the mean transmission loss is incorporated into the calibration. The window transmission is therefore not expected to affect the relative temperature trends, although wavelength-dependent transmission and possible spatial non-uniformity of the win-

dow remain sources of uncertainty in the absolute temperature measurement. The camera featured an uncooled microbolometer detector array with a resolution of 640 by 480 pixels, a frame rate of 50 Hz, and a spectral response range of 7.5–14.0 μm, providing a spatial resolution of approximately 6 px/mm. For in-situ IRT calibration, a portable infrared calibrator (Fluke 9132) with a quasi-black-body target ($\epsilon = 0.95$) was used. The calibration data were obtained by measuring the calibrator installed in the wind tunnel's test section through the Zinc-Selenide window [93]. The total radiant intensity detected by the camera, I_D, was expressed as follows, accounting for the effect of the window

$$I_D = \epsilon \frac{R}{e^{B/T_{obj}} - F} + (1 - \epsilon) \frac{R}{e^{B/T_{amb}} - F} + C, \tag{4.2}$$

where ϵ, T_{obj}, and T_{amb} denote the target emissivity, the object temperature, and the ambient environmental temperature, respectively, while R, B, F, and C represent coefficients of radiation and a constant. During the calibration process, the camera recorded the signal of the calibration target at 22 temperature points ranging from 303.3 K to 633.2 K. Collecting data from the calibration target took several hours, as the target requires several minutes to stabilise at each temperature. The average signal value at each temperature point was recorded. The Levenberg-Marquardt nonlinear least squares algorithm was used to calculate the calibration coefficients R, B, F, and C, as described in Eq. 4.2. The resulting calibration curve is presented in Fig. 4.8, and the calibration parameters, including the coefficient of determination and the root-mean-square (RMS) error, are summarised in Table 4.3.

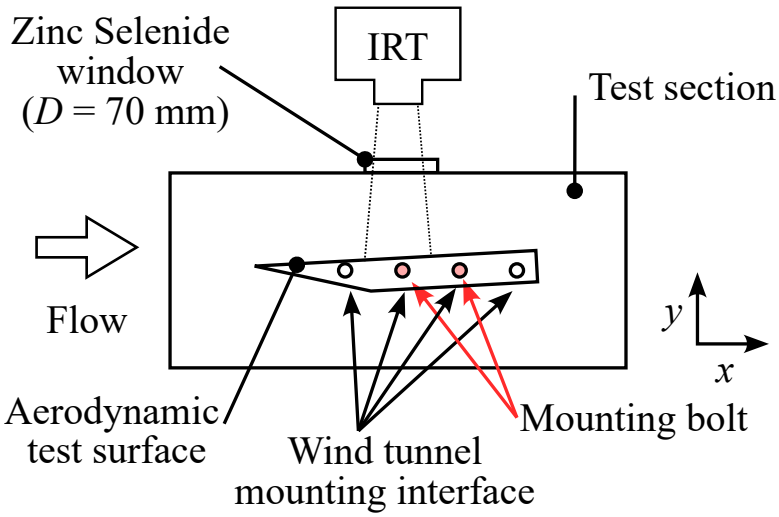


Figure 4.6: Schematic representation of the experimental setup for IRT measurements, showing the aerodynamic test surface and optical access via a Zinc Selenide window ($D = 70$ mm).

Following the in-situ calibration with the calibrator, an objective signal from the painted test surface

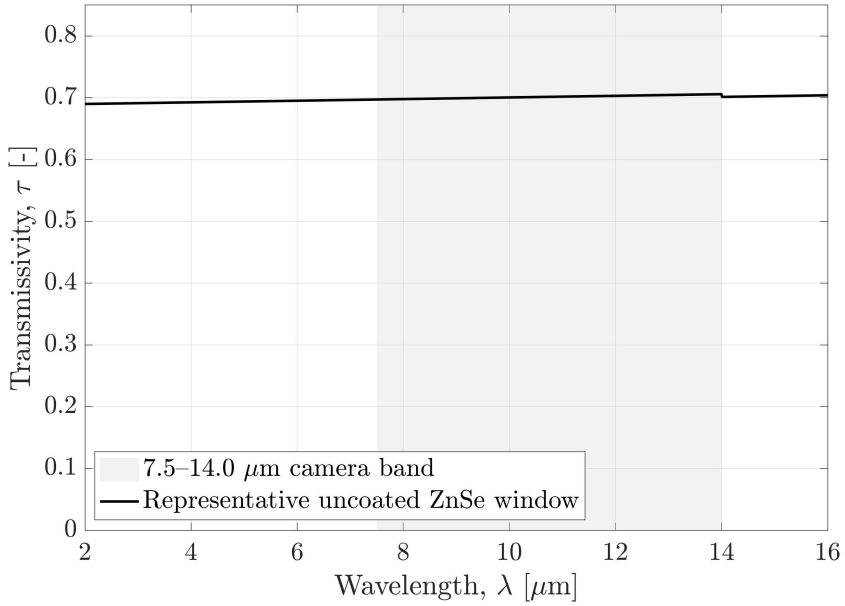


Figure 4.7: Representative spectral transmissivity of an uncoated ZnSe optical window with a thickness of 20 mm. The shaded region indicates the 7.5–14.0 μm spectral response range of the FLIR A655SC camera.

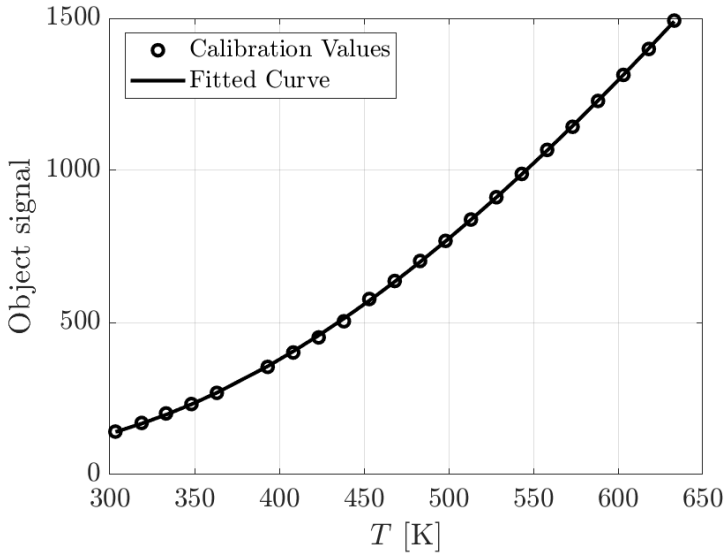


Figure 4.8: IRT camera calibration curves.

Table 4.3: Summary of the infrared camera calibration.

Parameter	Value
R	14794
B	1500
F	1.0
C	35.7
Coefficient of Determination	0.9999
RMS Error	3.27

was measured after heating to a known temperature. This objective signal was compared to the signal from the calibrator, and the surface emissivity was determined to be $\epsilon = 0.84$, with observed local variations of approximately $\pm 5\,\%$ across the measurement area. These variations were found to be systematic: the central area of the measurement data contains a slightly higher signal due to reflections between the IRT lens and the window. Additionally, the outer regions of the image captured by the infrared camera result in lower emissivity values due to the oblique angle from the lens. To overcome these problems, an in-situ calibration using the coated test surface was conducted to account for lens reflection and directional emissivity at each pixel. The emissivity value for each pixel was determined by analysing the object signal emitted from the coated test surface.

Spatial calibration was performed using a thin steel plate with 5 mm holes at 10 mm intervals. Placed directly over the coated test surface, this plate allowed adjustment of the camera's focus and scale by using the perforations as reference locations, a technique similar to that described by Cardone et al. [92]. Figure 4.9 shows the calibration plate and a corresponding raw IRT image. The image clearly resolves the reference holes while also showing minor artifacts, such as a central reflection from the IRT lens and the visible edges of the ZnSe window.

4.3.2 Laser Doppler Anemometry (LDA) Measurement and Datum Calibration

A two-component Laser Doppler Anemometry (LDA) system was employed to measure the velocity profiles of the turbulent boundary layer that develops over the test surface. The Dantec Dynamics Flow Explorer DPSS 300 system utilised two continuous-wave lasers with wavelengths of 532 nm and 561 nm, each providing 300 mW of power. The laser beams, with a diameter of 1.8 mm and separated by 60 mm, are focused using a lens of focal length $f_l = 500$ mm. The measurement volume is formed by two intersecting beam pairs at an angle $\theta_b = 6.9°$. Under this configuration, the resulting probe volume has a diameter of approximately 0.2 mm, a span of 3.3 mm, and a fringe spacing of 4.5 μm. Due

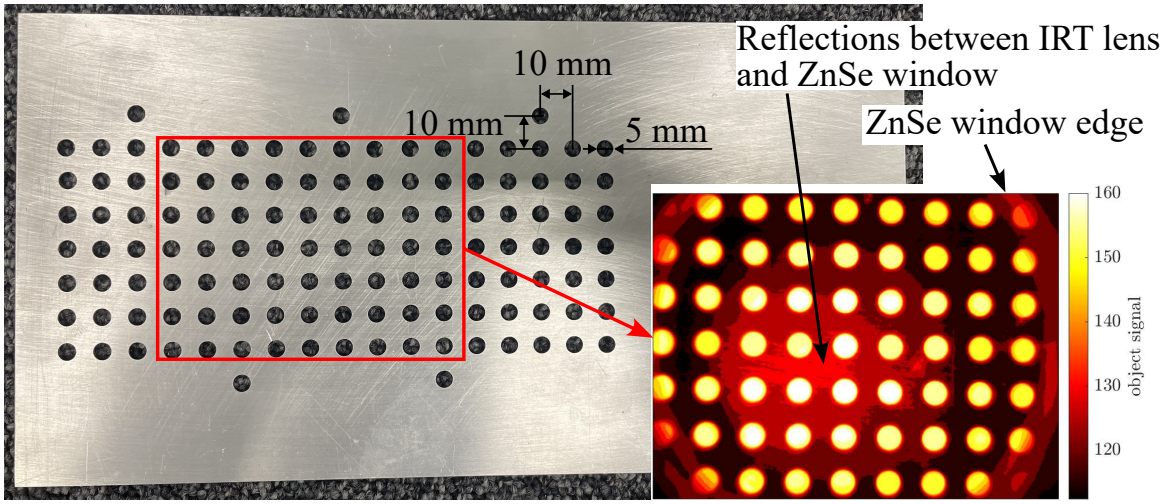


Figure 4.9: The steel target used in the experiments with an inset showing its raw IRT image.

to facility access limitations, the system operated in a backscatter configuration, where the receiving optics are integrated into the same assembly as the transmitting optics. Scattered light was collected by a photomultiplier tube (PMT), and a signal-to-noise ratio (SNR) filter was applied by the processor to minimize background noise. An overview of the optical setup is illustrated in Fig. 4.10.

In order to achieve the required velocity range, the two laser beam pairs are orientated at 45° to the flow direction. This arrangement ensures that the measured velocity components are roughly equal in magnitude and considerably lower than the total velocity vector (Fig. 4.11a). The mean time-averaged streamwise and wall-normal velocity components were subsequently reconstructed from the measured vector data. To avoid beam clipping near the surface, the LDA probe volume was tilted upward by 3° from the horizontal traverse plane, allowing the measurement volume to reach the wall (see Fig. 4.10).

Tracer particles were generated using two Dantec Flow Tracker seeding generators, which produce Di-Ethyl-Hexyl-Sebacate (DEHS) droplets with an average diameter of 1.9 μm. The seeding is introduced through two rakes located in the settling chamber upstream of the wind tunnel nozzle. The particle response time, estimated as $t_p = 21.3\,\mu$s, is based on DEHS fluid properties. The characteristic flow time scale, using turbulent boundary layer scaling, is $t_f \simeq \delta_{99.5}/U_\infty = 3 \times 10^{-3}/577 = 5.2\,\mu$s, where $\delta_{99.5}$ is the estimated boundary layer thickness and U_∞ is the freestream velocity. This yields a Stokes number of $St_k = t_p/t_f = 4.15$. The finite response time of the DEHS seeding particles should therefore be considered when interpreting the LDA measurements. The relatively high value of St_k indicates that the particles may not follow rapid changes in the gas velocity instantaneously, particularly across shocks

or in regions with strong acceleration or deceleration. Therefore, the measured velocity represents the seeded-particle velocity and may include a finite particle-lag error relative to the gas velocity. In the present experiment, however, the LDA measurements were performed downstream of the leading-edge shock and focused on mean boundary-layer velocity profiles rather than on the instantaneous shock-crossing process or high-frequency turbulent fluctuations. The leading-edge shock was weak for the present Mach 2.75 flat-plate configuration, and the particles were expected to relax towards the local gas velocity before the measurement region. The measurement region also did not involve strong flow unsteadiness, strong pressure gradients, or flow reversal. Consequently, the finite particle response is considered a source of measurement uncertainty, but it is not expected to change the main conclusions regarding the mean spanwise modulation of the boundary-layer velocity. Particle survival through the leading-edge shock was also considered. The estimated post-shock static temperature was approximately 123 K, which is far below the temperature required for significant evaporation of DEHS droplets. Therefore, particle evaporation through the shock is not expected to be significant. Similar DEHS seeding particles have also been used in previous supersonic LDA/PIV measurements under comparable flow conditions [94]. This supports the suitability of the seeding approach for the present measurements.

Spatial calibration of the measurement location was performed using a laser-cut plastic alignment plate featuring 0.2 mm reference holes (Fig. 4.11b). This plate is attached directly to the test article, enabling precise alignment of the LDA measurement volume through the reference point.

4.3.3 Test Matrix for IRT and LDA Campaign

To quantify both the realised wall-temperature field and the boundary-layer response to spanwise thermal forcing, the present chapter integrated two complementary datasets acquired in the Imperial College Supersonic Wind Tunnel: (i) surface temperature measurements using IRT and (ii) boundary-layer velocity measurements using LDA. The overall campaign comprises an unheated baseline and four heated cases (Cases 1–4), defined by the nominal initial plate temperature T_i (Table 4.4), with $T_i = 323$, 373, 423, and 523 K for Cases 1–4, respectively. While the nominal T_i setpoints are common to both measurement modalities, the achieved initial temperatures differed slightly between IRT and LDA due to operational variability in the preheating protocol; for the IRT runs, the initial-condition

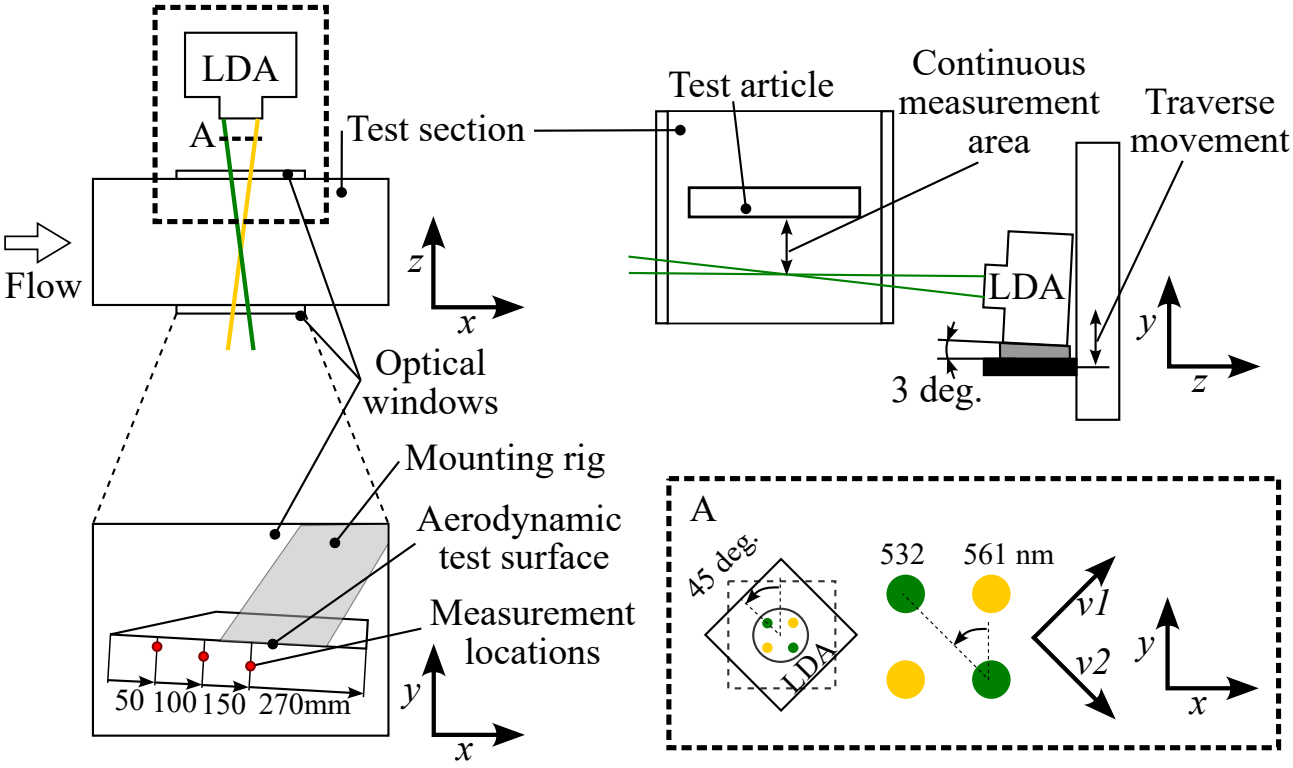
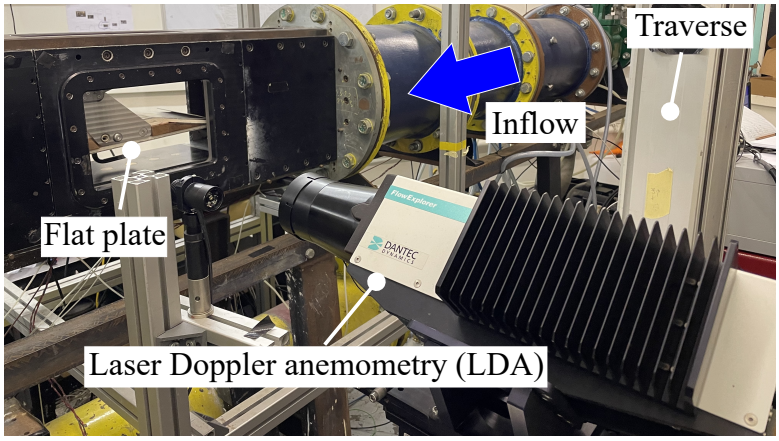


Figure 4.10: Schematic diagram of the LDA measurement system.

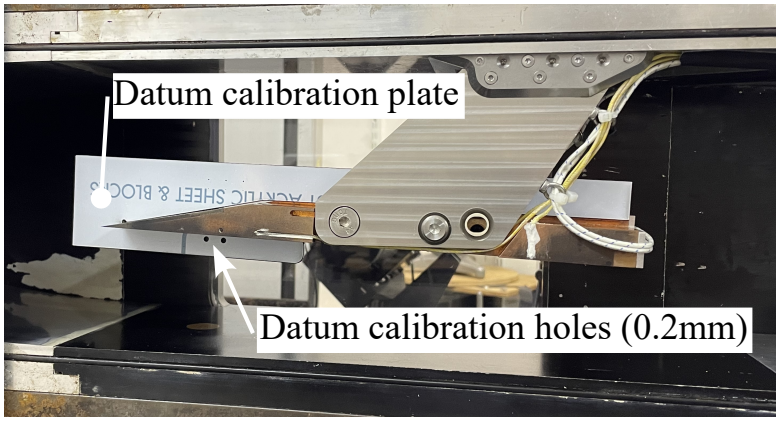
achievement and the associated surface-temperature distributions are assessed in Sec. 4.5.1, whereas for the LDA runs this is quantified via the achieved plate-averaged initial temperature $\overline{T}_i$ (Table 4.5).

The IRT campaign was conducted for heated Cases 1–3 and provided the surface temperature distributions required to characterise the imposed spanwise thermal non-uniformity and its evolution following tunnel start. No unheated baseline was included in the IRT campaign, and Case 4 was not tested with IRT.

The LDA campaign included an unheated baseline and heated Cases 1–4. The baseline condition provides an effectively isothermal reference: the initial model temperature is approximately 283 K, which is 8 K above the recovery temperature ($T_r = 275\,\mathrm{K}$). Although this offset introduces a small temperature difference between the insulator and conductor materials, the resulting spanwise variation remains within $\mathcal{O}(10\,\mathrm{K})$ and is therefore treated as negligible for defining the baseline. For heated cases (Cases 1–4), LDA velocity profiles were acquired at three streamwise locations, $x = 50$, 100, and 150 mm for Cases 1–3, with Case 4 limited to $x = 50$ and 100 mm due to technical constraints (Table 4.5). At each streamwise station, profiles were measured at multiple spanwise locations defined by $\lambda = z/\Lambda_{\mathrm{span}}$, where the spanwise wavelength is $\Lambda_{\mathrm{span}} = 15\,\mathrm{mm}$; the insulator centreline corresponds



(a) The LDA measurement setup



(b) The datum calibration plate inserted into the test article

Figure 4.11: Photographs of the LDA measurement setup and the datum calibration plate inserted into the test article.

to $\lambda = 0$ and the conductor centreline to $\lambda = 1$. Under the unheated baseline, measurements were performed at $\lambda = 0$ and 1, whereas under heated conditions measurements were obtained at $\lambda = 0$, 1/3, 2/3, and 1. This yielded 6 test points for the baseline (2 spanwise × 3 streamwise) and 12 test points for each of Cases 1–3 (4 spanwise × 3 streamwise); Case 4 comprises 8 test points (4 spanwise × 2 streamwise). For the LDA dataset, the achieved plate-averaged initial temperature $\overline{T}_i$ was recorded using thermocouples and was used as an input to the thermal model for predicting the corresponding surface temperature distributions. The uncertainty in $\overline{T}_i$ for the LDA campaign is within ±1 % of the mean value across the plate and across repeated runs.

Table 4.4: Integrated case definition for IRT and LDA campaigns. Cases are defined by the nominal initial plate temperature T_i (target setpoint).

Case	Condition	Nominal T_i (K)	IRT	LDA
Baseline	Unheated / quasi-isothermal	Ambient	–	✓
1	Spanwise thermal non-uniformity	323	✓	✓
2	Spanwise thermal non-uniformity	373	✓	✓
3	Spanwise thermal non-uniformity	423	✓	✓
4	Spanwise thermal non-uniformity	523	–	✓

Table 4.5: LDA test matrix and measurement locations.

Plate Type	Case No.	Nominal T_i (K)	Averaged $\overline{T}_i$ (K)	Streamwise loc. x (mm)	Spanwise loc. λ (-)
Unheated plate	Baseline	Ambient	-	50, 100, 150	0, 1
Heated plate	1	323	322.8	50, 100, 150	0, 1/3, 2/3, 1
Heated plate	2	373	372.4	50, 100, 150	0, 1/3, 2/3, 1
Heated plate	3	423	422.0	50, 100, 150	0, 1/3, 2/3, 1
Heated plate	4	523	521.4	50, 100	0, 1/3, 2/3, 1

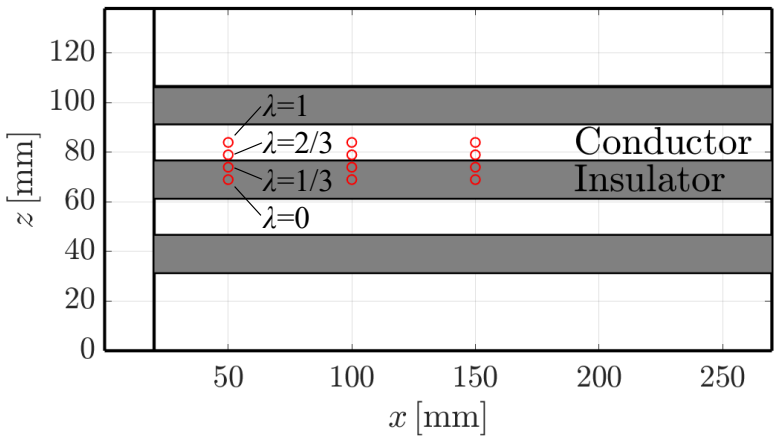


Figure 4.12: Schematic of LDA measurement locations (marked by red circles) on the flat plate geometry for Cases 1–3 at $x = 50$, 100, and 150 mm with $\lambda = 0, 1/3, 2/3$, and 1, and for Case 4 at $x = 50$ and 100 mm with $\lambda = 0, 1/3, 2/3$, and 1.

4.4 Thermal Modelling

4.4.1 Heat Transfer Coefficient and Thermal Model

The thermal model used to estimate the local surface temperature interacting with the boundary-layer convection follows the same methodology as described in the previous chapter (see 3.2.2). The overall modelling framework, and numerical implementation are consistent. The key difference in the present chapter is the treatment of the external convective boundary condition: whereas the previous chapter employed a laminar heat-transfer correlation for an idealised case, the wind-tunnel conditions considered here are representative of a turbulent boundary layer. Accordingly, a turbulent heat-transfer coefficient is adopted (see 3.2.2).

The Chilton–Colburn analogy [83] was utilised to relate the heat-transfer coefficient to the local Stanton number, St_x:

$$St_x = \frac{0.0296}{\sqrt[5]{Re_x}}\, Pr^{-2/3}, \tag{4.3}$$

where Re_x is the local Reynolds number and Pr is the Prandtl number. As in 3.2.2, reference conditions are used to compute the convection coefficient and are determined using the Meador–Smart method [95], which accounts for the thermal state in the near-wall region. Since the test article was mounted at an incidence angle of 3°, U_∞ was taken as the post-shock flow velocity (i.e. the boundary-layer edge velocity).

To reconstruct the time-dependent surface temperature distribution, transient heat conduction with imposed surface convection was solved using the MATLAB Partial Differential Equation (PDE) Toolbox, consistent with the approach in 3.2.2. The thermal domain was constructed from a 3D CAD model of the flat plate (Fig. 4.13a) and discretised using an unstructured tetrahedral mesh with a characteristic element size of 5 mm, refined to 2.5 mm near the aerodynamic surface (Fig. 4.13b). The resulting mesh comprised approximately 7.8×10^4 elements. A grid-independence study was performed to verify numerical accuracy; further mesh refinement produced negligible changes in the predicted surface temperature, confirming that the selected resolution is sufficient.

The geometry comprises three materials with dissimilar thermal properties: the leading edge is modelled as steel, the bulk substrate as copper, and the embedded strips as MACOR ceramic. The

material properties assigned to each region are summarised in Table 4.2. The cylindrical slots used for cartridge heaters in the physical model are simplified as rectangular voids of equivalent volume in the computational domain. This approximation facilitates mesh generation while preserving the local mass and overall thermal inertia of the assembly. The model surface was coated with a thin thermal paint layer to provide a uniform and high-emissivity surface for infrared thermography. The coating thickness was approximately $20\,\mu$m, and the surface was finished using #2000 sanding paper. Owing to the small thickness of the coating relative to the millimetre-scale substrate, its influence on the structural stiffness or compliance of the model wall is negligible. The main possible mechanical effect of the coating is therefore the introduction of surface roughness. This was assessed using the roughness Reynolds number,

$$k_s^+ = \frac{u_\tau k_s}{\nu_e}, \tag{4.4}$$

where k_s is the estimated roughness height, ν_e is the kinematic viscosity at the boundary-layer edge, and u_τ is the friction velocity, defined as

$$u_\tau = U_e\sqrt{\frac{C_f}{2}}. \tag{4.5}$$

Using an estimated roughness height of $k_s \approx 2\,\mu$m for the coated and polished surface, k_s^+ was approximately 2. Since this value is below the commonly used hydraulically smooth criterion of $k_s^+ < 5$, the coated surface is considered hydraulically smooth and is not expected to significantly alter the boundary-layer development through roughness effects. The thermal paint layer was not included as a separate solid layer in the heat-transfer model. Since detailed thermophysical properties of the coating were not available from the manufacturer, its influence was assessed using an order-of-magnitude estimate. The area-normalised thermal resistance of the coating can be estimated as

$$R_{th,c} = \frac{L_c}{\alpha_c}, \tag{4.6}$$

where L_c is the coating thickness and α_c is the thermal conductivity of the coating. Taking $L_c = 20\,\mu$m and a representative paint-like thermal conductivity range of $\alpha_c = 0.1{-}0.8$ W m^{-1}K^{-1} gives

$$R_{th,c} = 2.5\times10^{-5}{-}2.0\times10^{-4}\ \text{m}^2\text{K/W}. \tag{4.7}$$

The wall heat flux can be estimated from the Stanton number as

$$q'' = h(T_w - T_r), \qquad h = St_x \rho_e U_e c_p. \tag{4.8}$$

Using the estimated Stanton number for the present Mach 2.75 turbulent boundary-layer conditions gives a representative wall heat flux of $q'' = O(10^5)\,\mathrm{W/m^2}$. The corresponding temperature difference across the coating is therefore

$$\Delta T_c = q'' R_{th,c} = O(1{-}10)\,\mathrm{K}. \tag{4.9}$$

This temperature difference is small compared with the imposed wall-temperature level of 150−250°C and does not significantly alter the interpretation of the imposed surface-temperature distribution. The through-thickness thermal response time of the coating can also be estimated as

$$t_c \sim \frac{L_c^2}{k_c}, \tag{4.10}$$

where k_c is the thermal diffusivity of the coating. For a representative range of $k_c = 10^{-7}{-}10^{-6}\ \mathrm{m^2/s}$, this gives $t_c \approx 0.4{-}4$ ms. This is much shorter than the characteristic experimental and thermal-modelling time scales. The temperature difference across the coating and its thermal inertia are therefore small compared with the thermal response of the substrate, and the coating was neglected in the solid thermal model.

Convective boundary conditions were applied to the aerodynamic test surface and the backside surface, governed by the local heat-transfer coefficient derived via Eq. 3.8 (and converted to h using the reference properties). All remaining external surfaces are treated as adiabatic. The initial temperature distribution is prescribed from thermocouple measurements recorded immediately prior to each wind-tunnel run. A fixed time step of 0.1 s is employed, and the simulation is advanced for 15 s and 23 s for IRT and LDA measurements, respectively, to match the experimental timeline.

4.4.2 Freestream Characterisation for Thermal Boundary Conditions

To compute the time-varying convective heat transfer coefficient h (Eq. 3.8), the thermal model requires transient freestream flow properties, namely density, velocity, recovery temperature, and

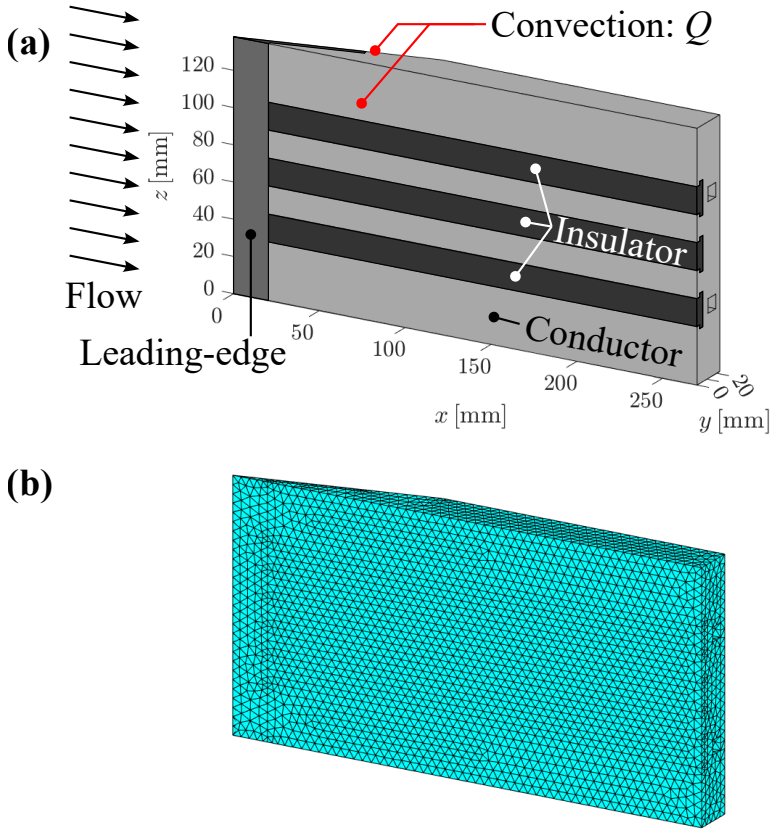


Figure 4.13: (a) The thermal model geometry showing the alternating conductor-insulator strips and the convective heat flux boundary condition (Q) applied to the aerodynamic test and back surfaces. (b) The unstructured mesh for the thermal modeling.

viscosity. Although these quantities are approximately constant during the steady-state portion of each run, they vary significantly during wind-tunnel start-up and therefore must be characterised in a time-resolved manner to provide synchronised thermal boundary conditions.

To capture this transient behaviour, wall pressure data were recorded using pressure taps synchronised with the wind-tunnel operation. Figure 4.14 presents representative wind-tunnel log data for Case 1, together with an ensemble-averaged profile over time. The test-section Mach number was derived from an upstream wall pressure tap using isentropic relations. In addition, the settling-chamber stagnation pressure P_0 was recorded throughout the run. For the LDA campaign, the stagnation temperature T_0 was also acquired. Data were sampled at a temporal resolution of 0.1 s.

Once the isentropic Mach number was estimated, freestream thermodynamic properties were determined using isentropic relations. The boundary-layer edge velocity, U_∞, was then computed by correcting the freestream for the oblique shock formed upstream of the test article due to the 3° incidence angle. The recovery temperature T_r was subsequently evaluated assuming calorically perfect gas behaviour with a constant Prandtl number.

As shown in Fig. 4.14, during the tunnel start-up phase the total pressure initially overshoots the target value (by approximately 8 %) due to the response characteristics of the PID control valve, before settling to a stable value approximately 5 s after flow initiation. Thereafter, steady-state conditions at Mach 2.75 were maintained. The resulting time-resolved freestream properties, ensemble-averaged across repeated runs (three runs in the IRT campaign and twelve runs in the LDA campaign for Case 1), were used as inputs to the thermal model to provide synchronised, quasi-one-dimensional thermal boundary conditions and to accurately capture transient aerodynamic heat transfer during tunnel transients.

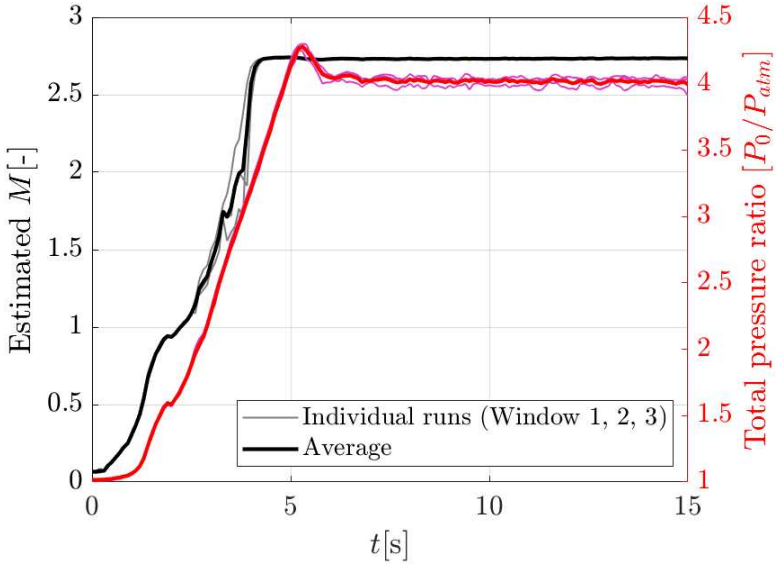


Figure 4.14: Time history of the isentropic Mach number for repeated runs (gray lines) and their ensemble average (black line) in Case 1.

4.5 Surface Temperature Characterisation

4.5.1 IRT Measurements

Initial Temperature of the Aerodynamic Test Surface

The study involved three primary test conditions, Cases 1, 2, and 3, with nominal target initial surface temperatures of 50, 100, and 150 °C, respectively, as summarised in Table 4.6. Due to the limited optical access of the observation window ($D = 70$ mm), multiple wind tunnel runs were conducted with the model positioned at different streamwise locations to construct the comprehensive surface temperature map. Specifically, the plate was moved 45 mm upstream from its Window 1 measurement position to acquire data for Window 2. For Window 3 measurements (where applicable), the model was shifted an additional 45 mm upstream from the Window 2 position. Consequently, Cases 1 and 2 included temperature measurements across three observation windows, while Case 3 was limited to Windows 1 and 2 due to a failure in the model's mounting system during testing.

The surface temperature at $t = 0.1$ s post-initiation of the datalogging was defined as the initial surface temperature T_i. Figure 4.15 presents this T_i distribution for Case 2 as a representative example, rendered as a composite image from the individual measurements across the observation windows.

This composite image was generated by spatially arranging the individual IRT recordings and, in areas where measurement windows overlapped, trimming each adjacent recording at the centerline of the shared region before stitching them together. To preserve the full contrast of local temperature variations, the raw IRT data were presented directly without any filtering or smoothing. The measurement area in the streamwise direction (x) spanned approximately 20 to 180 mm for Cases 1 and 2, and 20 to 140 mm for Case 3. In the spanwise direction (y), measurements extended from 40 to 100 mm, covering three insulator (MACOR) strips, two conductor (copper) strips, and a portion of the leading edge.

A consistent experimental challenge was an unavoidable drop in the plate's surface temperature prior to the wind tunnel run. This occurs because the preparation for each test, which includes removing an insulating heat shield and securing the wind tunnel door, takes several minutes. Active reheating during this interval is avoided, as heating without the insulation board would induce localised hot spots and degrade the thermal uniformity of the initial condition. During this period, the insulator strips typically exhibit slightly lower temperatures than the conductor strips due to their lower thermal diffusivity. This thermal distinction is quantified in the inset of Fig. 4.15, which shows a pixel count histogram for Window 2 of Case 2. The histogram reveals two distinct temperature peaks: $T_{i,ins}$=359.7 K for the insulator material and $T_{i,cond}$=364.8 K for the conductor, resulting in a spanwise temperature difference ($\Delta T_{i,stp}$) of 5.1 K for this specific window. Across Windows 1 and 3 of Case 2, this $\Delta T_{i,stp}$ ranges between 2 and 5 K. The average spanwise temperature difference for Case 2, $\Delta\overline{T}_{i,stp}$, is 3.8 K. This difference corresponds to approximately 5 % of the intended temperature elevation of the plate above ambient laboratory conditions (i.e., 5 % of $T_t - T_{atm}$). The mean initial surface temperature for Case 2 is $\overline{T_i}$=362.1 K. This value represents a reduction from the target temperature, equivalent to 14 % of the intended temperature elevation ($T_t - T_{atm}$). Across all test cases, the measured initial surface temperatures show a consistent reduction of 12–14 % relative to this target elevation. Similarly, spanwise temperature differences between the conductor and insulator strips are consistently in the range of 5–6 % of the target elevation. These observations confirm that the initial thermal conditions are established with reasonable consistency across the different measurement windows and that similar temperature drop trends are present in all cases.

Table 4.6: Number of windows and initial surface temperature.

Case	Window No.	T_t (K)	T_i (K)	$T_{i,conductor}$ (K)	$T_{i,insulator}$ (K)	$\overline{T_i}$ (K)	$\frac{T_t-\overline{T_i}}{T_t-T_{atm}}$ (%)	$\Delta\overline{T}_{i,stp}$ (K)	$\frac{\Delta\overline{T}_{i,stp}}{T_t-T_{atm}}$ (%)
	1		319.5	320.5	319.0				
Case 1	2	323.2	319.4	320.3	318.6	319.5	12	1.6	5
	3		319.5	320.2	318.6				
	1		361.4	364.0	360.0				
Case 2	2	373.2	362.3	364.8	359.7	362.1	14	3.8	5
	3		362.6	362.2	359.9				
	1		404.2	409.1	401.9				
Case 3	2	423.2	405.1	409.2	400.1	404.6	14	7.7	6

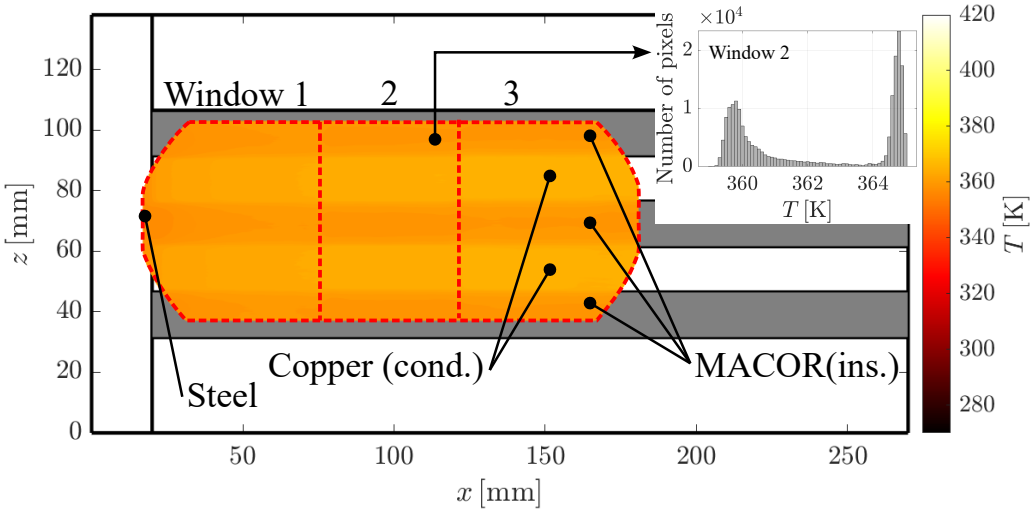


Figure 4.15: Initial surface temperature (T_i) distribution for Case 2 from the IRT measurement, overlaid on the test article outline. Inset: Pixel count histogram for Window 2 (Case 2) showing distinct temperature peaks for insulator (359.7 K) and conductor (364.8 K) regions.

The Aerodynamic Test Surface Temperature

Figure 4.16 presents the surface temperature distributions at the steady-state condition ($t = 15\,\text{s}$) for all cases. The experimental results are overlaid onto the thermal modeling predictions. A distinct temperature contrast between the different material strips is evident across the test article. The copper conductor strips consistently maintain an elevated temperature close to the initial pre-heated condition, while the MACOR insulator strips and the leading edge cool towards the aerodynamic recovery temperature. This result successfully demonstrates the efficacy of using a dissimilar materials approach for the passive control of local surface temperature. The thermal contrast becomes significantly more pronounced as the initial plate temperature increases from Case 1 through Case 3 (Fig. 4.16(b) and (c)). The numerical predictions accurately capture the key thermal phenomena

observed in the experiments. A strong correlation is evident, particularly for the copper conductor strips and the leading edge, where the predicted temperatures align closely with the IRT measurements. The model also accurately captures the sharp temperature gradients at the material interfaces, indicating a robust representation of the thermal junctions between the MACOR and copper. While minor discrepancies exist within the insulator regions (discussed in Sec. 4.5.2), the overall cooling trend and the magnitude of the temperatures are predicted quantitatively.

4.5.2 Discussion

Spanwise Temperature Distributions

Figure 4.17 presents the spanwise surface temperature distributions at $t = 15\,\mathrm{s}$ for each case, extracted at streamwise locations of $x = 15$, 50, and 100 mm. The temperature is normalised by the post-shock freestream temperature T_∞ to yield the non-dimensional temperature, $\Theta = T_w/T_\infty$. The primary goal of this comparison was to assess the model's ability to predict the sharp thermal contrast, which is the key feature of this passive thermal control method.

Overall, the thermal model demonstrated qualitative agreement with the experimental spanwise profiles, successfully capturing the characteristic 'step-like' structure of the temperature field. At the established downstream locations ($x = 50$ and 100 mm), a distinct thermal contrast was achieved between the strips, clearly distinguishing the conducting and insulating regions. Within the leading edge region ($0 < x < 20\,\mathrm{mm}$) at $x = 15\,\mathrm{mm}$, both the experiment and model showed how lateral conduction created a mild distortion in the profile, with temperatures slightly elevated in regions adjacent to the conductors. Further downstream, the distinction between the materials becomes more defined. The model accurately reproduced the uniform spanwise temperature across the copper conductor strips, a direct result of the material's high thermal diffusivity that eradicates local gradients. Minor localised temperature peaks were observed near the corners of the conductor strips at $x = 100\,\mathrm{mm}$ (see Fig. 4.17(b)); these are likely attributable to localised edge effects at the material interface not fully resolved by the thermal model. In contrast, the MACOR insulator regions exhibited a more complex, concave temperature profile, which is also well-replicated by the model in terms of its characteristic shape. However, while the profile shape is quantitatively matched, a consistent underprediction of the insulator's absolute temperature magnitude was observed. For example, in Case 2, the measured

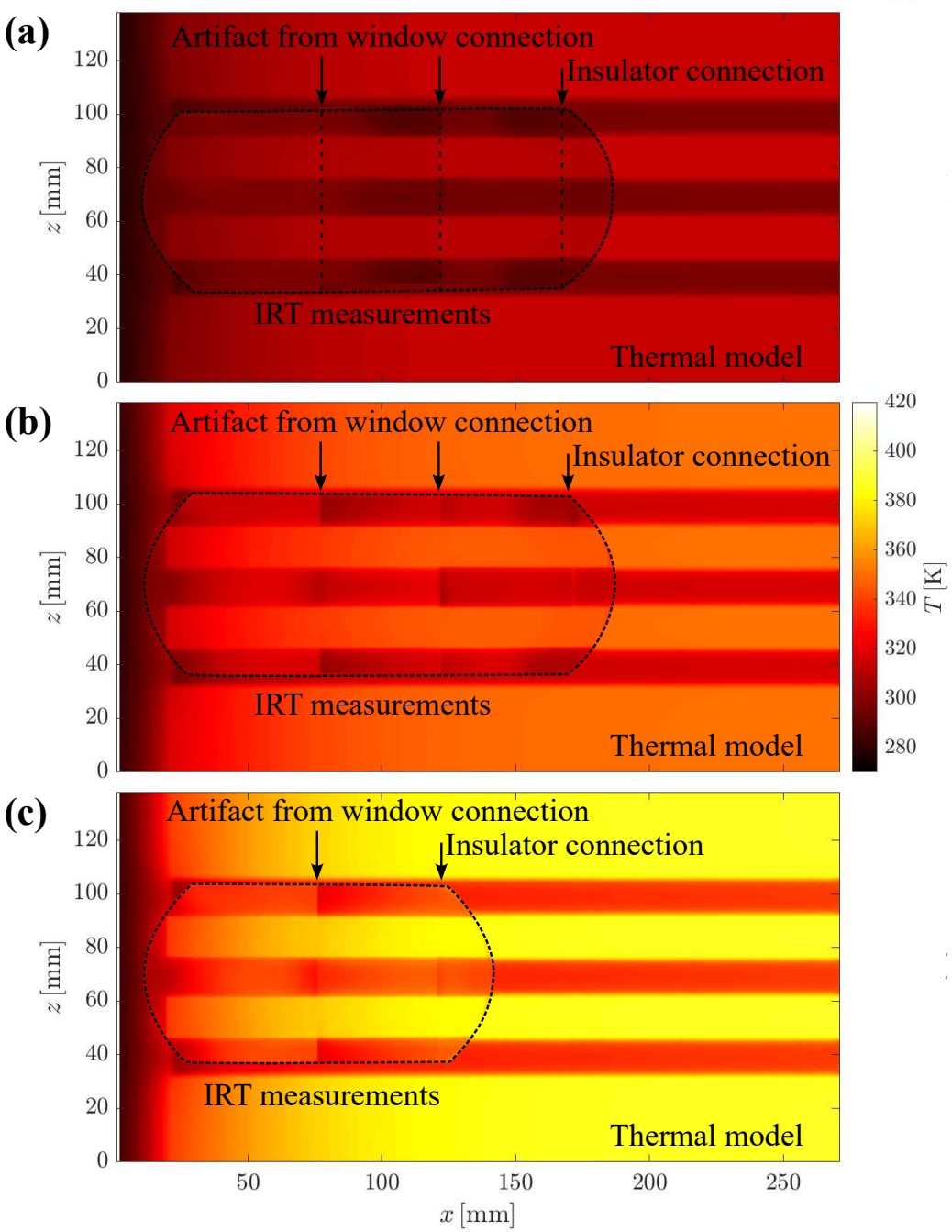


Figure 4.16: Overlay of experimental results onto the thermal modelling predictions of temperature distributions at 15 s for (a) Case 1, (b) Case 2, and (c) Case 3.

Θ is higher than the model's prediction by approximately 0.1 at $x = 50\,\text{mm}$ (2.7 measured vs. 2.6 predicted) and by 0.05 at $x = 100\,\text{mm}$. This deviation is more pronounced in Case 3, where the measured temperature is higher than the prediction by 0.18 at $x = 50\,\text{mm}$ and 0.11 at $x = 100\,\text{mm}$. This discrepancy is further analysed in Sec. 4.5.2 by correlating the transient temperature data with the wind tunnel start-up phase captured by Schlieren visualisation.

Despite the quantitative offset in the insulator regions, the model demonstrates a robust capability to predict the fundamental features of the spanwise thermal profile. It accurately predicts the magnitude and uniformity of the conductor temperatures and captures the fundamental shape of the insulator profiles. Most importantly, it validates the model's ability to reliably predict the sharp thermal gradients and overall temperature contrast at the material boundaries, which is a critical performance metric for this system.

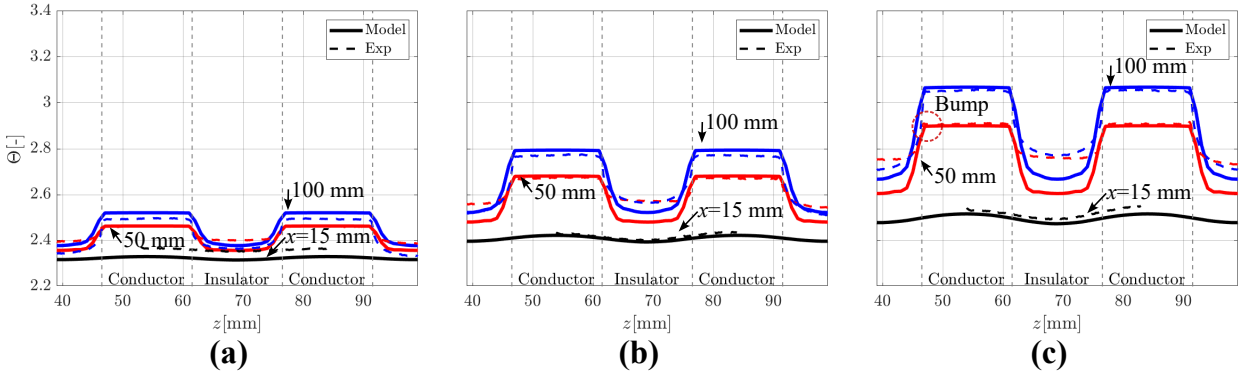


Figure 4.17: Spanwise normalized temperature profiles at $t = 15\,\text{s}$ at streamwise locations $x = 15$ (black), 50 (red), and 100 mm (blue). Experimental results (dashed lines) are compared with thermal modelling predictions (solid lines) for (a) Case 1, (b) Case 2, and (c) Case 3

Streamwise Temperature Distributions

The streamwise surface temperature profiles along the centerline of the central insulator strip and a conductor strip ($y = 54\,\text{mm}$) are presented in Fig. 4.18 for all three cases at $t = 15\,\text{s}$. For the copper conductor strips, the model exhibits excellent quantitative agreement with the experimental data across all cases. The profiles are characterised by a slight temperature dip at the leading edge followed by a nearly uniform temperature distribution downstream. This leading-edge cooling ($x < 20\,\text{mm}$) is primarily attributed to the high local Stanton number St_x in the region of low local Reynolds number Re_x, which results in a significantly elevated convective heat transfer rate. Downstream, the flat

temperature profile, accurately captured by the model, reflects the high thermal diffusivity of copper, which effectively resists convective cooling and smooths spatial gradients, even under complex flow conditions.

In contrast, while the model successfully reproduces the general cooling trend of the MACOR insulator strips, a quantitative discrepancy is apparent. For Case 1, the agreement is close; however, for Cases 2 and 3, the model consistently overpredicts the rate of cooling. Furthermore, the experimental profiles exhibit distinct, localized temperature fluctuations that are absent from the smooth model predictions. These sharp drops align with the physical gaps between the five separate insulator pieces (refer to Fig. 4.16). These gaps likely disturb the turbulent boundary layer, locally enhancing the convective heat transfer rate. The low thermal diffusivity of MACOR makes its surface temperature highly sensitive to these local disturbances, effectively imprinting a thermal signature of the assembly geometry.

The origin of the broader discrepancy in the cooling rate (the offset between model and experiment) likely lies in the fundamental assumption used to define the model's freestream conditions. The thermal model incorporates a time-varying freestream condition calculated from pressure data measured at the nozzle exit every 0.1 s, assuming these conditions uniformly describe the flow over the test article. However, the Schlieren visualisations presented in Fig. 4.19 reveal that this assumption is invalid during the highly dynamic wind tunnel start-up. The images show that the actual flow field is dominated by unsteady, structured shock waves interacting directly with the plate's surface. This complex aerodynamic environment dictates the true convective heating history, which is not captured by the nozzle-exit pressure data. The low thermal diffusivity of the MACOR makes it extremely sensitive to this actual heating history, effectively imprinting a thermal signature from the start-up phase that persists into the steady-state measurement period. This likely explains the discrepancy between the measured temperature and the model's prediction. Besides, the sharp, localised temperature drops seen experimentally also align with the physical gaps between the five separate insulator pieces. Ultimately, the model's limitation is its inability to account for the complex, localised flow structures that differ significantly from the simplified freestream conditions derived from upstream measurements.

A key practical insight also emerges from these streamwise profiles. Figure 4.18 clearly shows that the significant temperature difference between the conductor and insulator strips is established almost

immediately downstream of the leading edge and is then robustly sustained along the test article's length. This indicates that the desired thermal contrast for flow control applications does not require a long development section, providing valuable guidance for the placement of such material strips in future hypersonic experiment designs.

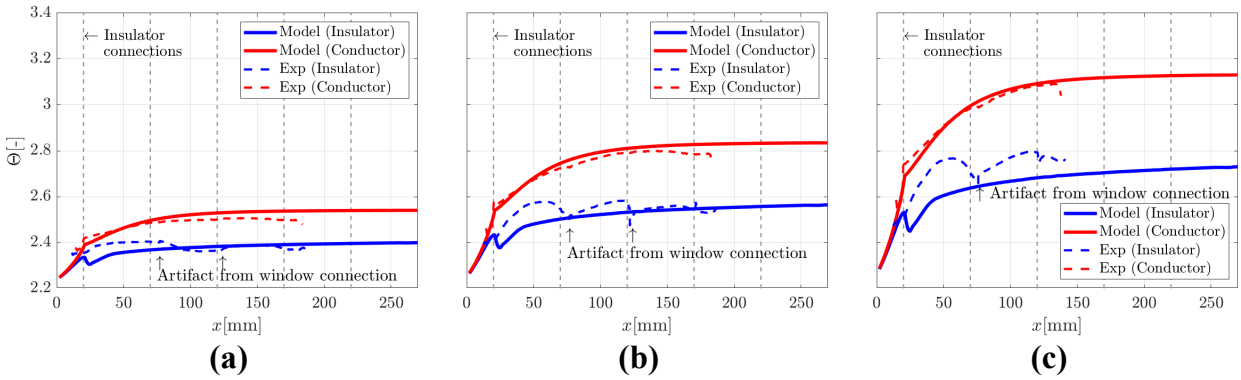


Figure 4.18: Streamwise normalized temperature profiles at $t = 15\,\mathrm{s}$ for (a) Case 1, (b) Case 2, and (c) Case 3. Thermal model predictions (solid lines) are compared with experimental results (dashed lines) for the center insulator (blue) and conductor (red).

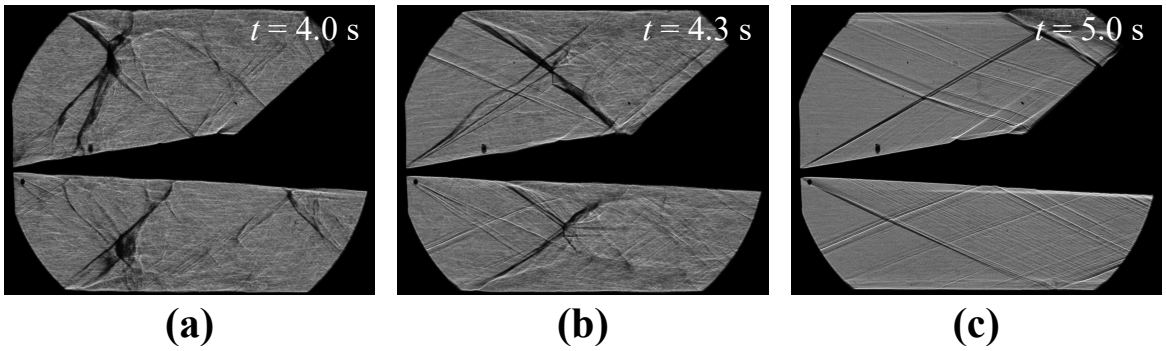


Figure 4.19: Schlieren visualization of the flow field during wind tunnel start-up. The images show the evolution of shock structures at (a) $t = 4.0\,\mathrm{s}$ and (b) $t = 4.3\,\mathrm{s}$ during the initial acceleration phase, and (c) the final steady-state flow at $t = 5.0\,\mathrm{s}$.

Transient Temperature Evolution

The transient temperature evolution at a downstream location of $x = 100\,\mathrm{mm}$ is presented in Fig. 4.20 for all three cases, directly comparing the experimental IRT measurements with the thermal modelling predictions. This temporal analysis provides critical insight into the system's response during the wind tunnel start-up phase and the subsequent approach to the steady state. Across all cases, a consistent trend is observed in the initial five seconds. The copper conductor cools gradually, whereas the MACOR insulator exhibits a much sharper and more immediate drop in temperature. This initial

phase is punctuated by a distinct and sudden temperature decrease in the experimental insulator data around $t = 4\,\text{s}$. This event corresponds precisely with a documented overshoot in the wind tunnel's PID-controlled pressure ramp (Fig. 4.14), which temporarily enhances convective cooling and disproportionately affects the thermally-sensitive MACOR surface.

The thermal model, which incorporates the measured pressure data as a boundary condition, successfully captures the timing and qualitative effect of this pressure spike. However, consistent with the analysis in the previous section, the model overpredicts the overall cooling rate for the insulator during this 0-5 second start-up period. This confirms the hypothesis that the simplified freestream conditions in the model do not fully account for the complex, unsteady shock phenomena that dictate the true convective environment during start-up. Beyond $t = 5\,\text{s}$, as the wind tunnel flow stabilises, the system transitions to the steady state. In this phase, the model and experimental data show excellent agreement. Both datasets show the conductor maintaining a stable temperature due to copper's high thermal inertia, while the insulator's cooling rate slows considerably as it asymptotically approaches the recovery temperature. The quantitative match in the cooling rates for both strips after the start-up phase is particularly notable. It demonstrates that the model accurately captures the fundamental heat transfer physics on the test surface once a steady aerodynamic state is achieved, reinforcing that the observed temperature offset on the insulator is a thermal artifact imprinted during the initial, complex transient phase.

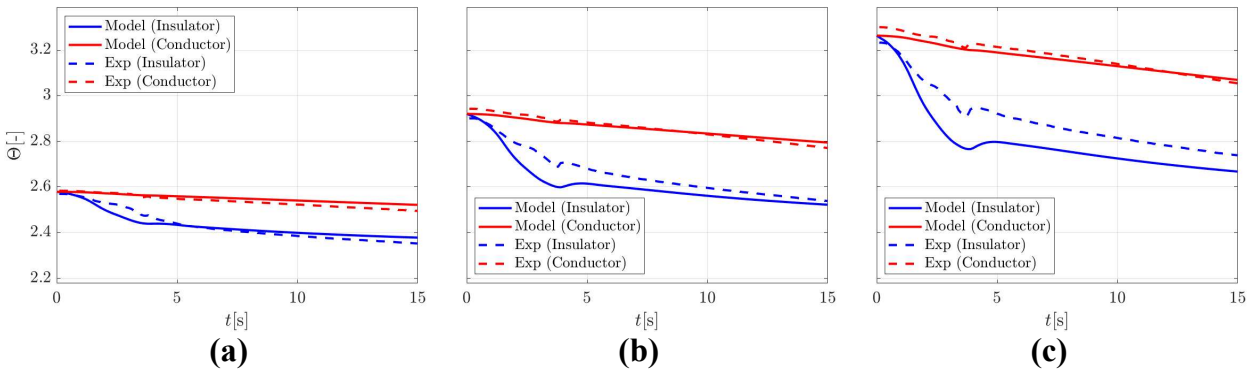


Figure 4.20: Transient temperature evolution at $x = 100\,\text{mm}$ during wind tunnel operation for (a) Case 1, (b) Case 2, and (c) Case 3. Comparison between experimental results (dashed lines) and thermal modelling predictions (solid lines) for the insulator and conductor.

Characterisation of the Temperature Difference with Initial Temperature

Figure 4.21 presents the normalised surface temperature profiles for both the insulator and conductor materials at $x = 100\,\text{mm}$ and $t = 15\,\text{s}$, across the range of initial model temperatures investigated. The thermal model simulations cover a broad range of nondimensional initial temperatures, Θ_i, from 1.8 to 4.2 (corresponding to absolute temperatures from 123 to 573 K), while the experimental cases span Θ_i=2.6 to 3.3 (Cases 1–3). The plot demonstrates how the thermal model successfully captures the underlying physics of surface temperature evolution. The linear decrease in normalised surface temperature for both materials as Θ approaches unity, i.e., as the initial model temperature approaches the recovery temperature T_r. This linearity highlights that the final surface temperature difference directly scales with the initial thermal offset relative to T_r. The results reinforce the principle that the surface temperature difference is primarily driven by the thermal contrast between the wall and the recovery temperature: when the initial temperature exceeds T_r, the surface cools, and conversely, when it is below T_r, the boundary layer heats the surface. This behaviour illustrates the importance of the recovery temperature in dictating the direction and magnitude of heat transfer to the surface. Furthermore, this parameter study is crucial as the magnitude of the surface temperature difference significantly impacts the generation and characteristics of velocity streaks within the boundary layer. For experimental control over streak intensity—for instance, to achieve greater streak prominence—it is necessary to either maximise the relative difference between the initial temperature and the recovery temperature, or to increase the convective heat transfer coefficient, such as under high-enthalpy flow conditions.

4.6 Boundary-Layer Characterisation

4.6.1 Time-Resolved Boundary Layer Measurement Strategy

Transient Surface-Temperature Response and Implications for LDA Measurements

This subsection synthesised the thermally driven surface forcing into practical constraints for the LDA campaign. The spatial structure of the imposed thermal pattern for Cases 1–3 has been established using IRT in the previous section; here, the focus is on (i) confirming the time required to reach a

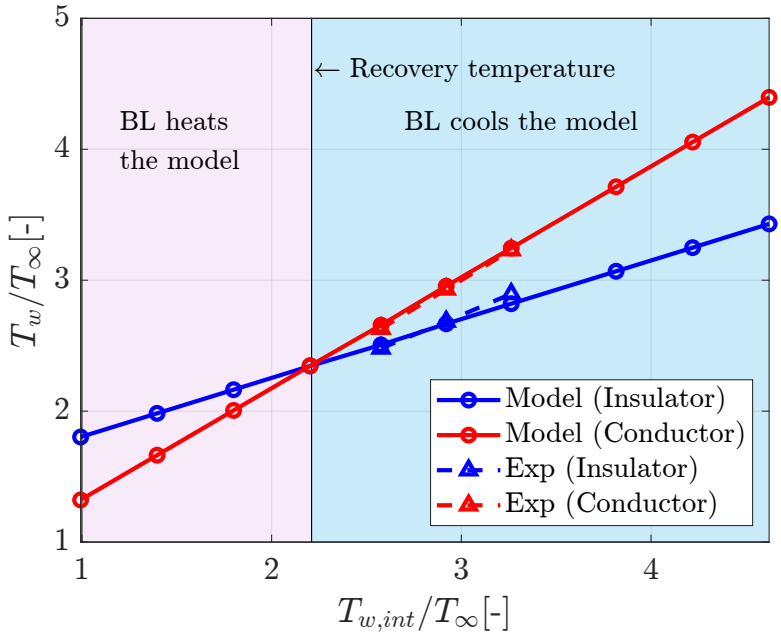


Figure 4.21: Normalised temperature profiles of the insulator and conductor at $x = 100\,\text{mm}$ at $t = 15\,\text{s}$ comparing the thermal model and the experimental results across different initial temperatures of the test article.

quasi-steady thermal forcing after tunnel start-up and (ii) quantifying the forcing magnitude at the LDA measurement stations. In particular, Case 4 (LDA-only) was considered as an LDA measurement case since the highest T_i can generate the largest conductor–insulator temperature difference, following the trend established in Sec. 4.5.1 due to increasing the difference between T_i and T_r. Thus, Case 4 was expected to yield the highest forcing magnitude and temporal establishment, therefore, Case 4 was central to designing the LDA measurement strategy.

To understand Case 4, the surface temperature field was defined using the thermal model. Figure 4.22 shows the predicted surface temperature distribution at $t = 20\,\text{s}$, demonstrating that the spanwise hot–cold pattern associated with the conductor/insulator arrangement was maintained at the elevated pre-heating level. The LDA measurement locations were organised using the non-dimensional spanwise coordinate $\lambda = z/\Lambda_{\text{span}}$, where $\Lambda_{\text{span}} = 15\,\text{mm}$. The insulator centreline corresponds to $\lambda = 0$, while the conductor centreline is at $\lambda = 1$. Since these centrelines are expected to achieve (approximately) the minimum and maximum surface temperatures within one spanwise period, they provide the most representative locations for assessing the boundary-layer response to thermal forcing. Accordingly, LDA sampling was prioritised along these centrelines, with additional intermediate locations ($\lambda = 1/3$ and $2/3$) included to capture the spanwise gradient between the extrema. To quantify streamwise

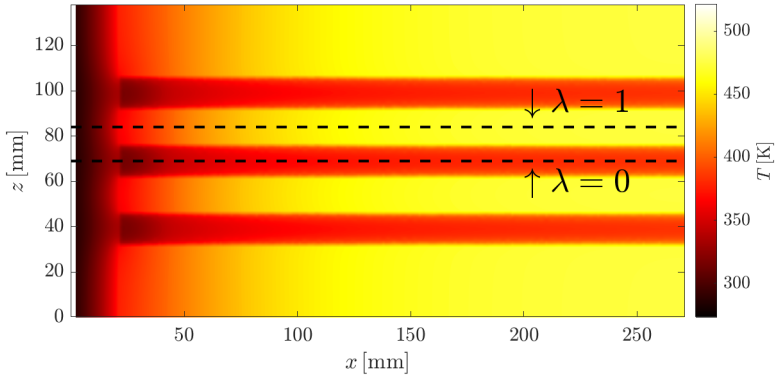


Figure 4.22: Thermal modeling predictions of the surface temperature distributions at $t = 20\,\mathrm{s}$ for Case 4

evolution of the response, measurements are planned at $x = 50$, 100, and 150 mm, corresponding to the streamwise stations used throughout the LDA campaign (with Case 4 limited to $x = 50$ and 100 mm due to technical constraints).

The temporal establishment of the thermal forcing was assessed using the thermal model and thermocouple time histories. Figure 4.23 shows the transient evolution at the conductor surface temperature at the streamwise stations during wind-tunnel operation for Case 4. The most rapid temperature changes occurred during the initial start-up transient, after which the evolution became gradual as the flow stabilised. Consistent with the wind-tunnel start-up behaviour discussed in Sec. 4.5.2, the first $\sim 5\,\mathrm{s}$ were therefore treated as a transient interval. In the subsequent boundary-layer analysis, LDA statistics were evaluated using data acquired after $t = 5\,\mathrm{s}$ to avoid contamination by start-up transients and to ensure that the thermal boundary condition is quasi-steady.

Finally, Fig. 4.24 summarises the forcing magnitude across the campaign by comparing the normalised surface temperature excess relative to the recovery temperature, $(\Theta_w - \Theta_r)$, for the conductor and insulator at $x = 100$ mm and $t = 20\,\mathrm{s}$. The results showed a clear trend: increasing the nominal initial temperature increased both the absolute surface temperature and the conductor–insulator temperature difference, thereby strengthening the spanwise thermal gradients available to perturb the boundary layer. In the present cases, at $t = 20\,\mathrm{s}$, the normalised surface temperature difference between the conductor and insulator (i.e., the dash lines on Fig. 4.22) reached approximately 0.2, 0.3, 0.4, and 0.7 for Cases 1 through 4, respectively. The resulting model-predicted surface temperature fields were used as the thermal boundary conditions for analysing the boundary-layer velocity profiles in the subsequent LDA results.

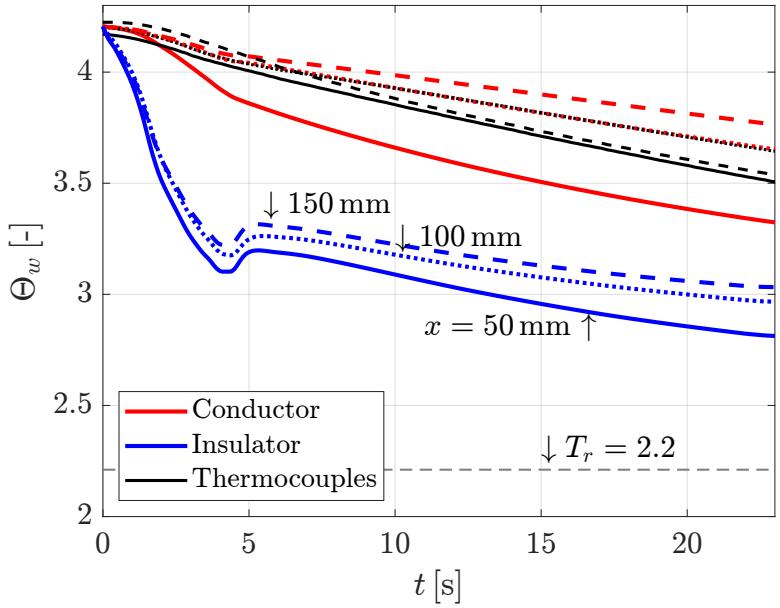


Figure 4.23: Transient evolution of the non-dimensional surface temperature ($\Theta_w = T_w/T_\infty$) on the copper conductor at $x = 50$, 100, 150 mm during wind tunnel operation for Case 4

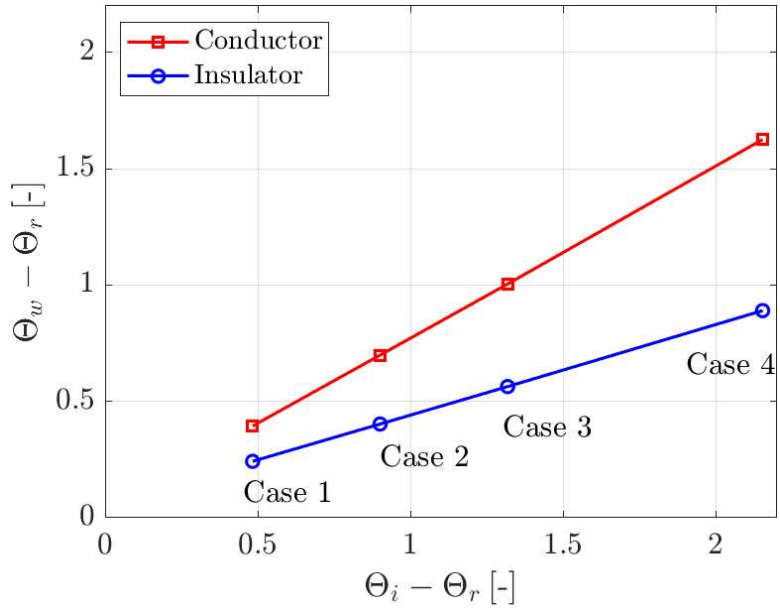


Figure 4.24: Normalized surface temperature excess relative to the recovery temperature ($\Theta_w - \Theta_r$) for the insulator and conductor at $x = 100$ mm and $t = 20$ s, plotted against the initial pre-heating temperature (Θ_i).

Traverse Movement for LDA Measurement

During the wind tunnel run, the aerodynamic test surface develops spatial temperature gradients following an initially uniform heating, as described in the previous section. As shown in Fig. 4.23, the transient surface temperatures at the centers of the conductor and insulator strips decrease over time. The conductor strip exhibits a gradual temperature decline, while the insulator strip experiences a sharp drop within the first 5 seconds, followed by a slower decrease. These evolving thermal conditions directly influence the development of the boundary layer.

Conventionally, in intermittent supersonic facilities, boundary layer profiles are acquired via a slow, point-by-point traverse. However, such an approach is unsuitable for the present experiment. Given the rapid thermal transients, a slow traverse would yield a distorted profile in which the near-wall and outer-layer measurements correspond to significantly different surface temperature states. To minimize this temporal aliasing, it is essential to capture the entire boundary layer velocity profile within a short time window. Consequently, a rapid traverse system was implemented to continuously scan the boundary layer during wind tunnel operation, enabling the rapid acquisition of full velocity profiles. The influence of the finite traverse time relative to the thermal and aerodynamic time scales was assessed in Section 4.6.2.

The LDA emitter system integrates receiver optics, mounted on a traverse mechanism that moves vertically relative to the test section. The traverse is precisely aligned in both horizontal and vertical directions. At each streamwise measurement location, the traverse moves in the vertical direction, with the travel range adjusted to cover approximately $1.5\delta_{99.5}$ (where $\delta_{99.5}$ is the estimated boundary layer thickness). This motion ensures accurate resolution of the velocity profile across the entire boundary layer and into the freestream.

Two distinct 3° inclinations are introduced in the experimental setup (Fig. 4.10). First, the test plate is mounted at a 3° incidence angle relative to the freestream, while the traverse moves vertically with respect to the test section coordinate system. This results in a slight offset in the wall-normal direction during vertical motion; however, the streamwise displacement is negligible, and the data are assumed to be taken at a constant x-location. Second, the LDA probe head is tilted upward by 3° in the y–z plane to prevent beam clipping when the measurement volume is close to the wall. This inclination results in a 3° deviation of the measurement plane from the true wall-normal direction. Accordingly,

the wall-normal velocity component is corrected using a trigonometric projection to account for this angular offset.

The traverse follows a triangular wave motion: it begins outside the boundary layer, descends to a target position approximately 0.3 mm below the wall surface (to ensure the wall is crossed), and then returns to its starting position. This cycle is repeated continuously throughout the wind tunnel run. The traverse motion was synchronized with the tunnel start-up, and the position history was recorded and time-stamped to allow the conversion of measurement time into spatial location. Figure 4.25 shows the wall-normal traverse position history for a representative test case. In this example, the traverse begins at 3 mm above the wall and descends to -0.3 mm. During the test, the traverse completes eight full cycles through the boundary layer. Data from the first two cycles are excluded from the analysis due to the transient flow effects during tunnel start-up. It is noted that slight mechanical vibrations occur when the traverse changes direction (i.e., at the top and bottom of each cycle). However, these vibrations are brief and occur only when the measurement volume is either in the freestream or virtually below the wall surface. As such, they do not affect the quality of the boundary layer velocity measurements.

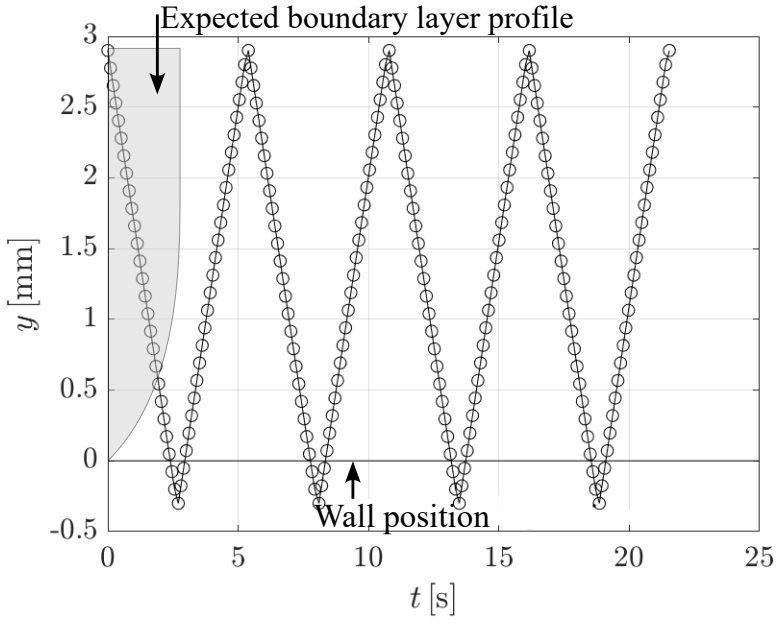


Figure 4.25: Traverse location history at T_i=250 K at $x = 100$ mm (Case 4).

Boundary Layer Profile Reconstruction

Velocity data were continuously recorded during the wind tunnel run while the LDA traverse system moved steadily across the boundary layer. Figure 4.26 shows the raw measured velocities of (a) v_1 and (b) v_2, corresponding to the two beam pairs, LDA 1 and LDA 2, respectively. The colour of the data points indicates the gate time, namely the transient measurement time for the seeding particle to pass through the measurement volume. During the initial wind tunnel start-up phase ($t < 5\,\mathrm{s}$), low velocities were observed. After start-up, significant noise scatter appeared in both v_1 and v_2. Due to low seeding density near the wall, the LDA system increased the sensitivity, which caused noise particularly in the velocity range of 50–200 m/s.

The boundary layer developed over a flat plate inclined at 3°, causing the velocity vector to incline toward the LDA 2 direction. As a result, v_2 exhibited higher velocity magnitudes than v_1 in the same measurement region (see Fig. 4.26). Velocity samples associated with low particle counts within a time-averaging window of $\Delta t = 0.05\,\mathrm{s}$ were classified as noise and excluded from the raw dataset. Further spurious data points were identified as outliers and removed based on the plausibility of their transit times. Specifically, only particles with transit times between 0.3 and 2.0 μs were retained. This range encompasses the expected instantaneous velocity range of the present measurements, including near-wall regions where velocity fluctuations associated with turbulence increase the spread of measured transit times. In addition, a particle-density criterion was applied to the velocity histograms. To identify and remove sparsely sampled velocity ranges associated with spurious detections, the velocity domain was discretized into uniform bins of width 10 m/s. This bin size is significantly larger than the measurement uncertainty of the LDA system and was selected to ensure robust statistical grouping without affecting the resolved velocity distribution. Bins containing fewer than three particle counts within each time window ($\Delta t = 0.05\,\mathrm{s}$) were excluded to ensure a minimum level of statistical convergence and to suppress isolated, non-physical samples arising from low seeding density, particularly in the near-wall region. This procedure removed sparsely populated velocity ranges associated with spurious detections. The combined filtering strategy effectively eliminated noise, particularly in low-velocity regions, while preserving physically meaningful instantaneous velocity samples throughout the boundary layer.

After this filtering step, v_1 and v_2 are time-averaged over the window of $\Delta t = 0.05\,\mathrm{s}$, corresponding

to a traverse displacement of approximately $\Delta y = 0.06\,\text{mm}$. This spatial resolution varies slightly depending on the initial y-position of the traverse, which is tied to the x-position of the measurement. The velocity is discontinuous near or immediately above the wall, primarily due to low seeding density, higher noise levels near the solid surface and scattering from the wall, where LDA measurements become less reliable. Figure 4.27a shows the velocity vector magnitude reconstructed from the two orthogonal LDA components. Each time-averaged window contains between 100 and 800 valid samples, depending on the measurement time/location, shown in Fig. 4.27b. LDA 1 generally detects fewer particles than LDA 2, which is likely due to a slight difference in system sensitivity or laser powers. The window-averaged streamwise and wall-normal components (U, V) were also reconstructed from the two channel means via a geometry-based linear transformation using the known measurement-axis angles. Uncertainty in the plate alignment angle introduces a systematic uncertainty in the reconstructed components, with a stronger influence on V than U. The measurement uncertainty of U was quantified using the standard error of the mean (SE). For $\Delta t = 0.05\,\text{s}$ averages, $SE_U = 0.81\,\text{m/s}$, corresponding to a 95 % confidence interval of approximately $U \pm 1.6\,\text{m/s}$. An additional systematic uncertainty arises from the plate alignment correction (nominally 3°), which primarily affects the reconstructed wall-normal component and is not central to the present analysis.

The reconstructed streamwise velocity is fitted to theoretical profiles. The outer layer is modelled using the compressible, non-adiabatic turbulent wake profile of Sun & Childs [96], adapted to include a van Driest compressibility transformation. For the fitting procedure, the best-fit values for the wall shear stress and the y-direction wall-offset parameters were obtained. The wall temperature was estimated from the thermal model output corresponding to the measurement time and location. The viscous sublayer is represented using the Musker fit [97]. A similar fitting approach for LDA-derived profiles has been employed by Titchener et al. [98] and Sabnis et al. [99]. The fitted compound boundary layer profile for Case 4 is shown in Fig. 4.28. The fitted profiles are subsequently used to compute the streak amplitude and characteristics boundary integral parameters. This approach mitigates errors associated with limited measurement resolution near the wall and with uncertainties in the wall location, thereby improving the accuracy of the boundary layer profile and then streak amplitude estimation. The boundary-layer properties are determined in their incompressible forms [99]. In this study, the processed LDA vector data typically contain approximately 30 measurement points within the boundary layer. The closest measurement point to the wall lies between $y^+ = 20$ and 80, depending

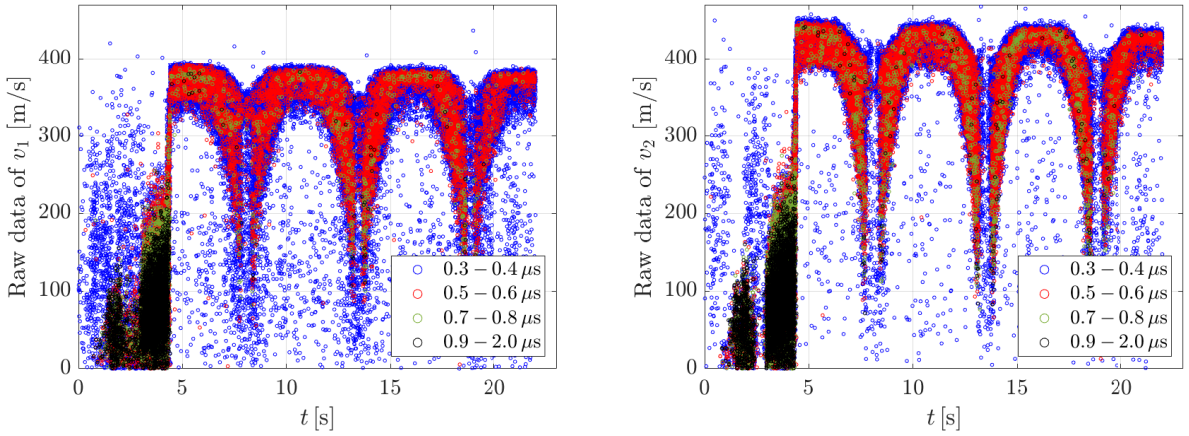
on the case, and the wall location uncertainty is $\Delta y_{\text{wall}}/\delta \approx 0.03$. It should be noted that the compound profile is used here as an empirical reconstruction method for sparse LDA velocity data, rather than as a fundamental compressible law-of-the-wall model. This approach follows previous supersonic boundary-layer studies in which compound fitting methods were used to reconstruct boundary-layer profiles and evaluate integral parameters from discrete measurements [98, 99]. In the present implementation, the Musker component provides a smooth near-wall closure in the region where reliable LDA measurements are unavailable, while the Sun and Childs formulation is used to represent the outer part of the turbulent boundary-layer profile. The nearest reliable LDA data point was typically located at $y \approx$ 0.25–0.30 mm from the corrected wall position for the heated streak-amplitude cases, corresponding to $y/\delta_{99.5} \approx 0.12$–$0.15$ and $y^+ \approx 40$–50, depending on the fitted profile. Across the complete dataset, the closest measurement point varies within approximately $y^+ = 20$–80. Therefore, the viscous sublayer and most of the canonical buffer layer are not directly resolved. Quantities derived below the first reliable measurement location should consequently be interpreted as reconstructed estimates. Given these constraints, the estimated error in the integral parameters can reach 20 % for an equilibrium turbulent boundary layer [98].

Figure 4.29 shows the reconstructed wall-normal velocity profile, V, referenced to the wall using the same wall-offset correction adopted in Fig. 4.28. The wall-normal component is of order 10 m/s, corresponding to $\approx 1.7\,\%$ of the freestream velocity magnitude. Although V can be obtained from the two-component LDA measurements, the present analysis focuses on the streamwise component U; therefore, V is not examined further.

4.6.2 LDA Measurements

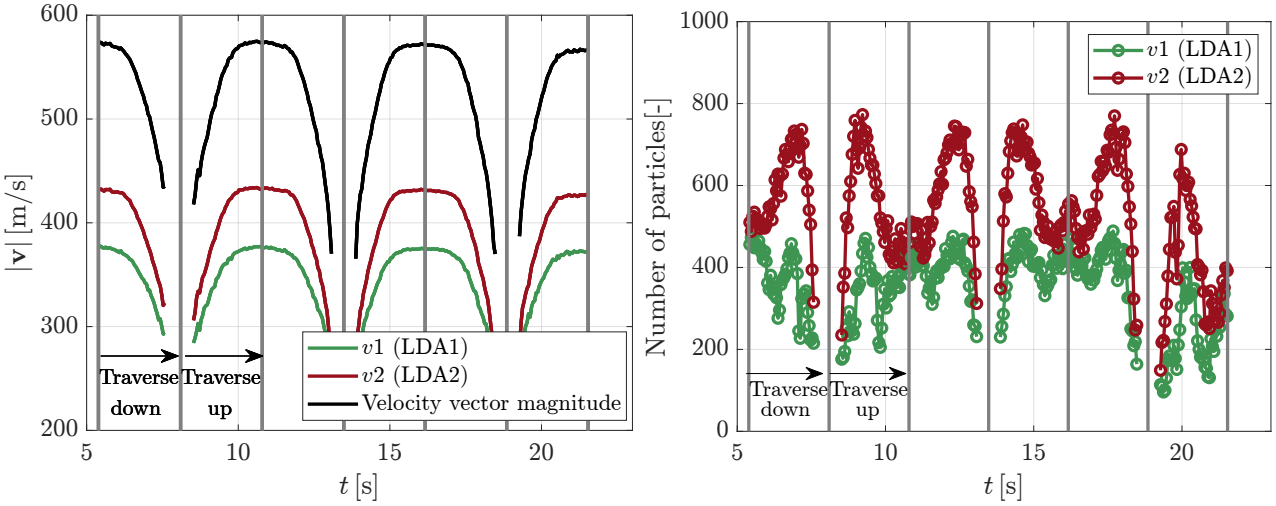
Baseline Boundary Layer Profile

The baseline configuration was the unheated flat plate with a 3° incidence to the freestream. Schlieren visualisation, illustrated in Fig. 4.19(c), confirmed a steady and uniform flow field over the plate. Boundary-layer profiles were measured at three streamwise stations, $x = 50$, 100, and 150 mm, following the LDA acquisition and vector reconstruction procedure described in Sec. 4.6.1. The reconstructed streamwise profiles (U/U_∞) are shown in Fig. 4.30, together with inner–outer (compound) model fits and the corresponding boundary-layer thickness $\delta_{99.5}$. The profiles exhibited monotonic boundary-



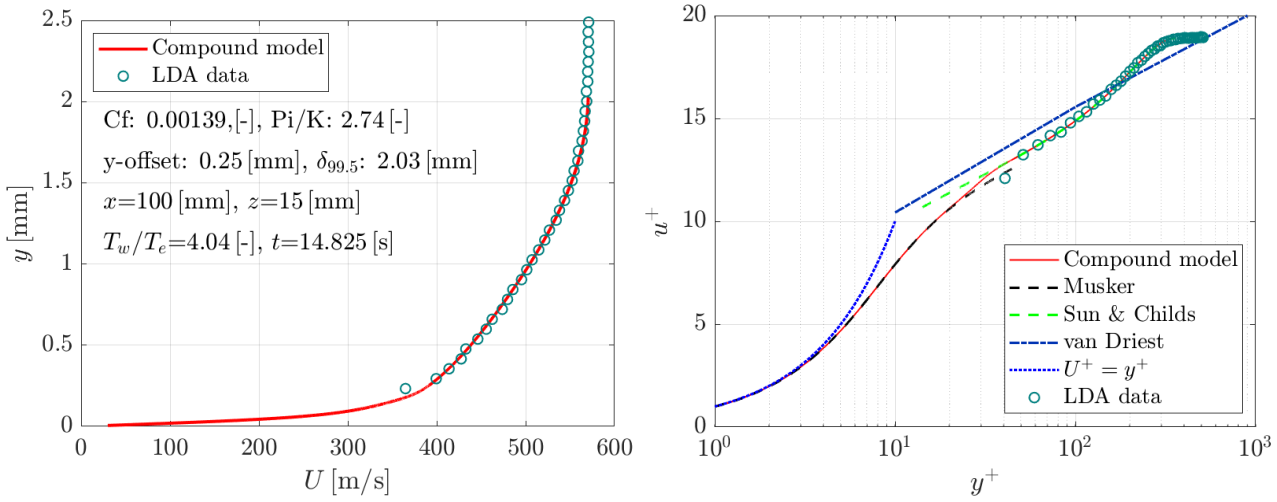
(a) v_1 from LDA 1. (b) v_2 from LDA 2.

Figure 4.26: Raw velocity data measured by (a) LDA 1 and (b) LDA 2, colored by transient measurement time. Conditions: $T_i = 523\,\mathrm{K}$, $x = 100\,\mathrm{mm}$



(a) Constructed velocity data from v_1 and v_2. (b) Particles number per averaged window.

Figure 4.27: (a) Reconstructed vector velocity from v_1 and v_2 after time-averaging. (b) Number of measured particles per time-averaged window.



(a) Velocity profile.

(b) Profile in wall coordinates (u^+ vs y^+).

Figure 4.28: LDA-measured velocity profiles and a fitted composite boundary layer model for Case 4. The composite profile combines a Musker near-wall fit with a Sun & Childs outer wake profile.

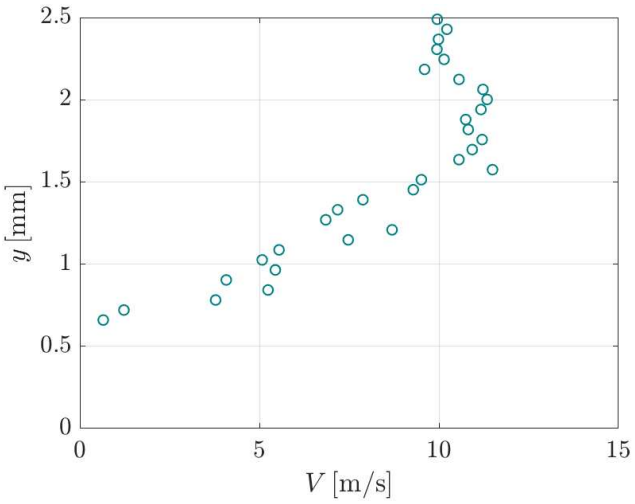


Figure 4.29: Wall-normal velocity profile for Case 4. The wall-normal coordinate y includes the same wall-offset correction applied in Fig. 4.28.

layer growth with downstream distance: $\delta_{99.5} \approx 0.9$, 1.8, and 2.9 mm at $x = 50$, 100, and 150 mm, respectively. The compound model reproduced the measured profiles across the wall-normal extent, including a well-defined inner region and a full outer wake, indicating a fully turbulent boundary layer from the most upstream station ($x = 50$ mm). Small near-wall deviations between data and model were attributed to reduced particle counts and seeding near the surface, consistent with the discussion in Sec. 4.6.1.

The integral parameters derived from the measured profiles are summarised in Table 4.7. The incompressible shape factor ($H_i = \delta_i^*/\theta_i$) remains essentially constant ($H_i \approx 1.40$) over $x = 50$–150 mm; the small differences between stations are within the uncertainty of the integral-parameter evaluation and therefore do not indicate any measurable streamwise evolution of the boundary-layer profile shape over the measurement range. All H_i values remain above the supersonic turbulent zero-pressure-gradient range ($H_i \approx 1.3$–1.35 for Mach 2.5 flow reported by Sabnis et al. [99]), consistent with an accelerated yet fully turbulent boundary layer, with no evidence of relaminarisation or separation. This case therefore provides a stable reference condition for the heated-wall measurements.

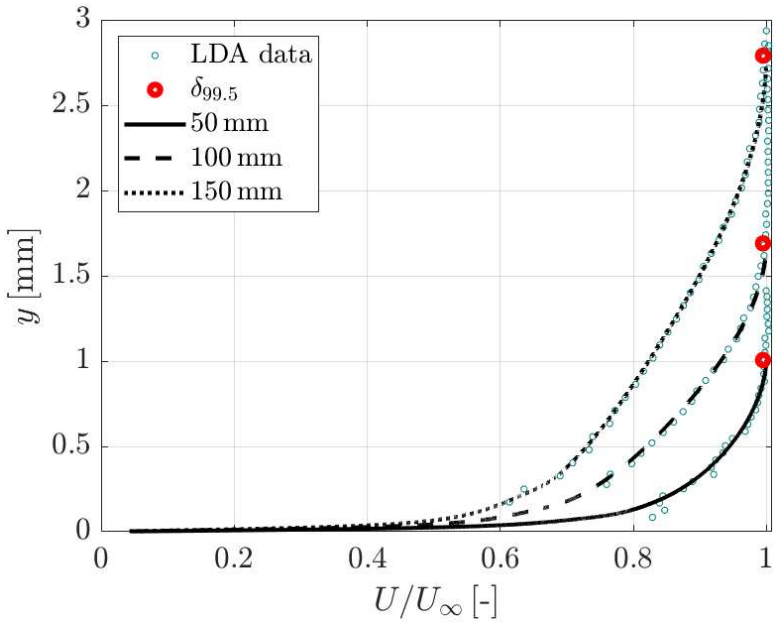


Figure 4.30: Baseline streamwise velocity profiles, U/U_∞, measured by LDA and fitted with the compound inner–outer model at streamwise stations $x = 50$, 100 and 150 mm. Symbols denote LDA measurements (circles) and solid and dashed lines denote the corresponding compound-model fits with $\delta_{99.5}$.

Table 4.7: Incompressible boundary-layer integral parameters for the baseline (unheated) flat plate. Integral parameters are calculated using the specified boundary-layer modeling approach, based on Sun & Childs [96] combined with Musker [97] models.

x (mm)	$\delta_{99.5}$ (mm)	δ_i^* (mm)	θ_i (mm)	H_i
50	1.0	0.10	0.07	1.40
100	1.7	0.23	0.17	1.41
150	2.8	0.40	0.29	1.39

Thermal Boundary Layer Profile

The thermal boundary layer development over the flat plate was investigated for four initial wall temperature cases, $T_i = [323, 373, 423, 523]$ K, as summarised in Table. 4.5. Measurements were performed in two wall regions (strips) corresponding to low- and high-temperature zones. Streamwise velocity profiles were reconstructed and normalised by the local freestream velocity U_∞, which accounts for transient variations in freestream speed due to the decrease of total temperature over time.

Figure 4.31 shows the reconstructed streamwise velocity profiles at $x = 150$ mm for Case 4 ($T_i = 523$ K) at $t \approx 9.4$ s. Four spanwise locations, $\lambda = [0, 1/3, 2/3, 1]$, are presented, normalised by the wavelength (centre-to-centre of the insulator and conductor). The profile on the hot wall ($\lambda = 1$) exhibits the thickest boundary layer, while the cold wall ($\lambda = 0$) exhibits the thinnest profile. The interpolated spanwise points ($\lambda = 1/3, 2/3$) lie between the hot and cold wall profiles and are distributed. These streamwise velocity profiles demonstrate that heating modifies boundary layer growth relative to the baseline, with stronger effects observed in the hot conductor strip. Across all cases, the compound model provides a good fit to the measured LDA profiles.

Figure 4.32 presents the transient evolution of the streamwise boundary layer profile at $\lambda = 0$ between $t \approx 9$–20 s for Case 4 at $x = 100$ mm. Each traverse across the boundary layer requires $t_{\text{trav}} = 2.7$ s, during which the mean surface temperature changes by 6 K (5% of T_∞) above the insulator and 7 K (6% of T_∞) above the conductor. The maximum wall-temperature change during a single traverse was therefore 7 K, which occurred for the highest initial wall-temperature case (Case 4), $T_i = 523$ K. This value is used here as a conservative estimate of the thermal drift during a traverse. Lower initial-temperature cases exhibited smaller wall-temperature changes over the same traverse time.

The corresponding maximum wall-temperature variation rate is

$$\left|\frac{\mathrm{d}T_w}{\mathrm{d}t}\right|_{\max} \approx \frac{7}{2.7} = 2.6\,\mathrm{K/s}. \tag{4.11}$$

The imposed spanwise wall-temperature difference in the present experiments is typically $\Delta T_{\mathrm{span}} =$ 30–90 K, depending on the initial wall-temperature condition. A representative thermal time scale associated with the evolution of this imposed temperature difference may therefore be estimated as

$$t_{\mathrm{th}} \sim \frac{\Delta T_{\mathrm{span}}}{|\mathrm{d}T_w/\mathrm{d}t|_{\max}} = 12\text{–}35\,\mathrm{s}. \tag{4.12}$$

The ratio between the LDA traverse time scale and the thermal time scale is therefore

$$\frac{t_{\mathrm{trav}}}{t_{\mathrm{th}}} \approx 0.08\text{–}0.23. \tag{4.13}$$

Thus, one traverse corresponds to at most approximately 8–23% of the thermal-evolution time scale associated with the imposed spanwise temperature difference. Since this estimate is based on the largest observed temperature change during a traverse, the ratio is smaller for the lower initial-temperature cases. The wall-temperature distribution therefore evolves during a traverse, but the change over one traverse remains small compared with the imposed spanwise temperature difference. The aerodynamic time scale is much shorter. Using the boundary-layer convection time scale,

$$t_{\mathrm{aero}} \sim \frac{\delta_{99.5}}{U_\infty} = \frac{3 \times 10^{-3}}{577} = 5.2\,\mu\mathrm{s}, \tag{4.14}$$

where $\delta_{99.5}$ is the estimated boundary-layer thickness and U_∞ is the freestream velocity. The ratio between the traverse time scale and the aerodynamic time scale is therefore

$$\frac{t_{\mathrm{trav}}}{t_{\mathrm{aero}}} = \frac{2.7}{5.2 \times 10^{-6}} \approx 5.2 \times 10^5. \tag{4.15}$$

The LDA traverse is therefore very slow relative to the aerodynamic response time of the boundary layer, but short relative to the thermal evolution of the wall-temperature distribution. The measured profiles are consequently interpreted as quasi-steady aerodynamic boundary-layer profiles associated with a slowly varying thermal boundary condition. The results show a clear shrinking of the boundary layer due to wall cooling, with $T_w - T_{aw}$ decreasing from 130 K to 115 K between $t = 9.4$ and 20.2 s.

The H-factor exhibits a slight increase as the boundary layer thickness reduces. This trend indicates that the boundary layer develops more rapidly over the colder wall.

A numeric summary of the measured cold and hot wall temperatures ($\lambda = 0, 1$) for Case 3 at $x = 50$, 100, and 150 mm, together with the corresponding boundary layer integral parameters, is presented in Table 4.8. This table lists the transient wall temperature in each region (from the thermal model), measurement time, $\delta_{99.5}$, incompressible displacement thickness δ_i^*, incompressible momentum thickness θ_i, and incompressible shape factor H_i for each case. The shape factor remains nearly constant over the measurement range ($H_i = 1.38$–1.41), with variations comparable to the baseline case and within the uncertainty of the integral-parameter evaluation. No systematic dependence of H_i on streamwise position or wall temperature can therefore be established. In contrast, $\delta_{99.5}$ increases consistently with increasing wall temperature, indicating a measurable thermal influence on boundary-layer thickness.

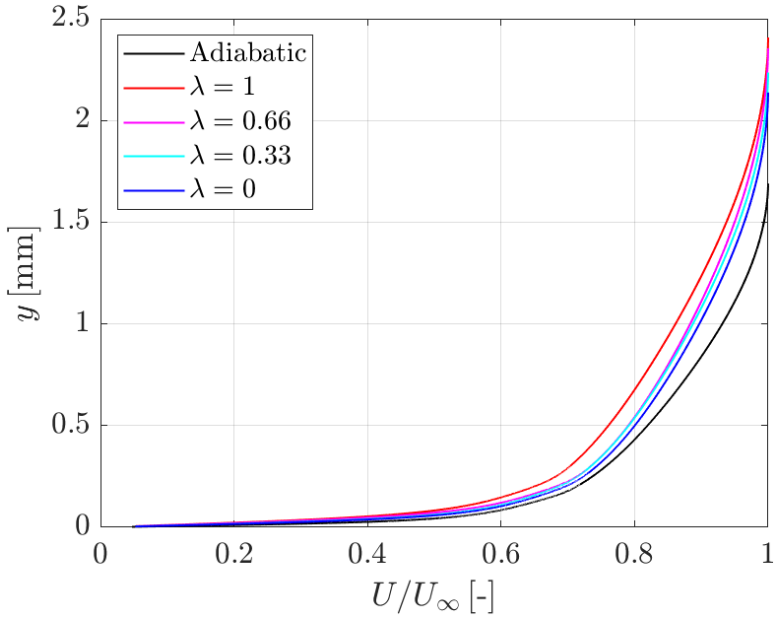


Figure 4.31: Reconstructed compound streamwise velocity profiles at $x = 100$ mm for Case 4 ($T_i = 523$ K) at four spanwise locations $\lambda = [0, 1/3, 2/3, 1]$. Hot wall ($\lambda = 1$) shows the thickest boundary layer, cold wall ($\lambda = 0$) the thinnest, and intermediate locations are linearly distributed.

4.6.3 Generated Streak Amplitude

The streak amplitude is defined as half the velocity difference between the streamwise velocity profiles measured at the hot-side and cold-side spanwise locations, normalized by the freestream velocity at

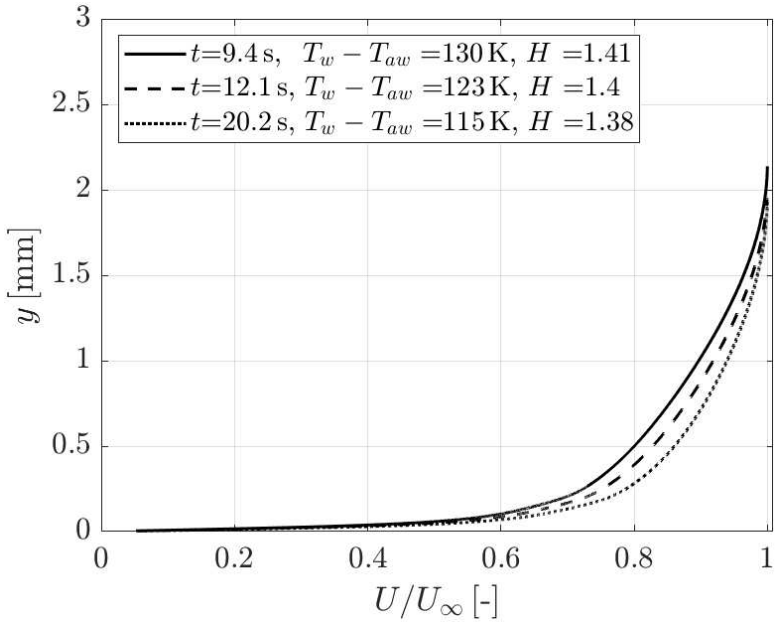


Figure 4.32: Transient evolution of the streamwise boundary layer profile at $x = 100$ mm, $\lambda = 0$, for Case 4 ($T_i = 523\,\mathrm{K}$) between $t \approx 9$–18 s.

Table 4.8: Summary of hot and cold wall temperatures ($\lambda = 0, 1$) and corresponding incompressible boundary layer integral parameters at $x = 100$ mm. Data includes transient wall temperature, measurement time, $\delta_{99.5}$, displacement thickness δ_i^*, momentum thickness θ_i, and shape factor H_i for each case.

Case	x [mm]	Wall (λ)	$T_w - T_{aw}$ [K]	Time [s]	$\delta_{99.5}$ [mm]	δ_i^* [mm]	θ_i [mm]	H_i
3	50	0	68.7	14.6	1.21	0.12	0.085	1.40
3	100	0	80.9	9.4	2.05	0.25	0.18	1.38
3	150	0	84.6	9.4	3.00	0.40	0.29	1.38
3	50	1	117.7	9.4	1.36	0.17	0.12	1.43
3	100	1	136.7	9.4	2.23	0.30	0.21	1.41
3	150	1	143.3	9.4	3.20	0.46	0.33	1.41

the measurement time. The wall-normal distribution of the streak amplitude is expressed as

$$A(y) = \frac{1}{2U_\infty(t)} \left[U_{\lambda=1}(y,t) - U_{\lambda=0}(y,t) \right], \tag{4.16}$$

$$A_{st}^{\mathrm{buf}} \equiv \max_{y \in \mathcal{I}_{\mathrm{buf}}} A(y), \tag{4.17}$$

$$A_{st}^{\log} \equiv \max_{y \in \mathcal{I}_{\log}} A(y), \tag{4.18}$$

where $\lambda = 0$ and $\lambda = 1$ denote the cold-side and hot-side measurement locations, respectively, and $A(y)$ represents the local streak amplitude at wall-normal location y. The quantities A_{st}^{buf} and $A_{st}^{\log}$ are retained here as notation for the near-wall/buffer-layer and outer/lower-log-region streak amplitudes, respectively. In the present work, these amplitudes are evaluated over the operational intervals

$\mathcal{I}_{\mathrm{buf}}/\delta_{99.5} = [0,\, 0.1]$ and $\mathcal{I}_{\mathrm{log}}/\delta_{99.5} = [0.1,\, 0.6]$, where $\delta_{99.5} \approx 2\,\mathrm{mm}$. These intervals are used to enable consistent case-to-case comparisons of the reconstructed streak-amplitude distribution, rather than to define strict canonical buffer-layer and logarithmic-layer regions.

Figure 4.33 shows the streamwise velocity profiles at $\lambda = 0$ (cold wall) and $\lambda = 1$ (hot wall) for Case 4 at $x = 100\,\mathrm{mm}$ and $t \approx 17.5\,\mathrm{s}$. The cold-wall profile ($\lambda = 0$) exhibited higher near-wall streamwise velocities and a steeper gradient compared to the hot-wall profile, consistent with boundary layer thinning due to wall cooling, as observed in Sec. 4.6.2. This behavior arises from the reduced density and increased viscosity over the hotter wall (193°C vs. 103°C), leading to a thicker boundary layer and lower near-wall streamwise velocities. The spanwise-varying wall temperatures generate streamwise streaks through density gradients and associated baroclinic vorticity production, modulating the local flow properties. Two distinct maxima are observed in $A(y)$: a near-wall (buffer-layer) peak (A_{st}^{buf}) and an outer (log-law) peak (A_{st}^{log}). The buffer-layer amplitude reaches $A_{st}^{\mathrm{buf}} \approx 4.8\%$ at $y \approx 0.019\,\delta_{99.5}$. In the outer log-law region, the streak amplitude reaches $A_{st}^{\mathrm{log}} \approx 2.4\,\%$ at $y \approx 0.14\,\delta_{99.5}$. The persistent amplitude in the outer/lower-log region is primarily driven by thermal effects, where the hotter wall thickens the boundary layer, resulting in a sustained spanwise modulation of streamwise velocity. In contrast, the pronounced near-wall peak occurs in the reconstructed part of the profile, at approximately $y^+ \approx 10$. This wall-normal location is consistent with the canonical region where near-wall turbulent motions and lift-up effects are expected to be strong [100], and with direct numerical simulations of supersonic and hypersonic turbulent boundary layers in which the root-mean-square streamwise velocity fluctuation peaks at $y^+ \approx 10$–20, with possible shifts under non-adiabatic conditions [101, 102]. However, in the present measurements this near-wall peak lies below the first reliable LDA measurement location. Therefore, its precise magnitude and shape are sensitive to the compound-profile reconstruction and the applied wall-offset correction. The near-wall/buffer-layer streak amplitude A_{st}^{buf} should therefore be interpreted as a reconstructed estimate of the near-wall velocity modulation, rather than as a directly measured buffer-layer quantity. By contrast, the outer/lower-log-region peak occurs at approximately $y/\delta_{99.5} \approx 0.14$, corresponding to $y^+ \approx 55$. This location is closer to the first reliable LDA data point and lies above most of the canonical buffer layer, so A_{st}^{log} is less sensitive to the near-wall closure than A_{st}^{buf}. The terminology of the amplitude regions is therefore operational rather than strictly canonical: A_{st}^{buf} denotes the maximum reconstructed amplitude in the near-wall/buffer-layer interval, while A_{st}^{log} denotes the maxi-

mum amplitude in the outer/lower-log-region interval. These quantities are used to provide consistent case-to-case comparisons of the reconstructed streak field. The main conclusion drawn from these profiles is therefore the systematic generation of a spanwise velocity modulation by the imposed wall-temperature difference, rather than the precise absolute value of the reconstructed near-wall peak.

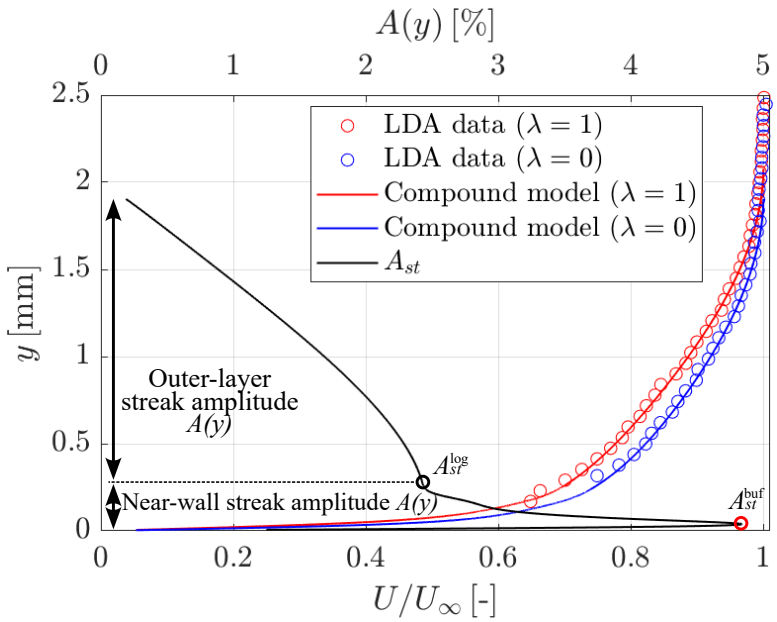


Figure 4.33: Streamwise velocity profiles at $\lambda = 0$ with the measured LDA data (blue line and circle) and $\lambda = 1$ with the measured LDA data (red line and circle) for Case 4 ($x = 100\,\text{mm}$, $t \approx 17.5\,\text{s}$). The velocity difference gives reconstructed streak amplitudes of approximately $A_{st}^{\text{buf}} = 4.8\,\%$ and $A_{st}^{\text{log}} = 2.4\,\%$ over the near-wall/buffer-layer and outer/lower-log-region intervals, respectively (black line). The two operational peak amplitudes are denoted A_{st}^{buf} and A_{st}^{log}, respectively (Eq. (4.17)–(4.18)).

The streamwise variation of streak amplitude, which takes a maximum value along the wall-normal direction, is shown in Fig. 4.34 for all cases. The plot excludes $x = 50\,\text{mm}$ because the thin boundary layer (less than 1 mm) is sensitive to slight noise, which significantly impacts the evaluation of streak amplitude. Between $x = 100$ and $150\,\text{mm}$, the amplitude remains nearly constant. As the initial temperature increases, the streak amplitude becomes larger, indicating that streak generation is most effective in regions with strong spanwise thermal gradients. Note that for Case 4 no measurement is available at $x = 150\,\text{mm}$ due to limitations of the experimental campaign.

Figure 4.35 summarizes the reconstructed near-wall/buffer-layer amplitude and the outer/lower-log-region amplitude for all four cases as a function of the wall temperature difference, $\Delta\Theta$. A near-linear dependence is observed for both operational regions, with A_{st}^{log} being approximately half of A_{st}^{buf}. These

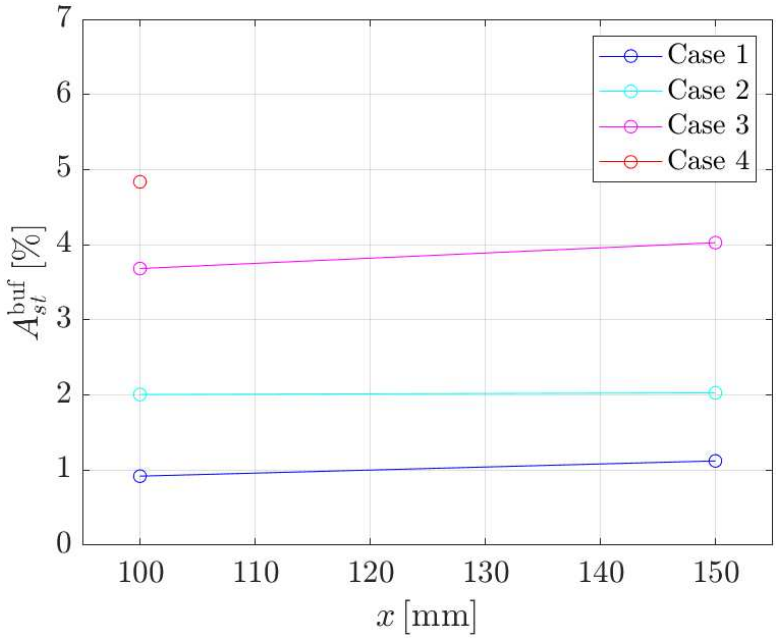


Figure 4.34: Streamwise evolution of the reconstructed near-wall/buffer-layer streak amplitude A_{st}^{buf} for all cases between $x = 100$ and 150 mm.

results indicate that the reconstructed streak amplitudes scale with the strength of thermal forcing.

The observed dependence of streak amplitude on $\Delta\Theta$ highlights the strong coupling between thermal boundary layer development and streamwise velocity modulation. The nearly linear relationship suggests that thermal forcing provides a predictable and scalable mechanism for streak generation, within the range of conditions examined. These findings support the interpretation that non-uniform surface heating can serve as a passive method of streak forcing, with potential application to high-speed boundary-layer transition control.

4.7 Summary

Generation of Surface Temperature Distributions

This chapter first demonstrated a passive method for generating spanwise non-uniform wall-temperature distributions using dissimilar materials with contrasting thermal diffusivities. A flat-plate model comprising alternating copper and MACOR strips was uniformly preheated and tested at Mach 2.75 in the Imperial College supersonic wind tunnel. Infrared thermography (IRT) confirmed that significant spanwise temperature variations developed shortly after flow onset, with larger variations obtained at higher initial surface temperatures. A physics-informed thermal model that accounted for wind-

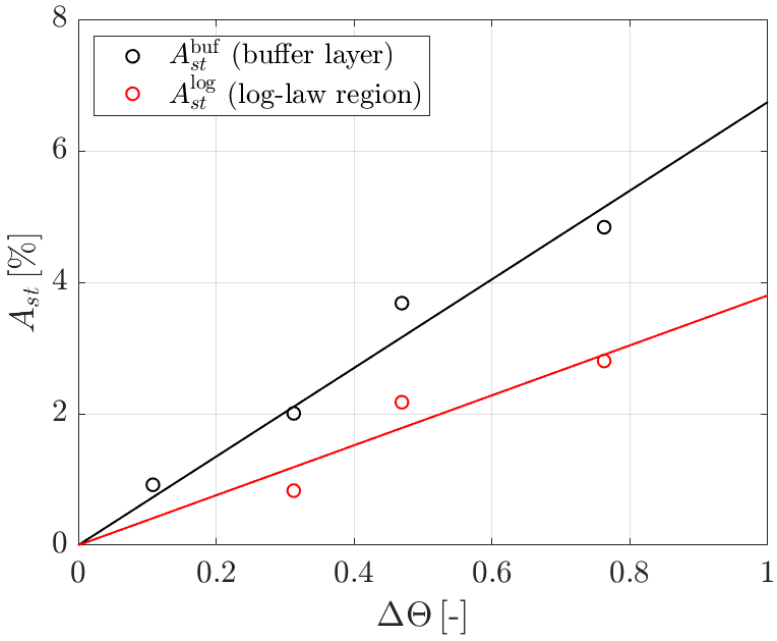


Figure 4.35: Streak amplitude in the buffer layer and log-law region versus normalized wall temperature difference ($\Delta\Theta = \Delta T_w/T_\infty$) at $x = 100\,\mathrm{mm}$ for all four initial temperature cases, with a linear fit.

tunnel start-up behaviour and preheating conditions accurately predicted the measured temperature fields across multiple initial temperatures. This agreement established that the surface-temperature evolution under strong convective loading can be predicted quantitatively, providing a practical basis for passive thermal actuation.

Thermally Forced Streaks

The chapter then demonstrated, for the first time, controlled generation of streamwise velocity streaks in a supersonic turbulent boundary layer using spanwise non-uniform wall-temperature forcing on the same flat plate. The thermal model provided the local, time-resolved wall-temperature input required to interpret the LDA measurements. A continuous-motion traverse system mounting the LDA probe was developed to allow continuous, spatially resolved scanning of the measurement volume. LDA showed that local heating and cooling systematically modified the boundary-layer thickness and produce organised spanwise velocity modulation. The shape factor remained near 1.4 while the boundary-layer thickness increased downstream for both the hot and cold strips. At the highest wall-temperature case, the reconstructed near-wall/buffer-layer streak amplitude reached approximately 5 %, while the outer/lower-log-region amplitude reached approximately 2 %. The near-wall/buffer-layer value should be interpreted as a reconstructed estimate because its peak lies below the first reliable LDA measurement location, whereas the outer/lower-log-region amplitude is less sensitive to

the near-wall closure. Once formed, the streak amplitude remained approximately constant over the measurement domain, $x = 100$–$150\,\mathrm{mm}$. Furthermore, the reconstructed streak amplitudes scaled nearly linearly with the normalised wall-temperature difference, indicating a predictable relationship between thermal forcing and flow response. Overall, these results provided experimental evidence that passive surface heating can impose organised streamwise velocity modulation in a high-speed boundary layer, motivating future investigations of thermally driven streak forcing for transition management and drag reduction.

Chapter 5

Hypersonic Transition Control via Surface Temperature Variations on a Waverider Model

5.1 Overview

This chapter assessed a passive thermal approach to hypersonic transition control, in which a spanwise non-uniform wall-temperature distribution was used to modify instability development in a Mach 5 boundary layer. The central objective was to provide experimental evidence, under wind-tunnel constraints, of how controlled thermal patterning altered surface thermal footprints and high-frequency wall-pressure signatures. The study was organised around comparisons between three configurations: an unheated baseline, a matched uniformly heated baseline, and a spanwise non-uniformly heated case.

The chapter was guided by recent direct numerical simulation (DNS) and linear stability theory (LST) results indicating that prescribed spanwise-periodic wall-temperature distributions can generate streamwise velocity streaks and influence second Mack mode amplification. The DNS/LST results summarised here were generated by the second author of the associated SciTech 2026 study [103] and were used solely to inform the selection of control parameters and sensor placement for the experiments.

Experiments were conducted using a dedicated Mach 5 configuration featuring a waverider-mounted flat-plate test surface inclined at 5° and an embedded heating patch designed to impose periodic spanwise temperature variations. Surface temperature fields were quantified using infrared thermography (IRT), and boundary-layer response was assessed using high-frequency wall-pressure measurements. The chapter then compared baseline, uniform-heating, and non-uniform-heating cases to isolate the effect of spanwise temperature non-uniformity from mean wall-temperature elevation, and discussed the implications for instability growth and transition behaviour.

5.2 Numerical Guidance for Experimental Design

Direct numerical simulation (DNS) and linear stability theory (LST) results were used in this chapter to guide the experimental design, specifically the selection of the heating-patch streamwise extent and the placement of high-frequency pressure sensors to capture second Mack mode amplification.

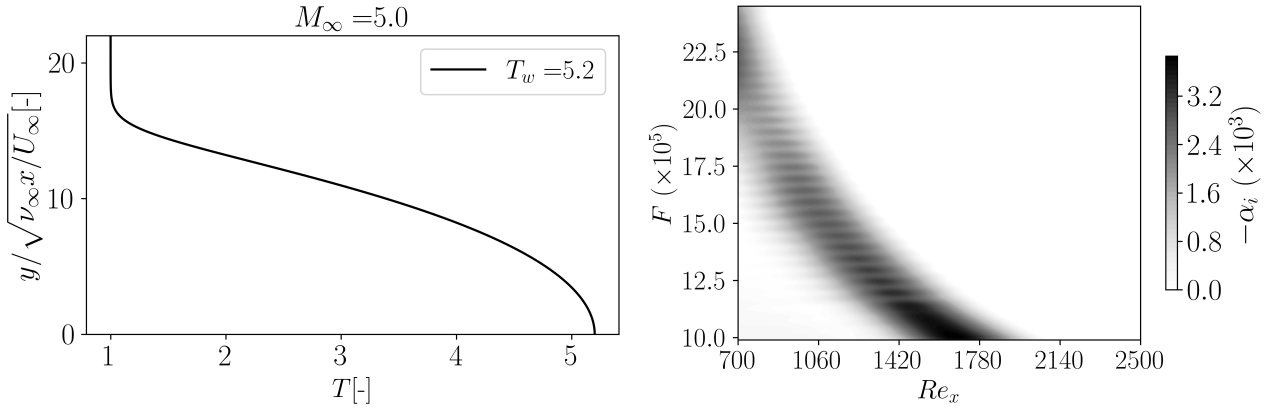
Authorship and Provenance.
The DNS and LST results summarised in this section were generated by the second author (Dr Luca Boscagli) of the collaborative SciTech 2026 study [103]. They were used here as design guidance; the present author's contribution was the experimental implementation and analysis presented in the subsequent sections.

5.2.1 LST Guidance: Second Mack Mode Band and Amplification Region

A spatial, parallel LST analysis was performed for a self-similar, compressible laminar boundary layer over an adiabatic flat plate at Mach 5, using a freestream stagnation temperature $T_0 = 300\,\mathrm{K}$ (Fig. 5.1). The analysis provided second Mack mode neutral stability curves over a range of non-dimensional frequency F spanning 1.0×10^6 to 2.4×10^6, corresponding to instability frequencies in the order of several hundred kHz for the present conditions (Fig. 5.1b). These neutral curves identified the streamwise region (equivalently, local Reynolds number range) over which second Mack mode disturbances were expected to amplify in the baseline configuration, and therefore provided guidance for locating the high-frequency wall-pressure sensors.

It is noted that introducing wall heating or cooling can shift the neutral stability boundaries in local

Reynolds number, and consequently the LST results were used here primarily to define baseline sensor placement and a target frequency band for the pressure spectral analysis.



(a) (b)

Figure 5.1: (*a*) Self-similar temperature profile and (*b*) second Mack mode neutral stability curves for a Mach 5 configuration with $T_0 = 300\,\mathrm{K}$ (from the SciTech 2026 collaborative study [103]).

5.2.2 DNS Guidance for Streak Amplitude Response and Heating-Patch Geometry

Three-dimensional DNS results were used here to guide the selection of the heating-patch streamwise extent and the spanwise wavelength of the imposed wall-temperature modulation. The baseline condition corresponds to $M_\infty = 5$ and a unit Reynolds number of $Re \approx 2.5 \times 10^7\,\mathrm{m}^{-1}$, matching the nominal wind-tunnel operating point used in the subsequent experiments. The computations considered a laminar boundary layer with a spanwise-periodic, sinusoidal wall-temperature distribution imposed over a finite streamwise strip, and periodic boundary conditions in the spanwise direction. For the present design studies, no additional external forcing was introduced beyond the prescribed wall-temperature modulation; consequently, the resulting steady streak corresponded to the fundamental spanwise harmonic of the imposed thermal pattern.

The numerical parametric study assessed (i) the effect of the streamwise extent and axial placement of the heated strip, and (ii) the effect of the spanwise wavelength λ_z on the induced streak amplitude. The streak amplitude (A_{st}) was evaluated consistently with the definition adopted in Chapter 4.7.

The imposed spanwise wall-temperature variation was defined between 300 K and 600 K, representative of room-temperature baseline conditions and typical attainable heater-surface temperatures in the

present rig. All cases were initiated from a uniform isothermal wall condition and subsequently imposed a spanwise temperature modulation over the control region, resulting in a wall temperature level of order $\overline{T}_w \sim 450\,\mathrm{K}$ across the heated strip (Fig. 5.2). For all configurations investigated, the boundary-layer thickness at the inlet of the computational domain, $\delta_{99.5,\mathrm{in}}$, was held constant to isolate the effects of heating-strip geometry and spanwise wavelength (Fig. 5.3a).

The heated-strip length was varied between 50 and 100 mm, with strip start locations satisfying $x \geq 50\,\mathrm{mm}$ to reflect practical integration constraints. Over this range, increasing the strip length from 50 to 100 mm increased the streak amplitude from approximately 2% to 2.5% of the freestream speed, indicating comparatively slow streak growth with downstream development (Fig. 5.3). In addition, shifting the heated strip downstream by a constant offset (e.g. comparing $x \in [50, 100]\,\mathrm{mm}$ and $x \in [80, 130]\,\mathrm{mm}$) produced a similar maximum streak amplitude, suggesting that the peak amplitude was relatively insensitive to a moderate streamwise translation of the control region within the investigated range. These trends motivated a heating-patch length of order $\mathcal{O}(100)\,\mathrm{mm}$ in the experiments, while allowing flexibility in the exact streamwise placement imposed by the rig geometry.

The effect of spanwise wavelength was evaluated by increasing λ_z (implemented in the DNS by increasing the computational domain width while maintaining resolution per wavelength). Increasing the wavelength from $\lambda_z \approx 10\delta_{99.5,\mathrm{in}}$ (corresponding to $\lambda_z \approx 15\,\mathrm{mm}$) to $\lambda_z \approx 25\delta_{99.5,\mathrm{in}}$ (corresponding to $\lambda_z \approx 30\,\mathrm{mm}$) increased the maximum streak amplitude from approximately 2.5% to nearly 4% (Fig. 5.4). Prior analyses indicate that the stabilisation effectiveness against second Mack mode disturbances decreases for wavelengths exceeding $\sim 15\delta_{99.5}$, although wavelengths up to $\sim 25\delta_{99.5}$ can remain beneficial [78]. Therefore, the experimental design targeted wavelengths in the range $\mathcal{O}(15$–$25)\delta_{99.5}$ as a compromise between achievable streak amplitude and anticipated control effectiveness.

Design Implications

The DNS trends motivated a heating-patch streamwise extent of order 100 mm and target spanwise wavelengths in the range $\lambda_z/\delta_{99.5} \sim 15$–$25$ for the experimental implementation; practical constraints and subsequent bench-top validation were used to finalise the patch configuration in Sec. 5.3.4.

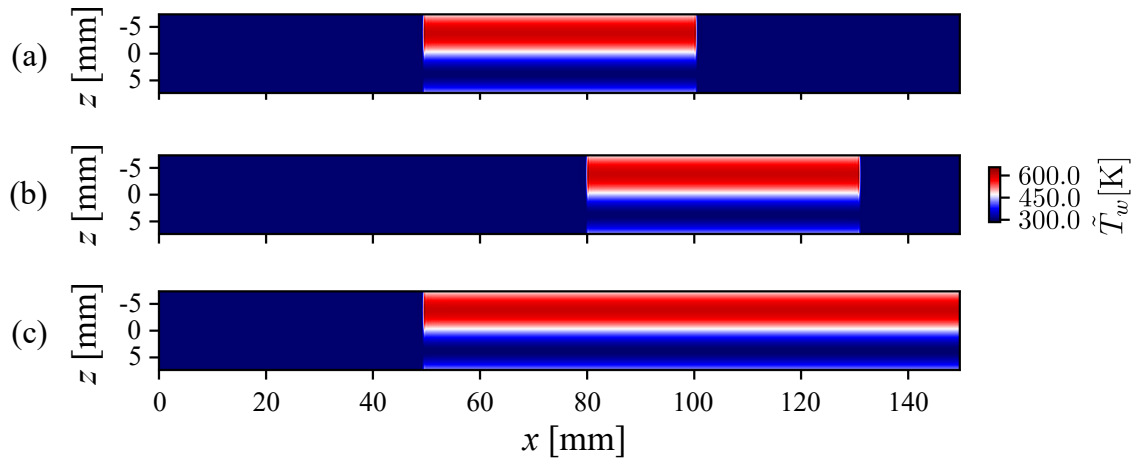
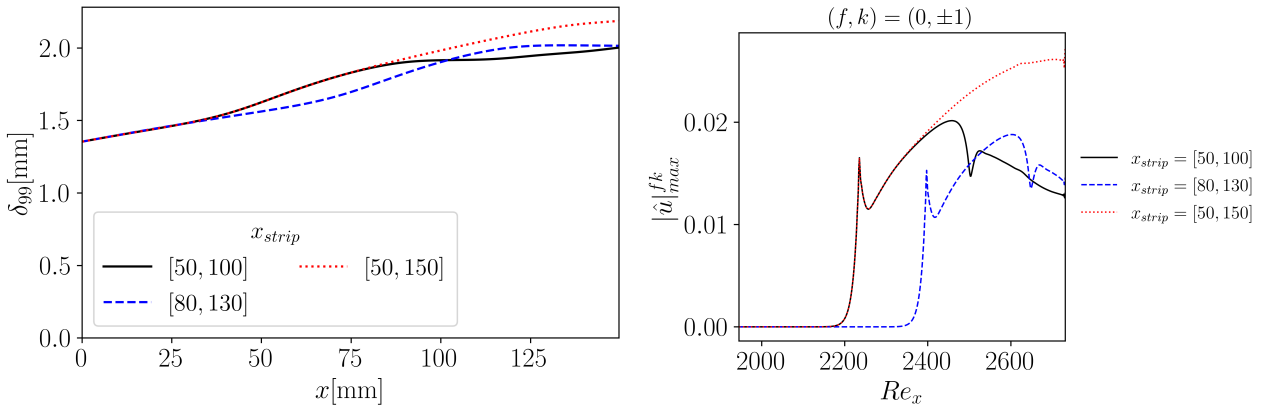


Figure 5.2: Imposed wall-temperature distributions used in the DNS parametric study for three streamwise strip configurations (from the SciTech 2026 collaborative study [103]).



(a) (b)

Figure 5.3: (a) Streamwise evolution of the base-flow boundary-layer thickness and (b) corresponding streak amplitude for three heating-strip configurations (from the SciTech 2026 collaborative study [103]).

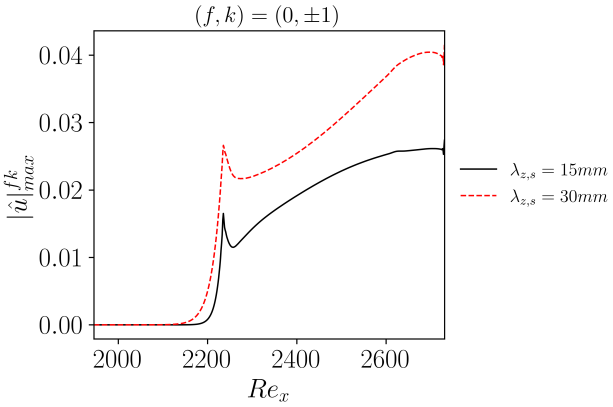


Figure 5.4: Effect of streak wavelength on the streamwise distribution of the streak amplitude (from the SciTech 2026 collaborative study [103]).

5.3 Experimental Model and Heating System

This section detailed the design specifications of the wind-tunnel model and the development of the heating control system. First, the hypersonic waverider geometry was defined, with sensor locations explicitly targeted based on the LST instability analysis presented in Sec. 5.3. Subsequently, the design of the localised heating patch was detailed, covering the numerical thermal analysis, material trade studies, and final selection. Finally, the fabrication of the heating system was described, concluding with a bench-top thermal characterisation to validate the hardware performance against the numerical predictions.

5.3.1 Waverider Model and Sensor Layout

Waverider-Based Geometry

The experimental test article utilised a waverider-based configuration designed to generate a controlled boundary layer over a flat aerodynamic surface, as illustrated in Fig. 5.5. The central test surface integrated a localised heating patch region and a downstream sensing region for boundary layer diagnostics via pressure sensors and IRT. The model had a streamwise length of 251 mm and a spanwise width of 140 mm (see Fig. 5.6). To reproduce the post-shock flow conditions of a reference 7-degree cone model tested at Sandia National Laboratories and Purdue University [19], the flat surface is inclined at a 5-degree compression angle relative to the freestream axis. Although the reference configuration is a 7-degree cone, the equivalent compression angle for the present flat aerodynamic surface is smaller because the conical flow is three-dimensional. In an axisymmetric conical flow, part of the compression is relieved by lateral/azimuthal flow around the body, so a cone of a given half-angle produces a weaker effective post-shock compression than a two-dimensional wedge of the same angle. A 5-degree compression angle was therefore selected for the waverider-based flat surface to approximate the post-shock edge-flow conditions of the 7-degree cone reference experiments, while retaining a planar test region suitable for controlled heating, pressure measurements, and infrared thermography. Integrated wing sections were positioned on both sides of the test surface to suppress lateral flow spillage, thereby enhancing the spanwise uniformity of the boundary layer. This configuration yielded an effective aerodynamic test surface of 251×60 mm within the central portion of the model.

A schematic of the waverider-based experimental configuration is shown in Fig. 5.7. The side view illustrates the freestream direction, the leading-edge shock generated by the sharp front edge, the shock surface over the model, the 5°-inclined aerodynamic test surface, the upstream heating surface, the downstream measurement surface, and the approximate boundary-layer development. The front view shows the model planform and the shock surface generated by the leading edge. This schematic is included to clarify the overall flowfield structure and the relative locations of the heated and measured regions.

The main body and mechanical mounting structure were fabricated from stainless steel (SUS 304), selected for its thermal resistance and structural integrity under hypersonic conditions. The heating region consisted of a heating plate installed from the backside of the test surface using a stepped recess geometry. This plate covered an area of 93×50 mm, starting 53 mm downstream of the leading edge, based on the DNS results (Sec. 5.2.2). To accommodate thermal expansion during active heating, a total clearance gap of 0.1 mm was maintained around the plate. Behind the plate, a heating system was installed.

Downstream of the heating region, a modular sensing zone was positioned 167 mm from the leading edge, spanning 50 mm in width and 70 mm in length, as illustrated in Fig. 5.6. This section was composed of a single 3D-printed resin insert, selected for its high infrared emissivity ($\epsilon \approx 0.9$) to facilitate thermography. The resin insert was designed to accommodate four fast-response pressure sensors (PCB 132B38).

5.3.2 Sensor Placement Based on LST

To capture the evolution of second Mack mode instabilities downstream of the heating patch, the placement of high-frequency PCB pressure sensors was determined based on the LST results summarised in Sec. 5.2.1. The neutral curves computed via LST, presented in Fig. 5.1b, indicate that the highest growth rates occur in the vicinity of the non-dimensional frequency $F = 1.0 \times 10^{-4}$. Here, F is defined as $F = f\nu/U_\infty^2$, where f is the frequency, ν is the kinematic viscosity, and U_∞ is the freestream velocity. For the specific test conditions of Mach 5 and $T_0 = 300$ K, this corresponds to a physical target frequency of $f \approx 278$ kHz. This selection aligns with prior experimental observations by Casper et al. [19], who reported persistent second Mack mode instabilities at this frequency under

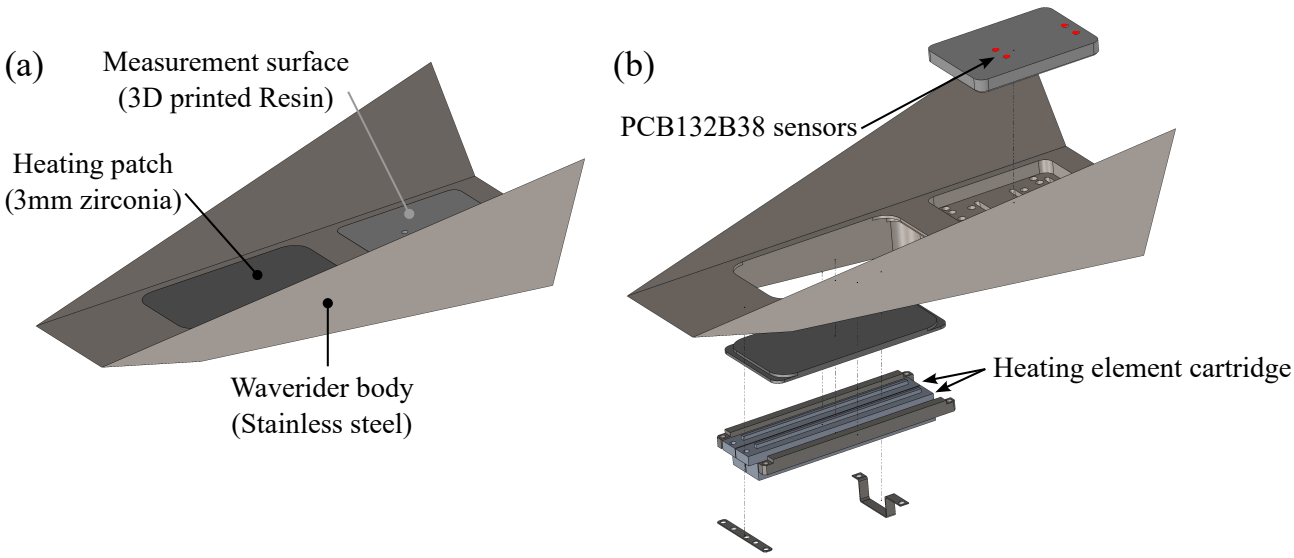


Figure 5.5: 3D CAD model of (a) the assembled waverider-based hypersonic test article, and (b) an exploded view illustrating individual components, including the zirconia heating plate and modular sensing patches.

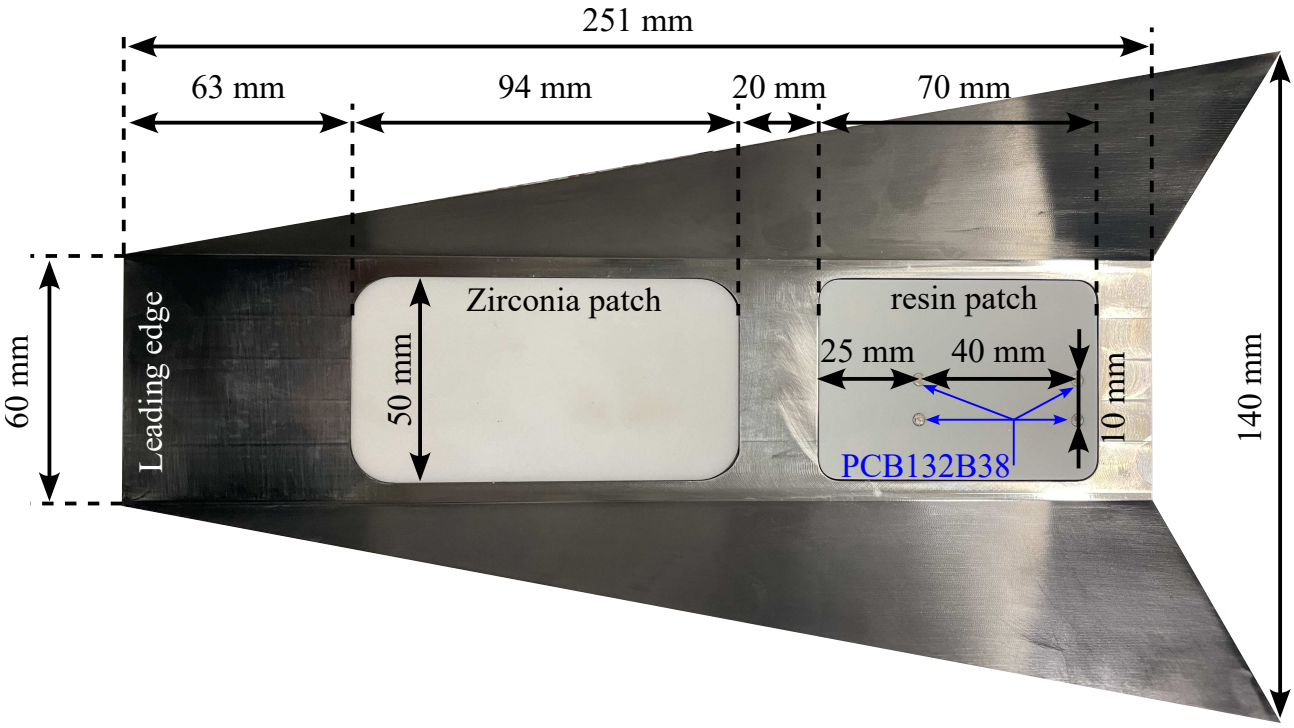


Figure 5.6: 3D CAD model of (a) the assembled waverider-based hypersonic test article, and (b) an exploded view illustrating individual components, including the zirconia heating plate and modular sensing patches.

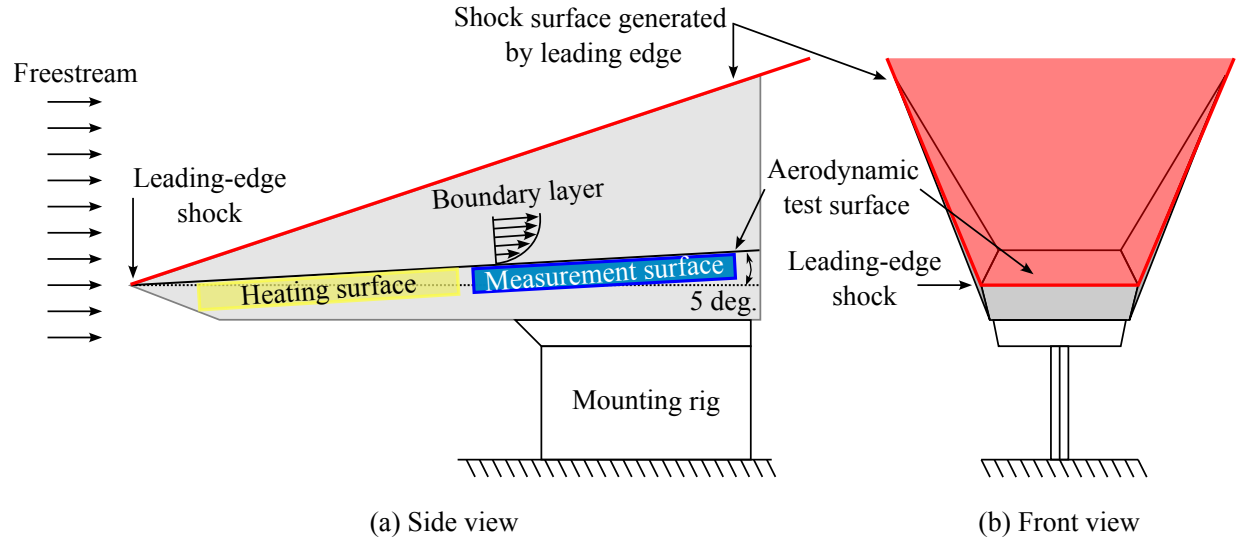


Figure 5.7: Schematic of the waverider-based Mach 5 experimental configuration. (a) Side view showing the freestream direction, leading-edge shock, shock surface, aerodynamic test surface, upstream heating surface, downstream measurement surface, and approximate boundary-layer development. (b) Front view showing the model planform and the shock surface generated by the leading edge.

similar hypersonic conditions.

As illustrated in Fig. 5.1b, the $f = 278\,\text{kHz}$ ($F = 1.0 \times 10^{-4}$) mode underwent significant amplification within the Reynolds number range of $Re_x = 1400$ to 2100. Mapping this Reynolds number range to physical coordinates (Fig. 5.8) corresponded to a streamwise region of approximately $x = 80$ to 180 mm. Consequently, the measurement region was located downstream of $x = 180\,\text{mm}$ to capture the developed wave packets. The chosen sensor layout, shown in Fig. 5.5b, consisted of two streamwise pairs positioned at $x = 192\,\text{mm}$ and $x = 232\,\text{mm}$ to capture the evolution of the developed second Mack mode wave packets. The primary pair was aligned with the model centerline ($z = 0$), while the secondary pair was laterally offset by $z = 10\,\text{mm}$ to detect potential spanwise variations induced by non-uniform heating.

5.3.3 Heating Patch Thermal Design

Thermal Modelling Framework

A transient three-dimensional heat conduction analysis was performed to predict the surface temperature response of the test plate under localised heating. The modelling approach follows the methodology established in previous studies [76, 77, 79, 80] and was implemented using the Partial

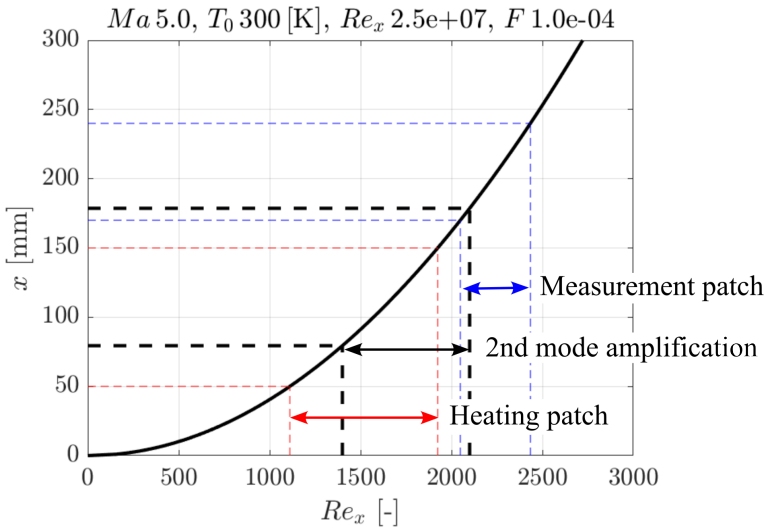


Figure 5.8: Predicted second Mack mode instability onset and growth range ($Re_x = 1400$ to 2100) shown for non-dimensional frequency $F = 1.0 \times 10^{-4}$ ($f = 278\,\text{kHz}$), used to guide sensor placement.

Differential Equation (PDE) Toolbox in MATLAB.

The computational domain represented a spanwise periodic unit cell of the heating configuration, illustrated in Fig. 5.9. The geometry consisted of spanwise segments that were 12 mm and 20 mm wide for the first and second configurations, respectively. Each segment included a 2 mm wide contact region for the heating cartridge and the adjacent lateral conduction path. In the streamwise direction, the domain was truncated to a representative length of 10 mm, rather than the full 94 mm patch length. This reduction was justified by the alignment of the heating system, where individual heating cartridges correspond directly to the longitudinal heat strips. As each cartridge delivered uniform thermal input along its entire length, the streamwise temperature gradient was assumed to be negligible.

Thermal boundary conditions were defined to replicate the experimental operating limits. A Dirichlet boundary condition of $T = 670\,\text{K}$ was applied at the heater interface, corresponding to the maximum rated operating temperature of the cartridge elements. All other external surfaces were treated as adiabatic, a valid assumption given the short duration of the heating phase relative to the thermal time constant of the mounting structure. Periodic boundary conditions were applied to the spanwise faces to model the repeating array of the heating system. The domain was discretised using an unstructured tetrahedral mesh with a characteristic element size of 1.0 mm.

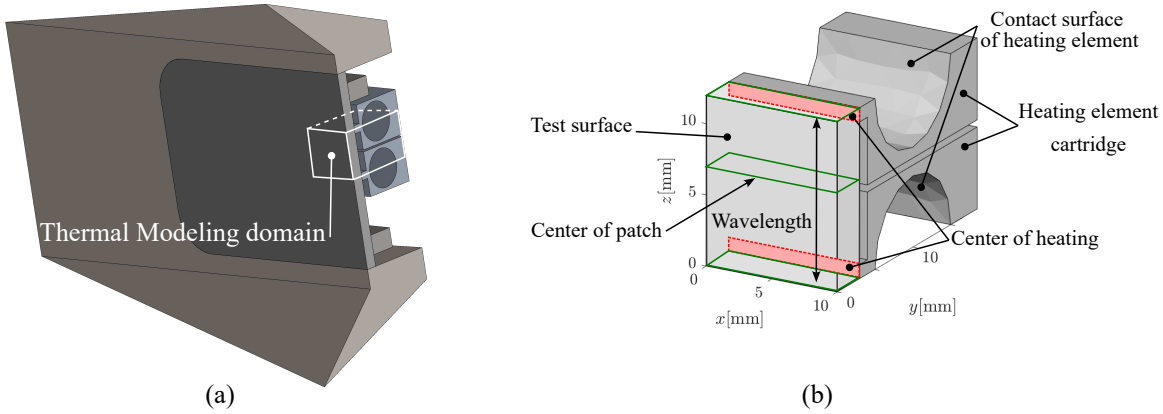


Figure 5.9: 3D CAD representation of the setup: (a) cross-sectional view of the assembly highlighting the thermal modelling domain; and (b) the spanwise unit cell showing the heating cartridge contact surfaces and test surface geometry (12 mm spanwise configuration).

Material Parameter Study and Selection

To maximise the surface temperature gradients required for instability control, a parametric study was conducted involving material properties and plate thickness. Three candidate ceramic materials—MACOR, Zirconia, and Alumina-Toughened Zirconia (ATZ)—were evaluated. These materials were selected for their low thermal diffusivity and high-temperature compatibility. Their relevant thermal and mechanical properties are summarised in Table 5.1.

Table 5.1: Thermal and mechanical properties of candidate materials used in the design trade study.

Material	ρ [kg/m^3]	α [W/m· K]	c_p [J/kg·K]	E [GPa]	α_{TE} [10^{-6}/K]
MACOR	2520	1.48	777	66.9	9.3
Zirconia	6070	3.00	480	200.0	10.0
ATZ	5500	6.00	570	340.0	8.0

The primary performance metric defined for this study is the spanwise surface temperature difference (ΔT), measured between the centre of the heated region and the unheated gap. First, the effect of plate thickness was assessed using MACOR. Figure 5.10 compares the time evolution of ΔT for 6 mm and 3 mm thick plates over a 30 s heating period. The thinner plate (3 mm) generates a significantly higher peak difference ($\Delta T \approx 130$ K) compared to the thicker plate ($\Delta T <$30 K) and sustains the gradient for a longer duration. This indicated that reducing the substrate thickness minimises lateral conduction losses and thermal mass, thereby enhancing surface responsiveness.

Consequently, 3 mm was adopted as the baseline thickness. The thermal response of MACOR was

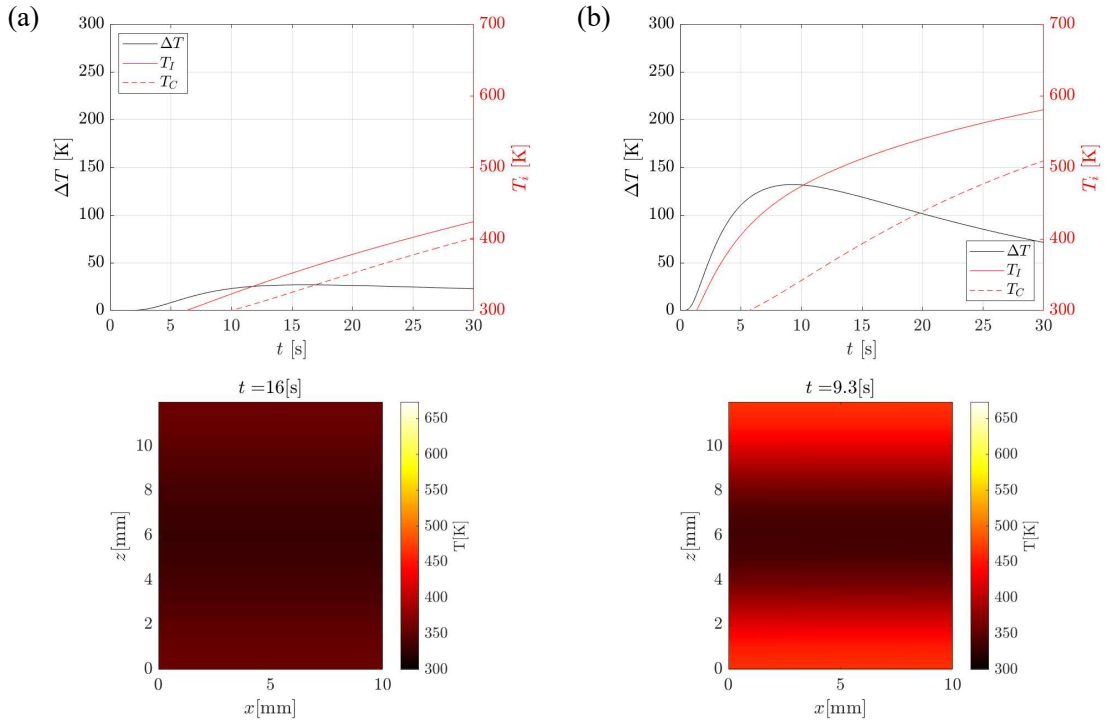


Figure 5.10: Predicted time evolution of spanwise temperature difference (ΔT) and surface temperature contours for MACOR plates with thickness: (a) 6 mm and (b) 3 mm. T_I is the surface temperature directly above the cartridge heater, while T_C is the surface temperature at the centerline of the plate between adjacent heaters.

then compared with that of zirconia and ATZ at this fixed geometry, as shown in Figs. 5.10b and 5.11a–b. While all candidates achieved a peak $\Delta T \approx 130\,\mathrm{K}$, their transient behaviour differed significantly. MACOR maintained the gradient for the longest duration due to its low thermal diffusivity. In contrast, ATZ dissipated the thermal input most rapidly, while zirconia exhibited intermediate behaviour.

However, thermal stress posed a critical constraint for brittle ceramics in high-gradient environments. The critical temperature difference (ΔT_{crit}) prior to failure was estimated using the linear elastic fracture criterion:

$$\Delta T_{\mathrm{crit}} = \frac{\sigma_f}{E\alpha_{TE}}, \tag{5.1}$$

where σ_f is the fracture strength, E is Young's modulus, and α_{TE} is the coefficient of thermal expansion. The calculated limits are presented in Table 5.2. The analysis revealed that the MACOR design operated at $\Delta T \approx 130\,\mathrm{K}$, which approached its estimated failure limit of 151 K, presenting a high risk of fracture during rapid thermal cycling. Conversely, zirconia provided a safety factor of approximately 4.6 while maintaining adequate thermal performance. Consequently, zirconia was selected as

the optimal substrate material, balancing thermal gradient generation with mechanical reliability.

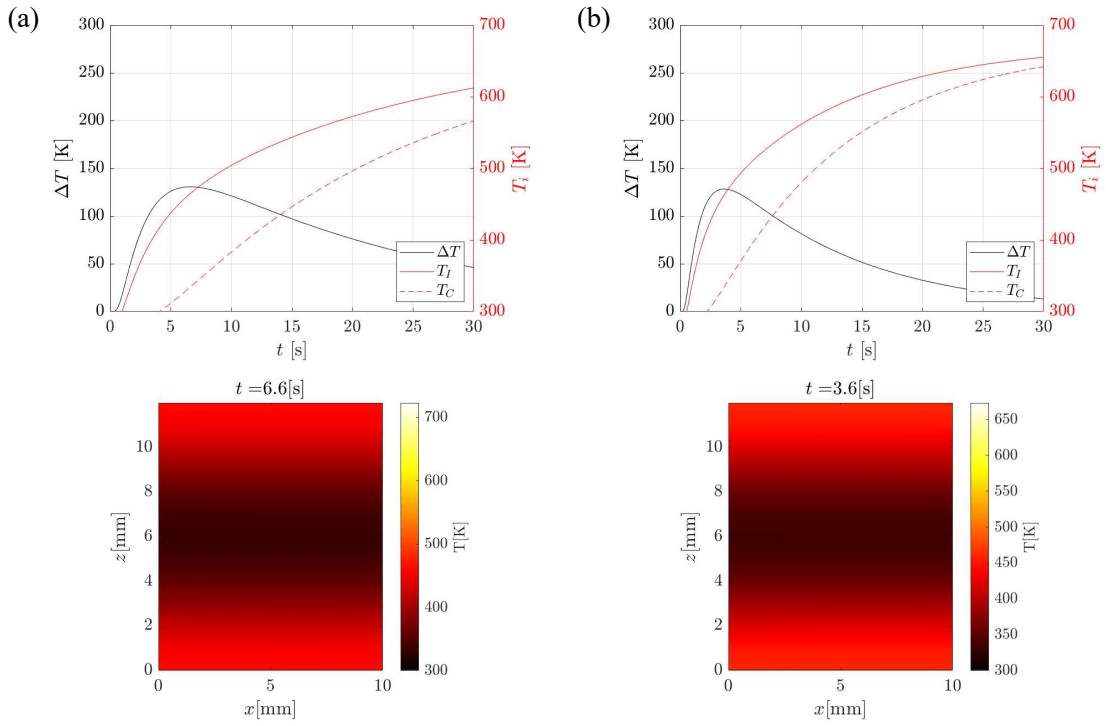


Figure 5.11: Comparison of ΔT evolution and surface temperature distributions with 3 mm thickness for (a) zirconia, and (b) ATZ.

Table 5.2: Structural safety analysis: Estimated critical temperature difference (ΔT_{crit}) versus operating conditions.

Material	σ_{fracture} [MPa]	ΔT_{crit} [K]	Predicted ΔT_{max} [K]	Safety Margin ($\Delta T_{\text{crit}}/\Delta T_{\text{max}}$)
MACOR	94	151	≈ 130	1.2
Zirconia	1200	600	≈ 130	4.6
ATZ	1800	662	≈ 130	5.1

Finally, the influence of the spanwise heating pitch (λ_z) on the thermal performance was evaluated using the optimised Zirconia substrate (3 mm thickness). Figure 5.12(a) compares the temporal evolution of ΔT for two spanwise configurations: a 12 mm pitch and a wider 20 mm pitch. The results demonstrated a significant performance advantage for the wider spacing. The 20 mm configuration achieved a peak temperature difference of $\Delta T \approx 210$ K, compared to 130 K for the 12 mm case. Furthermore, the decay rate of the thermal gradient was notably slower for the 20 mm pitch. This behaviour was attributed to the larger volume of unheated material between the heating elements, which acted as a thermal sink and delayed the spanwise thermal equilibration. Consequently, the 20 mm configuration was identified as capable of generating stronger and more persistent boundary-layer perturbations.

Final Heating Patch Configuration

Based on the thermal-design trade-off, the final heating patch utilised a Zirconia insert with a thickness of 3 mm. Although the thermal analysis suggested that thinner plates yield higher temperature gradients, the 3 mm thickness was dictated by manufacturing constraints. The stainless steel mounting base featured a stepped recess of 1.5 mm depth; a Zirconia plate thinner than 3 mm would compromise the structural integrity at the step interface during mounting and operation.

The streamwise length of the heating patch was determined using the DNS sensitivity studies presented in Section 5.3. The simulations indicated that the amplitude of the thermally induced streaks grows with streamwise distance and saturates after approximately 100 mm. Therefore, the patch length was fixed at approximately 94 mm to promote streak generation while avoiding an unnecessarily long heated region.

The final heating configuration included two spanwise periodic heater layouts designed to generate surface-temperature distributions with wavelengths of $\lambda_z = 12\,\text{mm}$ and 20 mm. Based on the DNS predictions, the local boundary-layer thickness near the instability-growth region was approximately $\delta_{99.5} \approx 1\,\text{mm}$. Consequently, the hardware produced non-dimensional spacings of $\lambda_z/\delta_{99.5} \approx 12$ and 20.

Although this spacing is larger than that considered in the preliminary Chapter 3 design study, the purpose of the Chapter 5 heating pattern is to impose a steady, large-scale spanwise modulation of the laminar/transitional mean boundary layer. This thermally induced mean-flow distortion modifies the local velocity and temperature fields encountered by the dominant instability waves, particularly the second Mack mode. The use of relatively large spacing is motivated by both aerodynamic and thermal considerations. From the aerodynamic perspective, the DNS and stability results discussed in Chapter 2 and Fig. 2.25a show that thermally induced streaks remain stabilising over relatively large spanwise wavelengths. In particular, Boscagli et al. [78] reported that second Mack mode stabilisation remained beneficial up to the largest wavelength considered, corresponding to $\lambda_z^* = 4.8$, with the strongest reduction occurring around $\lambda_z^* = 2.4$. This indicated that the effective wavelength range for thermally induced streak control is not limited to the smaller wavelengths explored in the preliminary Chapter 3 design study. From the thermal-actuation perspective, smaller spanwise spacings are less favourable for the present hardware because lateral conduction within the solid reduces the achievable

surface-temperature contrast. The thermal model and bench-top validation showed that the 20 mm configuration produced a larger and more persistent spanwise temperature difference than the 12 mm configuration. The larger pitch therefore provides a practical means of maintaining a stronger wall-temperature modulation during the short wind-tunnel test while remaining consistent with the DNS evidence that broad thermally induced streaks can attenuate second Mack mode growth.

5.3.4 Heater Fabrication and Validation

Heating System

The active heating inputs were generated by two cartridge-type electric heating elements (rated at 500 W, 230 V). These elements were mounted behind the Zirconia insert and controlled via a regulated AC power supply. To approximate the idealised line-source boundary condition used in the thermal model, the physical contact between each heater and the substrate was mechanically restricted to a narrow strip of 93×2 mm. High-temperature thermal grease was applied at this interface to smooth the contact interface and ensure uniform heating.

The cartridges were secured by a custom low-mass aluminium holder ($\approx$ 20 g). This lightweight design minimised the thermal mass of the assembly, allowing for rapid thermal response. Guided by the transient thermal analysis in Section 5.3.3, the operational protocol adopted a pre-heating duration of approximately 6.6 s and 13.6 s, respectively for each configuration, at maximum power. This duration allowed the Zirconia surface to achieve the peak target temperature gradient ($\Delta T_{\max}$) immediately prior to the wind-tunnel startup.

Bench-Top Thermal Characterisation

The thermal performance of the fabricated heating system was characterised using infrared thermography (IRT) prior to installation in the wind tunnel. Surface temperature distributions were recorded assuming a surface emissivity of $\epsilon \approx 0.7$ for the Zirconia substrate. Two spanwise heating configurations—a 12 mm pitch and a 20 mm pitch—were evaluated to validate the thermal condition.

The experimental results revealed a deviation from the numerical predictions regarding the transient rise time (Fig. 5.12(a)). While the numerical model assumed an instantaneous step-change in temper-

ature at the heater boundary, the physical system is governed by the thermal inertia of the cartridge elements. Consequently, the heating duration required to reach the target peak temperature ($\approx 600\,\mathrm{K}$) was extended from the predicted 30 s to 60 s. This slower ramp-up rate influenced the generation of spanwise gradients, as lateral conduction within the substrate smeared the temperature field before the peak was reached.

The impact of wavelength on gradient retention is shown in Fig. 5.12(a), which compares the temporal evolution of $\Delta\overline{T}$ (defined as the difference between the streamwise-averaged temperatures of the heated and unheated regions). At the 60-second mark, the 12 mm pitch case achieved an averaged spanwise temperature difference of only $\Delta\overline{T} = 37\,\mathrm{K}$. In contrast, the 20 mm configuration achieved a significantly higher difference of $\Delta\overline{T} = 85\,\mathrm{K}$. Due to the insufficient difference generated by the 12 mm case (see Fig. 5.12(a,b)), the 20 mm configuration was selected as the only control case for the wind tunnel experiments.

Based on these characterisation results, the operational protocol for the wind-tunnel experiments was defined. For the 20 mm configuration, the heating elements located at spanwise stations $z = 20\,\mathrm{mm}$ and 40 mm were powered for 60 s, then switched off ($t_{\mathrm{heat}} = 60\,\mathrm{s}$) simultaneously with the wind-tunnel startup. The primary data evaluation window was defined to start at $t = 62\,\mathrm{s}$ (2 seconds into the flow duration).

Figure 5.12(c) presents the 2D surface temperature contours at this evaluation time ($t = 62\,\mathrm{s}$). The spanwise distribution showed distinct thermal peaks at $z = 20\,\mathrm{mm}$ and 40 mm, separated by a cooler region along the model centerline ($z = 30\,\mathrm{mm}$). Quantitatively, the active heating zone exhibited a mean surface temperature of $\overline{T} = 462\,\mathrm{K}$. The local extrema occurred near $x = 84\,\mathrm{mm}$, where the temperature ranged from a minimum of $T_{\mathrm{min}} = 429\,\mathrm{K}$ in the unheated conductor centerline minima to a maximum of $T_{\mathrm{max}} = 541\,\mathrm{K}$ on the insulator peaks. Consequently, the peak local temperature difference reached 112 K, whereas the streamwise-averaged difference remained $\Delta\overline{T} = 85\,\mathrm{K}$. The streamwise profile was nominally uniform in both the conductor and insulator regions, though it exhibited a roll-off near the upstream and downstream edges due to conductive losses to the stainless steel mounting body. The downstream PCB sensors were positioned to capture these specific thermal footprints, allowing for a direct comparison of instability growth in the heated wakes versus the unheated centerline.

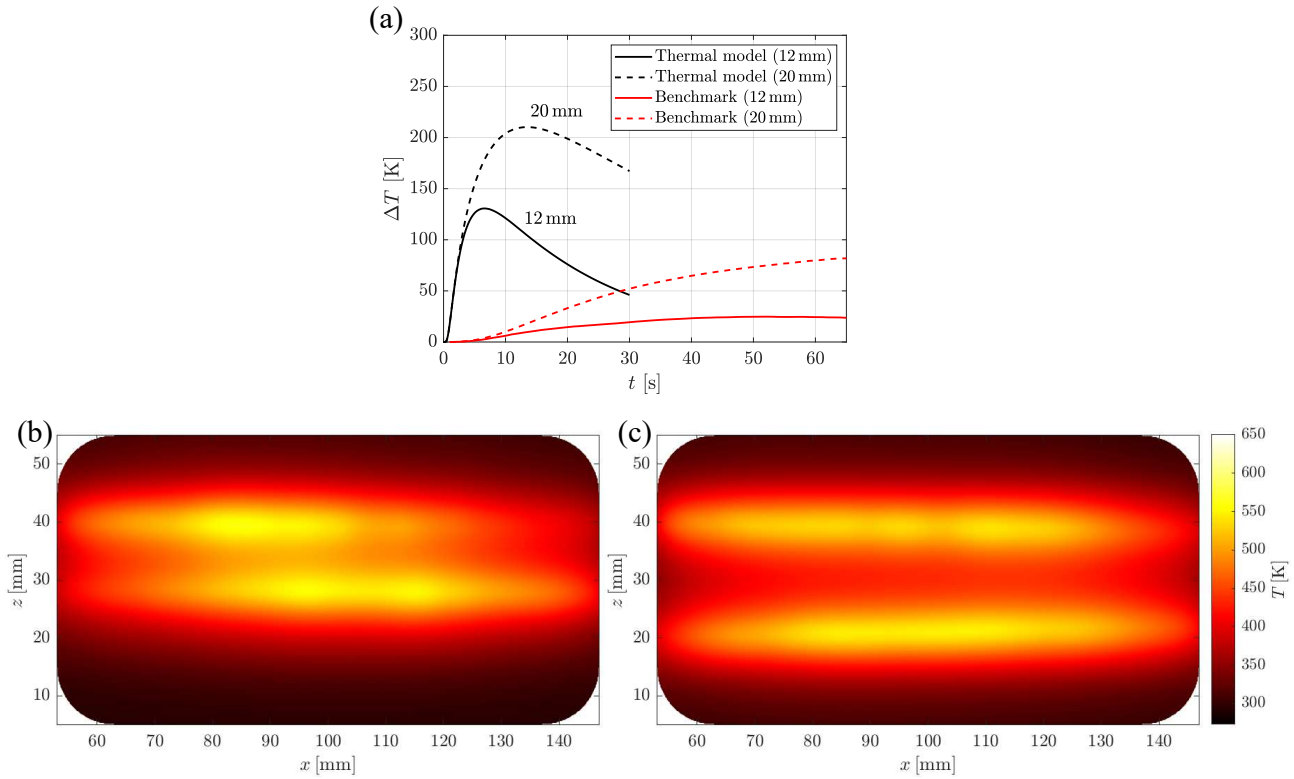


Figure 5.12: Bench-top thermal characterisation results. (a) Temporal evolution of the streamwise-averaged temperature difference ($\Delta\overline{T}$) for 12 mm and 20 mm configurations, comparing experimental measurements (red) with thermal model predictions (black). (b,c) Infrared temperature contour plot of the 12 mm, and 20 mm configurations, respectively, at the evaluation time (t=62 s).

5.4 Facility, Diagnostics, and Test Matrix

This section outlined the experimental apparatus and measurement techniques employed in this study. First, the specifications of the High Supersonic Tunnel were described, followed by details of the diagnostic instrumentation, which included high-frequency pressure sensors for spectral instability analysis and infrared thermography for surface temperature mapping. The section concluded with a definition of the experimental test matrix and the corresponding flow conditions.

5.4.1 High Supersonic Wind Tunnel

The experiments were conducted in the University of Manchester High Supersonic Tunnel (HSST). This facility is an intermittent, blow-down wind tunnel designed to generate Mach 5 flow. The tunnel operates by discharging compressed dry air from a high-pressure reservoir through an axisymmetric convergent-divergent nozzle into a test chamber connected to a vacuum tank. Independent control of stagnation pressure (P_0) and stagnation temperature (T_0) is maintained via a pressure regulating valve and a 15 kW electric resistive heater, capable of achieving temperatures up to 950 K. The test section utilises an open-jet configuration. For the current campaign, the standoff distance between the nozzle exit and the diffuser intake was set to approximately 250 mm. Optical access for infrared thermography was provided by a germanium window mounted on the top wall of the chamber. The model was supported by a rail system that allowed for precise streamwise positioning relative to the nozzle exit. The facility delivered steady supersonic flow for approximately 5 s, with a startup transient of less than 0.1 s. Two distinct operating conditions were selected for this study, summarised in Table 5.3. Case 1 represents a cold flow condition ($T_0 = 300$ K), yielding a high unit Reynolds number of $Re = 11.0 \times 10^6\,\mathrm{m}^{-1}$. Case 2 represents a heated flow condition ($T_0 = 600$ K), which reduces the unit Reynolds number to $Re = 4.8 \times 10^6\,\mathrm{m}^{-1}$. While the facility nozzle produces a freestream Mach number of $M = 5.0$, the 5-degree compression angle of the waverider model (described in Sec. 5.3.1) generates a post-shock boundary layer edge Mach number of approximately $M_e = 4.5$. The corresponding adiabatic wall recovery temperatures (T_r) on the test surface are approximately 261 K and 522 K for Case 1 and Case 2, respectively.

Table 5.3: Nominal flow conditions for the experimental campaign. Post-shock values correspond to the flow properties downstream of the waverider leading edge shock.

	Freestream Conditions ($M_\infty = 5.0$)				Post-Shock ($M_e = 4.5$)	
Condition	P_0 [kPa]	T_0 [K]	T_∞ [K]	Re [m^{-1}]	T_e [K]	T_r [K]
Case 1	300	300	50	11.0×10^6	60	261
Case 2	500	600	100	4.8×10^6	119	522

5.4.2 High-Frequency Pressure Instrumentation

High-frequency wall pressure fluctuations associated with the second Mack mode instability were resolved using piezoelectric pressure sensors (PCB Piezotronics, Model 132B38). These sensors feature a nominal resonant frequency greater than 1 MHz, providing a high-frequency response bandwidth sufficient to resolve the target second Mack mode instabilities ($f \approx 200 - 400$ kHz). The sensors were flush-mounted within the modular resin insert using a silicone adhesive to ensure a smooth aerodynamic interface and to isolate the sensing elements from structural vibration. The analogue output from the sensors was amplified and filtered by a signal conditioner (PCB 482C05). Data digitisation was performed using a PicoScope 6404C digital oscilloscope operating at a sampling rate of 3 MHz. The acquisition was triggered by the wind tunnel startup, capturing a continuous 5 s time series. To characterise the temporal evolution of the instability growth, the signal was segmented into 0.1 s interrogation windows for spectral analysis. Figure 5.5(b) illustrates the arrangement of the four pressure sensors within the downstream sensing insert.

5.4.3 Infrared Thermography System

Infrared thermography (IRT) was employed to obtain global surface temperature distributions and to infer convective heat transfer coefficients. The imaging system consisted of a FLIR A6750 mid-wave infrared (MWIR) camera with a spectral range of 3.0–5.0 μm. The camera viewed the test model through a germanium optical window mounted on the top wall of the test section. Data acquisition was performed at a full-frame rate of 125.7 Hz with an integration time optimised to prevent saturation during the heating phase. The acquisition system was synchronised with the wind tunnel startup trigger, configured with a 3 s pre-trigger buffer to capture the initial thermal state of the model prior to flow arrival. To ensure radiometric accuracy, a dedicated calibration was performed to account for

the transmissivity of the germanium window and the optical path. A Fluke 9132 portable infrared calibrator was utilized as a reference quasi-blackbody source ($\epsilon = 0.95$). The source was imaged through the optical window over a temperature range of 293 K to 573 K in 10 K increments, generating a transfer function between the camera digital levels and the surface temperature. The spectral transmissivity of a representative uncoated germanium window is shown in Fig. 5.13. Germanium transmits over the MWIR band used by the FLIR A6750 camera, but the absolute transmission of an uncoated window is limited by Fresnel reflection losses at the two air–germanium interfaces. Since the in-situ calibration was performed through the same window and optical path, the mean transmission effect is incorporated into the calibration curve. The transmissivity curve is nevertheless included to document the optical path and to identify wavelength-dependent transmission as a residual uncertainty in the infrared thermography measurement. For post-processing, surface emissivity values were assigned based on the material properties: $\epsilon = 0.95$ for the high-emissivity resin sensing insert and $\epsilon = 0.7$ for the zirconia heating patch.

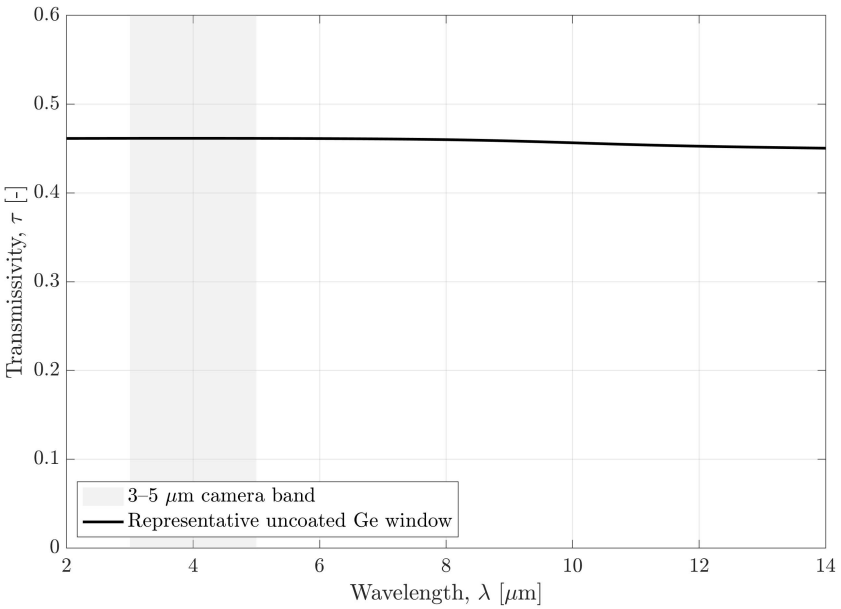


Figure 5.13: Representative spectral transmissivity of an uncoated germanium optical window used for infrared thermography. The shaded region indicates the 3–5 μm sensitivity range of the FLIR A6750 MWIR camera.

5.4.4 Test Matrix and Experimental Conditions

To quantify the influence of spanwise non-uniform surface heating on boundary layer disturbance growth, a structured test matrix was defined. The experimental matrix was designed to decouple the

effects of mean surface temperature (global heating) from the effects of spanwise thermal gradients (local heating).

To facilitate the non-dimensional scaling of the heating geometries, the reference laminar boundary layer thickness ($\delta_{99.5}$) was estimated using the compressible flat plate correlation provided by White [83], consistent with the methodology employed by Ivison [104]:

$$\delta_{99.5} = \frac{x}{\sqrt{Re_x}}\sqrt{C_w}\left[5 + \left(0.2 + 0.9\frac{T_w}{T_{aw}}\right)(\gamma - 1)M_e^2\right], \tag{5.2}$$

where M_e is the edge Mach number, T_{aw} is the adiabatic wall temperature, and $C_w = (\rho_w \mu_w)/(\rho_e \mu_e)$ is the Chapman-Rubesin parameter evaluated at wall conditions. For the test matrix definitions, $\delta_{99.5}$ was calculated at the streamwise station $x = 100\,\text{mm}$. This location was selected as the reference point because the LST results in Sec. 5.3.2 predicted the onset of significant second Mack mode amplification in this region, which also coincided with the centre of the heating patch. The complete test matrix is summarised in Table 5.4. The experiments were divided into two main flow categories:

Case 1 ($T_0 = 300\,\text{K}$): This condition ($Re = 11.0 \times 10^6\,\text{m}^{-1}$) was originally defined to replicate the flow parameters used in the Mach 5 DNS and LST computations presented in Sec. 5.3. Although the numerical analyses were conducted at Mach 5, the effective edge Mach number in the present experiments was $M_e = 4.5$ due to the imposed flow deflection. In addition, differences in facility operating pressure precluded exact matching of the unit Reynolds number: the LST computations employed $Re = 2.5 \times 10^7\,\text{m}^{-1}$, whereas the experiments were performed at $Re = 1.1 \times 10^7\,\text{m}^{-1}$. Consequently, the numerical and experimental conditions are not strictly identical in either viscous or compressibility scaling. Preliminary pressure measurements at the HSST facility, however, indicated that the boundary layer was already fully turbulent over the sensing region under these conditions. It is inferred that the comparatively elevated freestream turbulence intensity in the HSST facility introduced disturbances of sufficiently large initial amplitude at the leading edge, which were subsequently amplified within the boundary layer and led to premature transition upstream of the measurement region. Consequently, this case was restricted to the nominal wall temperature ($T_w = 291\,\text{K}$) to serve as a high-Reynolds-number reference, and no heating control experiments were conducted.

Case 2 ($T_0 = 600\,\text{K}$): This lower unit Reynolds number condition ($Re = 4.8 \times 10^6\,\text{m}^{-1}$) maintained a laminar/transitional boundary layer, making it the primary focus for the heating control study. The

sub-cases include:

- **Uniform Heating Baseline:** Four uniform wall temperature conditions ($T_w = 291, 423, 473, 513\,\mathrm{K}$) were tested ($\lambda_z = \infty$). This range was chosen to characterise the effect of bulk wall heating on instability amplification.
- **Non-Uniform Heating:** The selected 20 mm pitch configuration was tested ($\lambda_z \approx 13\delta_{99}$). Crucially, the spatially averaged wall temperature for this case was $\overline{T}_w = 462\,\mathrm{K}$. Consequently, the uniform $T_w = 473\,\mathrm{K}$ case served as the primary comparative baseline in order to assess the effect of the spanwise gradient.

Table 5.4: Summary of the experimental test matrix. The uniform $T_w = 473\,\mathrm{K}$ case serves as the baseline for comparison with the non-uniform heating configuration ($\overline{T}_w = 462\,\mathrm{K}$).

Condition	Patch T configuration	T_0 [K]	$\overline{T}_w$ [K]	$\delta_{99.5}$ [mm]	λ_z
Case 1	Uniform	300	291	1.4	∞
Case 2	Uniform	600	291	1.3	∞
	Uniform	600	423	1.5	∞
	Uniform (Baseline)	**600**	**473**	**1.5**	$\boldsymbol{\infty}$
	Uniform	600	513	1.6	∞
	Non-Uniform heating	600	462	1.5	$13\delta_{99.5}$

5.4.5 Measurement Uncertainty and Interpretation

The interpretation of the Chapter 5 measurements is affected by uncertainties associated with the flow condition, thermal actuation, infrared thermography, heat-flux reconstruction, radiation heat transfer, and high-frequency pressure measurements. These uncertainties primarily affect the absolute values of the reconstructed wall temperature, heat flux, Stanton number, and pressure-spectrum amplitude. The main conclusions of this chapter are therefore based on relative comparisons between cases acquired using the same facility, model, instrumentation, and post-processing procedure.

Infrared Thermography, Heat-Flux Reconstruction, and Radiation

For the infrared thermography measurements, the principal uncertainty sources are the camera calibration, the germanium-window transmissivity, the assumed surface emissivity, reflected ambient

radiation, viewing angle, and the material properties used to infer heat flux from the measured surface-temperature evolution. The calibration was performed through the germanium window and the same optical path used during the experiments, so the mean effect of the window transmission is included in the temperature calibration. However, wavelength-dependent transmission and possible spatial non-uniformity of the window remain sources of uncertainty. The spectral transmissivity of a representative uncoated germanium window over the camera sensitivity range is therefore included in Fig. 5.13.

The emissivity of the resin sensing insert and zirconia heating patch was treated as constant during post-processing, with representative values of $\epsilon = 0.95$ and $\epsilon = 0.7$, respectively. This assumption is considered acceptable for assessing the short-duration thermal response because the surface-temperature variation during the measurement interval is only $O(10\,\mathrm{K})$, so temperature-dependent changes in emissivity are expected to be small compared with the absolute uncertainty in the assumed emissivity. Nevertheless, the lower emissivity of zirconia makes the absolute temperature estimate over the heating patch more sensitive to emissivity uncertainty than that over the high-emissivity resin insert. Consequently, the infrared-derived heat flux and Stanton number are used primarily to assess relative streamwise and case-to-case heat-transfer trends, rather than to provide high-precision absolute heat-transfer values.

Additional uncertainty is introduced when converting the measured surface-temperature history into heat flux and Stanton number using the impulse-response method [105]. The heat-flux reconstruction depends on the temporal temperature response, the thermal properties of the substrate, the assumed one-dimensional conduction response implicit in the impulse method, impulse-response filtering, pixel registration, and spatial averaging. Lateral conduction within the resin can also smooth local temperature gradients, particularly near material interfaces and near the spanwise heating pattern. These effects can shift the absolute magnitude of $\dot{q}$ and St, but they are not expected to remove the observed relative difference between the uniform-heating and non-uniform-heating cases because both cases are processed using the same method and assumptions.

Radiative heat transfer was also estimated to assess the error associated with neglecting radiation. The radiative heat flux can be approximated as

$$\dot{q}_{\mathrm{rad}} = \epsilon\sigma \left(T_w^4 - T_{\mathrm{sur}}^4\right), \tag{5.3}$$

where ϵ is the surface emissivity, σ is the Stefan–Boltzmann constant, T_w is the wall temperature, and T_{sur} is the surrounding tunnel-wall temperature, taken here as approximately 300 K. The importance of this term differs between the upstream zirconia heating patch and the downstream resin sensing insert.

For the zirconia heating patch, representative wall temperatures are $T_w \approx 423$–$513\,\mathrm{K}$. Using the zirconia emissivity adopted in the infrared post-processing, $\epsilon = 0.7$, gives $\dot{q}_{\mathrm{rad}} \approx 0.95\,\mathrm{kW\,m^{-2}}$ at 423 K, $1.67\,\mathrm{kW\,m^{-2}}$ at 473 K, and $2.43\,\mathrm{kW\,m^{-2}}$ at 513 K. Radiation is therefore a non-negligible contribution to the thermal balance of the hot heating patch, particularly because the convective heat flux decreases as T_w approaches the recovery temperature.

A representative comparison with the convective heat-transfer level can be made using $\dot{q}_{\mathrm{conv}} \approx h(T_r - T_w)$. For the Case 2 condition, $T_r \approx 522\,\mathrm{K}$. Using the laminar Stanton-number estimate over the heating-patch region, $St_x = 0.332 Re_x^{-1/2} Pr^{-2/3}$, with $Re = 4.8 \times 10^6\,\mathrm{m^{-1}}$ and $x = 53$–$147\,\mathrm{mm}$, gives $h \approx 17$–$33\,\mathrm{W\,m^{-2}\,K^{-1}}$. The corresponding convective heat-transfer scale is therefore approximately 2.0–3.0 $\mathrm{kW\,m^{-2}}$ at $T_w = 423\,\mathrm{K}$, 1.0–1.5 $\mathrm{kW\,m^{-2}}$ at $T_w = 473\,\mathrm{K}$, and 0.18–0.27 $\mathrm{kW\,m^{-2}}$ at $T_w = 513\,\mathrm{K}$. Compared with the corresponding radiative heat fluxes of 0.95, 1.67, and $2.43\,\mathrm{kW\,m^{-2}}$, radiation is a significant part of the hot-patch energy balance and can dominate when T_w approaches the recovery temperature.

The zirconia heating-patch temperature was not measured directly during wind-tunnel operation; instead, the transient thermal behaviour of the heating patch was characterised in the bench-top validation tests prior to the wind-tunnel campaign. The thermal model was used only during the initial material and design assessment, and not as the basis for determining the realised heating-patch temperature in the final experiment. Since the pressure and infrared measurements are evaluated within the first few seconds of the run, typically approximately 1–2 s after tunnel start, the cumulative influence of radiation on the solid temperature field is limited by the short exposure time and the thermal inertia of the heating patch. Using the 3 mm zirconia thickness and the material properties in Table 5.1, the areal heat capacity of the patch is approximately $\rho c_p d \approx 8.7\,\mathrm{kJ\,m^{-2}\,K^{-1}}$. Even a radiative heat loss of $2.4\,\mathrm{kW\,m^{-2}}$ acting over 1–2 s corresponds to an idealised bulk temperature change of only 0.3–0.6 K. Radiation is therefore important in the instantaneous thermal balance, but its cumulative effect over the early measurement interval is small compared with the imposed spanwise

wall-temperature difference. Neglecting radiation may therefore bias the absolute thermal balance and the exact imposed ΔT, but it does not remove the imposed finite spanwise wall-temperature modulation.

For the downstream resin sensing insert, which is used for the infrared-derived heat-flux and Stanton-number trends, the surface-temperature variation during the measurement interval is much smaller, typically $O(10\,\mathrm{K})$. For example, using $\epsilon = 0.95$, the radiative heat flux relative to surroundings at 300 K is approximately $0.13\,\mathrm{kW\,m^{-2}}$ at 320 K and $0.20\,\mathrm{kW\,m^{-2}}$ at 330 K. This contribution is small relative to the convective heat-transfer levels inferred from the transient temperature response on the sensing insert. Consequently, neglecting radiation has a larger effect on the absolute thermal balance of the zirconia heating patch than on the relative heat-transfer trends measured over the resin sensing insert.

The omission of radiation is therefore treated as a source of uncertainty in the realised wall-temperature field, especially over the heated zirconia region. However, it is not expected to alter the main pressure-based conclusion, because the pressure spectra are compared between cases using the measured experimental state. It is also not expected to change the qualitative infrared-derived heat-transfer trend over the downstream sensing insert, although it may introduce a small bias in the absolute heat-flux and Stanton-number values.

Surface Roughness and Material Interfaces

The Chapter 5 experiment used exposed stainless steel, zirconia, and resin surfaces without an additional surface coating. Therefore, possible mechanical-roughness differences between the materials must be considered separately from coating-related roughness effects. The stainless-steel model surface and resin sensing insert were sanded using #2000 abrasive paper before testing, while the zirconia heating patch was supplied with a smooth surface finish. No intentional roughness elements were introduced.

The possible influence of surface roughness was estimated using the roughness Reynolds number defined in Eq. (4.4), with the friction velocity estimated from Eq. (4.5). The estimate was based on the Case 2 condition, since this is the transitional condition used for the main non-uniform heating comparison. Using the Case 2 unit Reynolds number $Re = 4.8 \times 10^6\,\mathrm{m^{-1}}$, the local Reynolds number

at the upstream edge of the resin sensing insert, $x = 167\,\mathrm{mm}$, is

$$Re_x = xRe = 4.8 \times 10^6 \times 0.167 \approx 8.0 \times 10^5. \tag{5.4}$$

Using a laminar flat-plate estimate,

$$C_f \approx \frac{0.664}{\sqrt{Re_x}} \approx 7.4 \times 10^{-4}, \tag{5.5}$$

gives

$$k_s^+ = Rek_s\sqrt{\frac{C_f}{2}}. \tag{5.6}$$

For representative equivalent roughness heights of $k_s = 2$, 5, and $10\,\mu$m, this gives

$$k_s^+ \approx 0.18, \quad 0.46, \quad 0.92, \tag{5.7}$$

respectively.

The same estimate can be repeated at the upstream edge of the zirconia heating patch, $x = 53\,\mathrm{mm}$, which gives a larger local skin-friction estimate because of the smaller Re_x. In this case, $Re_x \approx 2.5 \times 10^5$, $C_f \approx 1.3 \times 10^{-3}$, and

$$k_s^+ \approx 0.25, \quad 0.62, \quad 1.23 \tag{5.8}$$

for $k_s = 2$, 5, and $10\,\mu$m, respectively. Thus, for the expected roughness range of the prepared surfaces, $k_s = 2$–$5\,\mu$m, the roughness Reynolds number remains below unity over both the heating and sensing regions. Even the more conservative $k_s = 10\,\mu$m estimate gives a value only of order unity.

The exposed stainless-steel, zirconia, and resin surfaces are therefore expected to behave as hydraulically smooth surfaces for the purposes of the present boundary-layer measurements. Material interfaces may still introduce small local discontinuities in surface height, thermal properties, or wall temperature. However, the main comparison between uniform-heating and non-uniform-heating cases is made using the same model geometry and material layout. Any residual roughness or interface effect is therefore common to the compared cases, whereas the imposed spanwise wall-temperature

distribution is the controlled variable. Mechanical roughness differences between the exposed materials are consequently not expected to account for the observed pressure-spectral changes or the relative infrared-derived heat-transfer trends.

High-Frequency Pressure Measurements

The high-frequency pressure measurements contain uncertainties associated with sensor sensitivity, mounting flushness, silicone bonding, signal conditioning, sampling rate, spectral-window length, structural vibration, and facility acoustic noise. The PCB 132B38 sensors have a specified frequency response of 11 kHz to 1 MHz, which is sufficient to resolve the target second Mack mode frequency band considered in this study. The use of the same sensors, acquisition system, and spectral-processing procedure for the uniform and non-uniform heating cases means that the comparison of spectral trends is more robust than the absolute pressure-spectrum level. The 0.1 s interrogation windows provide a compromise between temporal localisation during the transient run and frequency resolution for identifying the dominant instability band. Unexplained spectral features outside the target instability band are not used to support the control-effectiveness conclusion unless they can be linked to the instability mechanism or shown to be repeatable across comparable cases.

Flow-Condition and Thermal-Actuation Uncertainty

Uncertainty in the nominal flow condition also affects interpretation of the results. Variations in stagnation pressure, stagnation temperature, model alignment, leading-edge shock position, and the timing of the wind-tunnel start-up can alter the local Reynolds number, recovery temperature, and boundary-layer thickness. These variations can shift the precise instability frequency and transition location. Therefore, the pressure spectra are not interpreted as providing an exact quantitative stability margin or N-factor reduction. Instead, they are used to identify whether the imposed non-uniform heating produces a measurable modification of the instability environment relative to the corresponding uniform-heating cases.

The thermal actuation itself is also subject to uncertainty. Cartridge-heater contact resistance, heater-to-heater variation, initial wall-temperature non-uniformity, and thermal-property uncertainty affect the realised spanwise wall-temperature distribution. Bench-top thermal validation was therefore used

to confirm that the selected heating configuration produced a measurable and repeatable spanwise temperature difference before wind-tunnel testing. The exact imposed ΔT should still be regarded as uncertain, but the presence of a finite spanwise wall-temperature modulation is robust.

Implications for the Chapter Conclusions

Overall, the uncertainties discussed above limit the precision with which absolute heat flux, Stanton number, and pressure-spectrum amplitudes can be reported. They do not, however, change the main interpretation of the Chapter 5 experiment: the non-uniform heating case produces a measurable change in the wall-pressure spectra relative to comparable uniform-heating cases, and the infrared-derived heat-transfer trend is consistent with a downstream-shifted rise in surface heat transfer. The conclusion is therefore stated in terms of measurable modification of the instability environment and heat-transfer trends consistent with delayed transition, rather than as a definitive quantitative measurement of transition delay or instability N-factor reduction.

5.5 Results and Discussion

This section presented the experimental results characterising the boundary layer and the response to thermal forcing. First, the baseline boundary layer was established. Second, the sensitivity of the frequency content of the pressure spectra to uniform wall heating was quantified. Finally, the influence of spanwise non-uniform heating on the boundary layer was analysed by comparing the case with the thermally generated streaks under actively heated conditions against the baseline configuration with spanwise uniform surface temperature.

5.5.1 Boundary Layer State Characterisation

The establishment of the hypersonic base flow maintained by the waverider model was validated using spanwise schlieren visualisation. Figure 5.14 presents a representative Schlieren image for the Case 1 ($T_0 = 300\,\mathrm{K}$) condition. The image confirmed that the leading-edge shock wave—which originated from the nozzle-inserted leading edge—was well established and attached to the exposed side sharp leading edges. This insertion configuration ensured the test surface remained within the uniform flow

core, avoiding interaction with the nozzle exit lip shock, while also mitigating unstart and leakage from the test surface.

To characterise the state of the boundary layer, the spectral content of the wall pressure fluctuations was analysed for the two unit Reynolds number cases defined in the test matrix. Figure 5.15 compares the Power Spectral Density (PSD) of the wall pressure signals measured at the centerline location ($x = 232\,\text{mm}$).

Case 1 ($T_0 = 300\,\text{K}$): The spectrum exhibited a broadband elevation in energy, gradually decaying. This spectral signature suggested that the boundary layer was likely turbulent over the sensing region at this high unit Reynolds number ($Re = 11 \times 10^6\,\text{m}^{-1}$). Consequently, this case served primarily as a facility reference and was excluded from the transition control analysis.

Case 2 ($T_0 = 600\,\text{K}$): In contrast, the lower unit Reynolds number case ($Re = 4.8 \times 10^6\,\text{m}^{-1}$, $T_w = 291\,\text{K}$) displayed a discrete spectral signature (red line). A prominent peak was observed centred approximately at $f \approx 170\,\text{kHz}$. This frequency range was consistent with prior experimental observations of the second Mack mode instability in similar hypersonic boundary layers, tested at $Re_\infty = 4 \times 10^6\,\text{m}^{-1}$, $T_0 = 454\,\text{K}$ [33]. Based on this similarity, the observed peak was attributed to the second Mack mode instability for the purposes of the present study. However, further investigation with the support of computations would be required to confirm this spectrum.

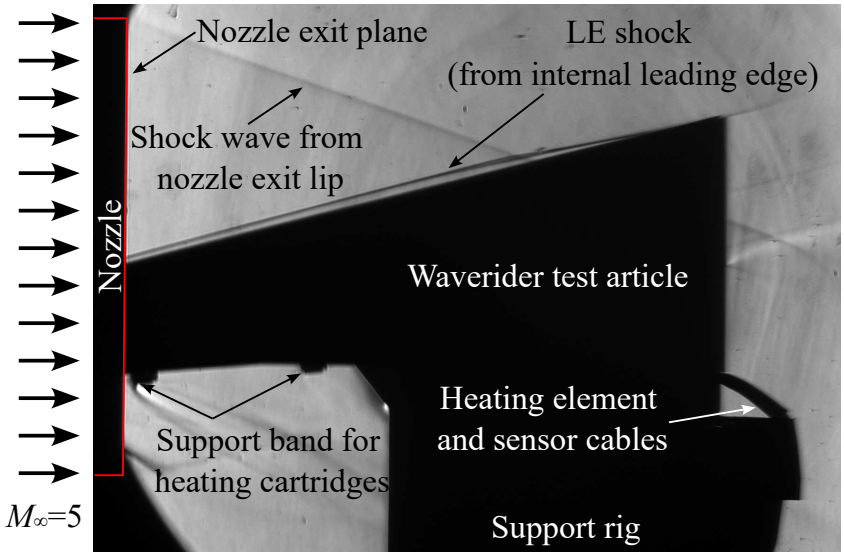


Figure 5.14: Schlieren visualisation at Mach 5 (Case 1). The waverider leading edge (LE) is positioned internally within the nozzle to ensure mitigation of blockage. The visible LE shock wave originates upstream of the nozzle exit plane.

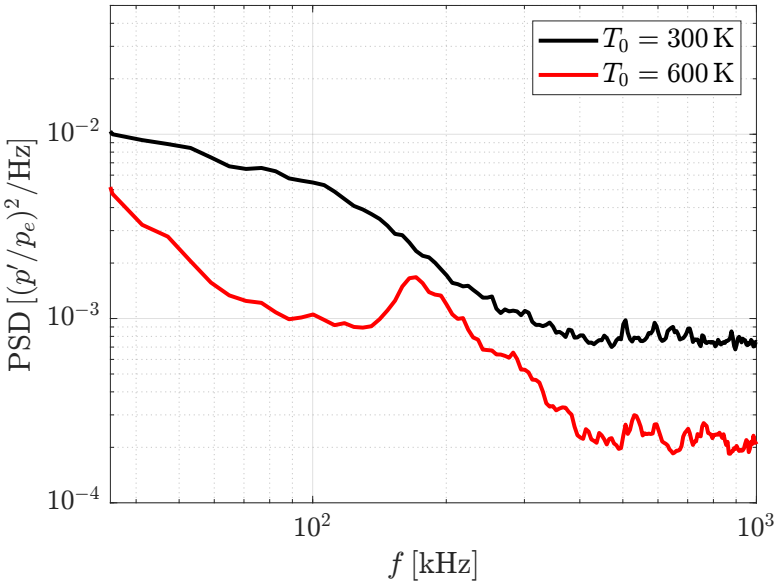


Figure 5.15: Comparison of wall pressure power spectral density (PSD) at $x = 232\,\mathrm{mm}$. The Case 1 ($Re = 11 \times 10^6\,\mathrm{m}^{-1}$) spectrum exhibits broadband turbulent fluctuations, while Case 2 ($Re = 4.8 \times 10^6\,\mathrm{m}^{-1}$) retains a laminar baseline with a distinct second Mack mode instability peak visible near $f \approx 170\,\mathrm{kHz}$.

5.5.2 Effect of Uniform Wall Temperature

Before assessing the non-uniform forcing, the state of the instability to the mean wall temperature was qualitatively assessed using the pressure spectra. Figure 5.16 presents the evolution of the wall pressure spectra at $x = 192$ and $232\,\mathrm{mm}$ for the three uniform heating cases, ranging from minimum heating ($T_w = 423\,\mathrm{K}$) to the maximum heated condition ($T_w = 513\,\mathrm{K}$).

The results indicated a consistent reduction of the variance with increasing wall temperature across both streamwise locations.

- **Upstream ($x = 192\,\mathrm{mm}$):** The spectra exhibited broadband energy elevations with local peaks identifiable around $f \approx 100\,\mathrm{kHz}$ and $250\,\mathrm{kHz}$. The highest spectral energy was observed at the lowest temperature case ($T_w = 423\,\mathrm{K}$, green line), while the maximum heating case ($T_w = 513\,\mathrm{K}$, red line) showed the greatest suppression.
- **Downstream ($x = 232\,\mathrm{mm}$):** The spectral peaks shifted to slightly higher frequencies, with signatures visible around $280\,\mathrm{kHz}$ and $325\,\mathrm{kHz}$. Notably, the lower-frequency peak observed around $100\,\mathrm{kHz}$ at the upstream location collapsed significantly at this station. This decay suggested a complex interaction, potentially involving the stabilisation of the second Mack mode

or interactions with lower-frequency first-mode disturbances. However, further analysis would be required to definitively identify the mechanism.

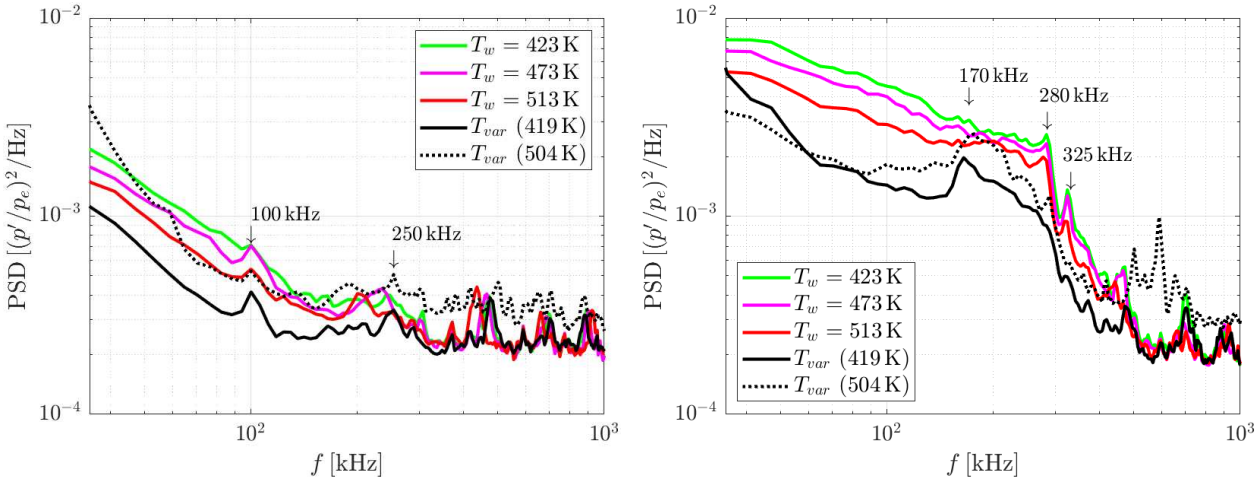


Figure 5.16: Evolution of wall pressure power spectral density (PSD) at (a) $x = 192\,\text{mm}$ and (b) $x = 232\,\text{mm}$. The plots compare uniform wall heating cases ranging from 423 K (green) to 513 K (red), with non-uniform heating cases (black).

5.5.3 Impact of Spanwise Non-Uniform Heating

The primary objective of this study was to isolate the effect of spanwise thermal gradients on instability growth. The non-uniform heating case ($\lambda_z = 13\delta_{99.5}$) imposed a spanwise periodic temperature field characterised by heated "Side" regions ($T_w = 504\,\text{K}$) and cooler centreline minima ($T_w = 419\,\text{K}$). The spectral response to this forcing was analysed by referencing the wall pressure spectra presented previously in Fig. 5.16, where the non-uniform data are plotted as black lines (Solid = Centre/Centerline minima; Dashed = Side/Peak).

The significant finding arose from comparing the non-uniform centre location (solid black line) against the uniform heating case with nearly identical local conditions. The non-uniform centreline minimum temperature was $T_w = 419\,\text{K}$, which was thermally similar to the uniform $T_w = 423\,\text{K}$ case (green line). While this uniform condition resulted in the highest spectral energy among all tested cases, the locally equivalent non-uniform region exhibited the lowest variance below 300 kHz at $x = 192$ and 232 mm.

The sensor located in the heated wake (side, dashed black line, $T_w = 504\,\text{K}$) exhibited a spectral

energy level generally comparable to that of the maximum uniform heating case ($T_w = 513\,\mathrm{K}$, red line). This indicated that, locally, the heated peak region sustained disturbance levels similar to those observed under uniformly high wall temperature conditions, whereas the spanwise temperature gradients suppressed disturbances within the centeline minima. A further notable feature emerged at the downstream station $x = 232\,\mathrm{mm}$. At this location, the spectra obtained at the peak and minima positions in the non-uniform case exhibited a near-collapse, with both showing similarly reduced PSD levels. This contrasted with the upstream station at $x = 192\,\mathrm{mm}$, where the peak location retained substantially higher energy, comparable to the uniformly heated cases. An additional peak is observed near 600 kHz on the hot side of the non-uniform heating case at $x = 232\,\mathrm{mm}$. The physical origin of this feature is presently unclear, and it is therefore not interpreted as part of the control mechanism. The discussion here focuses on the dominant instability band identified from the LST guidance and from the uniform-heating reference cases. The downstream reduction of spectral energy even at the locally heated peak positions indicated that the influence of the imposed spanwise thermal modulation extended beyond the centerline minimum regions and progressively modified the disturbance field across the span. The attenuation of PSD levels across both streak phases downstream therefore suggests a progressive stabilising effect associated with the thermally induced streak structure. Consequently, while the spectral modification is evident, the ultimate impact of this complex spanwise distribution on the downstream transition location requires further characterisation.

Figure 5.17 presents a comparison of the surface heat flux between the uniform ($T = 473\,\mathrm{K}$) and non-uniform (T_{var}) wall temperature cases. The contour plots revealed a distinct difference in the downstream thermal footprint: while the uniform baseline (Fig. 5.17a) exhibited a region of elevated heat flux emerging downstream of $x \approx 200\,\mathrm{mm}$, the non-uniform case (Fig. 5.17b) remained comparatively cool across the entire span. This observation was quantified in Fig. 5.18a, which compares the streamwise evolution of the heat flux. Representative uncertainty bands have been added to Fig. 5.18 to provide a quantitative indication of the uncertainty in the infrared-derived heat-transfer quantities. For $\dot{q}$, the uncertainty band was obtained by combining contributions from the infrared temperature-rise uncertainty, resin thermal-property uncertainty, impulse-response heat-flux reconstruction sensitivity, the one-dimensional conduction assumption, and the small radiation correction over the downstream resin sensing insert. These contributions gave a representative combined uncertainty of $\pm 13\%$ for $\dot{q}$. For St, this heat-flux uncertainty was further propagated through the normal-

isation by $\rho_e U_e c_p(T_{aw} - T_w)$, giving a representative combined uncertainty of $\pm 15\%$. The details of this uncertainty estimate are given in Section 5.4.5. The shaded bands in Fig. 5.18 should therefore be interpreted as representative combined measurement and reconstruction uncertainties, rather than pointwise statistical confidence intervals. The PCB pressure-sensor locations are marked by the vertical dash-dot lines. The infrared-derived $\dot{q}$ and St values are still plotted across these regions, but they should be interpreted with greater caution because the local surface is interrupted by the sensor installations and the one-dimensional conduction assumption is less reliable in their immediate vicinity. The uniform case (red line, spanwise-averaged $\dot{q}$) exhibited a pronounced downstream rise in heating rate, consistent with the onset and progression of boundary-layer transition. In contrast, the non-uniform case (T_{var}, blue line) showed a more gradual, near-monotonic increase, indicating delayed transition. Although the $\dot{q}$ uncertainty bands overlap locally, the uniform-heating case remains systematically higher than the non-uniform-heating case over most of the downstream resin sensing insert. The uncertainty therefore limits the precision of the absolute heat-flux values, but it does not remove the observed case-to-case trend that the T_{var} case exhibits a lower downstream heat-transfer level than the corresponding $T = 473\,\mathrm{K}$ case. Figure 5.18b shows the corresponding streamwise evolution of the Stanton number (St), together with Eckert laminar and turbulent reference correlations. Over the measurement window, the uniform $T = 473\,\mathrm{K}$ case increases from $St \approx 2.6 \times 10^{-3}$ to $St \approx 3.5 \times 10^{-3}$, whereas the T_{var} case remains lower, rising from $St \approx 1.9 \times 10^{-3}$ to $St \approx 2.6 \times 10^{-3}$. The same interpretation holds when the $\pm 15\%$ Stanton-number uncertainty band is considered. The uncertainty affects the absolute magnitude of St, but the $T = 473\,\mathrm{K}$ case still shows a stronger downstream rise and trends closer to the turbulent reference correlation than the T_{var} case. Accordingly, the uniform case trends toward the Eckert turbulent correlation downstream, while T_{var} stays closer to the laminar reference, consistent with a suppressed or delayed transition process. These results suggest that the induced streamwise streaks influence instability development; however, further quantitative analysis is required to fully characterise this interaction.

5.6 Summary

A waverider-based Mach 5 test article was developed to investigate transition control using spanwise-periodic surface heating, with the heating-patch geometry and sensor layout guided by DNS and

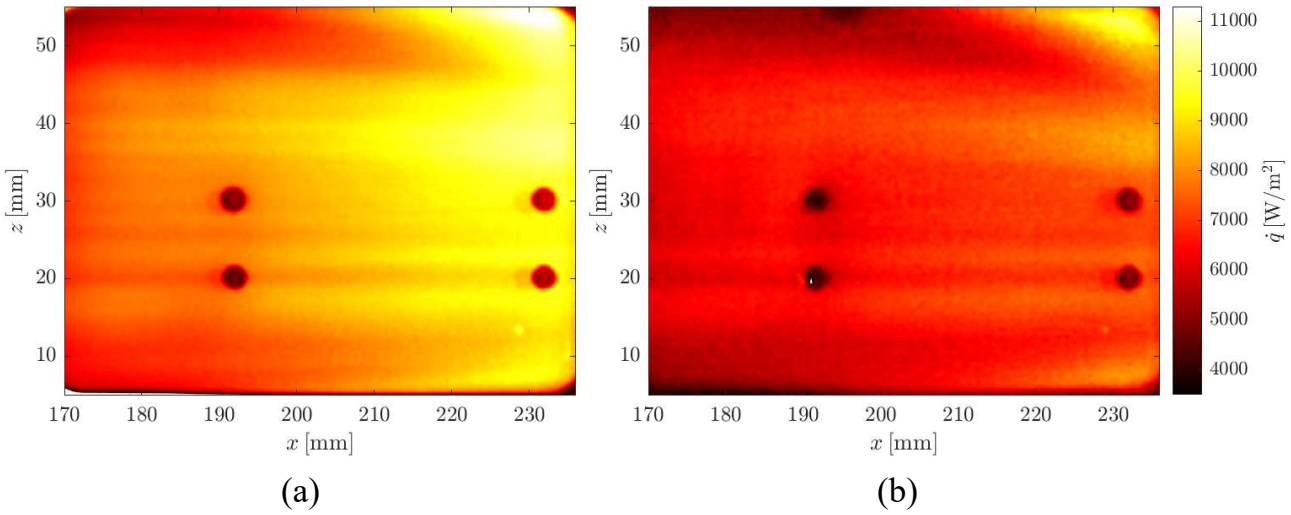


Figure 5.17: Surface heat flux ($\dot{q}$) measurements derived from infrared thermography. 2D contours for (a) the uniform heating baseline ($T_w = 473\,\mathrm{K}$) and (b) the non-uniform forcing case (T_{var}).

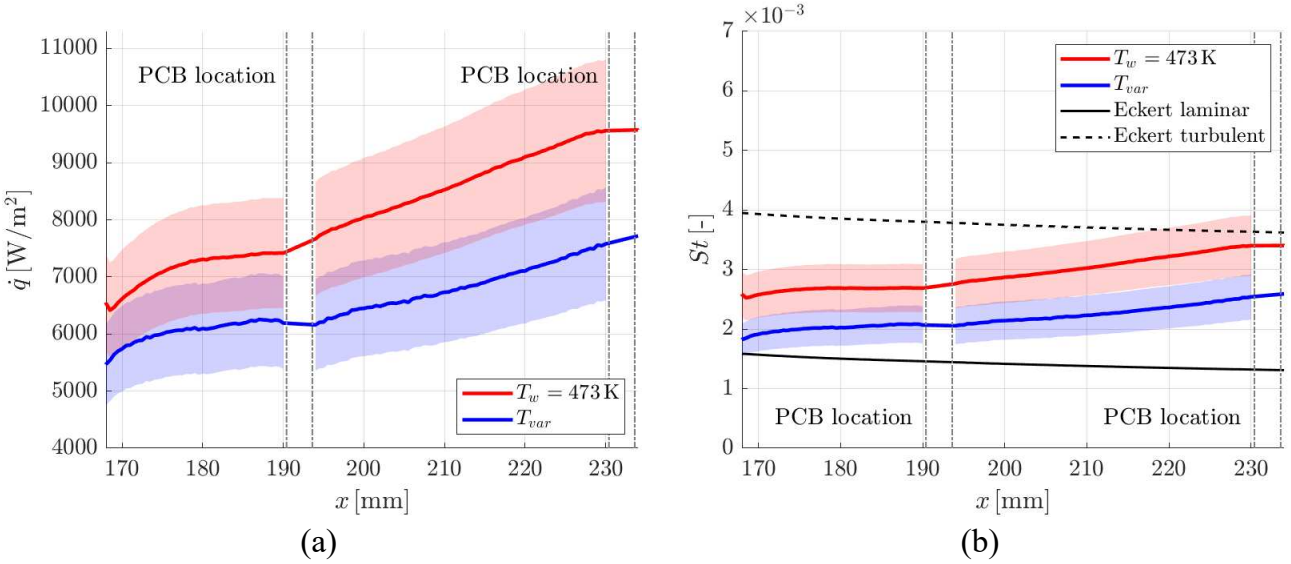


Figure 5.18: Infrared-derived heat-transfer profiles over the downstream resin sensing insert. (a) Reconstructed heat flux, $\dot{q}$. (b) Stanton number, St. The solid coloured lines show spanwise-mean profiles for the uniform $T = 473\,\mathrm{K}$ case and the non-uniform T_{var} case. The shaded bands indicate representative combined uncertainties of $\pm 13\%$ for $\dot{q}$ and $\pm 15\%$ for St. The vertical dash-dot lines mark the PCB pressure-sensor locations, where the infrared-derived values should be interpreted with additional caution.

LST analyses. A transient thermal trade study led to a 3 mm-thick zirconia heating substrate with a 20 mm pitch, producing a spanwise temperature difference of $\Delta T \approx 85\,\mathrm{K}$ and a forcing wavelength of $\lambda_z \approx 13\delta_{99}$ under the present test conditions.

Baseline measurements in the primary transitional operating condition ($Re = 4.8 \times 10^6\,\mathrm{m}^{-1}$) exhibited a high-frequency spectral peak near 170 kHz, consistent with the expected second Mack mode band. Uniform-heating tests over $T_w = 291$–$513\,\mathrm{K}$ modified the spectral characteristics of this peak, demonstrating a clear dependence of the measured pressure spectra on the mean wall temperature.

When spanwise non-uniform heating was applied, the wall-pressure spectra showed a reduction in spectral variance relative to the baseline case, indicating a measurable modification of the instability environment. In addition, infrared-based heat-flux mapping showed lower downstream heat-flux levels compared with the matched uniform-heating baseline. The streamwise evolution of the Stanton number showed a downstream-shifted rise in surface heat transfer for the non-uniform case, consistent with delayed transition. These results motivated a follow-on Mach 5 campaign combining instability-resolved measurements with boundary-layer profiling to directly link spectral changes to streak–instability interaction.

Chapter 6

Conclusion and Future Work

6.1 Thesis Objectives and Scope Revisited

The objective of this thesis was to develop and experimentally validate a physically realisable strategy for imposing controlled spanwise non-uniform wall-temperature distributions in high-speed boundary layers, motivated by numerical studies [76] showing that prescribed thermal patterning can generate steady streaks and influence instability development. The central challenge addressed here was practical implementation: under wind-tunnel constraints, the wall-temperature distribution cannot be prescribed arbitrarily, but must instead emerge from a feasible actuation concept whose thermal response is predictable, repeatable, and compatible with realistic materials, geometry, and transient start-up behaviour.

To address this challenge, the thesis developed passive thermal-actuation designs, supported by a physics-informed heat-conduction model, and validated them through wind-tunnel experiments employing infrared thermography, boundary-layer measurements, and heat-transfer diagnostics. The work proceeded from the development of actuation concepts and predictive modelling tools, through experimental demonstration of non-uniform temperature generation and the resulting boundary-layer response, to a Mach 5 configuration-level demonstration assessing implications for transition behaviour. The remainder of this chapter summarises the main contributions of the thesis and outlines priorities for future work.

6.2 Summary of Main Contributions

(i) Physically Realisable Passive Thermal Actuation

This thesis developed and assessed, using numerical modelling, a practical passive strategy for generating controlled spanwise non-uniform wall-temperature distributions, and assessed its feasibility under both flight-relevant steady thermal design considerations and short-duration wind-tunnel conditions. By exploiting material and geometric tailoring rather than prescribed thermal boundary conditions, the approach enables repeatable temperature patterning within realistic experimental constraints.

(ii) Predictive, Physics-Informed Thermal Modelling Framework

A three-dimensional heat-conduction model was developed to quantify the transient surface temperature response of thermally actuated walls under strong convective loading. The model incorporated experimentally derived boundary conditions, including wind-tunnel start-up behaviour and recovery temperature effects, and showed good agreement with infrared thermography measurements across a range of initial and operating conditions. This framework provides a reliable design tool for actuation development and experimental planning.

(iii) Experimental Validation of Non-Uniform Temperature Fields

Wind-tunnel experiments at Mach 2.75 demonstrated robust generation of spanwise non-uniform surface temperature distributions on a flat-plate configuration. Infrared thermography confirmed the magnitude, spatial structure, and temporal evolution of the imposed temperature patterns, establishing the feasibility and repeatability of passive thermal actuation under strong convective loading.

(iv) Boundary-Layer Response and Thermally Generated Streaks

Boundary-layer measurements revealed that the imposed temperature non-uniformity led to measurable modification of the mean velocity field, consistent with repeatable streak-like mean-flow modulation. These results complement earlier numerical investigations by demonstrating that physically realisable thermal actuation can produce repeatable streak-like mean-flow modulation under wind-tunnel constraints. To the author's knowledge, this is the first experimental demonstration of controlled streak-like mean-flow modulation induced by passive spanwise wall-temperature patterning in a high-speed boundary layer.

(v) Mach 5 Demonstration and Implications for Transition Behaviour

Experiments on a waverider configuration at Mach 5 showed reduced downstream heat transfer and a delayed rise in Stanton number relative to a matched uniform-heating baseline, indicative of a downstream shift in transition onset, as inferred from the surface heat-transfer behaviour. The results demonstrated the extension of passive thermal actuation concepts to a Mach 5 configuration-level experiment using a modular heating-patch system.

6.3 Synthesis and Implications

Taken together, the results of this thesis show that passive thermal actuation can bridge the gap between prescribed wall-temperature distributions considered in idealised studies and practical implementation under wind-tunnel constraints. Specifically, the work demonstrates how prescribed wall-temperature boundary conditions can be realised using experimentally implementable wall designs whose thermal response can be predicted and reproduced under short-duration facility constraints. The central outcome is that spanwise temperature patterning can be generated predictably and repeatably using physically realisable wall designs, and that this forcing produces a measurable boundary-layer response and a heat-transfer signature consistent with a downstream shift of the transition front.

The work also established key design implications for thermal actuation. The achievable temperature contrast is governed by the competition between spanwise diffusion within the wall and the external convective forcing set by recovery temperature and local heat-transfer coefficients. Practical actuation therefore requires material selection and construction that preserve spanwise temperature contrast over the relevant measurement window, together with control of interface effects (e.g. thermal contact resistance) and repeatable initial conditions. These considerations define the thermal-design basis for systematic parametric studies and extension to more complex geometries.

6.4 Limitations of the Present Work

The results of this thesis should be interpreted in light of limitations associated with the facilities and diagnostic scope considered here. First, in the blow-down wind tunnels used for the present Mach 2.75 and Mach 5 campaigns, the wall-temperature field is inherently time dependent during start-up and over the finite run time; achieving a fully developed thermally steady wall-temperature

distribution would require sustained thermal management (e.g. continuous heating and/or cooling) and/or longer-duration facilities.

For the Mach 2.75 flat-plate study, the scope of the measurements was intentionally focused on (i) demonstrating repeatable generation of non-uniform surface temperature distributions and (ii) quantifying the resulting modification of the boundary-layer mean flow using LDA. Accordingly, the present Mach 2.75 dataset was not designed to provide instability-mode identification or a detailed disturbance-budget analysis.

For the Mach 5 configuration-level demonstration, the assessment was based primarily on infrared-derived heat-flux mapping and the streamwise evolution of Stanton number relative to a matched uniform-heating baseline. The present dataset does not include instability-resolved measurements or detailed boundary-layer profiling at Mach 5, and therefore does not permit a direct mechanistic link between the thermal forcing and the underlying instability dynamics.

Finally, across both campaigns, the actuation parameter space and geometry set were necessarily limited by practical considerations. The spanwise wavelength, amplitude, and streamwise extent of the imposed temperature pattern were not systematically optimised, and only a small number of configurations were examined. Consequently, further work is required to establish scaling trends, robustness envelopes, and geometric generality beyond the cases considered here.

6.5 Future Work

(i) Instability-Resolved Characterisation and Experiment–Computation Interpretation
Future work should establish quantitative computational support for each experimental measurement case through one-to-one simulations forced with the experimentally measured wall-temperature distributions. The experimental data contain unsteady spectral signatures and heat-transfer trends associated with instability modes; corresponding simulations would enable direct interpretation of these observations in terms of modal growth, nonlinear interaction, and transition dynamics.

Where feasible, instability-resolved diagnostics should accompany this effort to isolate dominant modes and validate predicted amplification behaviour. The computational framework can additionally provide spatial and temporal resolution beyond current measurement capability, enabling mechanistic

understanding of how passive thermal actuation modifies instability development and alters the transition process.

(ii) Optimisation and Scaling of Thermal Actuation

Systematic variation of spanwise wavelength, temperature amplitude, streamwise placement, and transient history is required to establish robustness envelopes and scaling laws across Mach number, Reynolds number, and wall-to-recovery temperature ratio.

Wind-tunnel facilities capable of independently varying Mach number, unit Reynolds number, and total temperature should be used to quantify how instability response and transition shift scale with both external flow parameters and nondimensional actuation measures (e.g. wavelength relative to boundary-layer thickness and wall-to-recovery temperature ratio). A reconfigurable actuation rig allowing adjustment of wavelength, temperature contrast, and placement would enable systematic mapping of the actuation design space.

Given the multidimensional parameter space, computational parametric studies should first identify critical regimes and scaling trends. Targeted experiments can then be conducted at selected operating points to validate performance and refine predictive scaling laws for passive thermal actuation in high-speed flows.

(iii) Improved Actuation Hardware and Repeatability

Further development of the heating and preheating systems is required to enhance repeatability, controllability, and durability of the imposed thermal forcing. Improved regulation of initial temperature distributions and reduction of thermal contact resistance are necessary to minimise uncertainty in the applied wall-temperature boundary condition.

Thermally induced mechanical effects must also be systematically addressed. Strong temperature gradients, finite-area thermal contacts, or constrained expansion within single or multi-component assemblies can generate internal stresses, interfacial shear, or local surface distortion. Such effects may introduce gaps, compression, or waviness that alter boundary-layer receptivity and compromise structural integrity. Future designs should therefore incorporate thermo-mechanical analysis, expansion-tolerant assemblies, and robust modular architectures to ensure boundary-condition fidelity and repeatable operation.

(iv) Extension Beyond the Flat Plate and Towards Flight-Relevant Implementation

The present work provides a fundamental demonstration on a canonical flat plate and an initial demonstration on a waverider configuration. Future studies should extend the methodology to geometries representative of practical hypersonic vehicles and to longer-duration and/or higher-enthalpy facilities to assess feasibility beyond short-duration blow-down testing.

In such environments, the actuation strategy must be tailored to local boundary-layer conditions. Effective spanwise wavelength, temperature amplitude, and streamwise placement should be determined relative to boundary-layer thickness and dominant instability modes, rather than transferred directly from canonical configurations. Sustaining the prescribed non-uniform temperature distribution under intense and prolonged aerothermal loading will require efficient and robust thermal management.

Finally, thermomechanical integrity and system-level integration become critical in flight-relevant scenarios. Temperature-induced stresses must be controlled to preserve surface smoothness, while mass, volume, and structural integration constraints must be considered to avoid unacceptable penalties on vehicle performance.

Bibliography

[1] Watts, J. D., "Flight experience with shock impingement and interference heating on the X-15-2 research airplane," Tech. rep., NASA Flight Research Center, Edwards, CA, 1968, NASA-TM-X-1669.

[2] Bertin, J. J. and Cummings, R. M., "Fifty years of hypersonics: where we've been, where we're going," *Progress in Aerospace Sciences*, Vol. 39, No. 6-7, Aug. 2003, pp. 511–536.

[3] Bertin, J. J. and Cummings, R. M., "Critical Hypersonic Aerothermodynamic Phenomena," *Annual Review of Fluid Mechanics*, Vol. 38, No. 1, Jan. 2006, pp. 129–157.

[4] Reshotko, E., "Boundary-Layer Stability and Transition," *Annual Review of Fluid Mechanics*, Vol. 8, No. 1, Jan. 1976, pp. 311–349.

[5] Morkovin, M. V., "Transition in open flow systems-a reassessment," *Bull. Am. Phys. Soc.*, Vol. 39, 1994, pp. 1882.

[6] Fedorov, A., "Transition and Stability of High-Speed Boundary Layers," *Annual Review of Fluid Mechanics*, Vol. 43, No. 1, 2011, pp. 79–95.

[7] Schneider, S. P., "Flight Data for Boundary-Layer Transition at Hypersonic and Supersonic Speeds," *Journal of Spacecraft and Rockets*, Vol. 36, No. 1, Jan. 1999, pp. 8–20.

[8] Andersson, P., Berggren, M., and Henningson, D. S., "Optimal disturbances and bypass transition in boundary layers," *Physics of Fluids*, Vol. 11, No. 1, 1999, pp. 134–150.

[9] Kosinov, A. D., Maslov, A. A., and Shevelkov, S. G., "Experiments on the stability of supersonic laminar boundary layers," *Journal of Fluid Mechanics*, Vol. 219, 1990, pp. 621–633.

[10] Chang, C.-L. and Malik, M. R., "Oblique-mode breakdown and secondary instability in supersonic boundary layers," *Journal of Fluid Mechanics*, Vol. 273, 1994, pp. 323–360.

[11] Fasel, H., Thumm, A., and Bestek, H., "Direct numerical simulation of transition in supersonic boundary layers: oblique breakdown," *ASME-PUBLICATIONS-FED*, Vol. 151, 1993, pp. 77–77.

[12] Sandham, N. D., Adams, N. A., and Kleiser, L., "Direct simulation of breakdown to turbulence following oblique instability waves in a supersonic boundary layer," *Applied scientific research*, Vol. 54, No. 3, 1995, pp. 223–234.

[13] Mack, L. M., "Linear Stability Theory and the Problem of Supersonic Boundary- Layer Transition," *AIAA Journal*, Vol. 13, No. 3, March 1975, pp. 278–289.

[14] Mack, L. M., "Boundary-layer linear stability theory," *AGARD–R–709 Special course on stability and transition of laminar flow*, 1984, pp. 3.1–3.81.

[15] Zhang, C., Zhu, Y., Chen, X., Yuan, H., Wu, J., Chen, S., Lee, C., and Gad-el Hak, M., "Transition in hypersonic boundary layers," *AIP Advances*, Vol. 5, No. 10, Oct. 2015, pp. 107137.

[16] Casper, K. M., Beresh, S. J., Henfling, J. F., Spillers, R. W., Pruett, B. O. M., and Schneider, S. P., "Hypersonic Wind-Tunnel Measurements of Boundary-Layer Transition on a Slender Cone," *AIAA Journal*, Vol. 54, No. 4, April 2016, pp. 1250–1263.

[17] Laurence, S. J., Wagner, A., and Hannemann, K., "Experimental study of second-mode instability growth and breakdown in a hypersonic boundary layer using high-speed schlieren visualization," *Journal of Fluid Mechanics*, Vol. 797, June 2016, pp. 471–503.

[18] Zhang, C. and Lee, C., "Rayleigh-scattering visualization of the development of second-mode waves," *Journal of Visualization*, Vol. 20, No. 1, Feb. 2017, pp. 7–12.

[19] Casper, K., Beresh, S., Henfling, J., Spillers, R., Pruett, B., and Schneider, S., "Hypersonic Wind-Tunnel Measurements of Boundary-Layer Pressure Fluctuations," *39th AIAA Fluid Dynamics Conference*, American Institute of Aeronautics and Astronautics, San Antonio, Texas, June 2009.

[20] Siddiqui, F., Gragston, M., Saric, W. S., and Bowersox, R. D. W., "Mack-mode instabilities on a cooled flared cone with discrete roughness elements at Mach 6," *Experiments in Fluids*, Vol. 62, No. 10, 2021.

[21] Gui, Y., Zhang, C., Li, X., Xu, D., and Wu, J., "Hypersonic boundary-layer instability characterization and transition downstream of distributed roughness," *Experiments in Fluids*, Vol. 64, No. 10, Oct. 2023, pp. 159.

[22] Pruett, C. D. and Zang, T. A., "Direct numerical simulation of laminar breakdown in high-speed, axisymmetric boundary layers," *Theoretical and Computational Fluid Dynamics*, Vol. 3, No. 6, Sept. 1992, pp. 345–367.

[23] Pruett, C. D. and Chang, C.-L., "Spatial direct numerical simulation of high-speed boundary-layer flows Part II: Transition on a cone in Mach 8 flow," *Theoretical and Computational Fluid Dynamics*, Vol. 7, No. 5, Sept. 1995, pp. 397–424.

[24] Stetson, K. and Kimmel, R., "On the breakdown of a hypersonic laminar boundary layer," *31st Aerospace Sciences Meeting*, 1993, p. 896.

[25] Franko, K. J. and Lele, S. K., "Breakdown mechanisms and heat transfer overshoot in hypersonic zero pressure gradient boundary layers," *Journal of Fluid Mechanics*, Vol. 730, Sept. 2013, pp. 491–532.

[26] Sivasubramanian, J. and Fasel, H. F., "Direct numerical simulation of transition in a sharp cone boundary layer at Mach 6: fundamental breakdown," *Journal of Fluid Mechanics*, Vol. 768, April 2015, pp. 175–218.

[27] Kloker, M., "DNS of transitional boundary-layer flows at sub-and hypersonic speeds," *DGLR Paper JT2002-017, DGLR-Jahrestagung, Stuttgart*, 2002.

[28] Koevary, C., Laible, A., Mayer, C., and Fasel, H., "Numerical simulations of controlled transition for a circular cone at Mach 8," *40th Fluid Dynamics Conference and Exhibit*, 2010, p. 4598.

[29] Stetson, K., "Nosetip bluntness effects on cone frustum boundary layer transition in hypersonic flow," *16th Fluid and Plasmadynamics Conference*, American Institute of Aeronautics and Astronautics, Danvers,MA,U.S.A., July 1983.

[30] Schneider, S. P., "Hypersonic laminar–turbulent transition on circular cones and scramjet forebodies," *Progress in Aerospace Sciences*, Vol. 40, No. 1-2, Feb. 2004, pp. 1–50.

[31] Aleksandrova, E. A., Novikov, A. V., Utyuzhnikov, S. V., and Fedorov, A. V., "Experimental study of the laminar-turbulent transition on a blunt cone," *Journal of Applied Mechanics and Technical Physics*, Vol. 55, No. 3, May 2014, pp. 375–385.

[32] Paredes, P., Choudhari, M. M., Li, F., Jewell, J. S., Kimmel, R. L., Marineau, E. C., and Grossir, G., "Nose-Tip Bluntness Effects on Transition at Hypersonic Speeds," *Journal of Spacecraft and Rockets*, Vol. 56, No. 2, March 2019, pp. 369–387.

[33] Huang, R., Cheng, J., Chen, J., Yuan, X., and Wu, J., "Experimental study of bluntness effects on hypersonic boundary-layer transition over a slender cone using surface mounted pressure sensors," *Advances in Aerodynamics*, Vol. 4, No. 1, Nov. 2022, pp. 35.

[34] Malik, M., Spall, R., and Chang, C.-L., "Effect of nose bluntness on boundary layer stability and transition," *28th Aerospace Sciences Meeting*, American Institute of Aeronautics and Astronautics, Reno,NV,U.S.A., Jan. 1990.

[35] Horvath, T., Berry, S., Hollis, B., Singer, B., and Chang, C.-L., "Boundary Layer Transition on Slender Cones in Conventional and Low Disturbance Mach 6 Wind Tunnels," *32nd AIAA Fluid Dynamics Conference and Exhibit*, American Institute of Aeronautics and Astronautics, St. Louis, Missouri, June 2002.

[36] Paredes, P., Choudhari, M. M., and Li, F., "Mechanism for frustum transition over blunt cones at hypersonic speeds," *Journal of Fluid Mechanics*, Vol. 894, July 2020.

[37] Kara, K., Balakumar, P., and Kandil, O., "Effects of Wall Cooling on Hypersonic Boundary Layer Receptivity over a Cone," *38th Fluid Dynamics Conference and Exhibit*, American Institute of Aeronautics and Astronautics, Seattle, Washington, June 2008.

[38] Masad, J. A., "Relationship between transition and modes of instability in high-speed boundary layers," *AIAA journal*, Vol. 33, No. 4, 1995, pp. 774–776.

[39] Masad, J. A. and Abid, R., "On transition in supersonic and hypersonic boundary layers," *International Journal of Engineering Science*, Vol. 33, No. 13, Oct. 1995, pp. 1893–1919.

[40] Unnikrishnan, S. and Gaitonde, D. V., "Instabilities and transition in cooled wall hypersonic boundary layers," *Journal of Fluid Mechanics*, Vol. 915, May 2021, pp. A26.

[41] Oddo, R., Hill, J. L., Reeder, M. F., Chin, D., Embrador, J., Komives, J., Tufts, M., Borg, M., and Jewell, J. S., "Effect of surface cooling on second-mode dominated hypersonic boundary layer transition," *Experiments in Fluids*, Vol. 62, No. 7, July 2021, pp. 144.

[42] Polivanov, P., Gromyko, Y., Sidorenko, A., Maslov, A., Keller, M., Groskopf, G., and Kloker, M. J., "Effects of local wall heating and cooling on hypersonic boundary-layer stability," *Proceedings of the Summer Program*, Vol. 1, 2011.

[43] Soudakov, V., Fedorov, A., and Egorov, I., "Investigations of laminar-turbulent transition on a sharp cone with localized heating or cooling in high-speed flow," *51st AIAA Aerospace Sciences Meeting including the New Horizons Forum and Aerospace Exposition*, 2013, p. 524.

[44] Fedorov, A., Soudakov, V., Egorov, I., Sidorenko, A., Gromyko, Y., Bountin, D., Polivanov, P., and Maslov, A., "High-speed boundary-layer stability on a cone with localized wall heating or cooling," *AIAA Journal*, Vol. 53, No. 9, 2015, pp. 2512–2524.

[45] Sidorenko, A., Gromyko, Y., Bountin, D., Polivanov, P., and Maslov, A., "Effect of the local wall cooling/heating on the hypersonic boundary layer stability and transition," *Progress in Flight Physics–Volume 7*, Vol. 7, 2015, pp. 549–568.

[46] Zhao, R., Wen, C., Tian, X., Long, T., and Yuan, W., "Numerical simulation of local wall heating and cooling effect on the stability of a hypersonic boundary layer," *International Journal of Heat and Mass Transfer*, Vol. 121, June 2018, pp. 986–998.

[47] Batista, A. and Kuehl, J. J., "Local wall temperature effects on the second-mode instability," *Journal of Spacecraft and Rockets*, Vol. 57, No. 3, 2020, pp. 580–595.

[48] Oz, F., Goebel, T. E., Jewell, J. S., and Kara, K., "Local Wall Cooling Effects on Hypersonic Boundary-Layer Stability," *Journal of Spacecraft and Rockets*, Vol. 60, No. 2, March 2023, pp. 412–426.

[49] Poulain, A., Content, C., Rigas, G., Garnier, E., and Sipp, D., "Adjoint-based linear sensitivity of a supersonic boundary layer to steady wall blowing–suction/heating–cooling," *Journal of Fluid Mechanics*, Vol. 978, Jan. 2024, pp. A16.

[50] Fedorov, A. V., Malmuth, N. D., Rasheed, A., and Hornung, H. G., "Stabilization of Hypersonic Boundary Layers by Porous Coatings," *AIAA Journal*, Vol. 39, No. 4, April 2001, pp. 605–610.

[51] Fedorov, A., Shiplyuk, A., Maslov, A., Burov, E., and Malmuth, N., "Stabilization of a hypersonic boundary layer using an ultrasonically absorptive coating," *Journal of Fluid Mechanics*, Vol. 479, March 2003, pp. 99–124.

[52] Rasheed, A., Hornung, H. G., Fedorov, A. V., and Malmuth, N. D., "Experiments on Passive Hypervelocity Boundary-Layer Control Using an Ultrasonically Absorptive Surface," *AIAA Journal*, Vol. 40, No. 3, March 2002, pp. 481–489.

[53] Wagner, A., Kuhn, M., Martinez Schramm, J., and Hannemann, K., "Experiments on passive hypersonic boundary layer control using ultrasonically absorptive carbon–carbon material with random microstructure," *Experiments in Fluids*, Vol. 54, No. 10, Oct. 2013, pp. 1606.

[54] Wagner, A., Hannemann, K., and Kuhn, M., "Ultrasonic absorption characteristics of porous carbon–carbon ceramics with random microstructure for passive hypersonic boundary layer transition control," *Experiments in Fluids*, Vol. 55, No. 6, June 2014, pp. 1750.

[55] Sousa, V. C. B., Patel, D., Chapelier, J.-B., Wartemann, V., Wagner, A., and Scalo, C., "Numerical Investigation of Second-Mode Attenuation over Carbon/Carbon Porous Surfaces," *Journal of Spacecraft and Rockets*, Vol. 56, No. 2, March 2019, pp. 319–332.

[56] Running, C. L., Bemis, B. L., Hill, J. L., Borg, M. P., Redmond, J. J., Jantze, K., and Scalo, C., "Attenuation of hypersonic second-mode boundary-layer instability with an ultrasonically absorptive silicon-carbide foam," *Experiments in Fluids*, Vol. 64, No. 4, April 2023.

[57] Andersson, P., Brandt, L., Bottaro, A., and Henningson, D. S., "On the breakdown of boundary layer streaks," *Journal of Fluid Mechanics*, Vol. 428, Feb. 2001, pp. 29–60.

[58] Fransson, J. H. M., Brandt, L., Talamelli, A., and Cossu, C., "Experimental study of the stabilization of Tollmien–Schlichting waves by finite amplitude streaks," *Physics of Fluids*, Vol. 17, No. 5, May 2005.

[59] Fransson, J. H. M., Talamelli, A., Brandt, L., and Cossu, C., "Delaying Transition to Turbulence by a Passive Mechanism," *Physical Review Letters*, Vol. 96, No. 6, Feb. 2006.

[60] Bagheri, S. and Hanifi, A., "The stabilizing effect of streaks on Tollmien-Schlichting and oblique waves: A parametric study," *Physics of Fluids*, Vol. 19, No. 7, July 2007.

[61] Fransson, J. H. M. and Talamelli, A., "On the generation of steady streamwise streaks in flat-plate boundary layers," *Journal of Fluid Mechanics*, Vol. 698, May 2012, pp. 211–234.

[62] Ren, J., Fu, S., and Hanifi, A., "Stabilization of the hypersonic boundary layer by finite-amplitude streaks," *Physics of Fluids*, Vol. 28, No. 2, Feb. 2016, pp. 024110.

[63] Paredes, P., Choudhari, M. M., and Li, F., "Transition Delay in Hypersonic Boundary Layers via Optimal Perturbations," Vol. NASA/TM 2916-219210, 2016.

[64] Landahl, M. T., "A note on an algebraic instability of inviscid parallel shear flows," *Journal of Fluid Mechanics*, Vol. 98, No. 2, May 1980, pp. 243–251.

[65] Fransson, J. H. M., Brandt, L., Talamelli, A., and Cossu, C., "Experimental and theoretical investigation of the nonmodal growth of steady streaks in a flat plate boundary layer," *Physics of Fluids*, Vol. 16, No. 10, Oct. 2004, pp. 3627–3638.

[66] Marxen, O., Lang, M., and Rist, U., "Vortex formation and vortex breakup in a laminar separation bubble," *Journal of Fluid Mechanics*, Vol. 728, Aug. 2013, pp. 58–90.

[67] Shahinfar, S., Sattarzadeh, S. S., Fransson, J. H. M., and Talamelli, A., "Revival of Classical Vortex Generators Now for Transition Delay," *Physical Review Letters*, Vol. 109, No. 7, Aug. 2012.

[68] Shahinfar, S., Sattarzadeh, S., and Fransson, J., "Passive boundary layer control of oblique disturbances by finite-amplitude streaks," *Journal of Fluid Mechanics*, Vol. 749, June 2014, pp. 1–36.

[69] Holloway, P. F. and Sterrett, J. R., "Effect of controlled surface roughness on boundary-layer transition and heat transfer at mach numbers of 4.8 and 6.0," *NASA*, Vol. TR-D-2054, 1964.

[70] Fujii, K., "Experiment of the Two-Dimensional Roughness Effect on Hypersonic Boundary-Layer Transition," *Journal of Spacecraft and Rockets*, Vol. 43, No. 4, July 2006, pp. 731–738.

[71] Fiala, A., Hillier, R., and Estruch-Samper, D., "Roughness-induced turbulent wedges in a hypersonic blunt-body boundary layer," *Journal of Fluid Mechanics*, Vol. 754, Sept. 2014, pp. 208–231.

[72] Leidy, A., King, R., Choudhari, M. M., and Paredes, P., "Hypersonic Second Mode Instability Response to Shaped Roughness," *AIAA Scitech 2021 Forum*, American Institute of Aeronautics and Astronautics, VIRTUAL EVENT, Jan. 2021.

[73] Groskopf, G. and Kloker, M. J., "Instability and transition mechanisms induced by skewed roughness elements in a high-speed laminar boundary layer," *Journal of Fluid Mechanics*, Vol. 805, Oct. 2016, pp. 262–302.

[74] Taylor, O. W. and Bruce, P. J., "A Parametric Study into the Effects of Surface Roughness Spacing on the Transition of Hypersonic Boundary Layers," *54th AIAA Aerospace Sciences Meeting*, American Institute of Aeronautics and Astronautics, San Diego, California, USA, Jan. 2016.

[75] Taylor, O., *Effects of surface roughness on boundary layer transition in a hypersonic flow*, Ph.D. thesis, Imperial College London, Oct. 2018.

[76] Ozawa, K., Xia, C., Rigas, G., and Bruce, P., "Spanwise Nonuniform Surface Temperature Distributions for High-Speed Boundary-Layer Transition Control," *AIAA Journal*, Vol. 63, No. 10, Oct. 2025, pp. 4249–4260.

[77] Ozawa, K. and Bruce, P., "Generation of Streaks by Non-Uniform Surface Temperature Distributions for Hypersonic Boundary Layer Transition Control," *AIAA SCITECH 2025 Forum*, Orlando, FL, Jan. 2025, AIAA Paper 2025-0262.

[78] Boscagli, L., Marxen, O., Rigas, G., and Bruce, P., "Direct numerical simulations of hypersonic boundary layer transition control via non-uniform surface temperature distribution," *AIAA SCITECH 2025 Forum*, Orlando, FL, 2025, AIAA Paper 2025-0266.

[79] Gramola, M., Bruce, P. J., and Santer, M. J., "Temperature corrected Pressure Sensitive Paint measurements on a flexible surface," *AIAA SCITECH 2021 Forum*, San Francisco, CA, 2021, AIAA Paper 2021-0128.

[80] Gramola, M., Bruce, P. J., and Santer, M. J., "Engineering model for heat transfer to a complex-geometry deployable heat shield," *AIAA SCITECH 2021 Forum*, San Francisco, CA, 2021, AIAA Paper 2021-0355.

[81] Ozawa, K., Xia, C., Rigas, G., and Bruce, P. J., "Passive control of high-speed boundary layer transition using non-uniform surface temperature distributions," *AIAA SCITECH 2023 Forum*, National Harbor, MD & Online, Jan. 2023, AIAA Paper 2023-0849.

[82] Ozawa, K. and Bruce, P., "Experimental generation of non-uniform surface temperature distributions in high-speed flow," Preprint rs-7581926/v1, Research Square, Oct. 2025.

[83] White, F. M. and Majdalani, J., *Viscous Fluid Flow*, Vol. 3, McGraw-Hill New York, 2006.

[84] Van Driest, E. R., "Calculation of the Stability of the Laminar Boundary Layer in a Compressible Fluid on a Flat Plate with Heat Transfer," *Journal of the Aeronautical Sciences*, Vol. 19, No. 12, Dec. 1952, pp. 801–812.

[85] Ashby, M. F., *Materials selection in mechanical design*, Butterworth-Heinemann, Amsterdam ; Cambridge, MA, fifth edition ed., 2017.

[86] Threadgill, J. A. S. and Bruce, P. J. K., "Unsteady Flow Features Across Different Shock/Boundary-Layer Interaction Configurations," *AIAA Journal*, Vol. 58, No. 7, July 2020, pp. 3063–3075.

[87] Unutulmazsoy, Y., Cancellieri, C., Chiodi, M., Siol, S., Lin, L., and Jeurgens, L. P., "In situ oxidation studies of Cu thin films: Growth kinetics and oxide phase evolution," *Journal of Applied Physics*, Vol. 127, No. 6, 2020.

[88] Honkanen, M., Vippola, M., and Lepistö, T., "Low temperature oxidation of copper alloys—AEM and AFM characterization," *Journal of materials science*, Vol. 42, No. 12, 2007, pp. 4684–4691.

[89] Castrejón-Sánchez, V.-H., Solís, A. C., López, R., Encarnación-Gomez, C., Morales, F. M., Vargas, O. S., Mastache-Mastache, J. E., and Sánchez, G. V., "Thermal oxidation of copper over a broad temperature range: towards the formation of cupric oxide (CuO)," *Materials Research Express*, Vol. 6, No. 7, April 2019, pp. 075909.

[90] Ozawa, H., Laurence, S. J., Schramm, J. M., Wagner, A., and Hannemann, K., "Fast-response temperature-sensitive-paint measurements on a hypersonic transition cone," *Experiments in Fluids*, Vol. 56, No. 1, 2015, pp. 1853.

[91] Avallone, F., Greco, C. S., Schrijer, F. F. J., and Cardone, G., "A low-computational-cost inverse heat transfer technique for convective heat transfer measurements in hypersonic flows," *Experiments in Fluids*, Vol. 56, No. 4, April 2015.

[92] Cardone, G., Ianiro, A., Dello Ioio, G., and Passaro, A., "Temperature maps measurements on 3D surfaces with infrared thermography," *Experiments in Fluids*, Vol. 52, No. 2, Feb. 2012, pp. 375–385.

[93] Carlomagno, G. M. and Cardone, G., "Infrared thermography for convective heat transfer measurements," *Experiments in Fluids*, Vol. 49, No. 6, Dec. 2010, pp. 1187–1218.

[94] Grossman, I. J. and Bruce, P. J. K., "Confinement effects on regular–irregular transition in shock-wave–boundary-layer interactions," *Journal of Fluid Mechanics*, Vol. 853, Oct. 2018, pp. 171–204.

[95] Meador, W. E. and Smart, M. K., "Reference Enthalpy Method Developed from Solutions of the Boundary-Layer Equations," *AIAA Journal*, Vol. 43, No. 1, Jan. 2005, pp. 135–139.

[96] Sun, C.-C. and Childs, M. E., "Wall-wake velocity profile for compressible nonadiabatic flows," *AIAA Journal*, Vol. 14, No. 6, June 1976, pp. 820–822.

[97] Musker, A. J., "Explicit Expression for the Smooth Wall Velocity Distribution in a Turbulent Boundary Layer," *AIAA Journal*, Vol. 17, No. 6, June 1979, pp. 655–657.

[98] Titchener, N., Colliss, S., and Babinsky, H., "On the calculation of boundary-layer parameters from discrete data," *Experiments in Fluids*, Vol. 56, No. 8, Aug. 2015, pp. 159.

[99] Sabnis, K., Galbraith, D. S., Babinsky, H., and Benek, J. A., "Nozzle geometry effects on supersonic wind tunnel studies of shock–boundary-layer interactions," *Experiments in Fluids*, Vol. 63, No. 12, Dec. 2022, pp. 191.

[100] Brandt, L., "The lift-up effect: The linear mechanism behind transition and turbulence in shear flows," *European Journal of Mechanics - B/Fluids*, Vol. 47, Sept. 2014, pp. 80–96.

[101] Pirozzoli, S. and Bernardini, M., "Turbulence in supersonic boundary layers at moderate Reynolds number," *Journal of Fluid Mechanics*, Vol. 688, Dec. 2011, pp. 120–168.

[102] Duan, L., Beekman, I., and Martin, M. P., "Direct numerical simulation of hypersonic turbulent boundary layers. Part 2. Effect of wall temperature," *Journal of Fluid Mechanics*, Vol. 655, 2010, pp. 419–445, ISBN: 1469-7645.

[103] Ozawa, K., Boscagli, L., Rigas, G., Bruce, P. J., Gurbuz, M. T., Ozer, O., and Quinn, M. K., "Influence of Non-Uniform Surface Temperature Distributions on Hypersonic Boundary Layer," *AIAA SCITECH 2026 Forum*, American Institute of Aeronautics and Astronautics, Orlando, FL, Jan. 2026.

[104] Ivison, W., *Quantifying the effect of protuberances and interfaces from an aero-thermal-structural design perspective*, Ph.D. thesis, University of Oxford, 2024.

[105] Oldfield, M. L. G., "Impulse Response Processing of Transient Heat Transfer Gauge Signals," *Journal of Turbomachinery*, Vol. 130, No. 2, April 2008, pp. 021023.